

The Pennsylvania State University
The Graduate School
Eberly College of Science

**MEASUREMENT OF ATMOSPHERIC TAU NEUTRINO
APPEARANCE WITH ICECUBE/DEEPCORE**

A Dissertation in
Department of Physics
by
Feifei Huang

© 2018 Feifei Huang

Submitted in Partial Fulfillment
of the Requirements
for the Degree of

Doctor of Philosophy

July 2018

The dissertation of Feifei Huang was reviewed and approved* by the following:

Douglas Cowen
Professor of Physics
Professor of Astronomy and Astrophysics
Thesis Advisor, Chair of Committee

Stéphane Coutu
Professor of Physics
Professor of Astronomy and Astrophysics

Derek Brindley Fox
Associate Professor of Astronomy and Astrophysics

Miguel Alejandro Mostafá
Professor of Physics
Professor of Astronomy and Astrophysics

*Signatures are on file in the Graduate School.

Abstract

IceCube is a neutrino detector located inside a cubic kilometer of ice at the South Pole. Its geometry design makes it able to measure neutrinos in a large energy range from as low as 5 GeV up to a few PeV. The low energy subarray DeepCore can measure neutrinos as low as 5 GeV to roughly 100 GeV.

This dissertation presented a measurement of atmospheric tau neutrino appearance with three years of IceCube/DeepCore data.

The key physics parameter is ν_τ (CC + NC) normalization, a scale factor assigned to the signal ν_τ (CC+NC) events, varying between 0 and 1, where the value of one corresponds to the expected rate assuming the standard three-flavor neutrino oscillations.

The best fit ν_τ (CC + NC) normalization was 0.59 with the 68% C.I. in [0.34, 0.90], *i.e.*, $0.59^{+0.31}_{-0.25}$. The 90% C.I. was [0.18, 1.12]. This corresponds to 1379 ν_τ events out of a total of 40,959 events (which includes 39,070 all-neutrino-flavor events and 1,889 atmospheric muons).

To compare with two previous experiments, the measurement of ν_τ CC normalization was also conducted, where a scale factor ν_τ CC normalization is assigned to the signal ν_τ CC-only events. The best fit ν_τ CC normalization was 0.43, with the 68% C.I. being [0.12, 0.80], *i.e.*, $0.43^{+0.36}_{-0.43}$, and the 90% C.I. was [0, 1.07].

Both the measured ν_τ (CC + NC) normalization and ν_τ CC normalization are consistent with existing measurements and the standard three-flavor oscillation paradigm at 90% C.L.

Table of Contents

List of Figures	viii
List of Tables	xx
Acknowledgments	xxii
Chapter 1	
Neutrino Oscillations	2
1.1 Neutrinos	2
1.2 Neutrino Oscillations in Vacuum	3
1.2.1 PMNS matrix	3
1.2.2 The Two Neutrino Approximation	7
1.3 Neutrino Oscillations in Matter	8
1.3.1 MSW Effect	9
1.3.2 Matter Effects for DeepCore	10
1.4 Tau Neutrino Appearance	11
1.4.1 Tau Neutrinos	11
1.4.2 Tau Neutrino Appearance Experiments	12
1.4.2.1 OPERA	15
1.4.2.2 Super-K	16
Chapter 2	
Atmospheric Neutrinos	18
2.1 Cosmic Rays	19
2.2 Creation of Atmospheric Neutrinos	20
2.3 Oscillations of Atmospheric Neutrinos	25
2.4 Atmospheric Neutrino Flux Calculation Model	25
2.5 Flux Uncertainties	27

Chapter 3	
IceCube and Neutrino Detection	29
3.1 IceCube	29
3.1.1 DeepCore Fiducial Region	32
3.1.2 DOM Properties	32
3.1.3 Photoelectrons, Hits, and Local Coincidence	33
3.1.4 Data Flow	34
3.2 Neutrino Detection	36
3.2.1 Neutrino Interactions	37
3.2.2 ν_τ Deep Inelastic Scattering (DIS)	37
3.2.3 Detector Signatures	39
3.2.4 Cherenkov Radiation	40
3.3 Ice Properties	41
Chapter 4	
Monte Carlo Simulation and Reconstruction	46
4.1 Simulation	46
4.1.1 Event Generation	46
4.1.2 Propagation of Secondaries	48
4.1.3 Photon Propagation	49
4.1.4 Noise Simulation	49
4.1.5 DOM Simulation	49
4.1.6 Triggering	49
4.2 Reconstruction	50
4.2.1 Photon Tables	51
4.2.2 HybridReco	51
4.2.3 Pegleg	52
4.2.4 Likelihood Minimizer: MultiNest	53
4.3 Reconstruction Resolution	54
Chapter 5	
Event selection	57
5.1 Definition of DeepCore Fiducial Volume	58
5.2 Level 2: Online DeepCore Filter	59
5.2.1 Definition of “Particle Speed”	59
5.2.2 Cut Region of “Particle Speed”	62
5.3 Triggering and Vetoing in Level 3 and 4	63
5.3.1 Triggering in Level 4	63
5.3.2 Vetoing in Level 3	66
5.3.3 Vetoing in Level 4	68

5.4	Cut Using Boosted Decision Tree	68
5.5	Corridor Cut in Level 6	70
5.6	Containment Cuts	71
5.7	Background Estimation	72

Chapter 6

Analysis Techniques		75
6.1	Physics Parameter (ν_τ Normalization)	75
6.2	Binning	76
6.3	Fit Statistic	78
6.4	Confidence Interval	82
6.4.1	Feldman-Cousins Confidence Interval	82
6.5	Expected Sensitivity	83
6.6	Data Challenge	84
6.7	Treatment of Systematics	84
6.7.1	Smooth Systematics	85
6.7.2	Discrete Systematics	87
6.7.3	Hyperplane Parametrization for Discrete Systematics	88

Chapter 7

Systematic Uncertainties		97
7.1	Flux-Related Systematics	97
7.2	Oscillation-Related Systematics	98
7.3	Neutrino Interaction Systematics	99
7.4	Detector-Related Systematics	102
7.4.1	DOM Optical Efficiency	102
7.4.2	Ice Properties	103
7.4.2.1	Bulk Ice	103
7.4.2.2	Hole Ice	104
7.5	Normalization Systematics	107
7.6	N-1 Test	110

Chapter 8

Analysis Results		113
8.1	ν_τ Normalization	113
8.2	Best Fit Parameters	113
8.3	Good Runs	116
8.4	Goodness of Fit	116
8.5	Number of Events Expected (After Fit)	117
8.6	Event Distributions	117

Chapter 9	
Conclusions	133
Appendix A	
Past Work	134
A.1 Development of a Faster Reconstruction with HybridReco/MultiNest	134
A.2 PINGU Hardware Studies	140
A.2.1 Dynamic Range of PDOM	140
A.2.2 DOM-to-DOM Timing Precision	142
A.2.3 Physics Requirement for the Buffer Length of PDOM Firmware	148
A.2.4 Sampling rate study	151
Bibliography	154
Acronyms	164

List of Figures

1.1	The constraints on the six normalizations, taken from Ref. [6]. Solid lines are summations involving row elements, dashed lines are for column elements.	4
1.2	The constraints on the six unitary triangles, taken from Ref. [6]. Solid lines are summations involving row elements, dashed lines are for column elements.	5
1.3	Neutrino mass hierarchy. Normal hierarchy means $m_1 < m_2 < m_3$, inverted hierarchy means $m_3 < m_1 < m_2$. $\Delta m_{\text{sol}}^2 = \Delta m_{21}^2 > 0$. Δm_{atm}^2 is either Δm_{32}^2 under the normal hierarchy or $ \Delta m_{31}^2 $ under the inverted hierarchy. Figure taken from Ref. [7].	6
1.4	Feynman diagram of coherent forward scattering [10]. Left: charged current interaction. Right: neutral current interaction.	9
1.5	(a) The density of the Earth as a function of the radial distance from the center of the Earth from PREM. (b) The zenith angle of the neutrinos that travel along the border of the core and the mantle is 146.9° . The PREM density curve is placed on top to show the corresponding densities for each layer.	11
1.6	Survival probabilities of electron neutrinos as a function of neutrino energy and zenith angle. (a) assumes vacuum. (b) uses the 12-layer PREM model [12].	12
1.7	Probabilities of electron neutrinos disappearing into muon neutrinos as a function of neutrino energy and zenith angle. (a) assumes vacuum condition. (b) uses the 12-layer PREM model [12].	12
1.8	Probabilities of electron neutrinos disappearing into tau neutrinos as a function of neutrino energy and zenith angle. (a) assumes vacuum condition. (b) uses the 12-layer PREM model [12].	13
1.9	Probabilities of muon neutrinos disappearing into electron neutrinos as a function of neutrino energy and zenith angle. (a) assumes vacuum condition. (b) uses the 12-layer PREM model [12].	13

1.10	Survival probabilities of muon neutrinos as a function of neutrino energy and zenith angle. (a) assumes vacuum condition. (b) uses the 12-layer PREM model [12].	14
1.11	Probabilities of muon neutrinos disappearing into tau neutrinos as a function of neutrino energy and zenith angle. (a) assumes vacuum condition. (b) uses the 12-layer PREM model [12].	14
1.12	A display of OPERA's fifth event. V_0 is the primary vertex and V_1 the secondary vertex. The black stubs are the measurements in the films, taken from Ref. [17].	16
1.13	Super-K's event distribution in $\cos(\text{zenith})$ and NN output. See the definition of the zenith angle in Chapter 2. Fitted ν_τ signal is the gray colored part. The subplots are tau-like (NN>0.5), upward-going [$\cos(\theta_{\text{zen}}) < -0.2$], non-tau-like (NN<0.5) and downward-going [$\cos(\theta_{\text{zen}}) > 0.2$], taken from Ref. [14].	17
2.1	Neutrino fluxes from different sources, including naturally occurring and artificial neutrinos, such as reactor neutrinos [29].	19
2.2	The definition of the zenith angle θ_{zenith} and baseline L . d is the detector depth. D is the production height of the atmospheric neutrinos (used in simulation). R is the Earth's radius.	20
2.3	Left: Primary cosmic ray composition [33]. Right: The flux of cosmic rays as a function of the energy. Generally speaking, it falls off approximately proportional to E^{-3} (shown in green dashed line) [34].	21
2.4	Contributions from kaons and pions to muon neutrinos and muons at different energies, solid lines represent pions or kaons traveling vertically, dashed lines are those traveling with a zenith angle of 60° . We see that the contribution from kaons is smaller in our energy range of interest 10 – 100 GeV [36].	22
2.5	Flux comparisons of conventional neutrinos and prompt neutrinos. GH stands for the Gaisser and Honda model [36], TIG stands for the Thunman, Ingelman and Gondolo [37] model. DM stands for "dipole model" used for the prompt neutrino flux calculation in Ref. [38]. The gray band is the theoretical uncertainty of the prompt model. Figure taken from Ref. [38].	23
2.6	Comparison of prompt ν_μ fluxes and ν_τ fluxes [38].	24
2.7	Oscillation probabilities as a function of neutrino energy for atmospheric ν_e (left) and ν_μ (right) after traveling through the Earth along the Earth's diameter.	26

2.8	Comparison of measured neutrino fluxes and HKKM model. Measurements by IceCube are shown as triangles (blue and purple for ν_e , pink for ν_μ) [44].	27
2.9	(a) Distribution of atmospheric fluxes averaged over azimuth angles vs. zenith angles. Solid lines are averaged from June to August, and dashed lines from December to February. (b) The ratio of fluxes with different flavors vs. energy. (c) All-direction averaged fluxes vs. energy [41].	28
3.1	The IceCube Detector consists of 86 strings with digital optical modules on each string [47].	30
3.2	Top and side view of the IceCube detector. The DeepCore region includes seven regular IceCube strings and the eight strings marked with red stars and black triangles.	31
3.3	Left: Schematic view of the DOM. The mu-metal grid is used to shield the PMT from the Earth's magnetic field, the layer of Room-Temperature-Vulcanizing (RTV) gel to optically couple the PMT glass to the pressure vessel, the LED flasher board is used for calibration, and the HV generator and divider circuit for the voltage supply. Right: The PMT output waveform is fed into the 3 ATWD channels (ch0, ch1, ch2) and the FADC channel [48].	33
3.4	Feynman diagrams of neutrino-nucleon interactions. "l" can be e , μ , τ , and ν_l stands for the corresponding ν_e , ν_μ or ν_τ . "q" is a quark.	38
3.5	Cross section divided by energy as a function of energy for QE, RES and DIS scattering and their total cross section. Upper left: ν_μ neutrinos. Upper right: $\bar{\nu}_\mu$ neutrinos. Bottom: Comparison of ν_μ and ν_τ cross sections divided by energy vs. energy. We can see the ν_τ scattering only starts at 3.5 GeV [51, 53].	40
3.6	Geometry of the Cherenkov cone (without scattering).	41
3.7	Light emitted from an emitter (shown in red) and received by a receiver (shown in blue) [62].	42
3.8	The depth dependence of the effective absorption coefficient a (400 nm) (up) and scattering coefficient b_e (400 nm) (bottom). There are two models shown here. The solid black line is the Spice Mie model, and the grey band indicates its uncertainties. The dashed line is the AHA model used previously in AMANDA based on Ref. [59], extrapolated to IceCube depths. Its uncertainties at the AMANDA depths of 1730 ± 225 m are roughly 5% in b_e and roughly 14% in a . The right side of the plots shows the corresponding scattering and absorption lengths in meters [62].	44

3.9	The depth dependence of the effective absorption coefficient a (400 nm) (up) and scattering coefficient b_e (400 nm) (bottom) comparing the Spice Mie and the Spice Lea model [63]. The grey band is the uncertainties on the Spice Mie model reported in [62].	45
4.1	Generator volume along a given neutrino direction. The generated primary neutrino starts from the disk. Its radius, R , is called the injection radius. The neutrino is then propagated towards the detector. Each neutrino is simulated to interact within the cylinder whose height is called the detection length L . (The interaction probability is later added in the event weight as a correction.) The radius and length are optimized to different values to accommodate different flavors in different energy regions. For example, in the MC used for this analysis, $R=250$ m and $L=500$ m for ν_e flavor events.	47
4.2	The 8-parameter event hypothesis in HybridReco. Blue regions indicate where Cherenkov light has been created. For the muon track, only the Cherenkov cone at the wave front is depicted. . . .	52
4.3	(a): Black points are the active points sampled inside of the constructed ellipsoidal bounds (orange). (b) and (c): MultiNest can recover the highly multimodal two-dimensional likelihood space very well. (b) is the input likelihood function, (c) shows what MultiNest gets. Each dot is one lowest likelihood at one MultiNest iteration [84].	54
4.4	Left: Reconstructed energy vs. true energy in four flavor and interaction channels: ν_e CC, ν_μ CC, ν_τ CC and ν_{all} NC. Right: Reconstructed $\cos\theta_{\text{zen}}$ vs. true $\cos\theta_{\text{zen}}$	56
4.5	Left: Fractional difference between the reconstructed and true energy vs. true energy in four flavor and interaction channels: ν_e CC, ν_μ CC, ν_τ CC and ν_{all} NC. Right: Difference between the reconstructed and true zenith (in degrees) vs. true energy. Red dots are the median resolution in each energy bin, the bar's length the range where 50% of the events fall.	56
5.1	Number of events at each selection level expected in IceCube in three years' time. (Effective live time is 2.5 years.)	58
5.2	(a) The overhead view of the EDC fiducial region used in the Online DeepCore Filtering in level 2 and the cut on "EDC-VetoPE" in level 3; (b) The overhead view of DCC fiducial region used in the cut on "DCC_VetoPE" in level 4.	59

5.3	Online DeepCore Filter algorithm [47]. A simulated muon traveling downwards deposits photons in the DOMs. Each colored circle represents a hit DOM, with the earliest hits marked in red and the latest hits in blue. The largest circle is the CoG of the hits in the Extended DeepCore (EDC) fiducial region. The charges of these hits are also shown in the first histogram below, ordered by time. The second histogram is the “particle speeds” distribution. For example, the earlier hits in the upper left part of the detector have “particle speeds” consistent with speed of light travelling from the hit to the CoG, and therefore fall into the “cut region.” Events having at least one such hit in the cut region are removed.	61
5.4	(a) Particle speed probabilities per event for simulated atmospheric muons and simulated muons from atmospheric ν_μ interactions inside DeepCore. (b) Signal efficiency vs. background rejection for events falling into the speed cut region between +0.25 m/ns and a variety of upper values, ranging from +0.35 m/ns to +1.0 m/ns [47].	62
5.5	Left: A simulated ν_μ event in IceCube. The star is the interaction vertex, the line between the star and the string is the outgoing muon track. The blue circles represent hit DOMs, and their area represents how large the charge is in each DOM. Right: The signature left by the Cherenkov cone of the track on the string. The solid line is the signature hyperbola left by the true MC muon track. The purple circles are the photons located near the hyperbola left by a track fit; they are the direct photons arriving at the DOMs from the Cherenkov cone created by the track. Those that don’t match the hyperbola are the late photons and will be removed [82].	63
5.6	Causal Track Veto region [89]. The red region is the veto region in which events are likely to be produced by atmospheric muons. The blue region is the region where events produced by neutrinos are likely to locate.	69
5.7	Example “corridors.” The IceCube detector was constructed on a triangular lattice in the horizontal plane. The blue spot is string 86, the four red arrows represent the directions of possible background muons towards string 86 that sneak into the detector without triggering or only triggering very few DOMs in the veto region. Figure is adapted from a plot in Ref. [95].	71
5.8	Final containment cut. The red dashed region is for the starting positions, and the blue region is for the stopping positions. The green events are examples of allowed events, while the purple ones are examples of rejected events [95].	73

5.9	The estimated background muon template at the final level using the inverted CorridorCut method.	74
6.1	The fraction of final level events split in four channels vs. ΔLLH values. The ν_μ CC events become more dominant at higher ΔLLH values.	77
6.2	The cumulative distribution of the percentage of ν_μ CC events vs. ΔLLH values. The value $\Delta LLH = 2$ splits the ν_μ CC events into roughly two halves: 55% of the ν_μ CC events have $\Delta LLH \leq 2$, and 45% have $\Delta LLH > 2$	78
6.3	Expected histograms with parameters set to their nominal values: (a), the total expected events at level 6, (b), the signal (ν_τ (CC+NC)), and (c) the background which include ν_e (CC+NC), ν_μ (CC+NC) and atmospheric background muons.	79
6.4	Signal ν_τ (CC+NC) divided by the square-root of the background (ν_e , ν_μ and atmospheric μ) for each analysis bin. The figure includes both neutrinos and anti-neutrinos.	80
6.5	Illustration of the Neyman construction of confidence interval (figure from Ref. [97]). For each value of μ , calculate the acceptance region $[x_1, x_2]$ so that the probability of x being in the region $\sum_{x_1}^{x_2} P(x \mu)$ equals α . The acceptance regions are shown as the horizontal lines. The actual measurement of x gives one value of x . Drawing a vertical line at the position gives a range of values that intercept with the vertical line at $[\mu_1, \mu_2]$. $[\mu_1, \mu_2]$ is the confidence interval for the measurement.	83
6.6	Expected sensitivity of the ν_τ (CC + NC) normalization measurement with three years of IceCube/DeepCore data. $\Delta\chi^2$ is defined in Eq. 6.3. 21 ν_τ normalization values are scanned in the range of 0 – 2. At each value, 1000 profile likelihood ratio fits are conducted. The blue shaded regions are the 68% and 90% regions for $\Delta\chi^2$. The black line connects the median values of $\Delta\chi^2$ at each ν_τ normalization value. The grey lines are the asymptotic lines from Wilk's theorem. The intersections between the lines and the median line gives the expected confidence intervals shown in the lower half of the figure. The 68% and 90% C.I. are [0.68, 1.31] and [0.49, 1.58].	85
6.7	Data challenge. The y axis is the measured ν_τ (CC+NC) normalization, the x axis is the injected ν_τ (CC+NC) normalization for pseudo data.	86

6.8	The linear fit performed inside the bin $\cos\theta_{\text{zen}} [-1, -0.75]$, energy $[5.6, 7.5 \text{ GeV}]$, ΔLLH in $[-3, 2]$. One fit is performed in each bin. (a) The y axis is the ratio of the event rates in the bin from all seven <i>DOM efficiency</i> sets to the nominal event rate from the baseline data set (<i>DOM efficiency</i> at 1). The x axis is the deviation of the <i>DOM efficiency</i> values from the nominal value 1. (b) The same fits but for <i>hole ice</i> systematics sets.	88
6.9	2D plane fit to the two discrete systematics. The z axis is the ratio of the event rates from the systematics data sets with respect to the baseline set.	89
6.10	χ^2 distribution of the hyperplane fits (blue).	89
6.11	The projected hyperplane fits (for ν_μ CC events) onto the <i>DOM efficiency</i> dimension. Each subplot is for one bin in $(E, \cos\theta_{\text{zen}})$ space.	91
6.12	The projected hyperplane fits (for ν_μ CC flavor events) in the <i>hole ice</i> dimension. Each subplot is for one bin in $(E, \cos\theta_{\text{zen}})$ space.	92
6.13	The projected hyperplane fits (for ν_μ CC flavor events) in the <i>hole ice forward</i> dimension. Each subplot is for one bin in $(E, \cos\theta_{\text{zen}})$ space.	93
6.14	The projected hyperplane fits (for ν_μ CC flavor events) in the hole ice model (<i>spiciness</i>) dimension. Each subplot is for one bin in $(E, \cos\theta_{\text{zen}})$ space. There are six sets at one (SpiceHD model) and 28 at zero (Dima model). Each set has different model parameters, that's why we see there are multiple points at <i>spiciness</i> = 1. Each of the 28 Dima model sets also has different <i>DOM efficiency</i> , <i>hole ice</i> and <i>hole ice forward</i> values, but here only the baseline set is shown at <i>spiciness</i> = 0 because the difference between the SpiceHD model sets and the baseline Dima model set is what we care about.	94
6.15	The projected hyperplane fits (for ν_μ CC flavor events) in the <i>bulk ice scattering</i> dimension. Each subplot is for one bin in $(E, \cos\theta_{\text{zen}})$ space.	95
6.16	The projected hyperplane fits (for ν_μ CC flavor events) in the <i>bulk ice absorption</i> dimension. Each subplot is for one bin in $(E, \cos\theta_{\text{zen}})$ space.	96
7.1	The uncertainties of $\nu/\bar{\nu}$ as a function of energy and $\cos\theta_{\text{zen}}$ and <i>up/hor</i> flux ratio as a function of energy [45].	98
7.2	Effect of $\nu/\bar{\nu}$ ratio and <i>up/hor</i> ratio uncertainties on the nominal event distribution shown as a percentage change.	99

7.3	Effect of ν_e/ν_μ flux ratio and $\Delta\gamma$ uncertainties on the nominal event distribution shown as a percentage change.	100
7.4	The effect on the event distribution when setting θ_{23} at 43.1° instead of 41.6° , θ_{13} at 8.705° instead of 8.5° , and Δm_{31}^2 at $2.56 \times 10^{-3} \text{ eV}^2$ instead of $2.52 \times 10^{-3} \text{ eV}^2$	101
7.5	Effect of $+1\sigma M_A^{\text{RES}}$ and $+1\sigma M_A^{\text{CCQE}}$ on the nominal event distribution.	102
7.6	Effect of bulk ice absorption on the nominal event distribution. . .	103
7.7	Effect of bulk ice scattering on the nominal event distribution. . .	104
7.8	Sketch of hole ice.	105
7.9	Relative sensitivity as a function of the arrival direction of photons $\cos(\eta)$. (a) shows the comparison between the H2 model and the Dima model. (b) shows the change made on the Dima model by adding a forward parameter $p2$ in an exponential term, allowing it to transition from to H2 model (at 50 cm) in the forward region. Figure taken from Ref. [102].	107
7.10	Top: Effect of DOM efficiency (overall optical efficiency) at 10% above nominal value on the nominal event distribution. Bottom: effect of <i>hole ice</i> (lateral optical efficiency).	108
7.11	Effect of <i>hole ice forward</i> (head-on optical efficiency) and <i>spiciness</i> on the nominal event distribution.	109
7.12	Effect of ν NC normalization at $+1\sigma$ on the nominal event distribution shown as a percentage change.	109
8.1	Result of the tau neutrino appearance measurement with three years of IceCube/DeepCore data. Red lines are the $\Delta\chi^2$ values obtained based on the ordering principle of Feldman-cousins construction. The x axis is the injected ν_τ (CC + NC) normalization value used in generating pseudo data. At each ν_τ (CC + NC) normalization value, roughly 30,000 fits are performed. The resulting $\Delta\chi^2$ values are ordered from smallest to largest, then we find the value below which the cumulative area of this ordered $\Delta\chi^2$ distribution is 68% (1σ), 90% and 99.73% (3σ). The black line is the measured $\Delta\chi^2$ at each ν_τ (CC + NC) normalization scan. The intersection of the black line and the $\Delta\chi^2 = 0$ is the best fit value. Note that the 3σ line is not very smooth, because the number of total fits is 30,000, 3σ corresponds to a percentage of 99.73%, so there are on average only $(0.27\% \times 30,000 =)$ 81 points beyond the 3σ line at the tail of the ordered $\Delta\chi^2$ distribution.	114

8.2	Distributions of the fit statistic χ^2 from MC fits and the χ^2 values from the data fits. Top: ν_τ (CC + NC) normalization fit. Bottom: ν_τ CC normalization fit. The blue histogram is the distribution from doing fits with Poisson-fluctuated baseline MC (with ν_τ (CC + NC) normalization or ν_τ CC normalization set to 1) as the pseudo data. The red line is the location of the minimized χ^2 value after doing the fits with data.	118
8.3	Top: L/E plot for cascade-like events. Bottom: L/E plot for track-like events. Both are after the ν_τ (CC + NC) normalization fit. Signal ν_τ CC and ν_τ NC are shown in red and orange, respectively. The ratio of data to best fit is shown in the lower part of each figure.	120
8.4	Top: L/E plot for cascade-like events. Bottom: L/E plot for track-like events. Signal ν_τ CC is shown in red. The other three colors are ν_μ CC, ν_μ NC, and ν_{all} NC.	121
8.5	L/E plot for cascades and tracks combined. Top: L/E from the ν_τ (CC + NC) normalization fit. Bottom: L/E from the ν_τ CC normalization fit.	122
8.6	Reconstructed energy (top) and $\cos \theta_{\text{zen}}$ (bottom) distributions (cascades and tracks combined) for the ν_τ (CC + NC) normalization fit.	123
8.7	PID distributions (ΔLLH) for the ν_τ (CC + NC) normalization fit.	124
8.8	Background-subtracted event distributions for the ν_τ (CC+NC) normalization fit. Top: reconstructed energy distributions split into cascade-like and track-like channels. Middle: reconstructed $\cos \theta_{\text{zen}}$ distributions. Bottom: reconstructed energy, $\cos \theta_{\text{zen}}$, and particle identification (PID) distributions (cascades and tracks combined).	125
8.9	Background-subtracted event distributions for the ν_τ CC normalization fit. Top: reconstructed energy distributions split into cascade-like and track-like channels. Middle: reconstructed $\cos \theta_{\text{zen}}$ distributions. Bottom: reconstructed energy, $\cos \theta_{\text{zen}}$, and particle identification (PID) distributions (cascades and tracks combined).	126
8.10	“Total charge” and “Number of hit DOMs” distributions (cascades and tracks combined) for the ν_τ (CC + NC) normalization fit. Top: “Total charge”, it is the total charge of the SRT-TW-Cleaned DCC pulses (see Section 5.3.1 for its definition). Bottom: “Number of hit DOMs”. It is the number of hit DOMs in the SRT-TW-Cleaned DCC pulses.	127

8.11	“CoG σ_z ” and “Separation” distributions (cascades and tracks combined) for the ν_τ (CC + NC) normalization fit. Top: “CoG σ_z ” is the standard deviation of the z position of the charge-weighted CoG of the SRT-TW-cleaned DCC pulses. Bottom: “Separation”. The SRT-TW-cleaned DCC pulses are sorted by time into four subsets. “Separation” (Δr) is the spatial distance between the first and the fourth subsets of the hits.	128
8.12	Top: “CoG Q1 ρ ” distribution (cascades and tracks combined) for the ν_τ (CC + NC) normalization fit. It is the radial distance of the CoG of the first quarter of the time-sorted SRT-TW-cleaned DCC pulses. Bottom: “CoG Q1 z” distribution (cascades and tracks combined) for the ν_τ (CC + NC) normalization fit. It is the depth of the CoG of the first quarter of the time-sorted SRT-TW-cleaned DCC pulses.	129
8.13	Top: “QR3” distributions (cascades and tracks combined) for the ν_τ (CC + NC) normalization fit. “QR3” is the ratio of the charge in the first 300ns after the trigger time to the total charge. Bottom: “C2QR3” distributions, C2QR3 is the same as QR3, but excluding the first two pulses to reduce the impact of noise.	130
8.14	“Linefit speed” and “Linefit zenith” distributions (cascades and tracks combined) for the ν_τ (CC + NC) normalization fit. Top: “Linefit speed”. Bottom: “Linefit zenith”. They are the best fit track speed and zenith from Linefit [93].	131
8.15	“SPE11 zenith” distributions (cascades and tracks combined) for the ν_τ (CC + NC) normalization fit. It is the best fit zenith angle from SPE11 fit [92].	132
A.1	The proposed PINGU detector at the time of the study. Its proposed geometry consists of 40 strings, each with 60 PDOMs on it.	137
A.2	(a) The reconstruction time distributions for the first 5D fit (top) and the second seeded 8D fit (bottom) using a $b_d = 10$ m and 75 active points for the 5D fit and 50 active points for the 8D fit. The average times are 1.2 and 8.2 minutes, respectively. (b) The reconstruction time distributions for the full 8D fit.	138

A.3	The resolutions of x , y , z , t , $zenith$, and energy as a function of true neutrino energy. The red line is the median value at each energy bin. The median resolutions of the position parameters (x, y, z) are all around 3 m. The median resolution of time t is around 15 ns. For zenith angle, the median resolutions are all below 20° (at energies larger than 10 GeV, less than 10°). The median resolution of fractional energy (fractional energy = $(E_{\text{reconstructed}} - E_{\text{true}})/E_{\text{true}}$) is about 0.2.	139
A.4	Top: The distribution of maximum charge within 15 ns inside Ice-Cube DOMs. Bottom: The distribution of maximum charge within 15 ns inside PDOMs.	141
A.5	The $zenith_{\text{reco}} - zenith_{\text{true}}$ as a function of true neutrino energy, from these 5 reconstructions. The plot in the top-left corner (0 ns) is no-time-shift case. We see the reconstruction gets worse when we increase the Gaussian σ value from 0 to 48 ns. See more detailed comparison in Fig. A.9	143
A.6	The $E_{\text{reco}} - E_{\text{true}}$ as a function of the true neutrino energy from these 5 reconstructions. We see similar results for energy reconstruction, so the time shifts do not influence the energy reconstruction much. See more detailed comparison in Fig. A.9	144
A.7	Gaussian fits inside the 15 energy bins of the zenith resolution plot (Fig. A.5) with no time shift (0 ns). The x-axis name contains the energy bin range. This plot shows the distribution of $zenith_{\text{reco}} - zenith_{\text{true}}$ in each energy bin can be fitted by a Gaussian function well, so the standard deviation of the best fit Gaussian function is a good representation of the quality of reconstruction resolutions, the comparison of all the Gaussian standard deviations is shown in Fig. A.9.	145
A.8	Gaussian fits inside the 15 energy bins of the energy resolution plot (Fig. A.6) with no time shift (0 ns). The x-axis name contains the energy bin range. This plot shows the first 9 bins (energy range: 0 – 18 GeV) can be fitted by a Gaussian distribution well, but the rest 5 bins don't have enough statistics, so it's better to only compare standard deviations for the first 9 bins. The comparison of the Gaussian standard deviations is shown in Fig. A.9.	146

A.9	The fractional energy resolution (left) and the zenith resolution as a function of true energy. The resolutions are represented by the the standard deviations of the best fit Gaussian functions in each energy bin. The red line is the no-time-shift case, the green, blue, magenta, black lines represent the $\sigma = 6, 12, 24, 48$ ns case, respectively. From 0 to 48 ns, the zenith resolution gets worse, when $\sigma = 6$ ns, the zenith resolutions decreases by about 2 to 3 degrees; energy resolution stays about the same when $\sigma = 6, 12$ ns.	147
A.10	FADC counts vs time for one DOM (Run 116528), each one dot is one FADC sample, there are 256 samples, the FADC bin size is 25 ns, thus the total time is 256×25 ns = $6.4 \mu\text{s}$.	149
A.11	The raw FADC readout for one DOM of a simulated monopole event ($\beta = 0.0001, \lambda = 0.1$ m). It has a (30×25 ns =) $192 \mu\text{s}$ long FADC readout. The top figure shows all the readout, the bottom figure is a zoomed-in figure of the same event inside a smaller time range.	150
A.12	The blue dots are the output DOM launches using the original 300 MHz ATWD sampling rate, the magenta triangles are the new ATWD data points.	152
A.13	The median zenith and fractional energy resolutions using different ATWD sampling rates. Data used here: PINGU simulated ν_μ CC events. The blue bins are with the original 300 MHz sampling rate. We see the resolutions between a 300 MHz rate and 200 MHz (also 100 MHz) rate are comparable.	153

List of Tables

1.1	Oscillation parameters global best fit and ranges. “bfp” means “best fit point”. The first two columns are best fit results assuming the normal ordering and the inverted ordering, respectively. The third column is the best fit results that also fit with respect to the ordering. Note that $\Delta m_{3l}^2 = \Delta m_{31}^2 > 0$ for normal ordering, and $\Delta m_{3l}^2 = \Delta m_{32}^2 < 0$ for inverted ordering. Taken from NuFIT 3.2 (2018), www.nu-fit.org	7
3.1	Different trigger algorithms, their requirements and their typical event trigger rates as of May 2013. Trigger rates vary seasonally. Taken from Ref. [50]	35
3.2	The online data flow in IceCube [46].	36
5.1	The trigger/veto/quality cuts at each selection level	60
5.2	Number of expected events in three years at each selection level. .	60
5.3	Event rates in mHz at each selection level.	60
5.4	Triggers, their definitions and cut values.	66
5.5	Level 3 DC Veto and Level 4 Trigger	67
5.6	BDT input variables and their definitions.	70
6.1	The percentage of cascade-like events and track-like events for different event types. We see over 70% of the ν_e CC, ν_τ CC, ν_{all} NC events are in the cascade channel, and ν_μ CC events and atmospheric muons distribute evenly among the two channels.	78
6.2	Nuisance parameters and their associated prior central value and $\pm 1\sigma$ ranges.	81

7.1	The $\Delta\chi^2$ column is the difference between the χ^2 at ν_τ (CC+NC) normalization = 0 and the best fit ν_τ (CC + NC) normalization (here =1). From Wilk's theorem, the sensitivity of excluding the null hypothesis is $\sqrt{\Delta\chi^2(\nu_\tau \text{ norm.} = 0)}$. The “nominal” row is the nominal case where none of the systematics are fixed, each the rest of the rows shows the result when fixing that systematic to its baseline value. We see that θ_{23} has the biggest impact.	111
7.2	The 1σ Range column is the 1σ range for ν_τ (CC + NC) normalization using Wilk's theorem. Avg 1σ Range is the average of the 1σ range. The Impact column shows the percentage change in the average 1σ C.I., the values are ordered from the biggest impact to the smallest. The “nominal” row is the nominal case where none of the systematics are fixed, each the rest of the rows shows the result when fixing that systematic to its baseline value. Fixing <i>hole ice forward</i> makes the 1σ C.I. shrink by 14.9%.	112
8.1	The best fit results for all parameters.	115
8.2	The livetime for each year.	117
8.3	Number of Events from ν_τ (CC + NC) normalization fit.	119
8.4	Number of Events from ν_τ CC normalization fit.	119
A.1	Average reconstruction time per event under different settings for the 5D+seeded-8D fit.	136

Acknowledgments

First, I would like to express my gratitude to my advisor, Prof. Douglas Cowen, for giving me the opportunity to join the PSU IceCube group, for his patience, and for his strong support for me. He gave me good research direction guidance throughout my Ph.D. program. His insightful suggestions were extremely helpful.

I'm also grateful to other members of my doctoral committee: Stéphane Coutu, Derek Fox and Miguel Mostafá for spending time on reviewing my dissertation and giving me invaluable suggestions.

Next, I want to thank many colleagues and collaborators. Ryan Eagan helped me get everything ready when I first joined the group. Matthew Dunkman developed the event selection used for this tau neutrino appearance analysis. He also gave me good advice on one of my early projects. I especially want to thank João Pedro Athayde Marcondes de André who gave me tremendous help. He was always patient with my countless questions. Timothy C. Arlen introduced me to the earliest version of the code framework used for this dissertation. Philipp Eller was my collaborator on the tau appearance analysis. He improved the way I ran the analysis, and always came up with great ideas for solving problems. I learned a great deal from him. Justin Lanfranchi's work on developing the code framework was always amazing. He got CVMFS working on ACI, which made things so much easier for using IceCube software. Also, I have worked shortly with other colleagues: Daria Pankova, Tyler Anderson, and Azadeh Keivani. I also thank Gordana Tešić for letting me stay at her place during my visa visit in Canada. There is not enough time or space for me to write down everything I feel thankful for. I'll miss the coffee/tea breaks that were always enjoyable and inspiring.

I also want to thank my friends at Penn State: Hsiu-Chuan Hsu, Piali Aditya, Christian Cruz, Aruna Kesavan, Ying-tzu Huang, and Nicole Thomson. Your friendship added so much joy and comfort to my graduate student life.

I want to thank my parents for their unconditional love and support.

Finally, IceCube is funded by the following agencies and institutions: U.S. National Science Foundation-Office of Polar Programs, U.S. National Science Foundation-

Physics Division, University of Wisconsin Alumni Research Foundation, the Center for High Throughput Computing (CHTC) at the University of Wisconsin - Madison, the Open Science Grid (OSG) grid infrastructure and the Extreme Science and Engineering Discovery Environment (XSEDE); U.S. Department of Energy, and National Energy Research Scientific Computing Center; Natural Sciences and Engineering Research Council of Canada, Calcul Québec, Compute Ontario, West-Grid and Compute Canada; Swedish Research Council, Swedish Polar Research Secretariat, Swedish National Infrastructure for Computing (SNIC), and Knut and Alice Wallenberg Foundation, Sweden; German Ministry for Education and Research (BMBF), Deutsche Forschungsgemeinschaft (DFG), Helmholtz Alliance for Astroparticle Physics (HAP), Initiative and Networking Fund of the Helmholtz Association, Germany; Deutsches Elektronen Synchrotron (DESY); Funds for Scientific Research (FRS-FNRS and FWO), FWO Odysseus and Big Science programmes, Belgian Federal Science Policy Office (Belspo); Marsden Fund, New Zealand; Australian Research Council; Japan Society for Promotion of Science (JSPS) and Institute for Global Prominent Research (IGPR) of Chiba University; Swiss National Science Foundation (SNSF), Switzerland; National Research Foundation of Korea (NRF); Villum Fonden, Danish National Research Foundation (DNRF), Denmark; Particle Astrophysics research computing center at the University of Maryland; Institute for Cyber-Enabled Research at Michigan State University; High Performance Computing Cluster of the IT-Center of the RWTH Aachen University; Astroparticle Physics Computational Facility at Marquette University.

Dedication

To my parents Liaoning Xiao (肖了宁) and Sijing Huang (黄思静). They gave me life. They have always been wholeheartedly supportive of me. I wouldn't be here without them.

To my grandparents Ailan Xiang (向爱兰) and Xiangqiu Xiao (肖祥球), with whom I grew up before going to school. Their home is a safe haven for me.

Chapter 1 |

Neutrino Oscillations

1.1 Neutrinos

Neutrinos are elementary particles that only interact via the gravitational and weak interactions. There are three flavors of neutrinos when they interact weakly: ν_e , ν_μ and ν_τ , corresponding to the produced lepton e , μ and τ . The electron antineutrino was first discovered by Clyde Cowan and Frederick Reines [1] in 1956, using reactor electron antineutrinos that interact via inverse beta decay. The muon neutrino was discovered by Leon Lederman, Melvin Schwartz and Jack Steinberger [2] in 1962, using accelerator muon neutrinos. Lastly, the tau neutrino was discovered by the DONUT experiment [3] in 2000, using tau neutrinos produced via decay of charmed mesons.

Each flavor eigenstate (ν_e , ν_μ , ν_τ) is a superposition of the three mass eigenstates (ν_1 , ν_2 , ν_3). When a certain type of weak neutrino interaction happens, neutrinos are produced with a certain flavor, when those neutrinos travel through space, the three mass eigenstates m_1 , m_2 , m_3 travel with different speeds. After some distance, the composition of mass eigenstates is different from the initial state. If the neutrinos then interact weakly, the interactions can involve a different flavor. For example, a muon neutrino with energy E produced in a weak interaction at some initial position, after traveling some distance L , may then interact as a tau neutrino. This process of flavor change is called a neutrino oscillation and its probability depends on L/E . The following section discusses the theory of neutrino oscillations in detail.

1.2 Neutrino Oscillations in Vacuum

1.2.1 PMNS matrix

Bruno Pontecorvo first put forward the concept of neutrino oscillations in 1957 [4]. In 1962, Ziro Maki, Masami Nakagawa and Shoichi Sakata proposed the unitary mixing matrix [5] to describe the neutrino oscillations. Below is the 3 flavor case:

$$\begin{pmatrix} |\nu_e\rangle \\ |\nu_\mu\rangle \\ |\nu_\tau\rangle \end{pmatrix} = \begin{pmatrix} U_{e1} & U_{e2} & U_{e3} \\ U_{\mu1} & U_{\mu2} & U_{\mu3} \\ U_{\tau1} & U_{\tau2} & U_{\tau3} \end{pmatrix} \begin{pmatrix} |\nu_1\rangle \\ |\nu_2\rangle \\ |\nu_3\rangle \end{pmatrix}. \quad (1.1)$$

Each flavor eigenstate α ($\alpha = e, \mu, \tau$) is a superposition of the three mass eigenstates:

$$|\nu_\alpha\rangle = U_{\alpha1}|\nu_1\rangle + U_{\alpha2}|\nu_2\rangle + U_{\alpha3}|\nu_3\rangle = \sum_{i=1,2,3} U_{\alpha i}|\nu_i\rangle. \quad (1.2)$$

Then,

$$|\nu_i\rangle = \sum_{\alpha=e,\mu,\tau} (U^\dagger)_{i\alpha}|\nu_\alpha\rangle = \sum_{\alpha=e,\mu,\tau} U_{\alpha i}^*|\nu_\alpha\rangle. \quad (1.3)$$

The neutrino mixing matrix U in Eq. 1.1 is called the PMNS matrix after Pontecorvo, Maki, Nakagawa, and Sakata. Under the standard three-flavor oscillation paradigm, U is unitary, *i.e.*, it satisfies two equations:

$$\begin{aligned} U^\dagger U &= \mathcal{I}, \\ U U^\dagger &= \mathcal{I}, \end{aligned} \quad (1.4)$$

where \mathcal{I} is the identity matrix. The two equations can be expressed with their matrix elements:

$$\sum_i U_{\alpha i} U_{\beta i}^* = \delta_{\alpha\beta}, \quad (1.5)$$

$$\sum_\alpha U_{\alpha i} U_{\alpha j}^* = \delta_{ij}. \quad (1.6)$$

Eqs. 1.5 and 1.6 are the same as the six normalizations for the three row elements and three column elements below:

$$|U_{\alpha1}|^2 + |U_{\alpha2}|^2 + |U_{\alpha3}|^2 = 1 \quad (\alpha = e, \mu, \tau), \quad (1.7)$$

$$|U_{ei}|^2 + |U_{\mu i}|^2 + |U_{\tau i}|^2 = 1 \quad (i = 1, 2, 3), \quad (1.8)$$

and the six unitary angle closures below:

$$|U_{\alpha 1}U_{\beta 1}^* + U_{\alpha 2}U_{\beta 2}^* + U_{\alpha 3}U_{\beta 3}^*|^2 = 0 \quad ((\alpha, \beta) = (e, \mu), (e, \tau), (\mu, \tau)), \quad (1.9)$$

$$|U_{ei}U_{ej}^* + U_{\mu i}U_{\mu j}^* + U_{\tau i}U_{\tau j}^*|^2 = 0 \quad ((i, j) = (1, 2), (2, 3), (1, 3)). \quad (1.10)$$

The current constraints on these 12 sums are shown in Fig. 1.1 and Fig. 1.2. The sums that have no τ matrix elements are constrained on the order of a few percent, whereas sums having the τ element are constrained on the order of 10%.

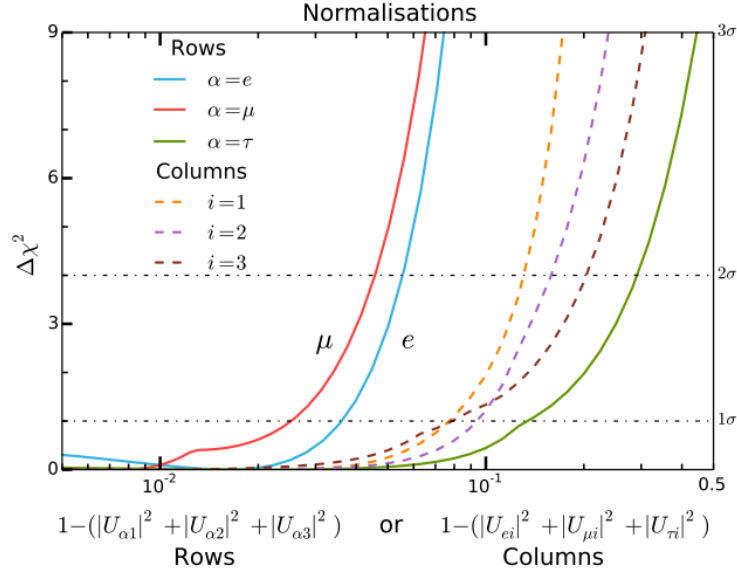


Figure 1.1: The constraints on the six normalizations, taken from Ref. [6]. Solid lines are summations involving row elements, dashed lines are for column elements.

The mass eigenstates at position x and time t are:

$$|\nu_i(x, t)\rangle = e^{-iE_i t} |\nu_i(x, 0)\rangle, \quad (1.11)$$

where E_i can be approximated as shown below when neutrinos are ultra-relativistic:

$$E_i = \sqrt{m_i^2 + p_i^2} \approx p_i + \frac{m_i^2}{2p_i} \approx E + \frac{m_i^2}{2E}. \quad (1.12)$$

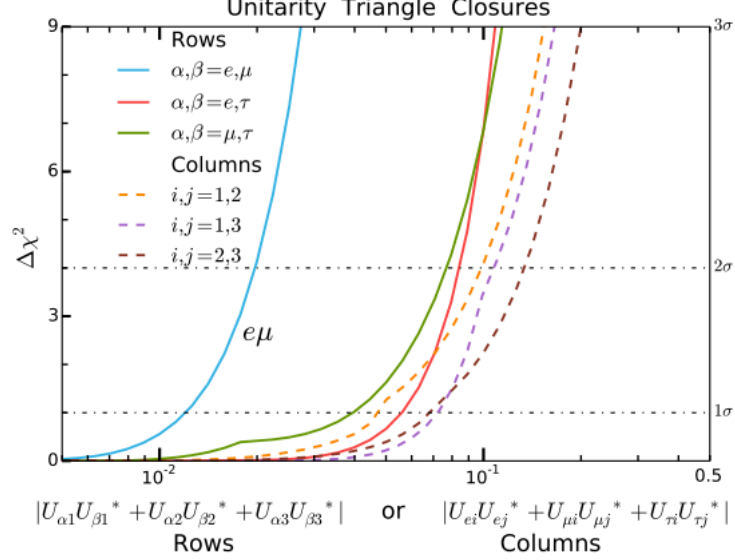


Figure 1.2: The constraints on the six unitary triangles, taken from Ref. [6]. Solid lines are summations involving row elements, dashed lines are for column elements.

Combining Eq. 1.11 and Eq. 1.2, the initial flavor eigenstate $|\nu_\alpha(x, 0)\rangle$ will evolve with time as follows:

$$|\nu_\alpha(x, t)\rangle = \sum_{i=1,2,3} U_{\alpha i} e^{-iE_i t} |\nu_i(x, 0)\rangle. \quad (1.13)$$

From Eqs. 1.12 and 1.13, the oscillation probability from one flavor α to another β is:

$$\begin{aligned} P(\nu_\alpha \rightarrow \nu_\beta) &= |\langle \nu_\beta | \nu_\alpha(x, t) \rangle|^2 = \left| \sum_i U_{\beta i} U_{\alpha i}^* \exp(-im_i^2 L/2E) \right|^2 \\ &= |U_{\alpha i} U_{\beta i}^*|^2 + 2\text{Re} \sum_{j>i} U_{\alpha i} U_{\alpha i}^* U_{\beta j}^* U_{\beta j} \exp(-i \frac{\Delta m_{ij}^2 L}{2E}), \end{aligned} \quad (1.14)$$

where $\Delta m_{ij}^2 = m_i^2 - m_j^2$. Using CP invariance, Eq. 1.14 can be written as:

$$\begin{aligned} P(\nu_\alpha \rightarrow \nu_\beta) &= |U_{\alpha i} U_{\beta i}^*|^2 + 2\text{Re} \sum_{j>i} U_{\alpha i} U_{\alpha i}^* U_{\beta j}^* U_{\beta j} \cos(\frac{\Delta m_{ij}^2 L}{2E}) \\ &= \delta_{\alpha\beta} - 4 \sum_{j>i} U_{\alpha i} U_{\alpha i}^* U_{\beta j}^* U_{\beta j} \sin^2(\frac{\Delta m_{ij}^2 L}{4E}). \end{aligned} \quad (1.15)$$

Assuming unitarity, we can parametrize the matrix as follows:

$$U = \begin{pmatrix} 1 & 0 & 0 \\ 0 & c_{23} & s_{23} \\ 0 & -s_{23} & c_{23} \end{pmatrix} \begin{pmatrix} c_{13} & 0 & s_{13}e^{-i\delta_{CP}} \\ 0 & 1 & 0 \\ -s_{13}e^{i\delta_{CP}} & 0 & c_{13} \end{pmatrix} \begin{pmatrix} c_{12} & s_{12} & 0 \\ -s_{12} & c_{12} & 0 \\ 0 & 0 & 1 \end{pmatrix} \begin{pmatrix} e^{i\alpha_1/2} & 0 & 0 \\ 0 & e^{i\alpha_2/2} & 0 \\ 0 & 0 & 1 \end{pmatrix}, \quad (1.16)$$

where $s_{ij} = \sin(\theta_{ij})$, $c_{ij} = \cos(\theta_{ij})$, $\delta = \delta_{CP}$. α_1 and α_2 are the Majorana phases that are only needed if neutrinos are Majorana particles, they don't influence the oscillation parameters either way.

Eq. 1.15 shows that the oscillation probabilities only depend on the difference between the squares of the masses: Δm_{ij}^2 . The sign of Δm_{21}^2 is determined to be positive from solar neutrino oscillation experiments. The signs of the other two mass splittings are not clear yet. Figure. 1.3 depicts the neutrino mass hierarchies: normal hierarchy ($m_1 < m_2 < m_3$) and inverted hierarchy ($m_3 < m_1 < m_2$). They are also referred to as the normal ordering and inverted ordering.

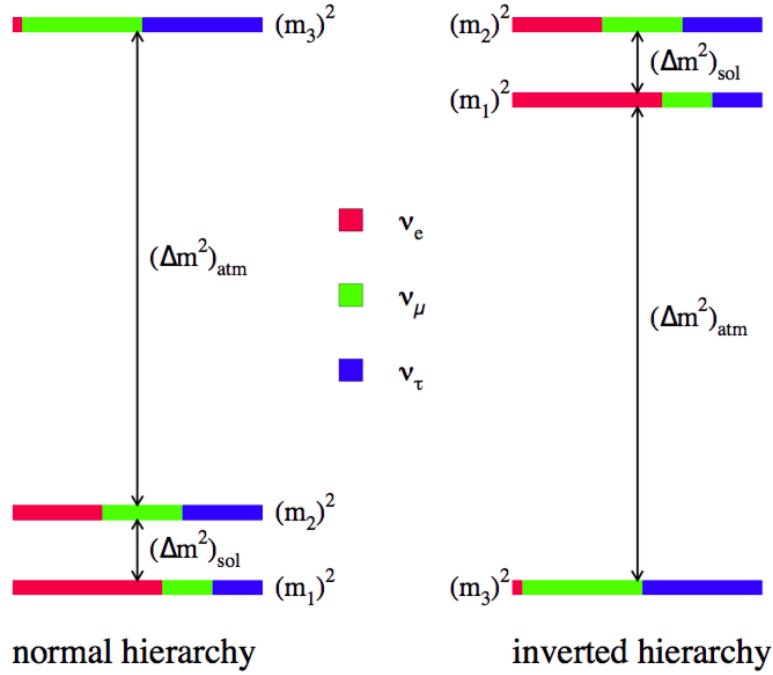


Figure 1.3: Neutrino mass hierarchy. Normal hierarchy means $m_1 < m_2 < m_3$, inverted hierarchy means $m_3 < m_1 < m_2$. $\Delta m_{\text{sol}}^2 = \Delta m_{21}^2 > 0$. Δm_{atm}^2 is either Δm_{32}^2 under the normal hierarchy or $|\Delta m_{31}^2|$ under the inverted hierarchy. Figure taken from Ref. [7].

	Normal Ordering (best fit)		Inverted Ordering ($\Delta\chi^2 = 4.14$)		Any Ordering
	bfp $\pm 1\sigma$	3σ range	bfp $\pm 1\sigma$	3σ range	3σ range
$\sin^2 \theta_{12}$	$0.307^{+0.013}_{-0.012}$	$0.272 \rightarrow 0.346$	$0.307^{+0.013}_{-0.012}$	$0.272 \rightarrow 0.346$	$0.272 \rightarrow 0.346$
$\theta_{12}/^\circ$	$33.62^{+0.78}_{-0.76}$	$31.42 \rightarrow 36.05$	$33.62^{+0.78}_{-0.76}$	$31.43 \rightarrow 36.06$	$31.42 \rightarrow 36.05$
$\sin^2 \theta_{23}$	$0.538^{+0.033}_{-0.069}$	$0.418 \rightarrow 0.613$	$0.554^{+0.023}_{-0.033}$	$0.435 \rightarrow 0.616$	$0.418 \rightarrow 0.613$
$\theta_{23}/^\circ$	$47.2^{+1.9}_{-3.9}$	$40.3 \rightarrow 51.5$	$48.1^{+1.4}_{-1.9}$	$41.3 \rightarrow 51.7$	$40.3 \rightarrow 51.5$
$\sin^2 \theta_{13}$	$0.02206^{+0.00075}_{-0.00075}$	$0.01981 \rightarrow 0.02436$	$0.02227^{+0.00074}_{-0.00074}$	$0.02006 \rightarrow 0.02452$	$0.01981 \rightarrow 0.02436$
$\theta_{13}/^\circ$	$8.54^{+0.15}_{-0.15}$	$8.09 \rightarrow 8.98$	$8.58^{+0.14}_{-0.14}$	$8.14 \rightarrow 9.01$	$8.09 \rightarrow 8.98$
$\delta_{\text{CP}}/^\circ$	234^{+43}_{-31}	$144 \rightarrow 374$	278^{+26}_{-29}	$192 \rightarrow 354$	$144 \rightarrow 374$
$\frac{\Delta m_{21}^2}{10^{-5} \text{ eV}^2}$	$7.40^{+0.21}_{-0.20}$	$6.80 \rightarrow 8.02$	$7.40^{+0.21}_{-0.20}$	$6.80 \rightarrow 8.02$	$6.80 \rightarrow 8.02$
$\frac{\Delta m_{3\ell}^2}{10^{-3} \text{ eV}^2}$	$+2.494^{+0.033}_{-0.031}$	$+2.399 \rightarrow +2.593$	$-2.465^{+0.032}_{-0.031}$	$-2.562 \rightarrow -2.369$	$[+2.399 \rightarrow +2.593]$ $[-2.536 \rightarrow -2.395]$

Table 1.1: Oscillation parameters global best fit and ranges. “bfp” means “best fit point”. The first two columns are best fit results assuming the normal ordering and the inverted ordering, respectively. The third column is the best fit results that also fit with respect to the ordering. Note that $\Delta m_{3l}^2 = \Delta m_{31}^2 > 0$ for normal ordering, and $\Delta m_{3l}^2 = \Delta m_{32}^2 < 0$ for inverted ordering. Taken from NuFIT 3.2 (2018), www.nu-fit.org.

The current global best fit values for these oscillation parameters are listed in Table 1.1, and the 3σ ranges of the matrix elements are listed in Eq. 1.17 [8, 9]:

$$|U|_{3\sigma} = \begin{pmatrix} 0.799 \rightarrow 0.844 & 0.516 \rightarrow 0.582 & 0.141 \rightarrow 0.156 \\ 0.242 \rightarrow 0.494 & 0.467 \rightarrow 0.678 & 0.639 \rightarrow 0.774 \\ 0.284 \rightarrow 0.521 & 0.490 \rightarrow 0.695 & 0.615 \rightarrow 0.754 \end{pmatrix}. \quad (1.17)$$

1.2.2 The Two Neutrino Approximation

The following two-neutrino approximation in vacuum is used for illustration:

$$P(\nu_\alpha \rightarrow \nu_\beta, \text{vacuum}) \approx \sin^2 2\theta \sin^2 \left(\Delta m^2 \frac{L}{4E} \right). \quad (1.18)$$

With SI units:

$$P(\nu_\alpha \rightarrow \nu_\beta, \text{vacuum}) \approx \sin^2 2\theta \sin^2 \left(1.27 \Delta m^2 \frac{L [\text{eV}^2][\text{km}]}{E [\text{GeV}]} \right). \quad (1.19)$$

Thus, the oscillation amplitude is determined by $\sin^2(2\theta)$, the oscillation phase is $\phi = \Delta m^2 \frac{L}{4E}$. The maximum probability condition then is the oscillation phase ϕ satisfying $\sin^2(\phi) = 1$. It follows that $\phi = (2n - 1)\frac{\pi}{2}$, where n is an integer and $n \geq 1$.

Thus, the maximum condition for neutrino energy is:

$$E = \frac{|\Delta m^2|L}{2\pi(2n - 1)}. \quad (1.20)$$

With fixed distance L and mass splitting Δm^2 , the larger the n , the smaller the energy. $n = 1$ corresponds to the first maximum condition, $n = 2$ corresponds to the second maximum.

From Table 1.1, the oscillation angle θ_{13} is small. So, approximately speaking, $\sin(\theta_{13}) \approx 0$, $\cos(\theta_{13}) \approx 1$. Also, $\Delta m_{21}^2 \sim 10^{-5} \text{ eV}^2$, $|\Delta m_{32}^2| \sim 10^3 \text{ eV}^2$, since the latter is larger by two orders of magnitude, we can use the following approximation: $|\Delta m_{31}^2| = |m_3^2 - m_1^2| = |m_3^2 - m_2^2 + m_2^2 - m_1^2| \approx |\Delta m_{32}^2| = \Delta m_{\text{atm}}^2$. Thus, using these approximations, we can get the leading order term for the probability of atmospheric muon neutrinos disappearing into tau neutrinos:

$$P(\nu_\mu \rightarrow \nu_\tau, \text{vacuum}) \approx \sin^2 2\theta_{23} \sin^2 \left(1.27 \Delta m_{\text{atm}}^2 \frac{L [\text{eV}^2][\text{km}]}{E [\text{GeV}]} \right). \quad (1.21)$$

The survival probability of ν_μ is:

$$P(\nu_\mu \rightarrow \nu_\mu, \text{vacuum}) \approx 1 - \sin^2 2\theta_{23} \sin^2 \left(1.27 \Delta m_{\text{atm}}^2 \frac{L [\text{eV}^2][\text{km}]}{E [\text{GeV}]} \right). \quad (1.22)$$

The baseline L for experiments that measure atmospheric neutrinos ranges from 0 to 10^4 km. For example, for the atmospheric ν_μ to ν_τ oscillation (with L = Earth diameter 12742 km), plug in the parameters values, it's easy to calculate that the energy around 25 GeV corresponds to the first maximum and the energy of roughly 8 GeV corresponds to the second maximum.

1.3 Neutrino Oscillations in Matter

Neutrinos propagating in matter can have coherent forward elastic scattering with its constituent electrons, protons and neutrons. Figure 1.4 shows the Feynman

diagram for the coherent forward elastic scattering process. There are electrons in the Sun and the Earth, thus ν_e traveling through the Sun (or Earth) can undergo either Charged Current (CC) or Neutral Current (NC) interaction, while ν_μ and ν_τ can only have the NC interaction.

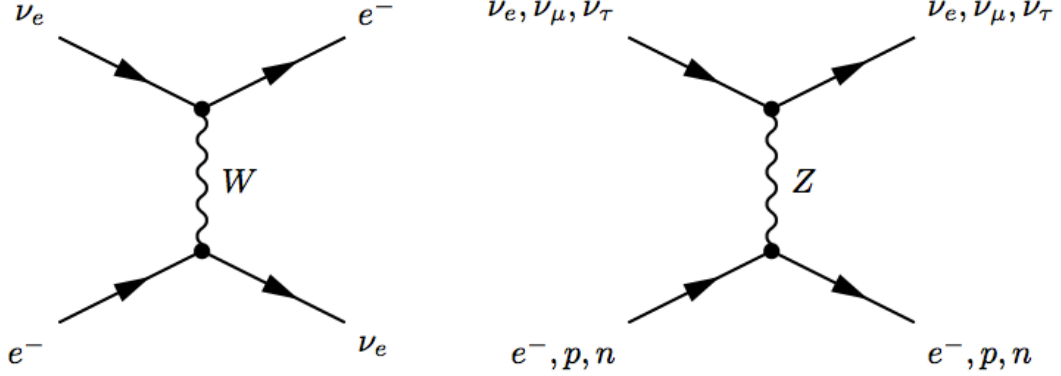


Figure 1.4: Feynman diagram of coherent forward scattering [10]. Left: charged current interaction. Right: neutral current interaction.

For the charged current interaction, this adds an additional potential term in the Hamiltonian [10]:

$$\begin{aligned} V_{CC} &= \sqrt{2}G_F N_e \\ V_{NC} &= -\frac{1}{2}\sqrt{2}G_F N_n, \end{aligned} \tag{1.23}$$

where N_e and N_n are the electron and neutron densities in matter and G_F is the Fermi coupling constant.

1.3.1 MSW Effect

Again using the two-neutrino ν_e to ν_μ oscillation for simplicity, the difference between the potentials of ν_e and ν_μ is:

$$V_{\nu_e} - V_{\nu_\mu} = \sqrt{2}G_F N_e. \tag{1.24}$$

The Hamiltonian changes to

$$H_F = H_0 + V, \tag{1.25}$$

where H_F is the effective Hamiltonian, H_0 is the Hamiltonian in vacuum, and H_F can be written into the flavor basis [10]:

$$H_F = \frac{1}{4E} \begin{pmatrix} -\Delta m^2 + A_{CC} & \Delta m^2 \sin(2\theta) \\ \Delta m^2 \sin(2\theta) & \Delta m^2 - A_{CC} \end{pmatrix} \quad (1.26)$$

where

$$A_{CC} = 2\sqrt{2}EG_F N_e. \quad (1.27)$$

Thus, the mass eigenstates change to the effective squared-mass difference:

$$\Delta m_M^2 = \sqrt{(\Delta m^2 \cos(2\theta) - A_{CC})^2 + (\Delta m^2 \sin(2\theta))^2}, \quad (1.28)$$

where the effective mixing angle is:

$$\tan 2\theta_M = \frac{\tan 2\theta}{1 - \frac{A_{CC}}{\Delta m^2 \cos 2\theta}}. \quad (1.29)$$

When A_{CC} is equal to $\Delta m^2 \cos 2\theta$, this produces a resonance, where the effective mixing angle is 45° . This is called the MSW (Mikheyev–Smirnov–Wolfenstein) effect, and was an important element of the solution to the solar neutrino problem [11].

1.3.2 Matter Effects for DeepCore

The Preliminary Reference Earth Model (PREM) [12] is the model of Earth that we use. In this analysis, 12 radial layers of constant density are used.

Figure 1.5 (a) shows the Earth's density profile under this model. Figure 1.5 (b) shows the neutrinos that travel along the border of the core and mantle. The direction of a neutrino is described by two angles: the zenith angle θ_{zenith} (simplified as θ_{zen}) and the azimuth angle (θ_{azi}). Thus, neutrinos with a θ_{zen} smaller than 146.9° will go through only the mantle, and neutrinos with a θ_{zen} larger than 146.9° go through both the mantle and the core.

Figures from 1.6 to 1.11 show the neutrino oscillograms, *i.e.*, oscillation probabilities of ν_e and ν_μ as a function of $\cos \theta_{\text{zen}}$ and neutrino energy. Each set of figures compares the oscillogram with the consideration of the Earth matter effects from PREM and the oscillogram with a vacuum assumption. In all the figures with the

PREM matter effects, the clear distinctions caused by the density difference in the mantle and the core can be seen. Each figure has two different parts separated by $\cos \theta_{\text{zen}} = \cos(146.9^\circ) = -0.73$. The core-crossing neutrinos are located in the small lower part with $\cos \theta_{\text{zen}} < -0.73$, and the mantle-only-crossing neutrinos are in the larger upper part with $\cos \theta_{\text{zen}} > -0.73$.

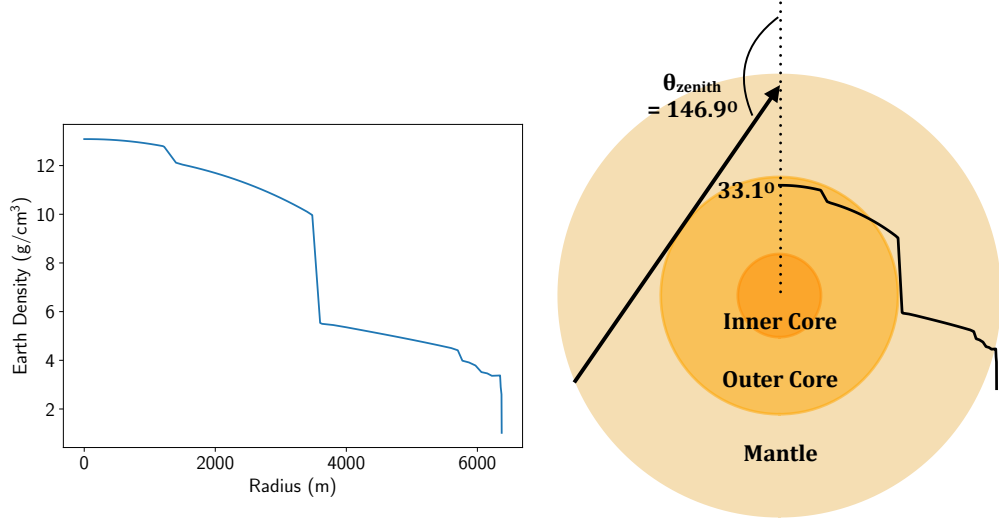


Figure 1.5: (a) The density of the Earth as a function of the radial distance from the center of the Earth from PREM. (b) The zenith angle of the neutrinos that travel along the border of the core and the mantle is 146.9° . The PREM density curve is placed on top to show the corresponding densities for each layer.

1.4 Tau Neutrino Appearance

1.4.1 Tau Neutrinos

Tau neutrinos are hard to detect. DONUT [3] is the first experiment to detect tau neutrinos, and it is the last type of neutrino to be detected even though its existence was predicted long ago [13]. One reason for its late discovery is that tau particles are heavy ($1.776 \text{ GeV}/c^2$). In order to make tau neutrino CC interactions happen, the energy of the tau neutrino must be above the threshold energy of 3.5 GeV. Moreover, direct observation of tau neutrino CC interactions is difficult because the tau lepton has a very short lifetime ($2.9 \times 10^{-13} \text{ s}$), so the length of the tau track produced from a 25 GeV tau neutrino is only on the millimeter scale.

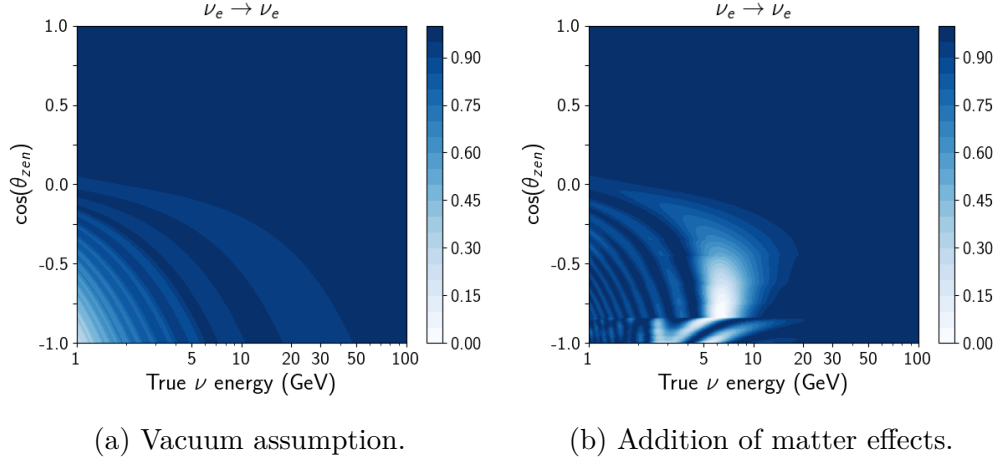


Figure 1.6: Survival probabilities of electron neutrinos as a function of neutrino energy and zenith angle. (a) assumes vacuum. (b) uses the 12-layer PREM model [12].

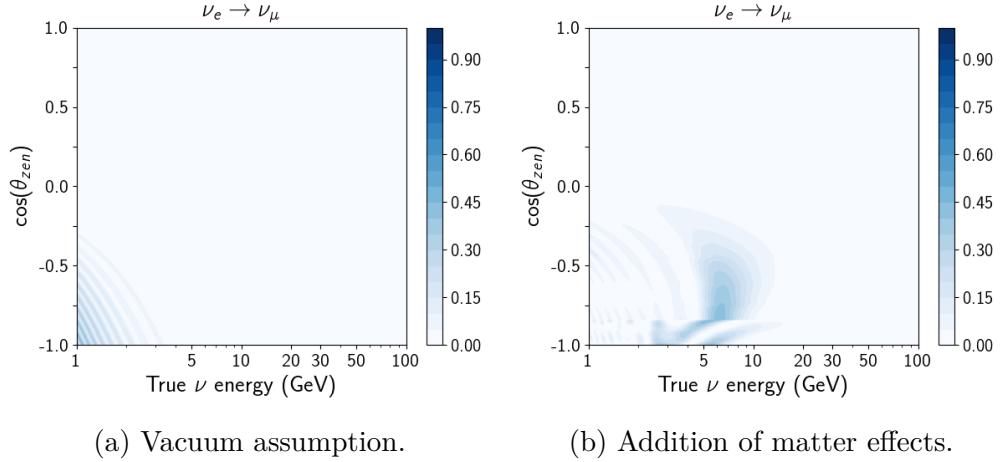


Figure 1.7: Probabilities of electron neutrinos disappearing into muon neutrinos as a function of neutrino energy and zenith angle. (a) assumes vacuum condition. (b) uses the 12-layer PREM model [12].

1.4.2 Tau Neutrino Appearance Experiments

Appearance experiments look for neutrino flavors that are not present in the initial neutrino flux but appear in the final flux.

Current tau neutrino appearance experiments are Super-Kamiokande (Super-K) and OPERA, both of which observe muon to tau neutrino oscillation. Ice-

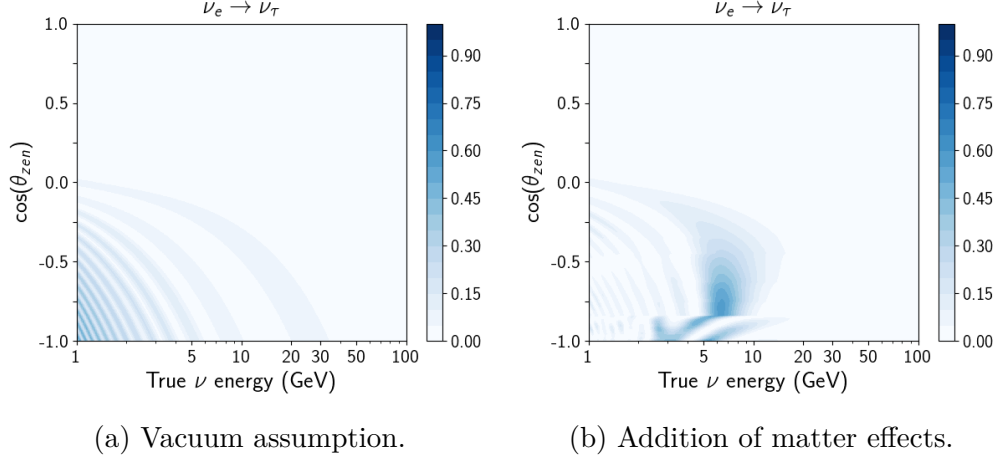


Figure 1.8: Probabilities of electron neutrinos disappearing into tau neutrinos as a function of neutrino energy and zenith angle. (a) assumes vacuum condition. (b) uses the 12-layer PREM model [12].

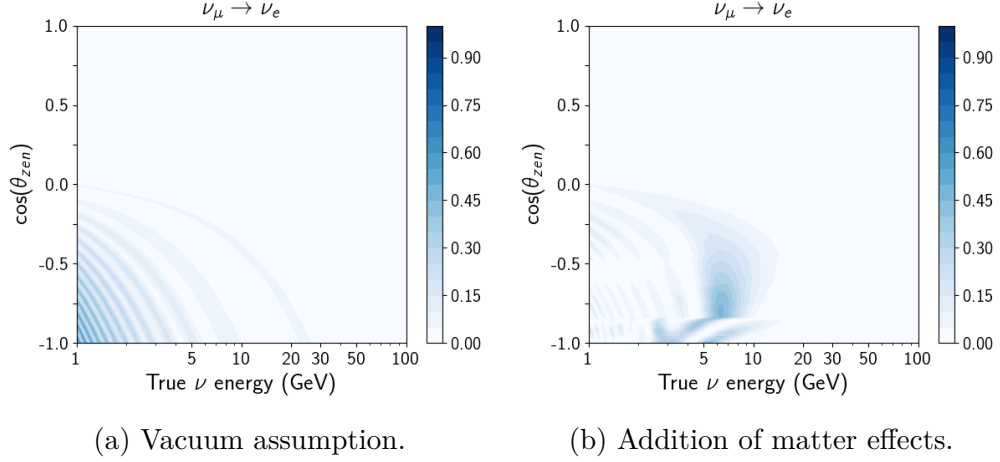


Figure 1.9: Probabilities of muon neutrinos disappearing into electron neutrinos as a function of neutrino energy and zenith angle. (a) assumes vacuum condition. (b) uses the 12-layer PREM model [12].

Cube/DeepCore is the third experiment to do such a measurement. The parameter to measure is the ν_τ signal strength called ν_τ normalization, it should be equal to one under the standard three oscillation picture.

OPERA uses accelerator muon neutrinos as a source, while Super-K uses atmospheric neutrinos. Electron and muon neutrinos are produced in the Earth's atmosphere, where intrinsic tau neutrino production is negligible, and then ν_e and

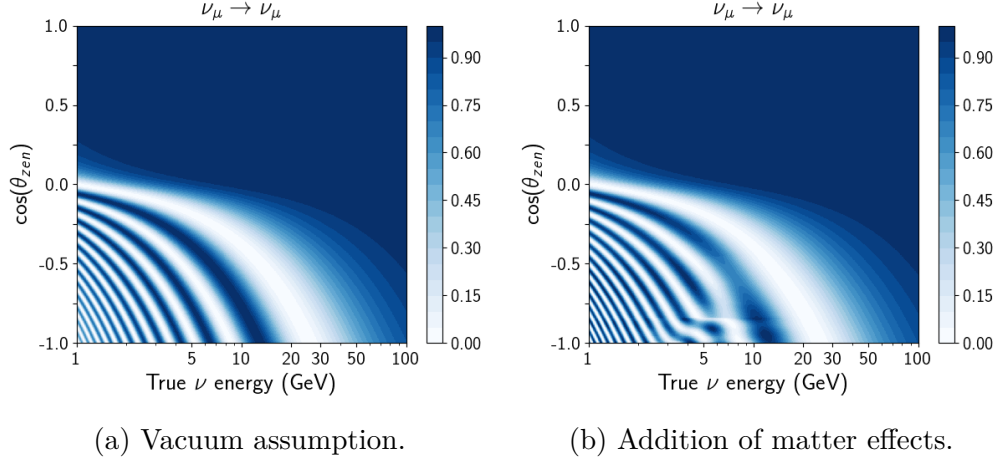


Figure 1.10: Survival probabilities of muon neutrinos as a function of neutrino energy and zenith angle. (a) assumes vacuum condition. (b) uses the 12-layer PREM model [12].

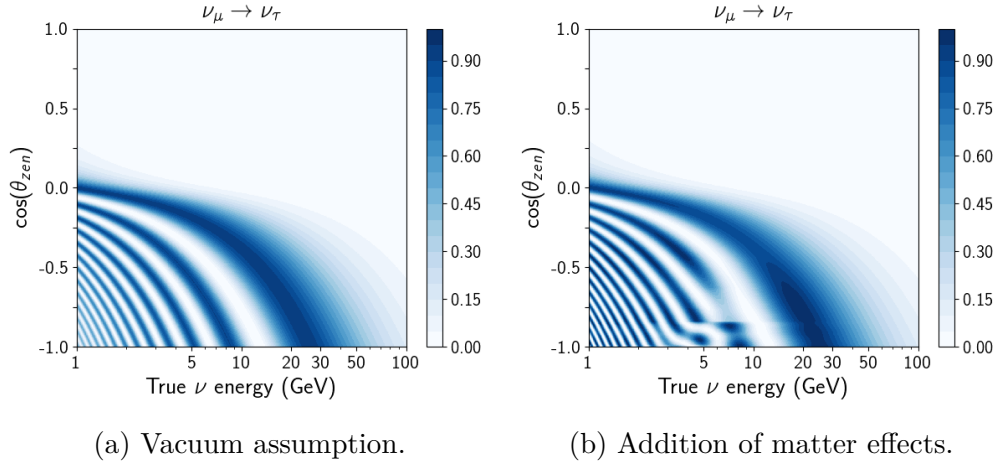


Figure 1.11: Probabilities of muon neutrinos disappearing into tau neutrinos as a function of neutrino energy and zenith angle. (a) assumes vacuum condition. (b) uses the 12-layer PREM model [12].

ν_μ oscillate while traveling through the Earth. When they interact weakly at the detector again, there can be tau neutrino interactions.

IceCube/DeepCore also detects atmospheric neutrinos, but it has a different energy range from Super-K. IceCube/DeepCore looks for neutrinos of 5 – 100 GeV energy - it can look for neutrino appearance at the first maximum. Super-K's energy range is on the order of GeV [14], so most of their tau neutrino events appear at the second maximum. The IceCube/DeepCore detector will be discussed

in Chapter 3.

It's worth mentioning also the neutrino disappearance experiments that measure the disappearance of neutrinos of one flavor changing into the other two flavors.

By comparing Figs.1.6 (b) to 1.11 (b), we can see that the oscillations between ν_μ and ν_τ are predominant, while probabilities of ν_e oscillating into the other two flavors are small, most ν_e stay as ν_e . Then, since the appearance of atmospheric ν_τ come mainly from the disappearance of atmospheric ν_μ , atmospheric neutrino experiments can measure both ν_μ disappearance (*i.e.*, measure the two oscillation parameters θ_{23} and Δm_{atm}^2) and the appearance of ν_τ neutrinos (*i.e.*, measure the ν_τ normalization).

The θ_{23} and Δm_{atm}^2 ($|\Delta m_{32}^2|$) measurements have been preformed by several experiments including Super-K and IceCube/DeepCore. This tau neutrino appearance analysis uses the same event sample developed for the ν_μ disappearance result [15] published in 2017. While both the ν_μ disappearance analysis and ν_τ appearance analysis can measure the oscillation parameters (as seen from Eqs. 1.21 and 1.22), the goal of a ν_τ appearance analysis is to measure the signal strength of the appeared ν_τ events. It tests against the null hypothesis that ν_μ and ν_e oscillate into some sterile neutrinos and not ν_τ . The ν_μ disappearance analysis, on the other hand, examines the null hypothesis that ν_μ do not oscillate into the other two flavors; it also measures the two oscillation parameters under the standard three oscillation paradigm - thus the ν_τ normalization is fixed to one in the ν_μ analysis. They have different goals even though they utilize the same events.

1.4.2.1 OPERA

The initial neutrino flux for OPERA is a muon neutrino beam produced at CERN, which reaches the detector located 732 km away. The protons on target count delivered to OPERA is 17.97×10^{19} . In 2015, among the 19505 neutrino interactions in their target fiducial volume, they observed 5 ν_τ candidates, with an estimated background 0.25 ± 0.05 .

The detector uses emulsion cloud chamber target units to record the neutrino interactions. Each brick has 57 emulsion films, interleaved with 1 mm thick lead plates and complementary electronic detectors. The electronic detectors are used to trigger events and identify the brick with the neutrino interaction vertex inside.

Then, the emulsion plates are scanned automatically to reconstruct vertex location, particle identification, momentum, and so on [16]. Figure 1.12 shows the fifth reconstructed event in a 2-d projection.

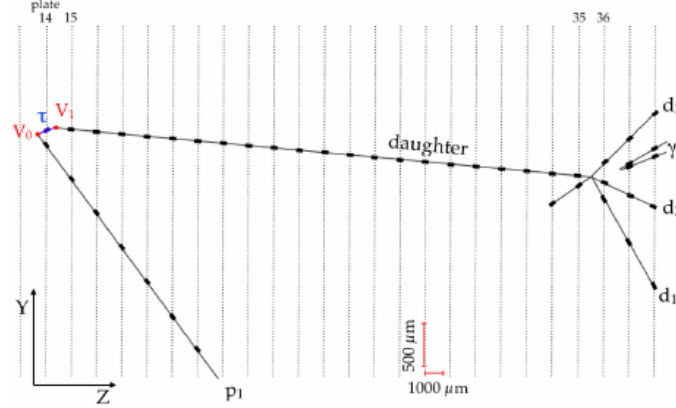


Figure 1.12: A display of OPERA's fifth event. V_0 is the primary vertex and V_1 the secondary vertex. The black stubs are the measurements in the films, taken from Ref. [17].

In 2018, a looser selection criterion is used in order to increase the statistics to 10 ν_τ events, allowing a better measurement of the oscillation parameters [18]. The total signal consists of 10 ν_τ events with a background estimated at 2.0 ± 0.4 . This excludes the no- ν_τ -appearance hypothesis at 6.1σ . Their measurement of the ν_τ CC interaction strength (ν_τ CC normalization) is $1.1^{+0.5}_{-0.4}$.

1.4.2.2 Super-K

Super-K is a water Cherenkov detector located in Japan. It does not observe tau neutrinos directly, but the separation of ν_τ events from ν_e or ν_μ events can be achieved by training a neural network (NN) algorithm.

In 2013, Super-K measured the ν_τ CC normalization to be $1.42 \pm 0.35^{+0.14}_{-0.12}$ using 2806 days of data, corresponding to $180.1 \pm 44.3(\text{stat})^{+17.8}_{-15.2}(\text{syst})$ tau neutrinos. It excludes the no- ν_τ -appearance hypothesis at 3.8σ [19]. In Ref. [14], the measurement is updated with 5326 days of data, and the result is 1.47 ± 0.32 corresponding to 338.1 ± 72.7 events, with the no- ν_τ -appearance-rejection significance at 4.6σ .

Figure 1.13 shows the fitted event distribution of Super-K. The ν_τ signal is shown in grey color, their direction is upward-going in Super-K's coordinates, *i.e.*, the tau neutrinos come from the other side of the Earth.

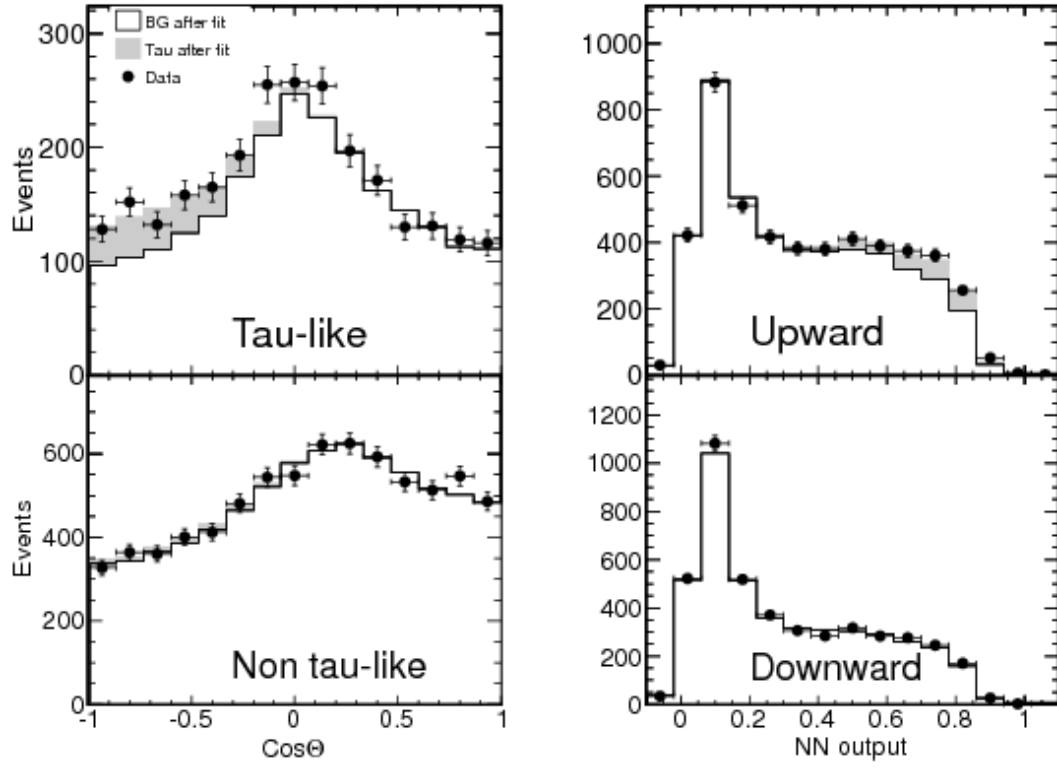


Figure 1.13: Super-K's event distribution in $\cos(\text{zenith})$ and NN output. See the definition of the zenith angle in Chapter 2. Fitted ν_τ signal is the gray colored part. The subplots are tau-like (NN>0.5), upward-going [$\cos(\theta_{\text{zen}}) < -0.2$], non-tau-like (NN<0.5) and downward-going [$\cos(\theta_{\text{zen}}) > 0.2$], taken from Ref. [14].

Chapter 2 |

Atmospheric Neutrinos

Neutrinos come from a variety of sources with a broad energy range. Figure 2.1 shows the measured and hypothesized fluxes from different sources over a wide range of energies. Cosmological neutrinos [20] are relic neutrinos from the Big Bang, they are estimated to have a temperature of roughly 1.95 K, but have not been directly observed yet. At the highest-energy end of the spectrum are the cosmogenic neutrinos, also referred to as the GZK neutrinos. They are produced by interactions of the cosmic ray protons with the cosmic microwave background (CMB). IceCube has the best limit on astrophysical neutrino fluxes. In 2013, IceCube first observed neutrino fluxes at the PeV scale [21–23], although not likely to be GZK neutrinos [24,25] or from Active Galactic Nuclei (AGN) [26]. ANTARES also observed results [27] consistent with IceCube’s.

In 2018, IceCube reported a 3.5σ evidence [28] for observing neutrino emission in 2014 – 2015 from a flaring blazar source. The blazar is a type of AGN. This result indicates that AGN is a likely source of high-energy cosmic rays.

All the other sources of neutrinos have been clearly discovered. Among them, atmospheric neutrinos provide a great tool for studying neutrino oscillations. They are produced by the decay of secondary particles from collisions of cosmic rays and air particles in the atmosphere.

The first experiment to provide evidence for neutrino oscillations was done by Super-K [30] using atmospheric neutrinos. The dominant oscillation Super-K observed is the oscillation from muon neutrinos to tau neutrinos. Figure 2.2 is a simple illustration of the two parameters L and zenith angle θ_{zen} commonly used in atmospheric neutrino experiments. Detectors are usually located underground to reduce the much more abundant atmospheric muons. Zenith angle (θ_{zen}) is the

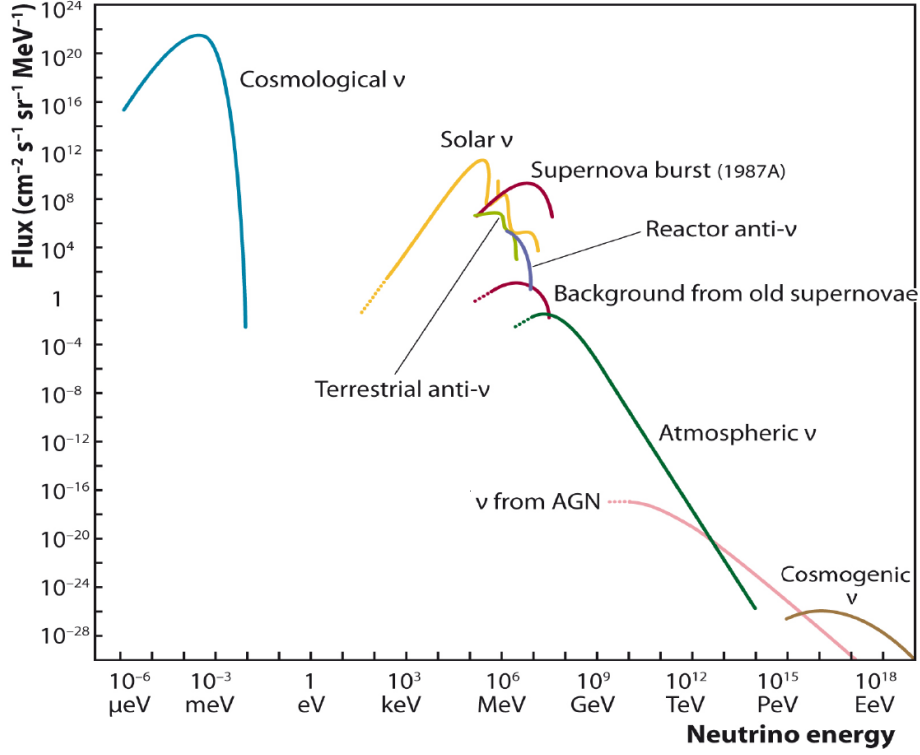


Figure 2.1: Neutrino fluxes from different sources, including naturally occurring and artificial neutrinos, such as reactor neutrinos [29].

angle between the incoming neutrino and the vertical direction of the detector. The baseline L is a function of the detector depth d , Earth radius R , and zenith angle θ_{zen} . For IceCube, events with zenith angles larger than 90° ($\cos(\theta_{\text{zen}}) < 0$) are called upward-going events.

This chapter describes the cosmic ray flux spectrum, the production of atmospheric neutrinos, their oscillations, and the flux model we use.

2.1 Cosmic Rays

Primary cosmic rays mainly come from outside the solar system. The Fermi experiment [31] shows that one source of cosmic rays is supernovae. IceCube's observation of neutrino emission in 2014 – 2015 from a blazar source [28] indicates one source of high-energy cosmic rays is likely AGN.

Roughly 99% of the primary cosmic rays are protons and alpha particles. The rest include electrons, carbon, oxygen, iron, and other nuclei. They have a very

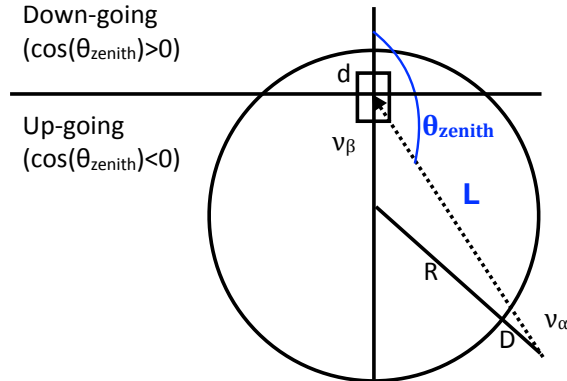


Figure 2.2: The definition of the zenith angle θ_{zenith} and baseline L . d is the detector depth. D is the production height of the atmospheric neutrinos (used in simulation). R is the Earth’s radius.

broad energy range from 10^9 to 10^{20} eV. The plot on the left in Fig. 2.3 shows the flux composition. The all-particle differential flux ϕ ($= \frac{dN}{dE dA d\Omega dt}$) vs. energy is shown on the right, $\frac{dN}{dE dA d\Omega dt} \propto E^{-\gamma}$, where γ , the particle spectral index, varies between 2.6 and 3.4 in different energy regions. Since the flux of neutrinos is directly proportional to the flux of primary cosmic rays, a change of the cosmic ray spectral index will also change the neutrino flux in a similar way. Thus we use a function $E^{\Delta\gamma}$ to account for this uncertainty, where E is neutrino energy. The primary cosmic ray spectrum changes according to the solar activity, because the solar wind blows lower energy cosmic rays away from the Earth. This greatly affects cosmic rays with energies below 10 GeV [32].

2.2 Creation of Atmospheric Neutrinos

Primary cosmic rays collide with the nuclei of particles in the Earth's atmosphere, generating pions and kaons. Eq. 2.1 shows the interaction, where X represents other possible hadrons

$$p + N \rightarrow \pi^+ + \pi^- + K^+ + K^- + X. \quad (2.1)$$

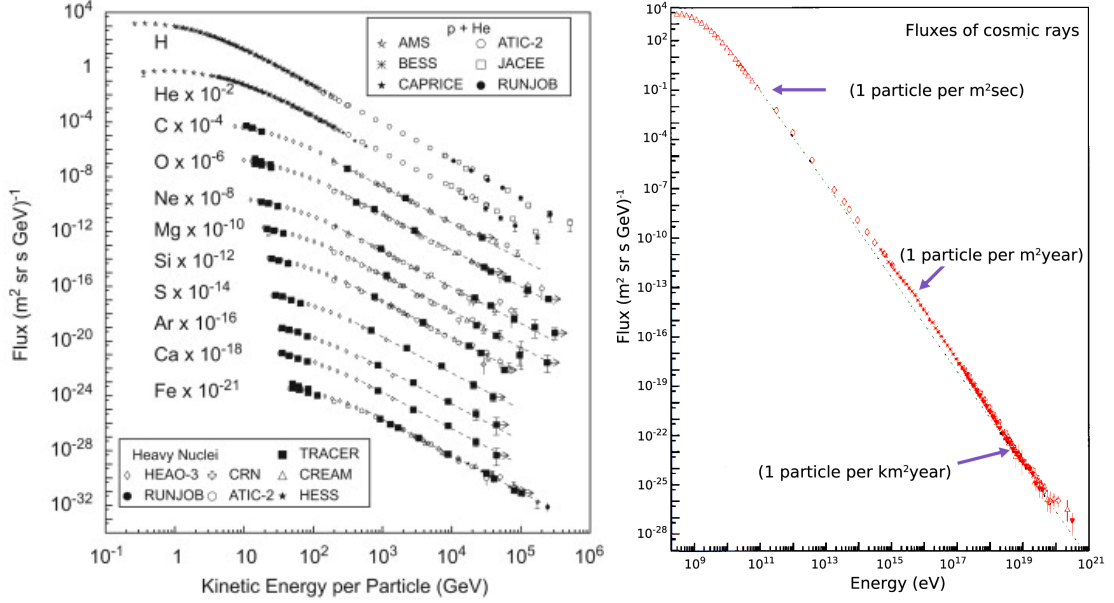


Figure 2.3: Left: Primary cosmic ray composition [33]. Right: The flux of cosmic rays as a function of the energy. Generally speaking, it falls off approximately proportional to E^{-3} (shown in green dashed line) [34].

The pions and kaons will then decay into muons and muon neutrinos as shown in Eq. 2.2



Figure 2.4 shows the fractional contributions from pions and kaons for muon neutrinos and muons, where the pion decay chain dominates in the energy range below 100 GeV and the kaon decay dominates at higher energies.

Muons can further decay into electrons, $\nu_e(\bar{\nu}_e)$ and $\nu_\mu(\bar{\nu}_\mu)$ (with an almost 100% branching ratio [35]) before they reach the ground:



The above muon decays are the main sources for the $\nu_e(\bar{\nu}_e)$ production below 1 GeV. Muons with energy of several GeV and above reach the ground before decaying, so the ratio of ν_e to ν_μ decreases with increasing energy. For $\nu_e(\bar{\nu}_e)$

above 1 GeV, the kaon decay mode shown in Eq. 2.4 is the dominant source

$$K_L \rightarrow \pi^+(\pi^-) + e^-(e^+) + \bar{\nu}_e(\nu_e). \quad (2.4)$$

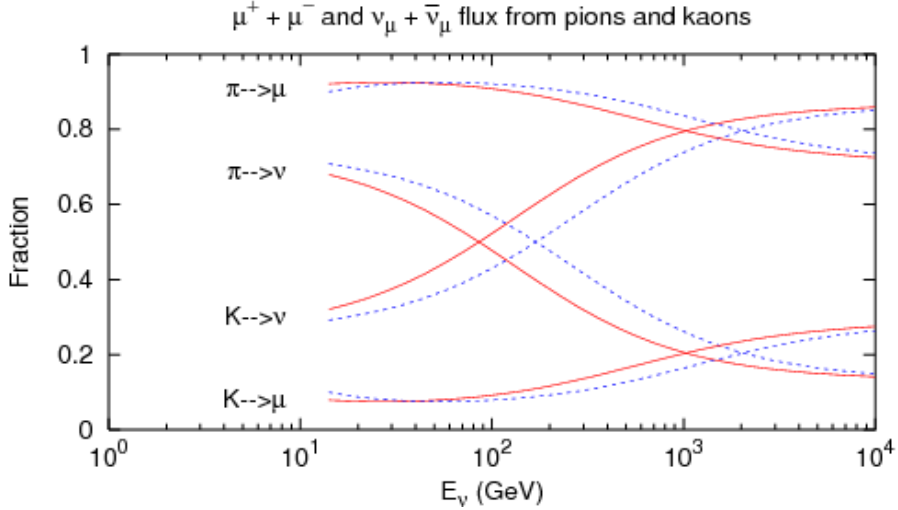


Figure 2.4: Contributions from kaons and pions to muon neutrinos and muons at different energies, solid lines represent pions or kaons traveling vertically, dashed lines are those traveling with a zenith angle of 60° . We see that the contribution from kaons is smaller in our energy range of interest 10 – 100 GeV [36].

From Eqs. 2.2 and 2.3, we know that the ratio of atmospheric ν_e to ν_μ is roughly 1:2 (below 1 GeV), and that the ratio of ν_μ to $\bar{\nu}_\mu$ is roughly 1:1, and the ratio of ν_e to $\bar{\nu}_e$ is proportional to $\mu^+ : \mu^-$.

These neutrinos produced from the decay of charged pions and kaons in Eqs 2.2, 2.3 and 2.4 are called the conventional atmospheric neutrinos. They do not contain ν_τ .

There are also neutrinos produced by the decay of heavier mesons containing a charm quark. These neutrinos are called prompt neutrinos. For example the D^+ meson (with the quark content: $c\bar{d}$) can decay into a muon neutrino or an electron neutrino (both with a branching ratio of 8.7% [35]):

$$\begin{aligned} D^+ &\rightarrow \bar{K}_0 + \mu^+ + \nu_\mu, \\ D^+ &\rightarrow \bar{K}_0 + e^+ + \nu_e. \end{aligned} \quad (2.5)$$

Also, the prompt tau neutrinos come from mainly the strange D meson D_s^+ decay with a branching ratio of 5.5% [35]:

$$D_s^+ \rightarrow \tau^+ + \nu_\tau. \quad (2.6)$$

The charm mesons have a mean lifetime on the order of 10^{-12} s, so they decay promptly almost all without interacting. Thus, these neutrinos are called the prompt neutrinos. Also, since the decay is prompt, the prompt neutrinos follow the same energy spectrum as the primary cosmic rays (roughly $E^{-2.7}$). The conventional neutrinos, however, have a steeper spectrum (roughly $E^{-3.7}$) because the pions and kaons may also interact since they have a longer lifetime (roughly 10^{-8} s).

Another difference is that the prompt neutrino fluxes of ν_μ and ν_e are identical, but the conventional ν_μ flux is roughly two times the ν_e flux.

Figure 2.5 shows the comparison of the prompt ν_μ flux and the conventional ν_μ flux. Only at energies around $10^5 - 10^6$ GeV, the prompt neutrino flux starts to dominate the conventional flux.

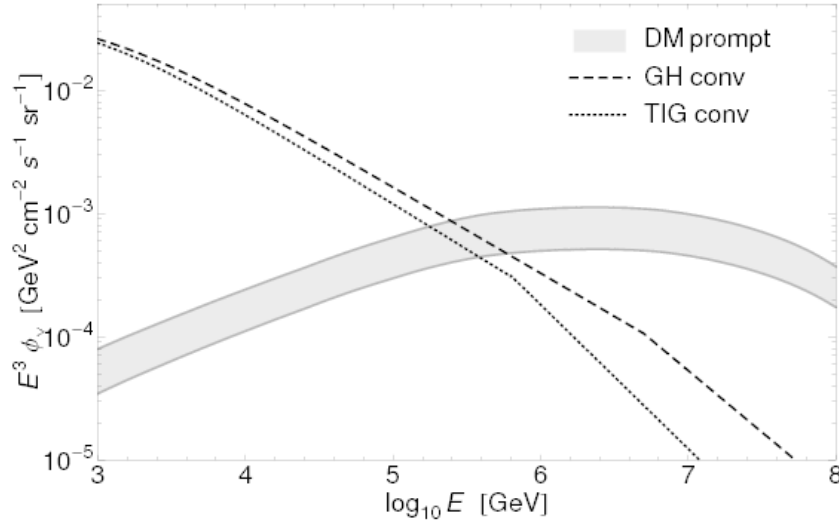


Figure 2.5: Flux comparisons of conventional neutrinos and prompt neutrinos. GH stands for the Gaisser and Honda model [36], TIG stands for the Thunman, Ingelman and Gondolo [37] model. DM stands for “dipole model” used for the prompt neutrino flux calculation in Ref. [38]. The gray band is the theoretical uncertainty of the prompt model. Figure taken from Ref. [38].

Figure 2.6 shows the comparison of the prompt ν_μ and ν_τ fluxes. The ν_τ

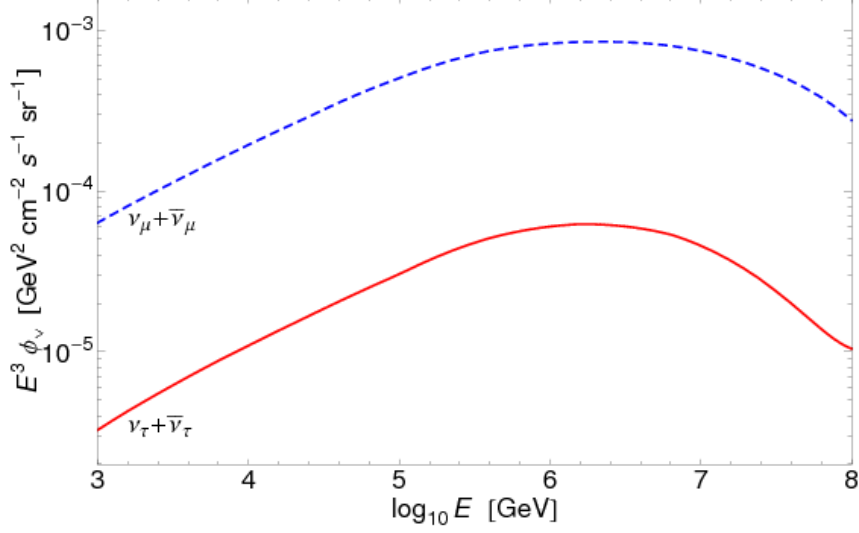


Figure 2.6: Comparison of prompt ν_μ fluxes and ν_τ fluxes [38].

flux is about one order of magnitude lower than the ν_μ (ν_e) flux. From Fig. 2.5 and Fig. 2.6, at energy 10^3 GeV, the intrinsic ν_τ fluxes are roughly three orders of magnitude less than the conventional ν_μ and ν_e fluxes, since the conventional neutrinos have a steeper spectrum than the prompt neutrinos, at lower energies below 10^3 GeV, the prompt neutrino fluxes to the conventional neutrino fluxes is even smaller. Thus, prompt neutrinos can be safely neglected in the energy of interest from 5–100 GeV.

Most atmospheric muons are produced at about 15 km [39] above the surface of Earth. Muons lose about 2 GeV to ionization before reaching the ground. The detector depth is 2 km below the surface. Atmospheric muons travel with a speed close to the speed of light, they have a mean lifetime of $2.2 \mu\text{s}$. The mean decay length of muons can be calculated using

$$L = \gamma\beta c\tau, \quad (2.7)$$

where γ is the Lorentz factor, β is the ratio of the particle speed v to the speed of light c , τ is the mean lifetime of the particle at rest ($\tau_\mu = 2.2 \mu\text{s}$), $c\tau_\mu = 659 \text{ m}$. For example, a muon with an energy of 2.4 GeV has a decay length of 15 km, but due to energy loss in the atmosphere it's reduced to 8.7 km [35].

The energy loss of muons traveling in matter can be described by

$$-\frac{dE_\mu}{dX} = a + bE_\mu, \quad (2.8)$$

where X is the distance the muon travels in matter, a is the ionization loss and b is the fractional energy loss by three radiation processes: bremsstrahlung, direct production of electron positron pairs, and photonuclear interactions [35]. Thus, the minimum energy required for muons passing through a distance d of ice is [40]:

$$E(d) = (E^{bd} - 1) a/b. \quad (2.9)$$

For the ice in IceCube, the values of a and b are $a = 0.163 \text{ GeV m}^{-1}$ and $b = 0.192 \times 10^{-3} \text{ m}^{-1}$ [40]. The IceCube detector depth is 2 km. Thus, a vertically traveling muon needs to have a threshold energy on the order of 400 GeV to penetrate the 2 km of ice to reach the IceCube detector.

Muons with energies large enough to reach the IceCube detector are an important part of the background. The number of atmospheric muons that trigger IceCube is roughly 10^6 times the number of neutrinos. Thus, we need to develop tools to reject these background muons while preserving the signal neutrinos. These tools will be discussed in Chapter 5.

2.3 Oscillations of Atmospheric Neutrinos

Since the intrinsic tau neutrinos produced in the atmosphere are negligible, atmospheric neutrinos are excellent neutrino source for tau neutrino appearance experiments .

Figure 2.7 shows the energy dependence of the oscillation probabilities of ν_e and ν_μ that travel vertically along the Earth's diameter, *i.e.*, their path length $L \simeq 12,700 \text{ km}$. The oscillations between ν_μ and ν_τ are predominant, since probabilities of ν_e oscillating into the other two flavors are small and close to zero for $E_\nu > 20 \text{ GeV}$. The first maximum of ν_μ to ν_τ probability happens near 25 GeV.

2.4 Atmospheric Neutrino Flux Calculation Model

In order to calculate the number of neutrinos we expect to observe, one important step is to get the expected neutrino flux for a neutrino with a certain flavor, energy,

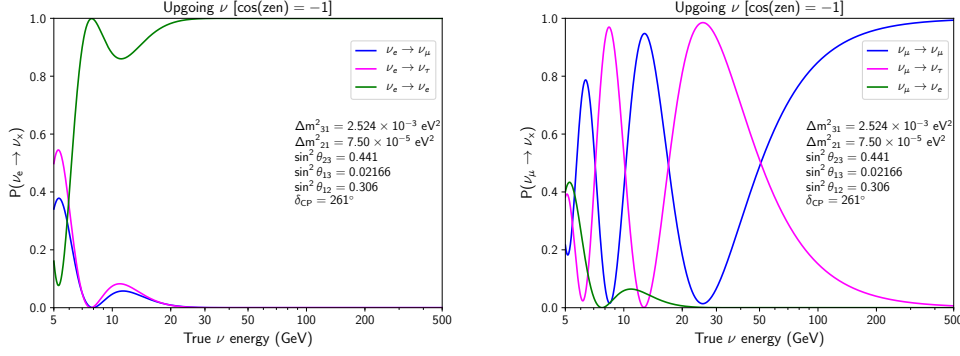


Figure 2.7: Oscillation probabilities as a function of neutrino energy for atmospheric ν_e (left) and ν_μ (right) after traveling through the Earth along the Earth's diameter.

and direction. We use the HKKM flux model [41] for the location of South Pole with the NRLMSISE-00 atmosphere model [42].

Figure 2.8 shows that the measured neutrino fluxes by IceCube and other experiments for neutrinos at the low-energy end, and roughly up to energies on the order of 10^2 GeV, agree well with the HKKM model. Figure 2.9 shows the flux distributions at the South Pole calculated from the HKKM model. Figure 2.9 (a) shows the fluxes as a function of $\cos \theta_{\text{zen}}$. $\cos \theta_{\text{zen}} = 0$ is the horizontal direction, so Fig. 2.9(a) shows that there are much more neutrinos produced near the horizon than the vertical direction. This is called the “secant theta” effect [43]. It occurs because horizontal pions and kaons have a larger traveling distance in less dense atmosphere than vertical ones. So there are more horizontal neutrinos produced than vertical neutrinos. The solid lines are the averaged fluxes from June to August (winter for the South Pole) and the dashed lines are from December to February (summer for the South Pole). This seasonal effects occur because of the variations of the air density. Air density at higher altitudes ($\gtrsim 15$ km) is higher in the summer at the South Pole [41].

We perform parametrizations on the ν_e and ν_μ fluxes provided by the HKKM model [41] at different zenith angles and energies.

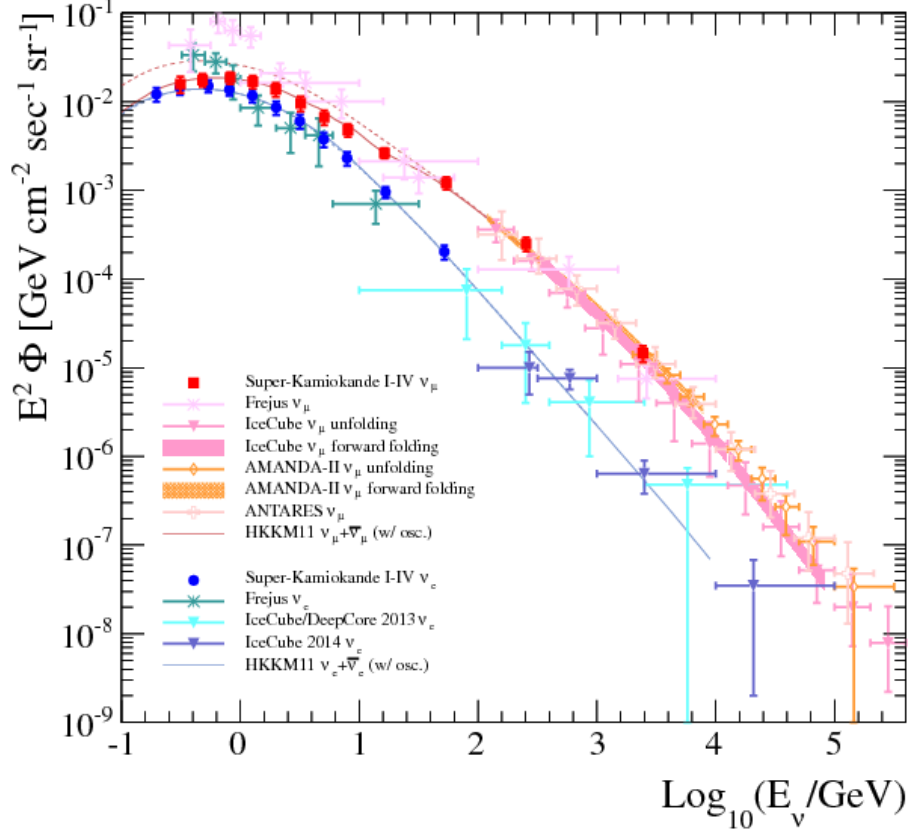
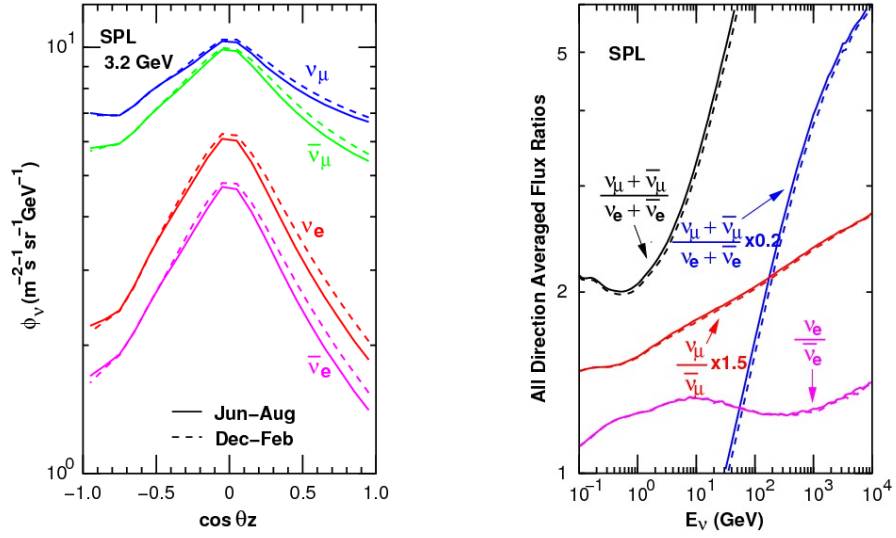


Figure 2.8: Comparison of measured neutrino fluxes and HKKM model. Measurements by IceCube are shown as triangles (blue and purple for ν_e , pink for ν_μ) [44].

2.5 Flux Uncertainties

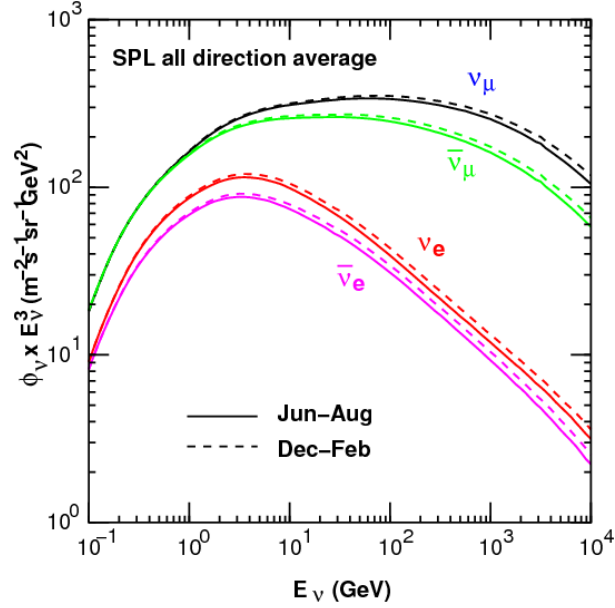
After obtaining the atmospheric fluxes from the parametrizations, we need to assess the flux uncertainties. Based on uncertainties calculated in Ref. [45], the dominant error in atmospheric neutrino fluxes results from uncertainties in hadron production, while the second largest is from uncertainties in the primary flux.

In this ν_τ analysis, we use four parameters to do modifications of the fluxes based on Ref. [45]: modification of the ratio of upward-going and horizontal neutrinos (up/hor ratio), modification of the ratio $\nu/\bar{\nu}$ ($\nu/\bar{\nu}$ ratio), deviation of spectral index ($\Delta\gamma$), and the flux ratio of ν_e/ν_μ (applied on both ν_e/ν_μ and $\bar{\nu}_e/\bar{\nu}_\mu$, but denoted as ν_e/ν_μ from now on). They are discussed in detail in Chapter 7.



(a) Azimuth-averaged flux

(b) Flux ratio



(c) All-direction averaged flux

Figure 2.9: (a) Distribution of atmospheric fluxes averaged over azimuth angles vs. zenith angles. Solid lines are averaged from June to August, and dashed lines from December to February. (b) The ratio of fluxes with different flavors vs. energy. (c) All-direction averaged fluxes vs. energy [41].

Chapter 3 |

IceCube and Neutrino Detection

IceCube is a neutrino detector at the South Pole at around 2000 meters below the surface. It consists of 5160 Digital Optical Modules (DOMs) embedded in the ice and occupies a volume of approximately 1 km^3 . AMANDA was the precursor to IceCube, aimed at mapping the ice properties. Its first four strings were deployed in 1996 and all 19 strings completed in 2000 before it was shut down in 2009. The ice properties vary with depth, correlated with the dust concentration in the ice. The largest dust concentration is at the depths between 2000 m to 2100 m from the surface, and is referred to as “dust layer.” In 2004, IceCube was approved and its deployment started. DeepCore is the dense sub-array of IceCube, deployed in the clearest ice below the dust layer in order to avoid strong light scattering and absorption. The deployment of the DeepCore strings started in 2009, finishing in 2010. In 2011, all 86 IceCube strings were installed, taking seven years in total. This chapter describes the IceCube detector, the ice properties, and how neutrinos are detected in IceCube.

3.1 IceCube

Figure 3.1 shows the geometry of the IceCube detector. Its in-ice array consists of 86 strings, each containing 60 Digital Optical Modules (DOM). Seventy-eight of the strings have a horizontal spacing of 125 m; the vertical spacing between the DOMs on each string is 17 m. The DOM is the detecting unit of IceCube. Each DOM contains a photomultiplier tube (PMT) that transforms a light signal into

an electronic signal. A detailed description is given in Section 3.1.2. These 78 strings are referred to as the standard IceCube strings and their DOMs (PMTs) as standard IceCube DOMs (PMTs).

The other eight strings are the DeepCore strings, which are mostly located 2100 m below the surface in the clearest ice. They have a horizontal spacing of 70 meters, and the vertical spacing between DOMs is either 7 m (below the dust layer) or 10 m (above the dust layer). See Fig. 3.2 for their distribution in space.

Six of the eight DeepCore strings consist of High Quantum Efficiency (HQE) DOMs, which contain PMTs having a higher quantum efficiency than the standard IceCube PMTs. The standard PMTs are the 10'-diameter Hamamatsu R7081-02 PMTs. The HQE DOMs are the Hamamatsu R7081-02MOD PMTs. In the wavelength range 300 nm – 650 nm, the standard PMTs have a peak quantum efficiency around 25% near 390 nm, and the HQE PMTs have a peak quantum efficiency of 34% [46]. Two of the DeepCore strings are a mix of both standard and HQE DOMs.

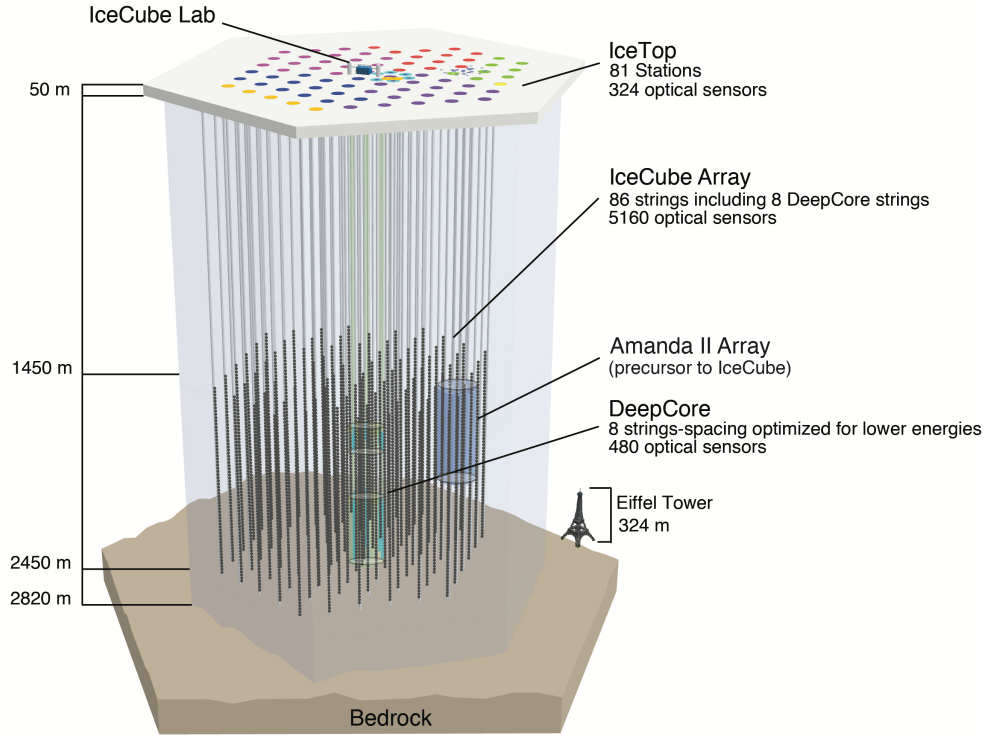


Figure 3.1: The IceCube Detector consists of 86 strings with digital optical modules on each string [47].

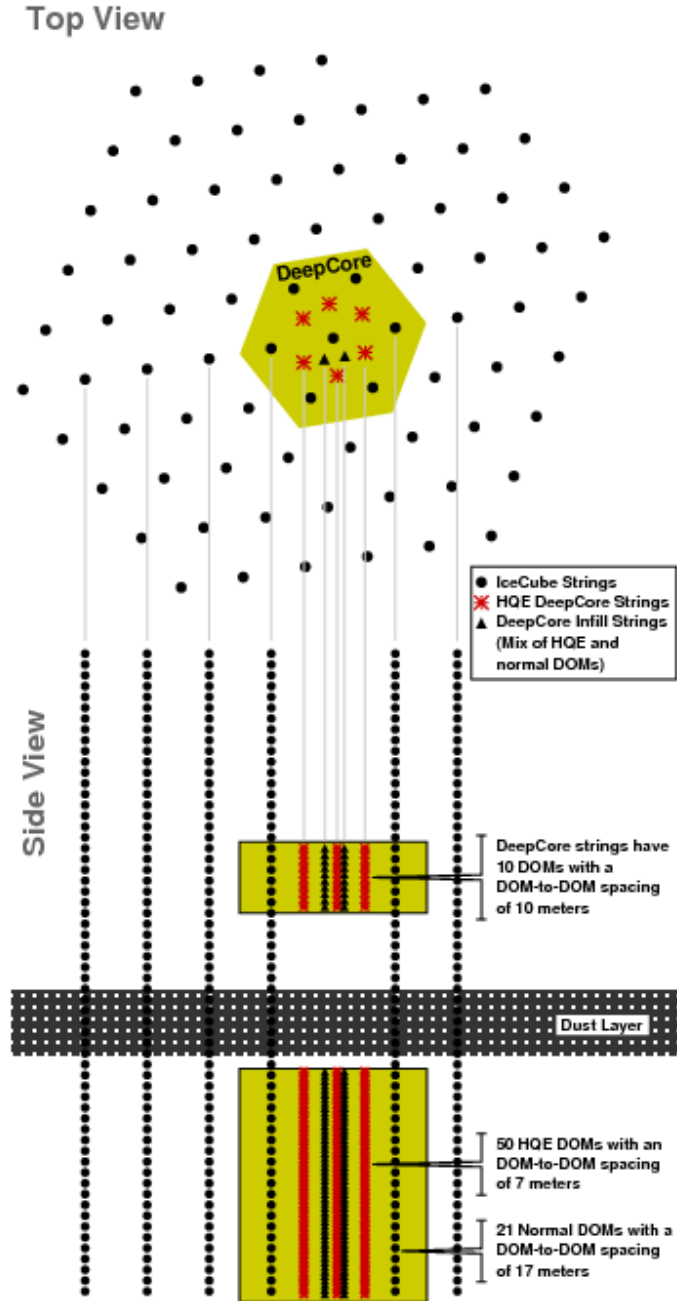


Figure 3.2: Top and side view of the IceCube detector. The DeepCore region includes seven regular IceCube strings and the eight strings marked with red stars and black triangles.

Apart from the in-ice array and the DeepCore sub-array, IceCube also has an IceTop surface array. It consists of 162 ice-filled tanks which contain PMTs for Cherenkov radiation detection. It is sensitive to primary cosmic rays in the energy range of PeV to EeV. For IceCube/DeepCore analyses with neutrinos, it is also used for the veto of downward-going atmospheric muons.

The geometry of the standard IceCube strings is designed to detect astrophysical neutrinos above 100 GeV. DeepCore is optimized for the detection of neutrinos in the 10 – 100 GeV energy range, where we expect to observe the maximum disappearance of atmospheric ν_μ into ν_τ .

3.1.1 DeepCore Fiducial Region

The DeepCore fiducial region is different from the DeepCore strings; the former contains the eight DeepCore strings and also seven standard IceCube strings. See Fig. 3.2 for the top and side view of the detector. In the figure, the yellow box below the dust layer shows the DeepCore fiducial region in the vertical direction, the yellow hexagon in the top view plot shows the region in the horizontal plane. Only events triggering the DeepCore fiducial region are recorded; its details will be discussed in Chapter 5. Similarly, the yellow box above the dust layer contains both standard IceCube strings and DeepCore strings, used as the veto region to help identify and reject atmospheric muons, especially the vertical muons. They can also be used to improve the reconstruction of low-energy, near-horizontal tracks in certain analyses [47].

3.1.2 DOM Properties

A DOM is a spherical optical detecting unit composed of a downward-facing 10-inch PMT, the DOM mainboard, and other electronics shown in Fig. 3.3. The outer DOM glass sphere can withstand enormous pressure exerted by the ice. The DOM mainboard contains an Analog Transient Waveform Digitizer (ATWD), a Fast Analog to Digital Converter (FADC), and an Field-Programmable Gate Array (FPGA) with an on-board processor, a flasher board and other ancillary electronics.

The ATWD and FADC are used for digitizing the analog PMT signals (called “waveforms”). There are three ATWD input channels, each with a different am-

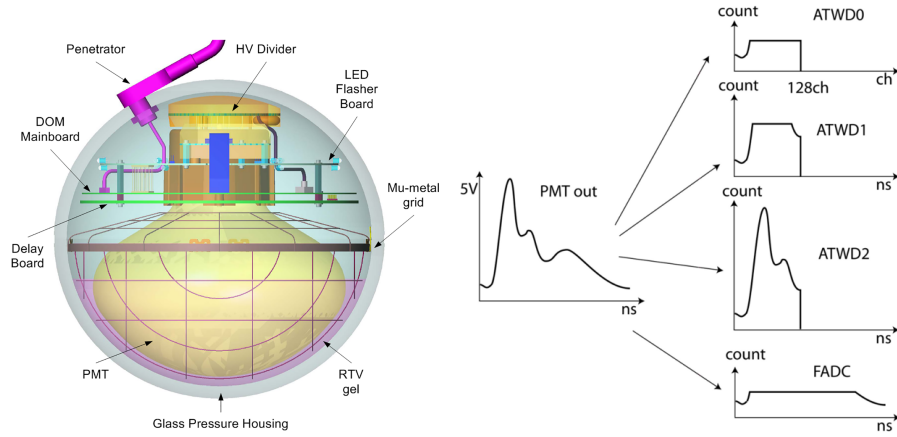


Figure 3.3: Left: Schematic view of the DOM. The mu-metal grid is used to shield the PMT from the Earth’s magnetic field, the layer of RTV gel to optically couple the PMT glass to the pressure vessel, the LED flasher board is used for calibration, and the HV generator and divider circuit for the voltage supply. Right: The PMT output waveform is fed into the 3 ATWD channels (ch0, ch1, ch2) and the FADC channel [48].

plification level as shown in Fig. 3.3. Each channel contains 128 samples with a bin size of 3.3 ns, covering a total interval of 422 ns. Each ATWD stores these waveform samples in capacitors. These signals can then be digitized if the local coincidence (*i.e.*, the 0.25 photoelectron (PE) threshold described in Section 3.1.3) is triggered, if not they are cleared. The FADC has one channel, stores 256 samples each with a bin size of 25 ns, covering a longer interval of 6.4 μ s. The three ATWD channels have different amplification levels (16, 2 and 0.25 for ch0, ch1, and ch2, respectively). The example waveform makes the highest amplification level ch0 saturate first, then the medium level ch1, and the lowest level ch3 is unsaturated [48, 49]. The digitized signals are then sent to the surface via cables.

3.1.3 Photoelectrons, Hits, and Local Coincidence

The photoelectron is a unit of charge. One PE is the charge recorded by a DOM that corresponds to a single photon that initially hits the DOM. A “hit” occurs when a DOM’s PMT exceeds the 0.25 PE threshold, and such a DOM is called a “hit DOM.”

Local Coincidence (LC) means the occurrence of several neighboring DOMs getting hit. This indicates a possible physics event and thus is used as the cri-

terion for keeping the digitized ATWD and FADC signals. The types of local coincidence are soft local coincidence (SLC) and hard local coincidence (HLC). The non-LC signals are mostly PMT dark noise and isolated single photons. Dark noise has several different sources, such as thermal noise, electronic noise, decaying radioactive isotopes in the PMT/DOM glass, scintillation, and Cherenkov light from radioactive decays.

There are two LC spans: LC span 1 is a coincidence between the direct neighbor DOMs, and LC span 2 includes two DOMs up and two DOMs downward. If either the LC1 or LC2 condition is met, the LC is called hard local coincidence (HLC) and the hit is called an HLC hit. The HLC condition leads to a full readout of the digitized 256 FADC and 364 ATWD channels. If one DOM is hit in isolation, it is called an SLC. So SLC is actually not a coincidence, and it leads to a SLC readout that's only 3 FADC samples out of the first 25 samples (the highest amplitude bin and its two neighbors), creating only a coarse time and charge stamp for this DOM.

3.1.4 Data Flow

The LC is the first level of data reduction, removing uncorrelated noise hits. The second level is the Data Acquisition System (DAQ) that takes place in the computers on the surface. The DAQ reads all DOM hits and runs different trigger algorithms and eventually creates “events” as its output.

Table 3.1 shows several trigger algorithms [50]. Most triggers are simple majority triggers (SMT), generally they look for a certain number of HLC hits within a time window. The first three rows are SMT for in-ice DOMs, DeepCore DOMs, and IceTop DOMs. The DeepCore SMT3 (used for this analysis) looks for at least 3 HLC hits within $2.5 \mu\text{s}$ in the DeepCore DOMs.

Other triggers have requirements on the geometrical distribution of the hits. The volumn trigger defines a cylinder around each hit DOM and look for certain multiple hits within the cylinder. It allows the triggering of localized low-energy events that do not trigger SMT. The cylinders' radius r and height h defined under the “Topology” column.

SLOP is Slow Particle (SLOP) trigger [46], designed to look for slow track-like events. For example, it can look for the hypothesized magnetic monopoles. It first

removes pairs of HLC hits that come too close in time ($\Delta t < T_{prox}$) to remove muon hits. Then, it looks for 3-tuples of pairs within a time window $[T_{min}, T_{max}]$, requiring the number of these tuple pairs to be at least $N_{tuple} = 5$. The geometry of each 3-tuple must satisfy track-like conditions. α_{min} is the minimum allowed angle of the obtuse inner angle of the triangle. v_{rel}^{max} is the largest allowed value for the “normalized velocity difference” v_{rel} , which is defined as $v_{rel} = 3 \frac{v_{12}^1 - v_{23}^1}{v_{12}^1 + v_{23}^1 + v_{13}^1}$, $v_{ij} = \Delta x_{ij} / \Delta t_{ij}$.

Fixed-rate trigger (FRT) reads out 10 ms of data in the full detector, it is used as a minimum-bias sample and for studies of DOM noise [50].

All trigger algorithms are run in parallel over all DOM hits since the same hits can satisfy multiple triggers, and overlapping triggers are merged to one single event [46].

Trigger	DOM set	N HLC hits	Window (μs)	Topology	Rate (Hz)
SMT	in-ice	8	5	—	2100
SMT	DeepCore	3	2.5	—	250
SMT	IceTop	6	5	—	25
Volume	in-ice	4	1	cylinder (r=175m, h=75m)	3700
Volume	IceTop infill	4	0.2	cylinder (r=60m, h=10m)	4
String	in-ice	5	1.5	7 adjacent vertical DOMs	2200
SLOP	in-ice	$N_{triplet} = 5$	$T_{prox} = 2.5,$ $T_{min} = 0,$ $T_{max} = 500$	$\alpha_{min} = 140^\circ, v_{rel}^{max} = 0.5$	12
FRT	all	—	—	—	0.003

Table 3.1: Different trigger algorithms, their requirements and their typical event trigger rates as of May 2013. Trigger rates vary seasonally. Taken from Ref. [50]

The third level is the Processing and Filtering (PnF), which takes the DAQ events to perform fast reconstructions and selections to reduce the data rate from 1 TB/day to 100 GB/day. The output events are then sent over satellite to the data warehouse in the Northern Hemisphere. Different filters are used for different types of physics events. For example, the DeepCore filter is used for filtering events triggering DeepCore. Other examples are: the cascade filter looking for more sphere-like events, the EHE (Extremely High Energy) filter looking for highly energetic events, and the Sun and Moon filter looking for events coming from the Sun and the Moon. The DAQ and PnF described above are part of the online

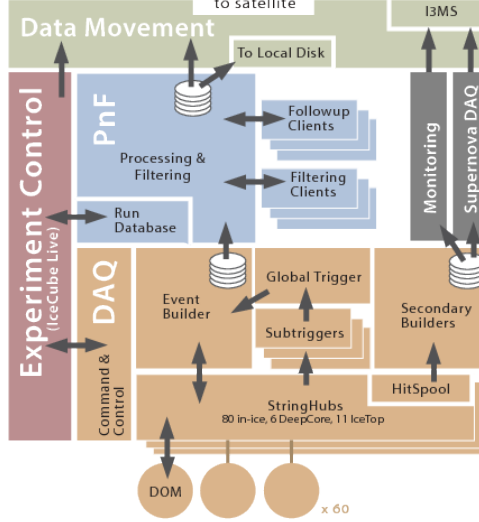


Table 3.2: The online data flow in IceCube [46].

systems (see Table 3.2 for the online data flow).

After the data get transferred to the North, the next steps are offline data filtering and processing. The data that are filtered offline and processed offline are internally termed “level 2” data. (“Level 1” data is the online data right before the filtering and processing.) After level 2, more levels of event selection are needed for specific analyses. For example, the level 3 of this ν_τ analysis contains a set of more stringent triggering and vetoing algorithms, while at level 5, a boosted decision tree (BDT) is developed to reject muon background. A detailed description of this process is in Chapter 5.

3.2 Neutrino Detection

Neutrinos can’t be observed directly in IceCube, but some of the secondary charged particles from neutrino interactions can be observed. The secondary particles’ Cherenkov radiation produces light; light travels in the ice and some of the photons get scattered along the way, but those that arrive at a DOM can be detected by the DOM’s PMT and digitized into electronic signals. By using the charge, temporal, and spatial information of the hit DOMs, the incoming neutrino’s direction and energy can be reconstructed (Chapter 4).

3.2.1 Neutrino Interactions

In the intermediate neutrino energy range $0.1 - 20$ GeV, the interactions of neutrino with matter include quasi-elastic (QE), NC elastic scattering, resonant single pion production (RES), coherent pion production, multi-pion production and kaon production. Neutrino scattering in this region is quite complex and not accurately known. Here we only discuss the RES and QE scattering. In the high energy region $20 - 500$ GeV, the neutrino is energetic enough to scatter off an individual quark inside the nucleon, and such a process is called deep inelastic scattering (DIS) [51], and is well understood.

The weak interactions have two types: charged-current (CC) interaction and neutral-current (NC) interaction. The former has the charged exchange particle W^\pm boson, and the latter a neutral Z^0 boson. Figure 3.4 shows example Feynman diagrams of CC DIS and CC QE, NC DIS, and NC elastic scattering. In the case of RES, the target first goes to an excited state then emits a pion. The main interactions are:

$$\begin{aligned}\nu_l + N &\rightarrow l + N^*, \\ N^* &\rightarrow \pi + N',\end{aligned}\tag{3.1}$$

$$\begin{aligned}\nu_l + N &\rightarrow l + \Delta^{++}, \quad \Delta^{++} \rightarrow p + \pi^+, \\ \nu_l + N &\rightarrow l + \Delta^+, \quad \Delta^+ \rightarrow n + \pi^+.\end{aligned}\tag{3.2}$$

These three types of interaction cross sections and the total cross section are shown in Fig. 3.5. The RES and QE scattering have a much larger uncertainty. In this analysis, the axial mass form factors for the CCQE scattering (M_A^{CCQE}) and RES (M_A^{res}) events are included as systematics. The DIS cross section uncertainty effect was also considered but it was found to be small and was therefore neglected (Chapter 7).

3.2.2 ν_τ Deep Inelastic Scattering (DIS)

The DIS is the main component of ν_τ -nucleon scattering. The NC DIS interaction is:

$$\nu_\tau + q \rightarrow \nu_\tau + q.\tag{3.3}$$

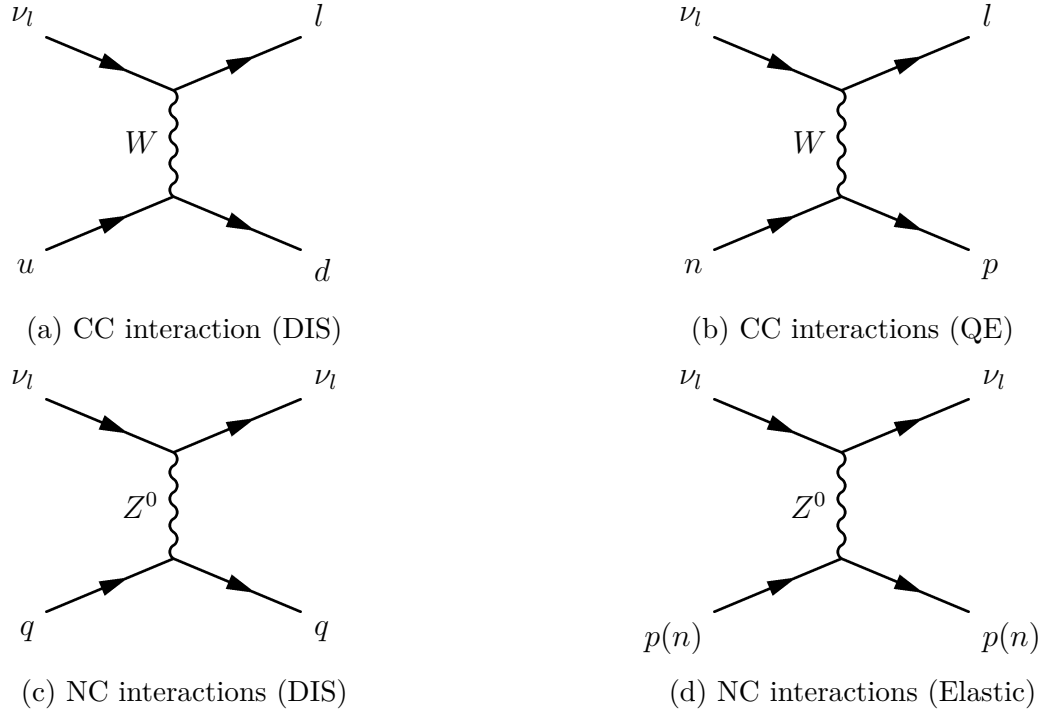


Figure 3.4: Feynman diagrams of neutrino-nucleon interactions. “l” can be e , μ , τ , and ν_l stands for the corresponding ν_e , ν_μ or ν_τ . “q” is a quark.

The CC DIS interaction is:

$$\nu_\tau + d \rightarrow \tau^- + u. \quad (3.4)$$

The heavy mass of the tau lepton (1.78 GeV) imposes a 3.5 GeV neutrino energy threshold to make the CC reaction occur. This is called kinematic suppression. The secondary τ^\pm particle has a short lifetime and quickly decays. The main decay channels and their branching ratios [52] are:

$$\begin{aligned}
 \tau &\rightarrow e^- + \bar{\nu}_e + \nu_\tau, & 17.82\% \\
 \tau &\rightarrow \mu^- + \bar{\nu}_\mu + \nu_\tau, & 17.39\% \\
 \tau &\rightarrow \pi^- + \nu_\tau, & 10.81\% \\
 \tau &\rightarrow \pi^- + \pi^0 + \nu_\tau, & 25.49\% \\
 \tau &\rightarrow \pi^- + 2\pi^0 + \nu_\tau (ex.K^0), & 9.26\% \\
 \tau &\rightarrow \pi^- + \pi^- + \pi^+ + \nu_\tau (ex.K^0, \omega). & 8.99\%
 \end{aligned} \quad (3.5)$$

The first two decays shown in Eq. 3.5 are leptonic. The first one’s output

lepton is an electron and the second one a muon, both have a similar branching ratio around 17%. The rest of tau decay modes are all hadronic, and in Eq. 3.5 we list the four dominant hadronic decay channels. The “ex. K^0 ” means the decay is a 3-prong decay without K^0 , similarly the “ex. K^0, ω ” means the decay has no K^0 or ω .

As mentioned in Section 2.2, the decay length can be calculated by

$$\begin{aligned} L &= \gamma\beta c\tau = \frac{p}{m_0 c}(c\tau) \\ &= \frac{\sqrt{E^2 - m_0^2}}{m_0 c}(c\tau). \end{aligned} \tag{3.6}$$

The mean lifetime of a τ is $(290.3 \pm 0.5) \times 10^{-15}$ s [35], so $c\tau_\tau = 87.03 \mu\text{s}$. This is very short. For example, the decay length of a 100 GeV τ is only 5 mm. A τ with energy as high as one PeV has a decay length of 50 m. So for atmospheric tau neutrinos below 100 GeV, IceCube is not able to clearly distinguish them from the other flavors.

3.2.3 Detector Signatures

The signatures of the light deposited by particles traveling in IceCube can be grouped into two categories: cascade-like and track-like. Cascade-like events have a hadronic shower resulting in a relatively spherical distribution of hit DOMs. Track-like neutrino events have both a cascade and a visible track left by a muon. So track-like events include sufficiently energetic ν_μ CC events, and some ν_τ CC events (via the $\tau \rightarrow \mu$ channel in Eq. 3.5). Downward-going atmospheric μ are mostly track-like. But muons that sneak in through the empty pathways of the detector without triggering too many DOMs might also be misidentified as cascade-like.

The neutrino interactions that produce cascade-like events are: all NC events, ν_e CC events, most of the ν_τ CC events, and low energy ν_μ CC events whose muon track is too short to be separated from the hadronic cascade.

Most of the ν_τ signal should end up in the cascade channel (82.61% of the ν_τ CC and ν_τ NC), only a small part (17.39% of ν_τ CC) is in the track channel.

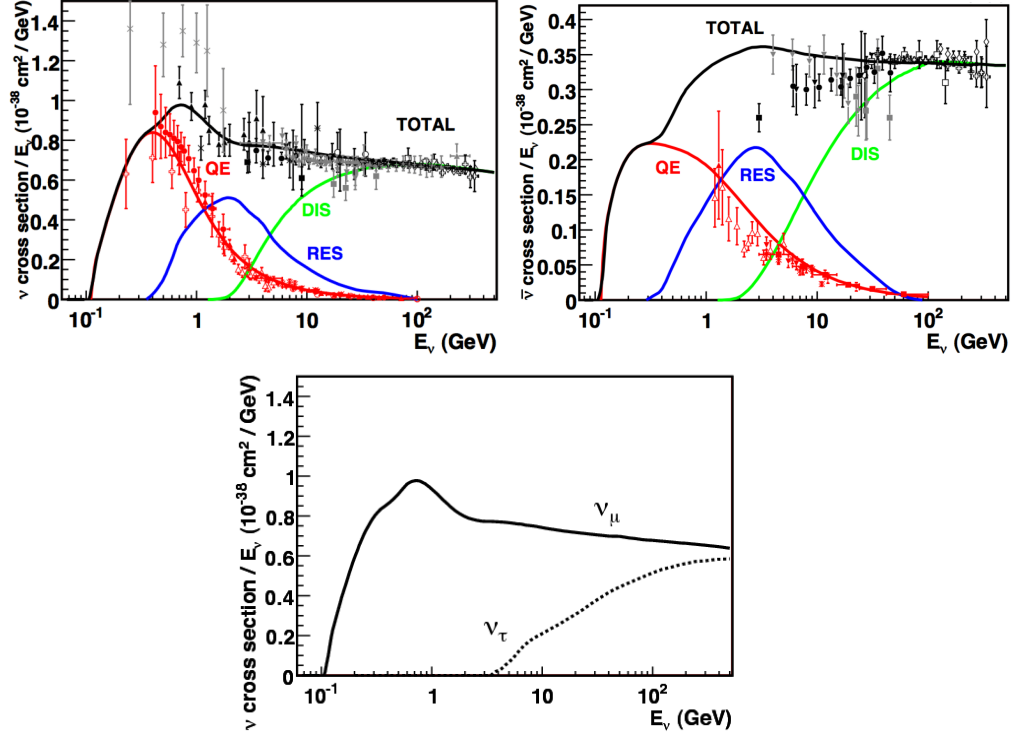


Figure 3.5: Cross section divided by energy as a function of energy for QE, RES and DIS scattering and their total cross section. Upper left: ν_μ neutrinos. Upper right: $\bar{\nu}_\mu$ neutrinos. Bottom: Comparison of ν_μ and ν_τ cross sections divided by energy vs. energy. We can see the ν_τ scattering only starts at 3.5 GeV [51, 53].

3.2.4 Cherenkov Radiation

Cherenkov radiation is the electromagnetic radiation produced from a charged particle with a traveling speed faster than light's phase velocity in the medium. It is analogous to the sonic boom created by a plane traveling faster than the speed of sound.

In Fig. 3.6, the red arrow represents the traveling direction of the particle with a speed βc . The blue circles represent the photons propagating in all directions with a speed c/n , where n is the refractive index of the medium and t is the time since their emission. So when $\beta c > c/n$, the direction of the wavefront of the photons (shown in two blue lines) form the Cherenkov cone. The angle between the wavefront direction and the particle's direction is called Cherenkov angle, θ_C , where $\cos(\theta_C) = 1/\beta n$ and equals roughly 41° for charged particles traveling in ice.

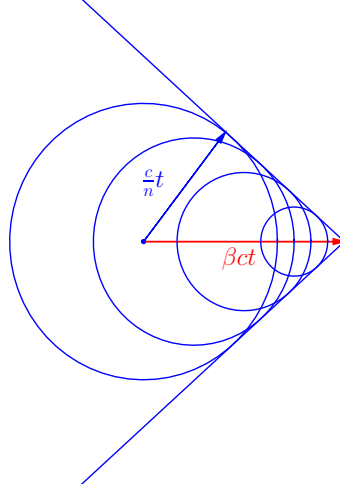


Figure 3.6: Geometry of the Cherenkov cone (without scattering).

3.3 Ice Properties

Since the light emitted will travel in the ice before arriving at the DOMs, we need to include the properties of the ice in our simulations and reconstructions. This section mainly talks about the bulk ice properties, for description of the hole ice, see Section 7.4.2.2.

The glacier ice at the South Pole is formed from hundreds of thousands of years of snow accumulation [54]. When snow falls, it adds weight on the lower layers of snow, turning them into firn, which is at the intermediate stage between snow and glacier ice. Firn is not dense enough for air to escape, it has various densities from $0.4 - 0.83 \text{ g/cm}^3$. When more snow falls and creates larger weights on the firn, its density will get larger and eventually when its density reaches around 0.83 g/cm^3 it starts to turn into ice. The air trapped in the firn then turns into air bubbles.

At larger depths from the surface, the hydro-static pressure gets larger thus the air bubbles get compressed into smaller sizes. But below 1200 m, the air bubbles begin to disappear [55]. The reason is at that depth, the pressure is huge enough to make the crystal structure of the ice to transform from hexagonal to cubic, which allows the air molecules to move inside and form the air clathrate hydrate [56, 57]. The transformation from the air bubbles to the solid clathrate hydrate state is very

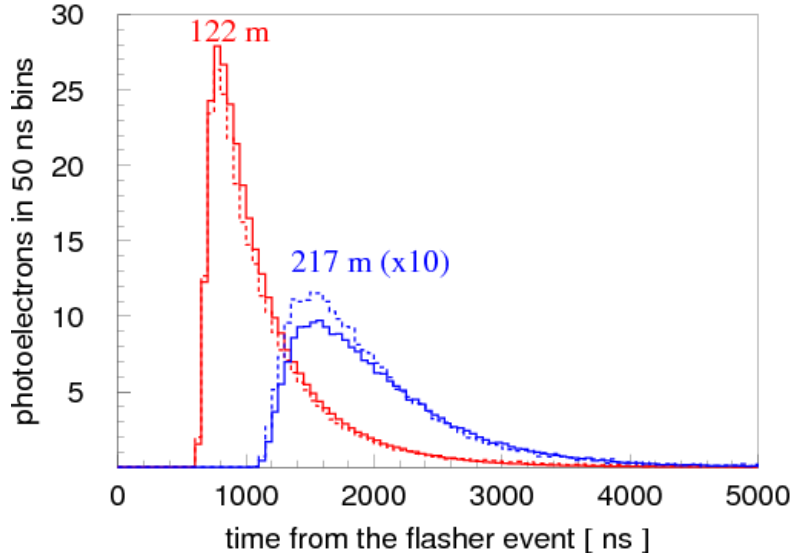


Figure 3.7: Light emitted from an emitter (shown in red) and received by a receiver (shown in blue) [62].

slow; they can coexist over the depth range of a few hundred meters [58].

At depths larger than 1500 m, the air bubbles disappear completely into air hydrates [59]. IceCube detector is built in the depth range of 1450 – 2450 m, so we don't need to worry about the air bubbles' effect on light scattering. One important property of the air hydrate is that its refractive index is almost identical to that of the normal ice [60]. So, the existence of air hydrates leaves almost no effect on the light propagation in the ice. Therefore, the scattering and absorption properties of the ice below 1500 m are dominated by the dust concentration in the ice.

The dust particles can be approximated as spherical particles. The Mie solution (or Mie scattering) describes the scattering of electromagnetic waves off homogeneous isotropic particles. It is the complete analytic solution to the Maxwell equations, computed by and named after Gustav Mie [61]. As mentioned before, each DOM has an LED flasher board used for calibration. Each flasher board has 12 light emitting diodes (LEDs) that emit light which can be received by other DOMs as far as 0.5 km away. The LEDs point towards six azimuth angles and two zenith angles. Figure 3.7 shows the light curves (solid line) received by nearby DOMs for one LED. There is one such light curve for each pair of emitter and receiver.

A flasher data set is the collection of these flasher light curves from multiple LEDs at various depths to cover the whole detector. In the ice model used for this analysis, the flasher data set was collected in 2008 when IceCube was in a 40-string configuration, there were at least 250 flashes from each DOM on string 63 (*i.e.*, 15,000 flashes in total), and the receiver DOMs were all the DOMs on the 40 strings.

One of the earliest ice models is the AHA model [59] based on AMANDA measurements. Spice (South Pole Ice) Mie [62] is the second generation of ice model, where ice is described by a table of depth-dependent parameters $b_e(400\text{ nm})$ and $a(400\text{ nm})$ related to scattering and absorption at a wavelength of 400 nm, by a depth-dependent relative temperature parameter, and other six global parameters. $a(400\text{ nm})$ is the absorption coefficient, and $b_e(400\text{ nm})$ is the effective scattering coefficient. The ice model used for this analysis is called Spice (South Pole Ice) Lea [63] based on Spice Mie. The difference is that Spice Lea takes into account the anisotropy of the ice.

A global fit is done to find the best $a(400\text{ nm})$ and $b_e(400\text{ nm})$ so that the simulation best matches the recorded flasher data.

Figure 3.8 shows the effective absorption and scattering coefficients as a function of depth comparing the AHA model and the Spice Mie model. The peak at depth around 2000 m is the location of the dust layer, which greatly affects the absorption and scattering properties of the ice. Figure 3.9 shows the comparison of the Spice Mie and Spice Lea models.

The uncertainties of the bulk ice scattering and absorption parameters are included as systematics in this analysis, and their effect on the final sample is shown in Chapter 7.

The installation of the DOMs and strings in the ice was done by drilling holes with hot water, which then cooled down and refroze. This refrozen ice column's ice properties are different from the bulk ice around it, mainly because of the bubbles formed during the refreezing process. In addition, this ice is located near the DOMs, so the light observed by each DOM is affected. These columns of ice are called "hole ice." Section 7.4.2.2 covers the systematics to describe its effect on the optical sensitivity of DOMs.

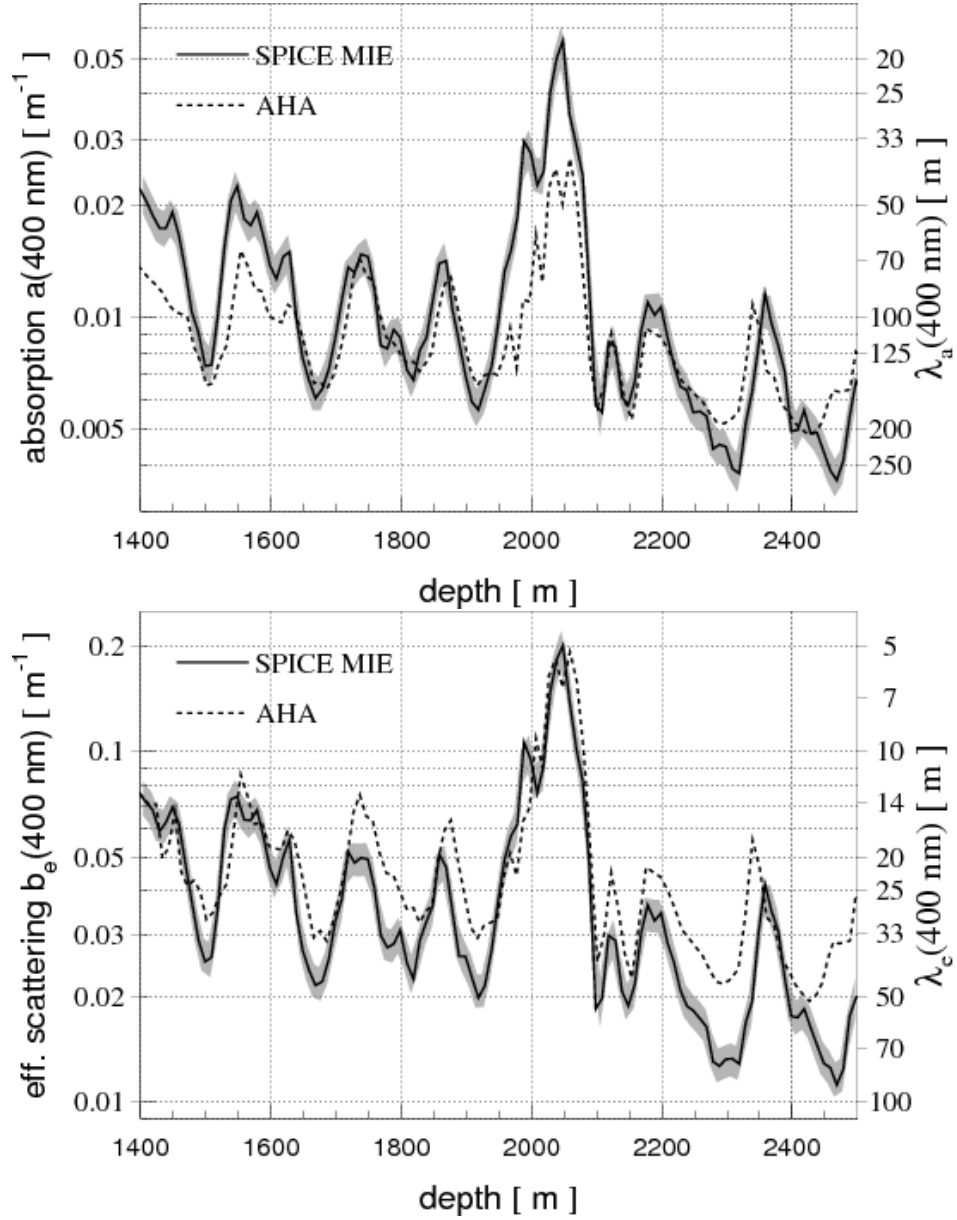


Figure 3.8: The depth dependence of the effective absorption coefficient a (400 nm) (up) and scattering coefficient b_e (400 nm) (bottom). There are two models shown here. The solid black line is the Spice Mie model, and the grey band indicates its uncertainties. The dashed line is the AHA model used previously in AMANDA based on Ref. [59], extrapolated to IceCube depths. Its uncertainties at the AMANDA depths of 1730 ± 225 m are roughly 5% in b_e and roughly 14% in a . The right side of the plots shows the corresponding scattering and absorption lengths in meters [62].

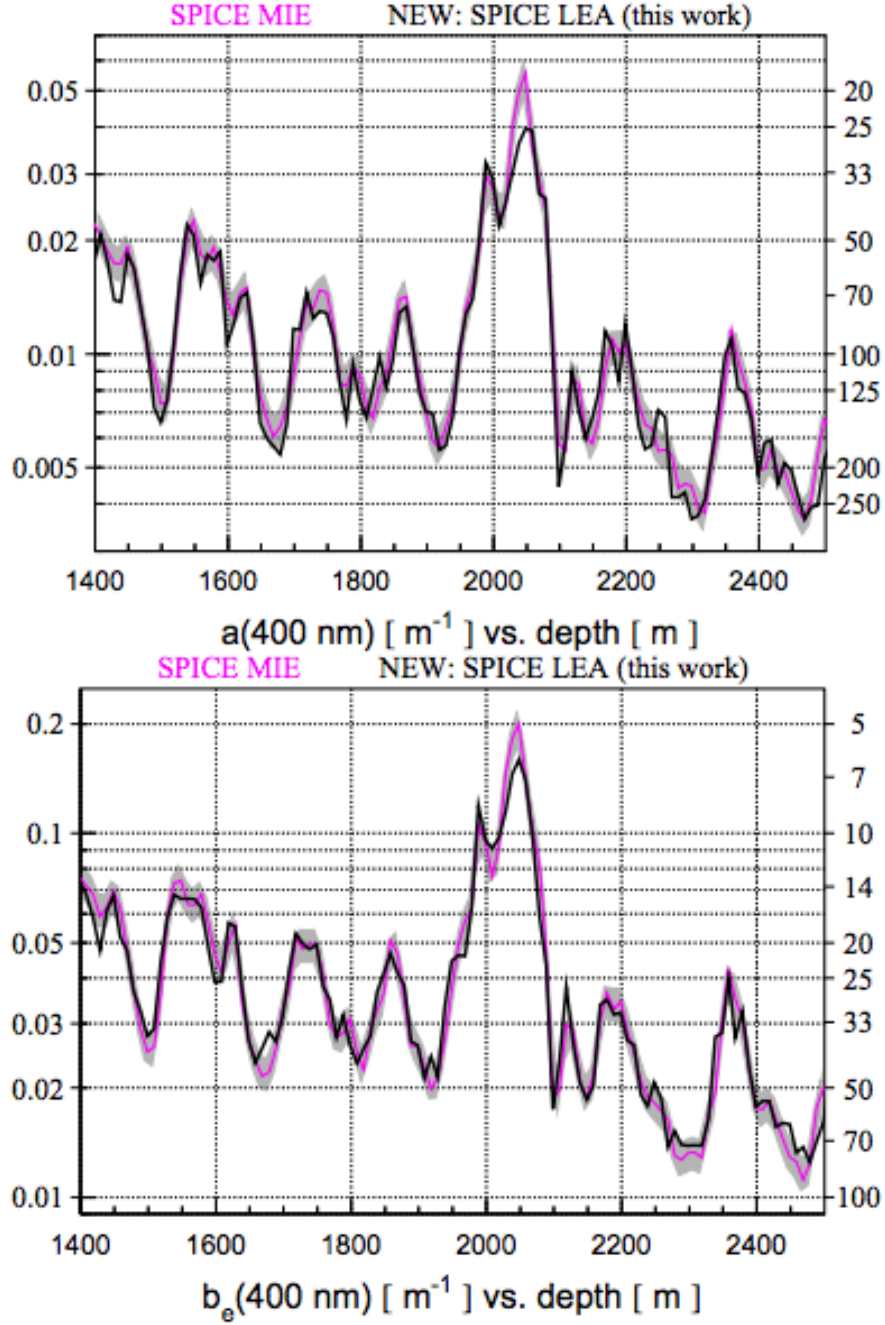


Figure 3.9: The depth dependence of the effective absorption coefficient a (400 nm) (up) and scattering coefficient b_e (400 nm) (bottom) comparing the Spice Mie and the Spice Lea model [63]. The grey band is the uncertainties on the Spice Mie model reported in [62].

Chapter 4 |

Monte Carlo Simulation and Reconstruction

This chapter discusses the Monte Carlo simulation in IceCube, focusing on the simulation of neutrino events and the reconstruction used in this analysis.

4.1 Simulation

The simulation chain has the following six components: event generation, propagation of secondaries, photon propagation, noise simulation, DOM simulation and triggering.

4.1.1 Event Generation

The first step of simulation is to create the primary particle, its interaction, and the created secondary particles.

For this analysis studying neutrinos in a relatively lower energy range, we use the event generation module “genie-icetray.” It first generates neutrinos inside the generation cylinder shown in Fig. 4.1 and propagated towards IceCube. The generator volume is taken into account in the weight for this event. The neutrinos are simulated with some chosen spectral indexes. The energy range is 1 – 1000 GeV for ν_e and ν_μ , and 4 – 1000 GeV for ν_τ . 70% of the simulation are neutrinos and 30% are anti-neutrinos. Similarly, these factors are taken into account in the weighting. One limitation of genie-icetray is that it can only propagate particles through water and cannot add Earth matter effects. That’s why they are added

later in the data analysis.

In the next step of *genie-icetray*, the neutrino interactions are done with GENIE 2.8.6 [64, 65], which provides comprehensive neutrino interaction modelling from 100 MeV to a few hundred GeV. It includes the RFG nuclear model (Bodek and Ritchie version [66]), cross section models and hadronization AGKY model [67], which uses the KNO [68] model in the low invariant mass region, and the PYTHIA/-JETSET [69] model in the high invariant mass region. The hadronization models provide the full final state particles.

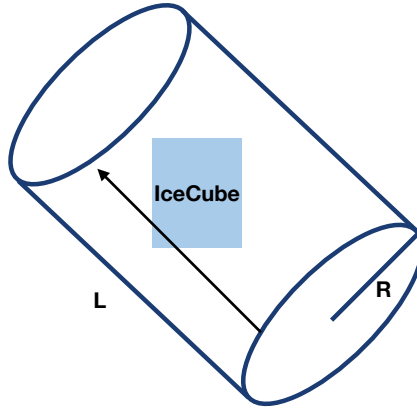


Figure 4.1: Generator volume along a given neutrino direction. The generated primary neutrino starts from the disk. Its radius, R , is called the injection radius. The neutrino is then propagated towards the detector. Each neutrino is simulated to interact within the cylinder whose height is called the detection length L . (The interaction probability is later added in the event weight as a correction.) The radius and length are optimized to different values to accommodate different flavors in different energy regions. For example, in the MC used for this analysis, $R=250$ m and $L=500$ m for ν_e flavor events.

For neutrinos at higher energies (usually above 200 GeV), the event generation uses the “neutrino-generator” module, which implements the All Neutrino Interaction Simulation (ANIS) [70]. Similar to *genie-icetray*, it first generates the primary neutrinos, injects them in the Earth, and propagates them through the Earth (which means the Earth matter effects are taken into account here). In its second step, it does not use GENIE to do the detailed event-by-event interaction simulation, but instead uses simple parametrizations and approximations. For example, it only considers deep inelastic scattering cross sections since the

contributions from CCQE and RES are very small (see Fig. 3.5). Also, it only simulates one hadronic blob, while the genie-icetray uses GENIE to produce all the final state particles in the hadronic shower.

The atmospheric muons in IceCube are simulated by the CORSIKA [71] package and MuonGun [72]. CORSIKA (COsmic Ray SIMulations for KAscade) simulates extensive air shower events initiated by cosmic particles hitting the Earth’s atmosphere. It begins with primary cosmic ray particles, propagates them through the atmosphere towards the Earth, and then generates their interactions with the air nuclei, creating secondary particles and their possible subsequent decay products. Because CORSIKA simulates primary cosmic rays all the way from their source location in the atmosphere to the final location detector, it has the best accuracy for generating the atmospheric muon events, however, it is also computationally expensive. For example, when an event selection can eventually reduce the number of atmospheric muons from the original 10^6 times the number of neutrinos to rough parity, it is hard to simulate enough atmospheric muon statistics for that sample. MuonGun is a faster simulation method that simulates muons in the ice using a parametrization of the muon fluxes. Muons are then weighted according to the cosmic ray interaction in the air. Due to the reasons explained above, this analysis instead uses a data-based background shape estimation for the atmospheric muons. It achieves reasonable agreement with both CORSIKA and MuonGun.

4.1.2 Propagation of Secondaries

The second step is the propagation of secondaries. For neutrinos, secondaries include the electrons, muons and τ produced in their CC events, and the hadronic showers. The electron produces an electromagnetic shower, the tau may also decay into a muon. Muons created in ν_μ CC interactions are propagated through the ice using PROPOSAL [73]. Tau leptons and their decayed muons, hadronic showers, and electromagnetic (EM) showers below 100 MeV are propagated with GEANT4 [74]. For events with EM showers above 100 MeV, shower-to-shower variations are small enough to use parametrizations [75] which are based on GEANT4 simulations.

For atmospheric muons, at low energies, CLsim [76] is used to propagate all

secondary particles in the detector. For muons at high energies, either the Muon Monte Carlo program (MMC) [77] or PROPOSAL [73] is used for their propagation from the Earth’s surface to the detector.

4.1.3 Photon Propagation

The third step is the propagation of photons produced by Cherenkov radiation in the ice. CLSim [76] is used for generating the light yield. It uses OpenCL to run these processes in parallel. It first creates photons from Cherenkov radiation, propagates them in the ice, and stores those that impact a DOM. In this process, the South Pole Ice model (SPICE [63]) is applied. Then the photons are passed on to the next step.

4.1.4 Noise Simulation

Before simulating the DOM response induced by the photons from the previous step, photons from dark noise need to be included. Dark noise comes mostly from thermal noise, electronic noise, and decaying radioisotopes in the PMT/DOM glass. The software is called Vuvuzela [78]. The average total noise rate is 560 Hz for standard DOMs and 780 Hz for HQE DOMs [46].

4.1.5 DOM Simulation

The fifth step is the DOM simulation using an IceCube module named “DOM-Launcher.” It simulates PMT response and the digitization process that essentially transforms the photons into photoelectrons and eventually digitized ATWD and FADC signals, simulating the DOM data acquisition process.

4.1.6 Triggering

Finally, the trigger algorithms are applied across the full detector to produce the final simulated data set. Trigger algorithms are simulated based on triggering described in Section 3.1.4. As with real data, after triggering, offline filtering and processing are applied. At this point, the generated data is called level 2 simulation. The details of these first two levels and the higher levels are discussed in Chapter 5.

4.2 Reconstruction

After triggering, the next step is to do offline processing. The IceCube module to do this step is called “WaveDeform” [79], it takes the ATWD and FADC waveforms and deconvolves them into photon information. They are called “RecoPulse” (“reco pulse”) meaning “reconstructed pulses”. Each reco pulse contains three parameters: the pulse time, pulse charge and pulse width. A DOM may observe one or several pulses. The collection of these pulses in all the hit DOMs in an event is called reco pulse series (or simply referred to as reco pulses). These reco pulses are usually cleaned before being used in the event reconstruction. For example, several pulse cleaning algorithms are discussed below.

Event reconstruction algorithm tries different neutrino event hypotheses and finds the one whose expected pulse charge distribution gives the best agreement with the observed pulse charge distribution in the detector. The Poisson likelihood obtained from comparing the expected and the observed charge is the fundamental quantity used to estimate how good the agreement is.

There are several different types of reconstructions: track directional reconstructions, track energy reconstructions, cascade energy reconstructions, and cascade directional/energy reconstructions [80]. The track directional reconstructions fit with a track hypothesis and usually are used as a fast first step estimation. For example the “LineFit” algorithm assumes an infinitely long track and ignores the Cherenkov cone geometry [81].

For oscillation analyses, we need to have both the cascade and the track hypotheses in the fit. For example, SANTA (The Single string ANTares-inspired Analysis) is used for IceCube’s 2015 ν_μ disappearance result [82]. SANTA first uses the geometry of the direct Cherenkov light to fit pulses on each string to a hyperbola and extract only pulses that are direct hits (SANTA hit cleaning). Then the hyperbolas formed by the cleaned pulses are fitted to a track and cascade cone. For this analysis, SANTA hit cleaning is only used as a trigger in level 3, and the algorithm used for event reconstruction is the Pegleg/MultiNest reconstruction. Pegleg is the event hypothesis construction based on HybridReco, which is the reconstruction algorithm used in the 2017 IceCube ν_μ disappearance result [15]. MultiNest [83,84] is the optimization algorithm.

4.2.1 Photon Tables

Photon tables are produced with simulation of photon propagation in the ice for each DOM. One photon table corresponds to one light source in the detector. Putting together the photon tables from a wide range of possible sources gives a complete picture. The tables are binned in six dimensions: z (source), zenith (source), (x, y, z) of the observer relative to the source, and t (time).

The reconstruction is done by maximizing the Poisson likelihood between the expected and the observed charge. The observed charge is the light deposited in the DOMs. The expected charge is obtained using splined photon tables which give the amount of charge in each DOM under a given event hypothesis. (“Splined” refers to using splines to get a smooth parametrization of the tables [85, 86].)

4.2.2 HybridReco

HybridReco is the event reconstruction algorithm developed for low energy analyses, the “hybrid” in its name means a hybrid of cascade and track hypothesis. A neutrino interaction contains the incoming neutrino, the hadronic and/or EM cascade, and a muon track if it exists.

Since deep-inelastic scattering is the dominant interaction type for DeepCore energy region, HybridReco assumes that all energy not transferred to the outgoing muon is converted to a single hadronic cascade. Eight parameters are considered to describe an event: $(x, y, z, t, \text{zenith}, \text{azimuth}, E_{\text{cascade}}, L_{\text{track}})$. See Fig. 4.2 for a sketch of the event signature.

The first four parameters (x, y, z, t) are the position and time of the neutrino interaction vertex, $(\text{zenith}, \text{azimuth})$ is the direction of the hypothesized output muon, and track length L_{track} is the distance the muon travels in the ice before it stops or leaves the detector. E_{cascade} is the energy of the hadronic cascade, whose starting position is the same as the neutrino vertex and has a collinear direction as the muon track. Thus from momentum conservation, $(\text{zenith}, \text{azimuth})$ is also the primary neutrino’s direction.

We first do a fit with all eight parameters turned on and call it a 8-d fit or the “cascade+track fit”. In our energy range, the outgoing muon undergoes ionization with a constant $dE/dX = 1 \text{ GeV}/4.5 \text{ m}$, where X is the distance it travels, thus allowing the track length to be translated into the energy emitted by

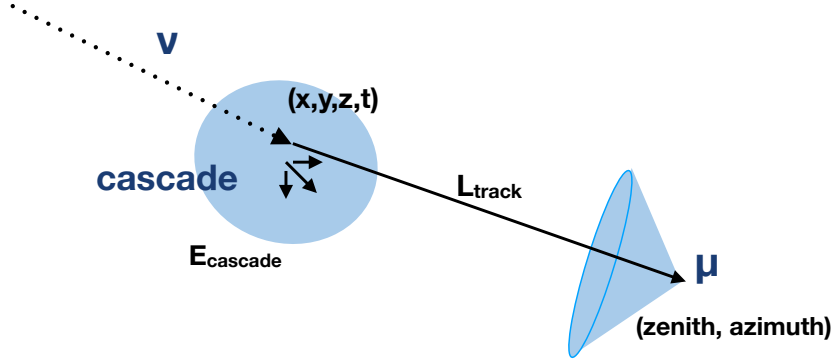


Figure 4.2: The 8-parameter event hypothesis in HybridReco. Blue regions indicate where Cherenkov light has been created. For the muon track, only the Cherenkov cone at the wave front is depicted.

the muon. The total neutrino energy is then roughly $E_\nu \simeq E_{\text{cascade}} + L_{\text{track}}/4.5$. The reconstructed energy E_ν and $\cos \theta_{\text{zen}}$ are two dimensions for the 3-dimensional binning of the events.

Then, the track length is set to zero to perform a 7-d fit with only the cascade hypothesis (“cascade-only fit”). If an event gives roughly equal values of likelihoods from the two fits, then it’s considered a cascade-like event. If the “cascade+track fit” achieves a much better likelihood, the event is considered a track-like event. This difference between the two log likelihoods (ΔLLH) is used as the third dimension in the binning.

4.2.3 Pegleg

Pegleg is a similar reconstruction method based on HybridReco, and has a similar reconstruction resolution to that of HybridReco, but runs faster. The event hypothesis and the two fits are still the same. It is faster mainly because it has a faster implementation of likelihood service so that when doing the 8-d fit, it’s only internally doing a look-up in 6-d (not including the cascade energy and the track length) likelihood space, while the other two parameters are done separately. This cuts down the photon table look-up time.

4.2.4 Likelihood Minimizer: MultiNest

MultiNest is short for the Multimodal Nested sampling algorithm developed [83, 84]. It is one type of Bayesian inference, which is a method based on Bayes' theorem to get the posterior probability given the prior available information (or "evidence"). For this analysis, MultiNest is used to calculate the evidence in the Pegleg reconstruction. Bayes' theorem [87] is:

$$P(H | E) = \frac{P(E | H) \cdot P(H)}{P(E)}, \quad (4.1)$$

where $P(H | E)$ is the posterior probability: the probability of the hypothesis H being true after seeing the current evidence E . $P(E | H)$ is the likelihood: the probability of seeing evidence E given the hypothesis H . $P(H)$ is the prior probability: the probability of the existence of hypothesis H before seeing E . $P(E) = Z$ is the Bayesian evidence or the marginalized likelihood: $Z = \int_H P(E | H)P(H)$.

If we want to determine a set of parameters of a hypothesis H : θ , then the above equation [83] becomes:

$$P(\theta | E, H) = \frac{P(E | \theta, H) \cdot P(\theta | H)}{P(E | H)}. \quad (4.2)$$

Here, $Z = \int_{\theta} P(E | \theta, H)P(\theta | H) d\theta$. When we need to determine which hypothesis gives a better posterior probability, such as in the case of minimization, the fitter needs to obtain the higher probability from comparing two sets of parameters. Using Eq. 4.1:

$$\frac{P(H_1 | E)}{P(H_2 | E)} = \frac{P(E | H_1) \cdot P(H_1)}{P(E | H_2) \cdot P(H_2)} = \frac{Z_1 \cdot P(H_1)}{Z_2 \cdot P(H_2)}. \quad (4.3)$$

Thus the calculation of the evidence Z becomes important and if the likelihood space is multi-modal it could be time-consuming. Nested sampling [88] provides an efficient way to calculate Z . MultiNest is an implementation of the nested sampling for multimodal posterior spaces.

MultiNest throws "active points" into the parameter space, then partitions them into clusters and constructs ellipsoidal bounds around the clusters. These ellipsoids can be overlapping. In each iteration, the probabilities are evaluated and

the point with the lowest likelihood inside an ellipsoid is dropped as an “inactive point,” making the ellipsoid’s volume smaller. Then a new “active point” is generated inside this smaller ellipsoid satisfying the requirement that its likelihood is larger than the one dropped. As iterations proceed, the algorithm moves inside these “nested” likelihood shells until the stopping criterion (a tolerance on the final evidence) is met. Figure 4.3 (a) shows the multiple overlapping “ellipsoids” constructed by MultiNest. Figures 4.3(b) and (c) show how well it can recover a multimodal likelihood space in a toy model.

One disadvantage of MultiNest is that it uses random active points, and our likelihood space could be spiky with local minima, the randomness of the thrown active points gives rise to instability in the best fit neutrino zenith angle, energy, and ΔLLH , the 3 parameters for the final binning of the events. This means different reconstructions can create migration of events between bins if the bin sizes are too small. By choosing the bin sizes larger than the standard deviations for each parameter’s distribution, the migration is greatly reduced. Our final binning is eight energy bins in $[5.6, 56]$ GeV, eight $\cos \theta_{\text{zen}}$ bins in $[-1, 1]$, and two ΔLLH bins: $[-3, 2, \infty]$.

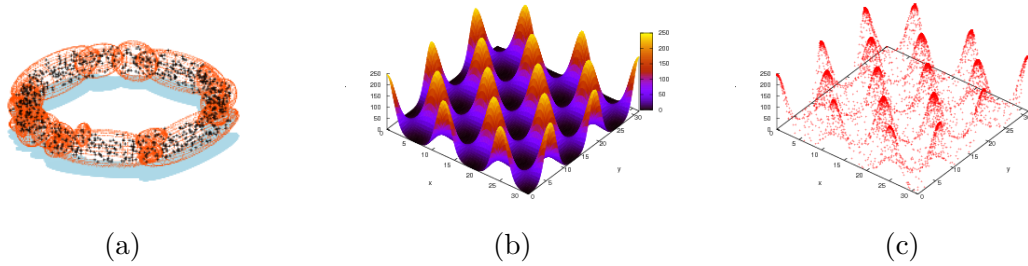


Figure 4.3: (a): Black points are the active points sampled inside of the constructed ellipsoidal bounds (orange). (b) and (c): MultiNest can recover the highly multimodal two-dimensional likelihood space very well. (b) is the input likelihood function, (c) shows what MultiNest gets. Each dot is one lowest likelihood at one MultiNest iteration [84].

4.3 Reconstruction Resolution

The final events are binned into 3-dimensional histograms, where the three bins are the reconstructed energy, reconstructed $\cos \theta_{\text{zen}}$ and ΔLLH .

As mentioned in Chapter 1 and Chapter 2, the leading term for tau neutrino appearance probability is

$$P(\nu_\mu \rightarrow \nu_\tau, \text{vacuum}) \approx \sin^2 2\theta_{23} \sin^2 \left(1.27 \Delta m_{\text{atm}}^2 \frac{L [\text{eV}^2][\text{km}]}{E [\text{GeV}]} \right), \quad (4.4)$$

where L is a function of $\cos(\theta_{\text{zen}})$. Thus, the tau neutrino appearance measurement depends greatly on how well we can reconstruct the neutrino zenith angle θ_{zen} and the neutrino energy E .

Figure 4.4 shows the comparison of reconstructed energy and $\cos(\theta_{\text{zen}})$ vs. their true values in four (flavor, interaction) channels: ν_e CC, ν_μ CC, ν_τ CC and ν_{all} NC. Figure 4.5 shows the fractional energy vs. true energy and the $\theta_{\text{reco}} - \theta_{\text{true}}$ vs. true energy in the four channels.

Note that in all four channels, at energies below 10 GeV, the reconstructed energy is consistently higher than the true energy. This is because the trigger threshold creates a selection of events - only events that have a charge higher than trigger level end up in the sample. Thus, among low energy neutrino events where the true neutrino energy is not high enough to produce light to pass the trigger, those having an energy reconstructed higher than the true energy can get triggered but those with the energy reconstructed lower than the true energy do not get triggered and do not end up in the event sample. This means essentially a selection of events with overestimated energy.

For ν_τ CC and ν_{all} NC events, the energy reconstructions are biased at energies above 10 GeV, where the reconstructed energy is consistently lower than the true neutrino energy.

The reason is that the ν_τ CC interaction produces a ν_τ which carries away a fraction of the primary ν_τ energy. (See the detailed interactions in Section 3.2.1.). Similarly, for all neutral current events where there is an outgoing ν , the ν also carries away a fraction of the incoming ν energy.

For ν_e CC events, we see a consistent overestimation of energy, the reason is that the ν_e CC interaction have an electromagnetic shower produced, but the reconstruction algorithm assumes one hadronic cascade - this causes the bias seen in the figure.

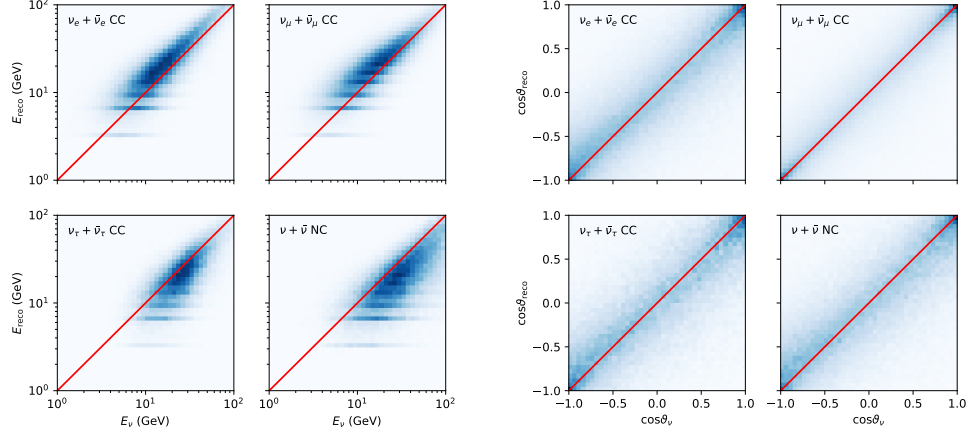


Figure 4.4: Left: Reconstructed energy vs. true energy in four flavor and interaction channels: ν_e CC, ν_μ CC, ν_τ CC and ν_{all} NC. Right: Reconstructed $\cos \theta_{\text{zen}}$ vs. true $\cos \theta_{\text{zen}}$.

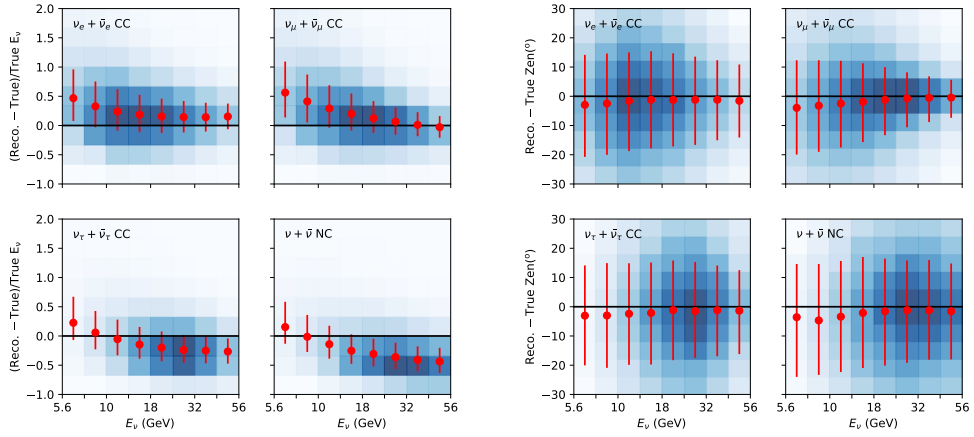


Figure 4.5: Left: Fractional difference between the reconstructed and true energy vs. true energy in four flavor and interaction channels: ν_e CC, ν_μ CC, ν_τ CC and ν_{all} NC. Right: Difference between the reconstructed and true zenith (in degrees) vs. true energy. Red dots are the median resolution in each energy bin, the bar's length the range where 50% of the events fall.

Chapter 5 |

Event selection

This chapter discusses the analysis event selection, developed by Matthew Dunkman [89]. It is used for the ν_μ disappearance analysis published as the 2017 IceCube ν_μ disappearance result [15].

The major variables being cuts at each selection level are shown in Table 5.1 under three categories: trigger, veto and quality cuts. Trigger cuts are used to select physics events out of noise events. Veto cuts are used to remove atmospheric muons, the major background for IceCube. Quality cuts are used in higher levels to improve the quality of the events; in this sample, the quality cuts are two containment cuts to select events contained in DeepCore.

Level 1 is already discussed in Section 3.1.4; for our analysis, we use the DeepCore SMT3 trigger; it requires at least 3 HLC hits within $2.5 \mu s$ in the DeepCore DOMs.

Before discussing the selection cuts, Section 5.1 first describes two definitions of DeepCore fiducial volumes used in this analysis.

Section 5.2 discusses level 2. Section 5.3 discusses the further triggering and vetoing in levels 3 and 4. Section 5.4 discusses the Boosted Decision Tree (BDT) cut in level 5. Section 5.5 is about the Corridor Cut used in level 6. Section 5.6 discusses the quality cuts. Section 5.7 talks about the background estimation technique.

The event rates for the six flavor-interaction channels at each level is shown in Fig. 5.1. It shows the number of neutrino events expected with three years of IceCube/DeepCore data, see the numbers in Table 5.2. Table 5.3 shows the rates in mHz combining the interaction types for each flavor. The level 6 here includes the final binning of the events, *i.e.*, the cuts placed on the reconstructed energy

and ΔLLH : $5.6 \text{ GeV} \leq E_{\text{reco}} \leq 56 \text{ GeV}$ $\Delta LLH \geq -3$.

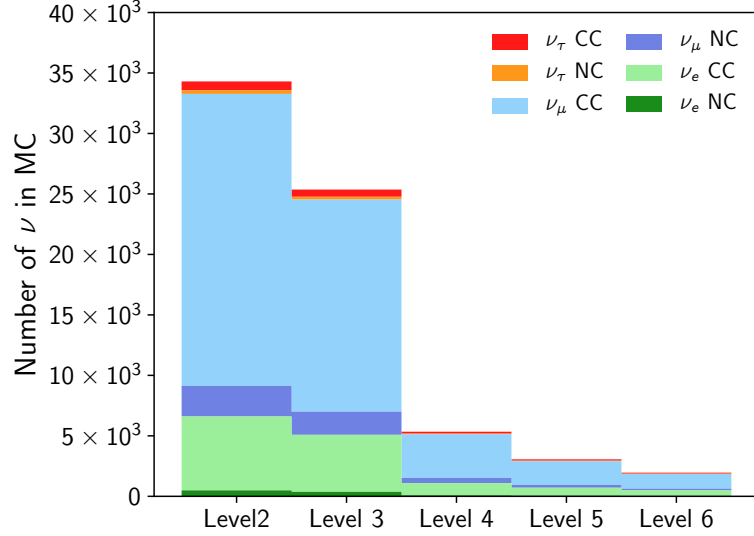


Figure 5.1: Number of events at each selection level expected in IceCube in three years' time. (Effective live time is 2.5 years.)

5.1 Definition of DeepCore Fiducial Volume

Two definitions of DeepCore fiducial volumes (regions) are used in this analysis. Fig. 5.2 shows the comparison of the top view of the two volumes. (The side view can be seen in Fig. 3.2.)

The Extended DeepCore (EDC) fiducial region contains the DOMs on 12 IceCube strings and eight DeepCore strings below 2100 m (see the overhead view in Fig. 5.2(a)). The EDC veto region is the region surrounding the EDC fiducial region, *i.e.*, the outer three layers of IceCube strings.

The DeepCore Classic (DCC) fiducial region contains the DOMs on seven IceCube strings and eight DeepCore strings below 2100 m (see the overhead view in Fig. 5.2(b)). The DCC veto region is the region surrounding the DCC fiducial region.

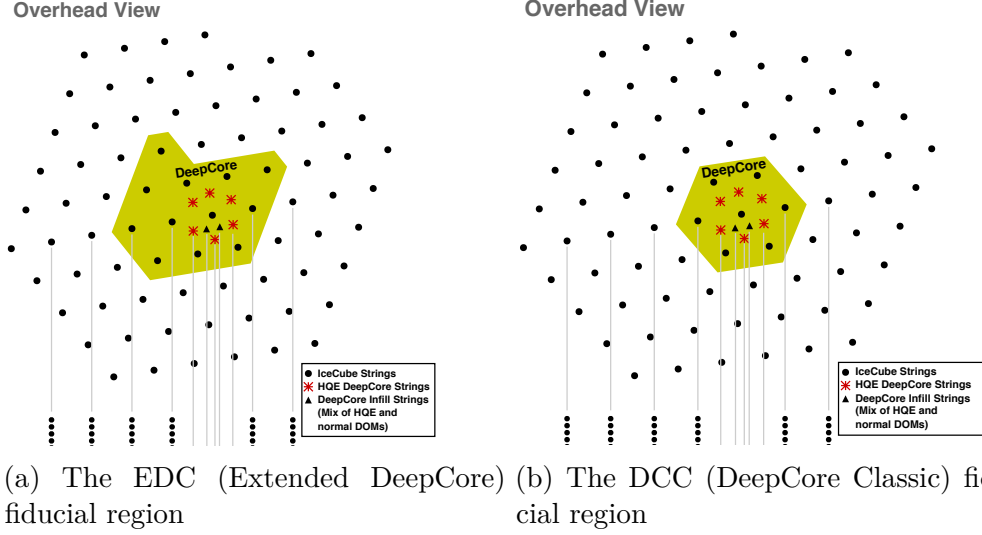


Figure 5.2: (a) The overhead view of the EDC fiducial region used in the Online DeepCore Filtering in level 2 and the cut on “EDC-VetoPE” in level 3; (b) The overhead view of DCC fiducial region used in the cut on “DCC_VetoPE” in level 4.

5.2 Level 2: Online DeepCore Filter

As seen from Table 5.1, Level 2 is the Online DeepCore Filter, it aims at removing most of the events caused by atmospheric muons, while at the same time keeping a good amount of signal neutrino events.

This section first discusses the definition of the “particle speed” parameter, then discusses the cut region placed on it. The online DeepCore filter removes events having more than one hit DOM whose associated “particle speed” is in the cut region.

5.2.1 Definition of “Particle Speed”

The filter removes events having one or more HLC hits in the EDC veto region that, relative to the time and position of the event’s center of gravity in the EDC fiducial region, are consistent with having been produced by a muon moving with nearly the speed of light. Figure 5.3 explains the filtering algorithm.

The center of mass of a rigid object is a concept used often in mechanics. It is a point around which the distribution of mass of the object is balanced. If we apply

Table 5.1: The trigger/veto/quality cuts at each selection level

Levels	Trigger	Veto	Quality cut
Level 1	Online Trigger (SMT3)		
Level 2		Online Filter	
Level 3		EDC_VetoPE Modified 2012 DC Veto	
Level 4	SANTA direct DOMs RT Fiducial Charge Event Size (σ_z, σ_t) Space-time Interval SRT-TW-cleaned DOMs	DCC_VetoPE Causal Track Veto	Preliminary Containment
Level 5		BDT Cut	
Level 6		Corridor Cut	Final Containment

Table 5.2: Number of expected events in three years at each selection level.

flavor+type	L2	L3	L4	L5	L6
ν_e CC	122254	61874	20321	13203	9201
ν_e NC	9831	4901	1597	1019	703
ν_μ CC	482778	230436	72422	39406	24310
ν_μ NC	50565	25424	8388	4586	2706
ν_τ CC	14668	7741	3091	2212	1646
ν_τ NC	5962	3038	1019	776	593

a force at the center of mass of a rigid object to change its velocity, the velocity change will have the same direction as the force. In a uniform gravity field, it is the same as the center of gravity (CoG).

The concept is borrowed here to find a point in space to represent an event. The center of gravity (CoG) of the event is calculated via a three-step process.

Table 5.3: Event rates in mHz at each selection level.

	L2	L3	L4	L5	L6
ν_e (CC+NC)	1.674	1.289	0.278	0.180	0.126
ν_μ (CC+NC)	6.760	4.930	1.024	0.558	0.342
ν_τ (CC+NC)	0.262	0.210	0.052	0.038	0.028
all ν	8.696	6.430	1.354	0.776	0.496

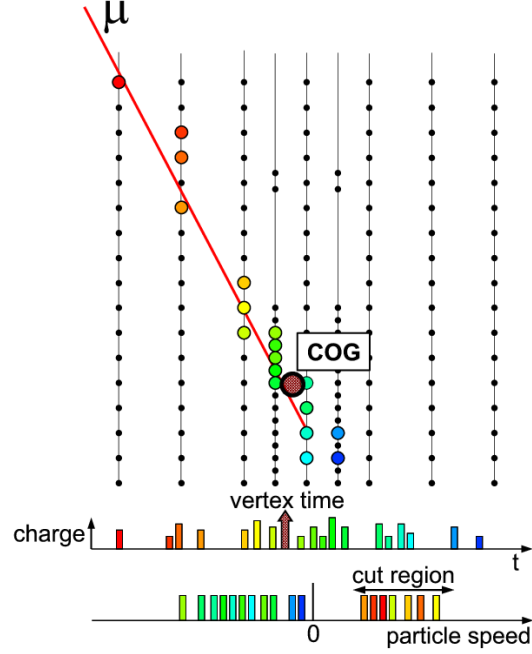


Figure 5.3: Online DeepCore Filter algorithm [47]. A simulated muon traveling downwards deposits photons in the DOMs. Each colored circle represents a hit DOM, with the earliest hits marked in red and the latest hits in blue. The largest circle is the CoG of the hits in the Extended DeepCore (EDC) fiducial region. The charges of these hits are also shown in the first histogram below, ordered by time. The second histogram is the “particle speeds” distribution. For example, the earlier hits in the upper left part of the detector have “particle speeds” consistent with speed of light travelling from the hit to the CoG, and therefore fall into the “cut region.” Events having at least one such hit in the cut region are removed.

First, get a position \vec{r} and time t by simply taking the average position and time of the hits inside the EDC fiducial region. Second, select a subset of hits whose hit times are within one standard deviation of the average time t , these subset hits’ average position is the CoG position \vec{r}_{CoG} . Last, get “corrected” hit times for each hit by subtracting the time it takes for unscattered light to travel from the CoG position \vec{r}_{CoG} to each DOM, take the average of these corrected hit times, and use it as the event CoG’s time t_{CoG} .

Once the position and time $(\vec{r}_{\text{CoG}}, t_{\text{CoG}})$ of the CoG are obtained, we define a “particle speed” (v) parameter for each hit DOM:

$$v = \frac{|\vec{r}_{\text{CoG}} - \vec{r}_{\text{DOM}}|}{t_{\text{CoG}} - t_{\text{DOM}}}, \quad (5.1)$$

where r_{DOM} and t_{DOM} are the position and time of a DOM, respectively. So, the “particle speed” is positive if a hit occurs before the CoG time and negative if it occurs after. See Fig. 5.4(a) for the speed probabilities for simulated atmospheric μ and ν_μ events. Events having one or more hits in the particle speed cut region $[0.25 \text{ m/ns}, 0.4 \text{ m/ns}]$ are removed.

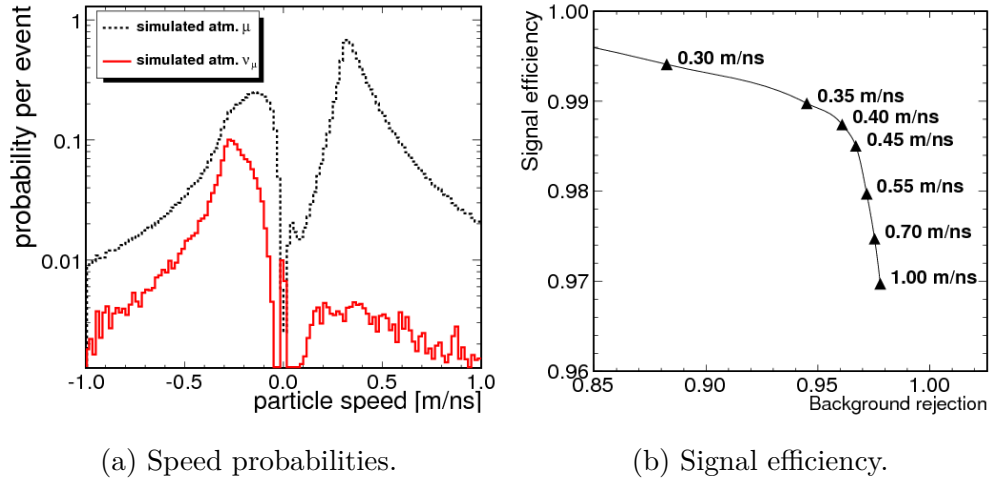


Figure 5.4: (a) Particle speed probabilities per event for simulated atmospheric muons and simulated muons from atmospheric ν_μ interactions inside DeepCore. (b) Signal efficiency vs. background rejection for events falling into the speed cut region between $+0.25 \text{ m/ns}$ and a variety of upper values, ranging from $+0.35 \text{ m/ns}$ to $+1.0 \text{ m/ns}$ [47].

5.2.2 Cut Region of “Particle Speed”

The “particle speed” for hits in the EDC veto region are mostly close to $c = 0.3 \text{ m/ns}$. In Fig. 5.4(a) we can see the peak location for the atmospheric muons is located at roughly 0.3 m/ns . Speeds smaller than 0.3 m/ns occur due to scattering in the ice. In principle, speeds larger than 0.3 m/ns are non-causal, but here r' is the average position of hits, while t' is the corrected average time, which represents the time of a starting muon (either from a neutrino interaction or being an incoming atmospheric muon). This time is slightly earlier than the hit times of the DOMs. So, in Eq. 5.1, the particle speed is slightly overestimated, which is why in Fig. 5.4(a) particle speeds can be larger than 0.3 m/ns .

The cut region is $[0.25 \text{ m/ns}, 0.4 \text{ m/ns}]$, which is chosen by studying the signal

efficiency vs. background rejection plot (Fig. 5.4 (b)). It removes 96% of the background muons and keeps 98.8% of the signal.

5.3 Triggering and Vetoing in Level 3 and 4

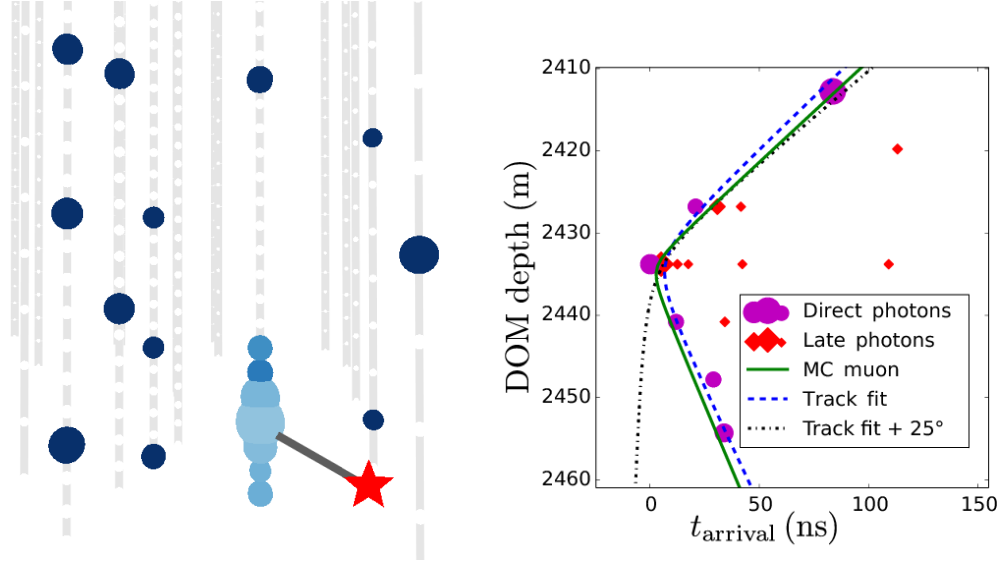


Figure 5.5: Left: A simulated ν_μ event in IceCube. The star is the interaction vertex, the line between the star and the string is the outgoing muon track. The blue circles represent hit DOMs, and their area represents how large the charge is in each DOM. Right: The signature left by the Cherenkov cone of the track on the string. The solid line is the signature hyperbola left by the true MC muon track. The purple circles are the photons located near the hyperbola left by a track fit; they are the direct photons arriving at the DOMs from the Cherenkov cone created by the track. Those that don't match the hyperbola are the late photons and will be removed [82].

5.3.1 Triggering in Level 4

This section covers triggering in level 4. The second table in Table 5.5 lists the cuts. Note that in levels 2 and 3, the EDC fiducial region contains 12 IceCube strings and eight DeepCore strings. Here in level 4, the fiducial volume used is the “DeepCore Classic” (DCC) volume.

There are six cuts in level 4 triggering.

First, “SANTA direct DOMs ≥ 3 .” SANTA (The Single string ANTares-inspired Analysis) is a track plus cascade reconstruction algorithm inspired by the ANTARES experiment [90]. It was implemented and used as the event reconstruction method in the 2015 IceCube muon neutrino oscillation result [82]. SANTA consists of three parts: a hit selection, a directional reconstruction, and a cascade/track discriminator. All three take advantage of the signature of the Cherenkov light left on the strings.

The Cherenkov cone produced by a (muon) track or a cascade intersects with a string and can leave a unique signature on the strings. For a track, the moving Cherenkov cone leaves a hyperbola-like signature. The shape of the hyperbola projected in the string is described by 4 quantities: the minimum distance between the cone’s axis and the string, the angle between the cone’s axis and the string, the time of the point of closest approach, and the z position (depth) of the point of closest approach. For a cascade, the Cherenkov cone is much fuzzier and the signature does not depend on the direction. It’s similar to a horizontal track, leaving roughly two arms of the same length.

Here, only the output of the first hit selection part of SANTA is used, which removes scattered hits and saves only DOM hits that are likely produced by direct Cherenkov light. Figure 5.5 explains this process. SANTA direct DOMs is the number of DOMs having such SANTA-cleaned hits. We require at least three SANTA-cleaned direct hit DOMs.

Second, the $RTFidQ$ is the charge deposited in the largest RT cluster in the DCC fiducial region. The RT cluster is the output of an RT-cleaning module, which removes hits that have no other hit within a time-window T and a distance radius R . Here $R = 150$ m, $T = [-250, 500]$ ns, and we require a RT cluster having at least seven PE.

Third, the CoG σ_z and CoG σ_t are two geometrical cuts on the charge-weighted CoG of the SRT-TW-cleaned pulses in DCC fiducial region. The SRT-TW-cleaning contains the SeededRT cleaning (SRT) and a time window (TW) cleaning. SeededRT-cleaning is different from the aforementioned RT-cleaning, although both conduct cleaning on hits based on their spatial and temporal distributions. SeededRT-cleaning starts out with a list of “seeds” - HLC hits in this case, which are likely to be physics-related hits - and adds all further hits found within a RT-range around each seed (HLC hit) to the list. It repeats this adding process for each hit, until

no more hits can be added to the list. This SeededRT-cleaning is better than the RT-cleaning, because RT-cleaning is not able to remove clustered noise hits. The cleaned pulses used in this analysis are the SRT-TW-cleaned DCC pulses or simplified to be referred to as SRT-TW-cleaned pulses.

Time Window cleaning is a static time window (STW) cut with the $[-5, 4] \mu\text{s}$ window around the trigger time of the event to remove early hits and late hits.

The output SRT-TW-cleaned DCC pulses represent clean hits caused by physical events and not noise. The charge-weighted CoG of the cleaned pulses then is a good indicator of the interaction vertex for this event. CoG σ_z is the standard deviation of the depth (z) of the pulses, CoG σ_t is standard deviation of the time (t) of the pulses. The cuts are CoG $\sigma_t < 1000 \text{ ns}$ and CoG σ_z in $[7, 100] \text{ m}$.

Next, SRT-TW-cleaned pulses are sorted by time into four subsets. $(\Delta s)^2$ is the space-time interval between CoG of the 1st quarter of pulses and the CoG of 4th quarter defined below:

$$(\Delta s)^2 = (\Delta r)^2 - (ct_{Q1} - ct_{Q4})^2, \quad (5.2)$$

where Δr is the spatial distance between the CoG of the 1st quarter and the 4th quarter of pulses. t_{Q1} and t_{Q4} are the times of the CoG of the 1st quarter and the 4th quarter, respectively.

We select events with $-400 \leq (\Delta s)^2 \leq 0$.

If these two quarters of pulses are generated by the same neutrino that travels at nearly the speed of light, then, the value of Δs^2 is either equal to zero or smaller than zero. $\Delta s^2 = 0$ means the light observed are direct light. $\Delta s^2 < 0$ means the light observed are scattered, thus taking a longer time to arrive at the DOMs, making Δs^2 negative.

A value of $\Delta s^2 > 0$ can only be explained by uncorrelated hits, *i.e.*, the two quarters of pulses are not generated by the same neutrino. It's non-causal for one neutrino to create light at two locations (r_{Q1}, r_{Q4}) at times (t_{Q1}, t_{Q4}) whose spatial distance is larger than what speed of light can travel in the time window $[t_{Q1}, t_{Q4}]$.

That's why we choose the upper cut value at $(\Delta s)^2 \leq 0$. The lower cut value -400 m^2 is chosen because at -400 m^2 the event distribution for neutrino events falls off much more rapidly than muons.

The last cut is a requirement of a minimum of eight of the number of DOMs having SRT-TW-cleaned DCC pulses. The cleaned pulses are also used for event

Table 5.4: Triggers, their definitions and cut values.

Level	Parameters	Definitions	Cuts
1	Online Trigger (SMT3 DC)	Minimum of 3 HLC hits within a sliding $2.5 \mu\text{s}$ window in the DeepCore subarray	$N_{\text{HLC}} \geq 3$
4	SANTA direct DOMs	Number of DOMs having SANTA-cleaned hits produced by direct Cherenkov light	≥ 3
	RT Fiducial charge	The charge of a RT cluster in the fiducial volume (cluster radius $R = 150 \text{ m}$, time window $T = [-250, 500] \text{ ns}$ around trigger)	$\geq 7 \text{ PE}$
	CoG σ_z	The standard deviation of the z position of the charge-weighted CoG of the SRT-TW-cleaned pulses in DCC	$[7, 100] \text{ m}$
	CoG σ_t	The standard deviation of the time of the charge-weighted CoG of the SRT-TW-cleaned pulses in DCC	$\leq 1000 \text{ ns}$
	Space-time interval	Pulses are sorted by time into four subsets. Space-time interval between the 1st and 4th subset.	$[-400, 0] \text{ m}^2$
	SRT-TW-cleaned DOMs	Number of DOMs having SRT-TW-cleaned DCC hits	≥ 8

reconstruction. Table 5.4 summarizes all the trigger cuts used in all levels.

5.3.2 Vetoing in Level 3

Veto cuts are used to remove atmospheric muon events. In level 3, there are two cuts: EDC Veto and the modified 2012 DC Veto cut. So, in the level 2 online DeepCore filter, events having one or more HLC hits in the EDC veto region are rejected; at level 3 EDC Veto serves as an offline filter, rejecting events having seven or more PE in the same online filter window, *i.e.*, keeping events with “EDC_VetoPE” $< 7 \text{ PE}$.

The modified 2012 DC Veto is used to further remove muon events. It has cuts on 8 parameters: *NoiseEngine*, *MicroCountHits*, *MicroCountPE*, *NAbove200*, *FiducialQ*, *VertexGuessZ*, *VetoQ/FidQ*, and *C2QR6*. It is “modified” because the standard “2012 DC Veto” has 9 parameters and has a slightly shorter time window in the DTW cleaning. So the modified 2012 DC Veto has a slightly larger event rate at level 3 than the standard one.

NoiseEngine is a module for identifying events that are likely triggered by

Table 5.5: Level 3 DC Veto and Level 4 Trigger

Level 3 DC Veto		Level 4 Trigger	
NoiseEngine	True	RTFidQ	≥ 7 PE
MicroCountHits	> 2	CoG σ_z	$[7, 100]$ m
MicroCountPE	> 2 PE	CoG σ_t	≤ 1000 ns
NAbove200	< 12	$(\Delta s)^2$	$[-400, 0]$ m ²
VertexGuessZ	< -120 m	SRT-TW	≥ 8
C2QR6	> 0.4	-cleaned	
FiducialQ	> 0	DOMs	
VetoQ/FidQ	< 1.5		

random noise. It first performs a static time window (STW) cut and the RT-cleaning on the pulses. The STW cut removes pulses that are outside of the static time window $[-3, 2]$ μs around the event trigger time. The RT-cleaning is used to remove isolated hits. A hit is kept if it has another hit within a radius R and a time window T with it (here $T = 750$ ns, $R = 150$ m). Then, the STW-RT-cleaned hits are mapped into all possible pairs with velocities inside a speed window $[0.1, 1.0]$ m/ns, and a sliding time window of 750 ns. The pairs are then projected onto a binned Healpix sphere. If more than three pairs land in a single bin, the event passes. This is intended to select events with at least some possible hits compatible with the speed of light. The parameters are also designed to be easy for physics events to pass.

MicroCountHits and *MicroCountPE* are the charge and pulse information from a dynamic time window (DTW) cleaning. The time window is 300 ns and applied onto the pulses only in the EDC fiducial volume. Events having more than 2 PE of charge (*MicroCountPE* > 2) and more than 2 pulses (*MicroCountHits* > 2) in the window get passed.

NAbove200 is the number of hits above the depth $z = -200$ m prior to the DeepCore trigger time. Events are required to have no more than 12 PE in the region. In IceCube's coordinate system, the origin $(x, y, z) = (0, 0, 0)$ is located at the mid point of the IceCube array, so $z = 0$ is the location between the 30th and 31st DOM, which is roughly 2000 m below the surface. Its exact point is 46500'E, 52200'N, at an elevation of 2900 ft (883.9 m). This cut removes events having some hits in the upper side of the detector that are more likely to be caused by atmospheric muons.

VertexGuessZ is the z position of a simple vertex hypothesis for each event, which is given by the earliest pulse in the SRT-TW-Cleaned DCC hit series for the event. The Z-location of this vertex must be located below -200 m in detector coordinates or the event will be removed.

C2QR6 is the ratio of the charge deposited in the first 600 ns to the total charge. The hit series used here is the SRT-TW-Cleaned DCC hit series but with the first two hits removed. Muons will have a lower ratio because their light is more evenly distributed over time and over a longer timescale. We require *C2QR6* to be greater than 0.4.

QVeto/QFid is the ratio of the charge deposited in the DCC Veto region to the charge in the DCC fiducial region. Having a smaller ratio means the event is more likely to be neutrino-induced rather than atmospheric-muon-induced. Events with a ratio smaller than 1.5 are kept.

5.3.3 Vetoing in Level 4

The vetoing in level 4 has two parts: the DCC (DeepCore Classic) Veto cut and the “Causal Track Veto,” which defines a new veto region using the trigger as a reference. The DCC Veto cut requires less than 5 PE (“DCC_VetoPE” ≤ 5) in the DCC veto region (see its definition in Section 5.1).

The Causal Track Veto’s “causal” veto region is defined by using the hit whose time is closest to the trigger time as a reference point. Hits with a distance Δr in space and Δt in time with respect to the reference hit satisfying the following criteria fall into this veto region: $\Delta r/c < 2.5 \mu s$, $\Delta r/c < -\frac{2}{3}\Delta t + \frac{1}{3} \mu s$ and $\Delta t - 0.15 \mu s < \Delta r/c < \Delta t + 1.85 \mu s$. No more than seven PE deposited charge in this causal veto region are allowed. Figure 5.6 illustrates the veto region in a speed vs. time plot.

5.4 Cut Using Boosted Decision Tree

A boosted decision tree (BDT) [91] was trained to further reduce the atmospheric muon background. The input for the BDT uses the charge, timing, and geometrical information of the remaining hit DOM signals, along with best-fit zenith angles and particle speed from crude but fast track reconstructions.

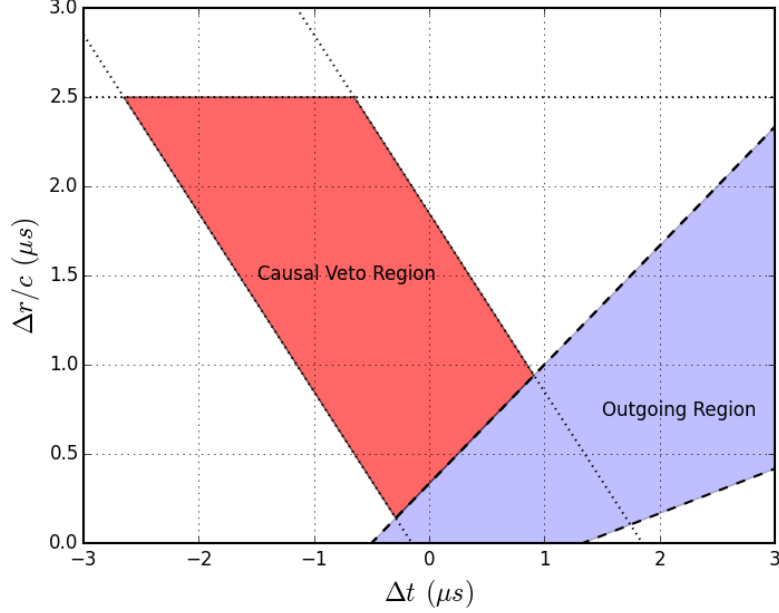


Figure 5.6: Causal Track Veto region [89]. The red region is the veto region in which events are likely to be produced by atmospheric muons. The blue region is the region where events produced by neutrinos are likely to locate.

Table 5.6 lists the 11 input variables and their definitions. The first four are charge-related variables of the SRT-TW-Cleaned DCC pulses. For example, “QR3” is the ratio of the charge in the first 300ns after the trigger time to the total charge, atmospheric muons tend to have a smaller “QR3” value than neutrinos, because the light they deposit in the detector is more evenly distributed over time and over a longer timescale.

The next four are geometry-related variables. For example, σ_z is the standard deviation of the depth (z) of the pulses. As mentioned in Chapter 5.3.1, cleaned pulses are sorted by time into four subsets. “Separation” (Δr) is the spatial distance between the first and the fourth subsets of the hits. Atmospheric-muon-like events tend to have a larger Δr value, neutrino-like events tend to have a smaller Δr . “CoG Q1 z” is the z position of the CoG of the first quarter of hits, atmospheric-muon-like events tend to have a higher z position, because most of them are downward-going and deposit light when they enter the detector. Similarly, “CoG Q1 ρ ” also tends to be larger for atmospheric-muon-like events, because when horizontal (or close to horizontal) atmospheric muons enter the detector, they

Table 5.6: BDT input variables and their definitions.

BDT Variables	Definitions
No. of hit DOMs	Number of hits in SRT-TW-Cleaned DCC pulses
Total Charge	Total charge in SRT-TW-Cleaned DCC pulses
QR3	Ratio of the charge in the first 300ns after the trigger time to the total charge
C2QR3	Same as QR3, but excluding the first two pulses after the trigger to reduce the impact of noise
CoG σ_z	The standard deviation of the z position of the charge-weighted CoG of the SRT-TW-cleaned DCC pulses
CoG Q1 ρ	The radial distance of the CoG of the first subset of hits
CoG Q1 z	The depth (z) of the CoG of the first subset of hits
Separation	The distance between the first and the fourth subset of hits.
SPE11 zenith	Best fit zenith from SPE fit
Linefit zenith	Best fit zenith angle from Linefit
Linefit speed	Best fit particle speed from Linefit

are likely to deposit light in the outer three layers of IceCube strings surrounding the DeepCore fiducial volume, whereas, neutrinos that have interactions inside DeepCore (or deposit light inside DeepCore) will leave less light in the outer three IceCube strings.

The last three are from two fast track reconstructions: SPE11 [92] fit, and Linefit [93] fit. “SPE11 zenith” is the best fit track direction from the 11-iteration SPE (Single Photoelectron) fit. “Linefit zenith” and “Linefit speed” are the best fit track direction and particle speed from Linefit.

Requiring events to have a BDT score > 0.2 removes 99.9% of the atmospheric muon background while keeping 58% of all neutrinos from simulations.

5.5 Corridor Cut in Level 6

The CorridorCut [94] is developed to reject events with tracks that pass through several “corridor” regions where the detector coverage is most sparse. See Fig. 5.7 for some example corridors through which background muons might be able to enter DeepCore without depositing detectable light in the veto region, enabling them to evade the veto.

The CorridorCut algorithm is as follows: First, find the earliest hit DOM

above threshold in a clean hit series, using SANTA-cleaned pulses and a threshold of 0.3 PE, and record the hit DOM's position and time. Second, do a look-up on the possible corridors for the string that the DOM is located at. Third, for each corridor, create hypothesized tracks with one azimuth step and several zenith steps per corridor. Find the direct hits that could have been produced by each track - hits in a $[-75, 250]$ ns window and within 150 m distance to the track are included. The track hypotheses with largest number of hits are saved. The cut can be placed on the number of hits. In our sample, events having none or only one such hit are kept.

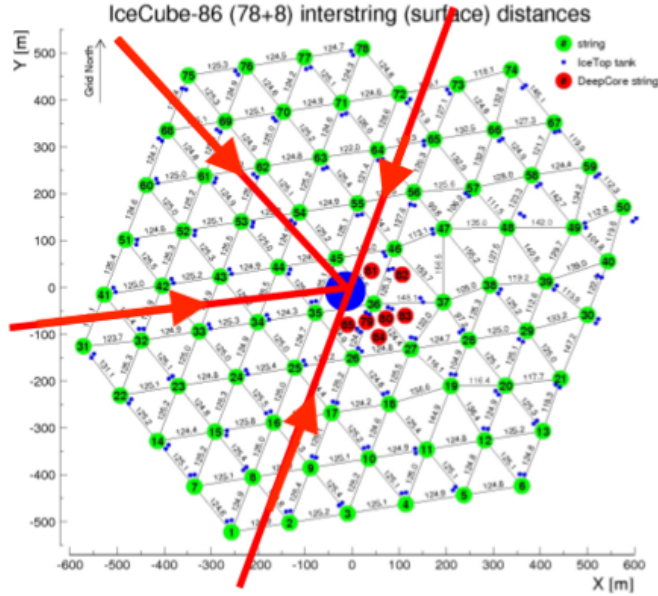


Figure 5.7: Example “corridors.” The IceCube detector was constructed on a triangular lattice in the horizontal plane. The blue spot is string 86, the four red arrows represent the directions of possible background muons towards string 86 that sneak into the detector without triggering or only triggering very few DOMs in the veto region. Figure is adapted from a plot in Ref. [95].

5.6 Containment Cuts

Additional “containment” criteria retain events that interact inside the DeepCore volume. They are used to further remove atmospheric muons. First, in level 4, we require the position of the first HLC pulse and the CoG of the first subset of charge to be within a cylindrical region centered on the DeepCore sub-array:

$$\begin{aligned}
-125 &\leq Z'_{\text{first}} \leq 150 \\
\rho'_{\text{first}} &\leq 150 \\
-125 &\leq Z'_{\text{Q1}} \leq 200 \\
\rho'_{\text{Q1}} &\leq 150,
\end{aligned} \tag{5.3}$$

where the unit is in m, the coordinate system is relative to the center of DeepCore:

$$\begin{aligned}
X' &= X - X(\text{String 36}) \\
Y' &= Y - Y(\text{String 36}) \\
Z' &= Z - (-350).
\end{aligned} \tag{5.4}$$

Then, in level 6, after reconstructing events, we require the starting and stopping positions of their tracks to be inside two regions surrounding DeepCore. The containment regions are shown in Figure 5.8, which also shows examples of allowed events and rejected events. Their equations are:

$$\begin{aligned}
-125 &\leq Z'_{\text{start}} \text{ or } (Z'_{\text{start}} \geq 0 \text{ and } r'_{\text{start}} \leq 125), \\
\rho'_{\text{start}} &\leq 100, \\
-150 &\leq Z'_{\text{stop}} \leq 150, \\
\rho'_{\text{stop}} &\leq 150.
\end{aligned} \tag{5.5}$$

The starting position is required to be coming from the inner smaller region, so that we can better reject atmospheric muon events. If an event is not fully contained, for example, if part of its track extends outside of the detector, the reconstructed neutrino energy will be smaller than the true energy. So, the stopping point is constrained to ensure the entire track is within the more densely instrumented DeepCore region, thereby improving the energy resolution.

5.7 Background Estimation

Background muons in the first level dominate the events in IceCube. After six levels of selection, the amount of background muons is greatly reduced. The ratio of number of the atmospheric muons to the number of neutrinos is reduced from 10^6 at the trigger level to 5% at the final level. Thus, it's too time-consuming to simulate

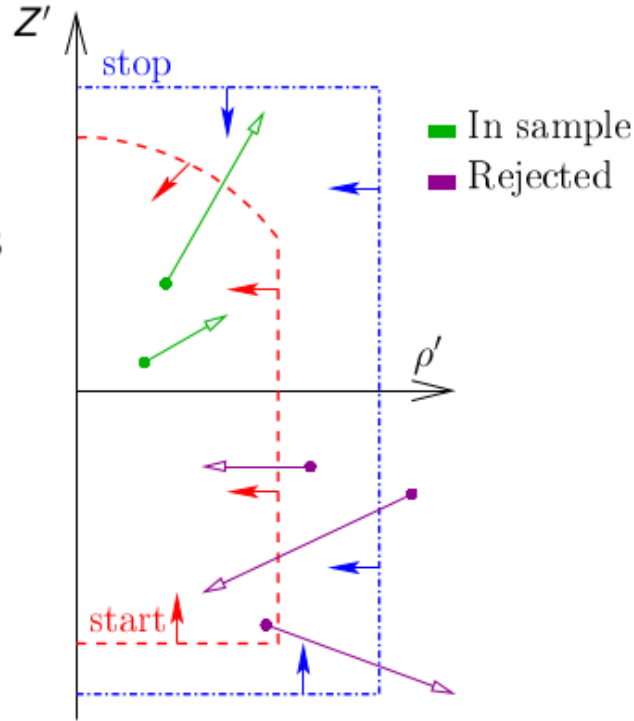


Figure 5.8: Final containment cut. The red dashed region is for the starting positions, and the blue region is for the stopping positions. The green events are examples of allowed events, while the purple ones are examples of rejected events [95].

muon events at the earliest level to achieve a reasonable amount of statistics for the final level. So, a data-driven background shape estimation is developed. From Section 5.5, the CorridorCut is effective in removing events that sneak in through the empty “corridors” in IceCube. By inverting this CorridorCut and keeping all the other selection cuts, we are able to do a good estimation of the background muon shape. This data-driven method achieved a reasonable agreement with the direct simulation method using CORSIKA [71] and MuonGUN [72]. Figure 5.9 shows the estimated background shape at the final level using this method.

The uncertainty of this background shape is estimated from two such background shapes when modifying the selection cuts. The difference is requiring more than one hit and more than two hits in the veto region. The former is used as the background shape, the latter is a more pure sample, and the difference of the two is used as the uncertainty. This uncertainty is added in quadrature with other

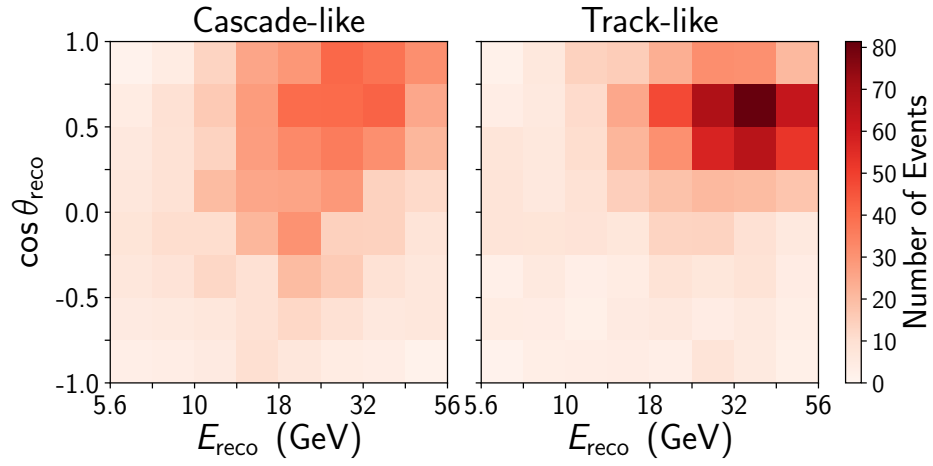


Figure 5.9: The estimated background muon template at the final level using the inverted CorridorCut method.

terms such as the term to account for the limits of statistics in the fit statistic χ^2 defined in Chapter 6.

Chapter 6 |

Analysis Techniques

Using the simulation chain described in Section 4.1, we can simulate neutrinos and their interactions in the detector. Then, applying the selection cuts described in Chapter 5, we achieve a final sample which consists of roughly 5% atmospheric muons and 95% neutrinos, of which roughly 5% are tau neutrinos. Then, using the deposited light observed by the DOMs (Section 4.2), we do reconstructions mainly to get the energy and direction of the incoming neutrino for each event. The next step then is to analyze the reconstructed events to perform the tau neutrino appearance measurement. This chapter discusses the physics parameters measured and the analysis techniques used for the measurement.

6.1 Physics Parameter (ν_τ Normalization)

The physics parameter we measure is ν_τ (CC + NC) normalization, a scale factor assigned to the ν_τ signal histograms, varying between 0 and 1. A value of one means we measured the same amount of tau neutrinos predicted by the standard three-flavor oscillation theory.

OPERA [18] and Super-K [14] both measure the ν_τ CC signal strength. IceCube/DeepCore measures the combined ν_τ CC and NC normalization because the detector observes both CC and NC events, even though the ν_τ NC events cannot be distinguished from the other two flavors. When measuring ν_τ (CC+NC) normalization, the null hypothesis is the absence of ν_τ , *i.e.*, ν_e and ν_μ don't oscillate into ν_τ (but into some sterile neutrinos that don't interact with matter). When measuring ν_τ CC-only normalization, the null hypothesis is that ν_τ CC normalization = 0 and at the same time ν_τ NC normalization $\neq 0$, *i.e.*, there are ν_τ produced from

oscillations but they only participate in the NC interaction. We believe it is more logical to do the former measurement with IceCube. To compare with the other two results, the measurement of ν_τ CC normalization is also conducted, but ν_τ (CC + NC) normalization is our main result.

6.2 Binning

The reconstructed events at the final level are grouped into a 3-dimensional histogram. The bins are eight energy bins between $[5.6, 56.2]$ GeV, eight $\cos \theta_{\text{zen}}$ bins between $[-1, 1]$, and two ΔLLH bins: $[-3, 2, \infty]$.

The energy bound interval $[5.6, 56.2]$ GeV is actually $[10^{0.75}, 10^{1.75}]$ GeV, where 0.75 and 1.75 are chosen because they are two good round numbers. These two bound values are not optimized specifically but are chosen to satisfy the simple requirement that the lower bound should be larger than the energy threshold for ν_τ CC interactions (3.5 GeV), and the fact that we don't see much oscillations above 60 GeV (see Fig. 1.11.)

The $\cos \theta_{\text{zen}}$ bound interval $[-1, 1]$ means we use neutrinos from both the Northern sky (upward-going) and the Southern sky (downward-going). Even though there is no oscillation in the downward-going region, the addition of downward-going events is useful for constraining systematics.

As mentioned in Section 4.2.2, ΔLLH is the difference of the log likelihoods between the 7-d cascade-only reconstruction and the full 8-d cascade+track reconstruction. A larger ΔLLH value means adding the track length as one extra dimension in the reconstruction improves the reconstruction likelihood, thus the event is more likely to be track-like. Similarly, a low ΔLLH value means the event is more cascade-like. Figure 6.1 shows the fraction of events split in four channels as a function of ΔLLH values, where the fraction of ν_μ CC events are higher at higher ΔLLH values.

Ideally speaking, all ν_μ CC events should be track-like, but because of the spacing between the detector strings, some lower energy ν_μ CC events won't produce a μ track energetic enough to trigger several DOMs. Thus, those low energy ν_μ CC events won't be distinguished from cascade-like events.

For this analysis, two ΔLLH bins are used to roughly classify the two event topologies. Events with ΔLLH in $[-3, 2)$ are considered cascade-like and $[2, \infty)$ are

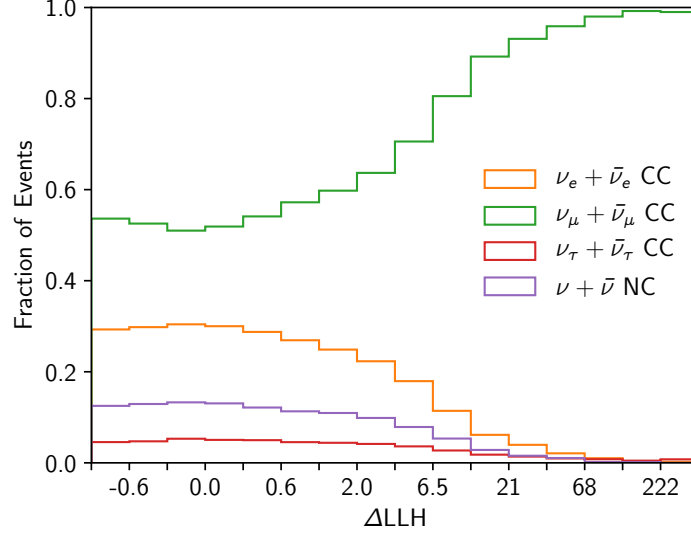


Figure 6.1: The fraction of final level events split in four channels vs. ΔLLH values. The ν_μ CC events become more dominant at higher ΔLLH values.

track-like. Originally, the event classification was performed empirically - the MC neutrino sample was divided into three regions of approximately equal statistics: region A with $\Delta LLH \in [3, 0)$, region B with $\Delta LLH \in [0, 3)$, and region C with $\Delta LLH \in [3, \infty)$ [89]. But later, the event migration issue caused by reconstruction instability (Section 4.2.4) was found. To mitigate this problem, the number of bins is then reduced to two and the bins were changed to $[-3, 2]$ and $[2, \infty]$, where the value 2 is chosen to ensure also roughly the equal statistics in the two bins.

Fig. 6.2 shows the cumulative distribution plot of the percentage of ν_μ CC events vs. ΔLLH value, from which we can calculate that 55% of the ν_μ CC events have $\Delta LLH \leq 2$, and 45% have $\Delta LLH > 2$, so roughly half of the ν_μ CC events are located in each channel. In Table 6.1, we can compare the percentage of cascade-like and track-like events in all five event types: ν_e CC, ν_μ CC, ν_τ CC, ν_{all} NC and atmospheric muons.

Figure 6.3 shows the binned histograms expected at the final selection level. Figure 6.3 (b) is the ν_τ (CC+NC) signal histograms assuming ν_τ CC normalization equal to unity. Figure 6.4 shows S/\sqrt{B} distribution, where S and B are the number of signal and background events in each bin. The figure indicates that upward-going cascade events with reconstructed energies around 20 GeV dominate the measurement.

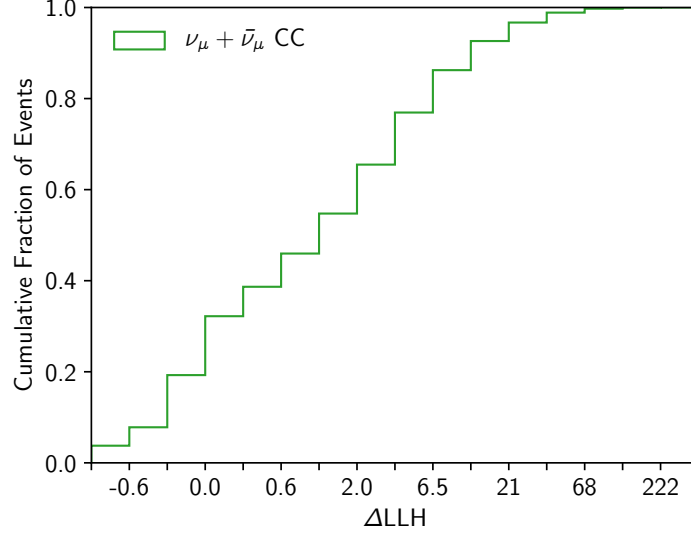


Figure 6.2: The cumulative distribution of the percentage of ν_μ CC events vs. ΔLLH values. The value $\Delta LLH = 2$ splits the ν_μ CC events into roughly two halves: 55% of the ν_μ CC events have $\Delta LLH \leq 2$, and 45% have $\Delta LLH > 2$.

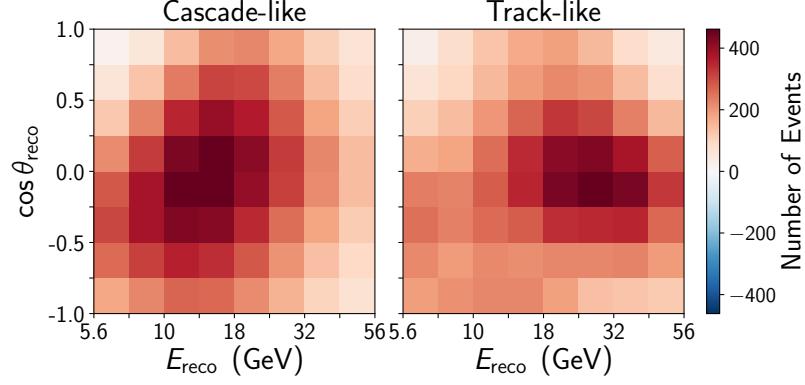
	$[-3, 2]$	$(2, \infty)$
ν_e CC	0.7711	0.2289
ν_μ CC	0.5475	0.4525
ν_τ CC	0.7312	0.2688
ν_{all} NC	0.7660	0.2340
muons	0.503	0.497

Table 6.1: The percentage of cascade-like events and track-like events for different event types. We see over 70% of the ν_e CC, ν_τ CC, ν_{all} NC events are in the cascade channel, and ν_μ CC events and atmospheric muons distribute evenly among the two channels.

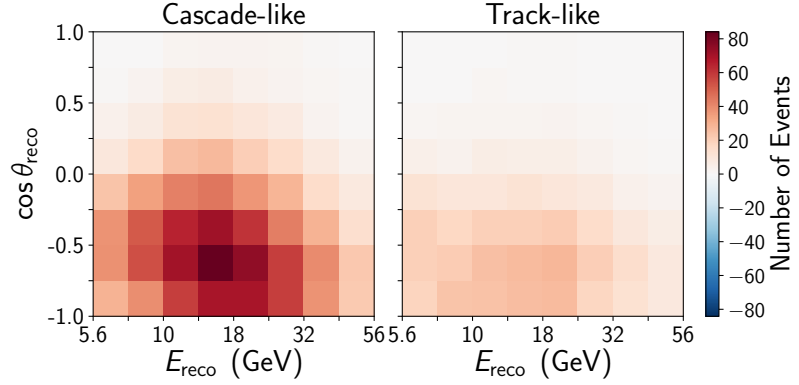
6.3 Fit Statistic

The goodness-of-fit statistic is the quantity that measures how well a theoretical model describes the observation. In our case, the theoretical model is the expected histogram determined by the physics and nuisance parameters. The observation is the binned data histogram using the same selection cuts and reconstruction as simulated data.

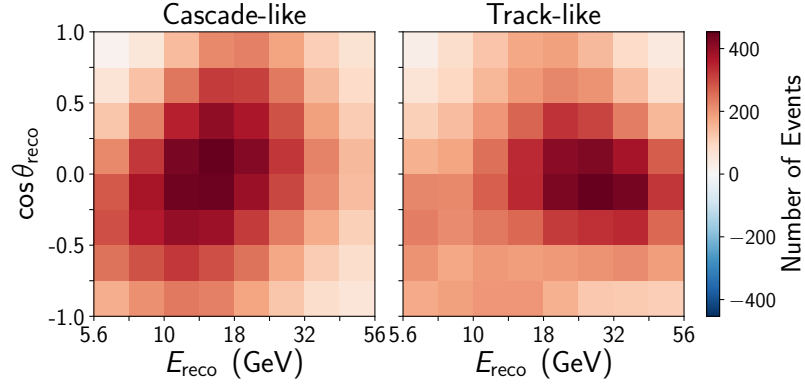
We perform a χ^2 minimization. The minimizer gets the best agreement by varying the parameter of interest (ν_τ normalization) and other nuisance parameters



(a) The expected distributions at the final level.



(b) The expected ν_τ (CC+NC) signal distributions at the final level.



(c) The expected background distribution at the final level.

Figure 6.3: Expected histograms with parameters set to their nominal values: (a), the total expected events at level 6, (b), the signal (ν_τ (CC+NC)), and (c) the background which include ν_e (CC+NC), ν_μ (CC+NC) and atmospheric background muons.

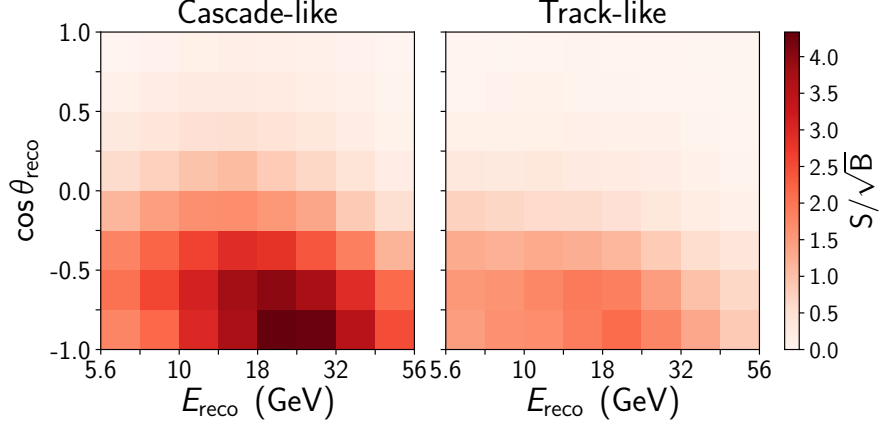


Figure 6.4: Signal ν_τ (CC+NC) divided by the square-root of the background (ν_e , ν_μ and atmospheric μ) for each analysis bin. The figure includes both neutrinos and anti-neutrinos.

(systematics). The fit statistic is a χ^2 function defined as:

$$\chi^2 = \sum_{i \in \{\text{bins}\}} \frac{(N_i^{\text{exp}} - N_i^{\text{obs}})^2}{(\sqrt{N_i^{\text{exp}}})^2 + (\sigma_i^{\text{exp}})^2} + \sum_{j \in \{\text{syst}\}} \frac{(s_j - \hat{s}_j)^2}{\hat{\sigma}_{s_j}^2}, \quad (6.1)$$

where $(\sigma_i^{\text{exp}})^2 = (\sigma_i^{\text{MC}})^2 + (\sigma_i^{\text{ICC}})^2$.

The first term is the sum of all bins i with observed count N_i^{obs} , and expected count N_i^{exp} and the associated uncertainties. $\sqrt{N_i^{\text{exp}}}$ is the uncertainty from Poisson statistics. The σ^{MC} is the uncertainty from finite MC statistics. “ICC” (Inverted Corridor Cut) refers to the background estimated using ICC. The term σ^{ICC} represents both the finite ICC background statistics and its shape uncertainty. The second term is the penalty term that sums over all nuisance parameters s that have a Gaussian prior imposed on them with an uncertainty $\hat{\sigma}$.

Most nuisance parameters have an associated prior; their central value and $\pm 1\sigma$ ranges are listed in the Prior column in Table 6.2. Other parameters are left floating freely with a uniform prior. For example, θ_{23} is allowed in the region $[31^\circ, 59^\circ]$ (which is much larger than their global fit 3σ range $[8, 9]$).

Δm_{31}^2 is also allowed in a region larger than its global 3σ range. Since Δm_{31}^2

Table 6.2: Nuisance parameters and their associated prior central value and $\pm 1\sigma$ ranges.

Parameter	Prior
Flux	
ν_e/ν_μ ratio	1.0 ± 0.05
ν_e up/hor ratio (σ)	0.0 ± 1.0
$\nu/\bar{\nu}$ ratio (σ)	0.0 ± 1.0
$\Delta\gamma$ (spectral index)	0.0 ± 0.1
Neutrino Interaction	
M_A (quasi-elastic) (GeV)	$0.99^{+0.248}_{-0.149}$
M_A (resonance) (GeV)	1.12 ± 0.22
Oscillation	
θ_{13} ($^\circ$)	8.5 ± 0.21
θ_{23} ($^\circ$)	-
Δm_{31}^2 (10^{-3} eV 2)	-
Detector	
<i>bulk ice scattering</i>	$0.0 \pm 10\%$
<i>bulk ice absorption</i>	$0.0 \pm 10\%$
<i>DOM efficiency</i> (%)	100 ± 10
<i>hole ice</i> (σ)	0.0 ± 1.0
<i>hole ice forward</i> (a.u.)	-
<i>hole ice model (spiciness)</i>	-
Normalization	
ν NC normalization	1.0 ± 0.2
effective lifetime (y)	-
Atm. μ scale	-

can be either larger than zero (under normal hierarchy) or smaller than zero (under inverted hierarchy), each one fit (either with data or pseudo data in MC studies) actually consists of two fits. The fitter starts with a fit under normal hierarchy assumption, where Δm_{31}^2 is allowed in a positive range $[1 \times 10^{-3}, 7^{-3}]$ eV 2 . Then, it switches to the inverted hierarchy assumption with Δm_{31}^2 floating in the negative range $[-7 \times 10^{-3}, -1 \times 10^{-3}]$ eV 2 . Finally the fitter compares the two fits and returns the better fit.

6.4 Confidence Interval

When an experiment measures a parameter of interest, the parameter's true value may be different from what is measured. A confidence interval (C.I.) is the range of values calculated from the experiment that the true parameter might lie in. The true value is never known, but one can get more and more confident in how likely the true parameter is located inside the interval. A confidence level (C.L.) is the quantity to measure this confidence [96], usually represented by α . Having $\alpha = 90\%$ for a confidence interval means that if we repeat the experiment independently many times, 90% of the time the true parameter lies in that interval.

Figure 6.5 shows the classical Neyman's method [96] to construct the confidence interval. Here, we use μ to represent the parameter of interest whose true value is unknown, and x is the measured value for μ . The probability density function $P(x|\mu)$ is the probability of measuring a value of x given the true parameter μ . In a counting experiment, $P(x|\mu)$ is the Poisson likelihood function.

6.4.1 Feldman-Cousins Confidence Interval

In the ν_τ (CC + NC) normalization measurement with real data, we use the Feldman-Cousins construction [97] for the calculation of the confidence interval. It has an advantage over the classical construction because it can eliminate the unphysical region.

The Feldman-Cousins construction is based on the Neyman construction, but differs in how the acceptance region $[x_1, x_2]$ is produced. It does not choose the x values for the acceptance region based on $P(x|\mu)$, instead it uses a principle of ordering on the profile likelihood ratio to construct the acceptance region. The profile likelihood ratio is defined as:

$$R = \frac{P(x|\mu)}{P(x|\mu_{\text{best}})}, \quad (6.2)$$

where μ_{best} is the best fit value for μ in performing the maximized likelihood estimation (MLE).

The R values produced from the MLE trials are then sorted in decreasing order. The x values with the highest R value are added to the acceptance region first,

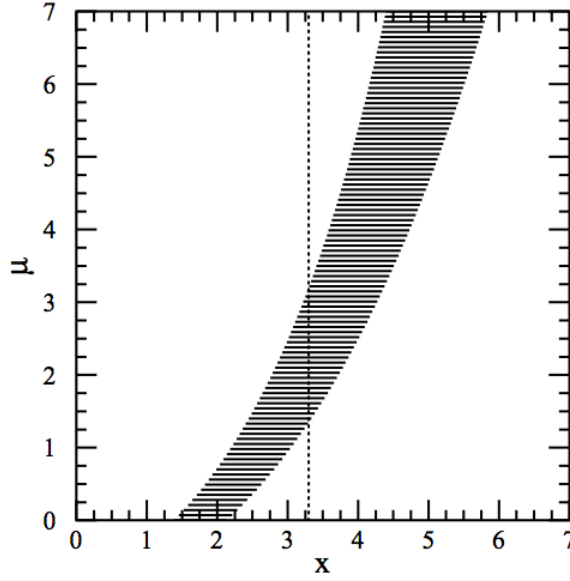


Figure 6.5: Illustration of the Neyman construction of confidence interval (figure from Ref. [97]). For each value of μ , calculate the acceptance region $[x_1, x_2]$ so that the probability of x being in the region $\sum_{x_1}^{x_2} P(x|\mu)$ equals α . The acceptance regions are shown as the horizontal lines. The actual measurement of x gives one value of x . Drawing a vertical line at the position gives a range of values that intercept with the vertical line at $[\mu_1, \mu_2]$. $[\mu_1, \mu_2]$ is the confidence interval for the measurement.

then the next highest R is added. This process repeats until the sum of the $P(x|\mu)$ reaches the desired confidence level.

6.5 Expected Sensitivity

In our case, we use χ^2 as our fit statistic, μ is ν_τ normalization, and the profile likelihood ratio is then:

$$\Delta\chi^2 = \chi^2(x|\nu_\tau \text{ norm}, \theta_{\text{best}}) - \chi^2(x|\nu_\tau \text{ norm}_{\text{best}}, \theta_{\text{best}}), \quad (6.3)$$

where θ represents the nuisance parameters, and θ_{best} is the best fit value. The first term in the $\Delta\chi^2$ is the conditional fit with ν_τ (CC + NC) normalization fixed at various values and the nuisance parameters free, the second term is the global fit with ν_τ (CC + NC) normalization freely floating together with other nuisance

parameters.

The Feldman-Cousins construction is accurate but computationally expensive. Thus, in Monte Carlo studies, we calculate the expected sensitivity using an asymptotic approximation (Wilk’s theorem [98]), since our binned histograms have a large number of events. Figure 6.6 shows the expected MC sensitivity of roughly 31% on the ν_τ (CC + NC) normalization. The expected significance to exclude the no-appearance null hypothesis is, according to the Wilk’s theorem, 3.6σ ($=\sqrt{\Delta\chi^2(\nu_\tau\text{norm.}=0)} = \sqrt{13.1}$).

6.6 Data Challenge

There are statistical tests necessary to do before we look at the data. A “data challenge” is used to test if the analysis code can recover the injected signal value. We add Poisson fluctuations to the expected event histogram to produce the pseudo data histogram. The physics parameter of this pseudo data is set to values other than the nominal value. Then, we perform fits to the pseudo data to test if we can recover the injected parameter. In our analysis, we generate Poisson-fluctuated pseudo data with ν_τ (CC + NC) normalization set to values from 0 to 2.

Fig. 6.7 plots the measured ν_τ (CC + NC) normalization vs the injected values. The central black curve is the median values of the measured ν_τ (CC+NC) normalization at each injected value of pseudo data. The light green region is the 95% confidence belt using the F-C C.I. construction. The thin solid and dashed lines are the classical Neyman C.I. construction. This shows that the fitter can recover the injected parameter well.

6.7 Treatment of Systematics

This section covers how the systematic uncertainties are handled in the analysis. The actual calculation and estimation of the uncertainties are discussed in Chapter 7. This section has two parts: the first part is about the smooth systematics whose effect can be applied on individual event weights using analytic functions, and the second part discusses the discrete systematics.

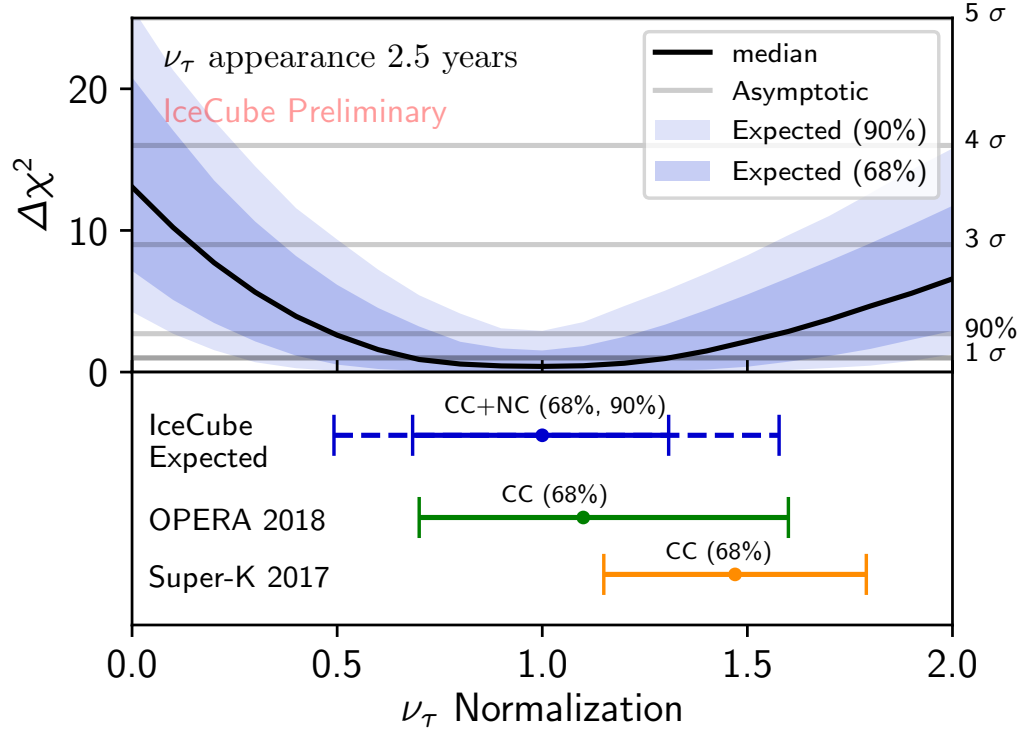


Figure 6.6: Expected sensitivity of the ν_τ (CC + NC) normalization measurement with three years of IceCube/DeepCore data. $\Delta\chi^2$ is defined in Eq. 6.3. 21 ν_τ normalization values are scanned in the range of 0 – 2. At each value, 1000 profile likelihood ratio fits are conducted. The blue shaded regions are the 68% and 90% regions for $\Delta\chi^2$. The black line connects the median values of $\Delta\chi^2$ at each ν_τ normalization value. The grey lines are the asymptotic lines from Wilk’s theorem. The intersections between the lines and the median line gives the expected confidence intervals shown in the lower half of the figure. The 68% and 90% C.I. are [0.68, 1.31] and [0.49, 1.58].

6.7.1 Smooth Systematics

The term “smooth” is used here to refer to systematics whose effects on event weights are smooth functions of the systematics together with some physics parameters for each individual event. Each event weight is composed of factors coming from the fluxes, oscillation probabilities, and interaction cross sections. So the effect of oscillation parameters is simply a matter of calculation of the oscillation probabilities for each event at true $(E, \cos\theta_{\text{zen}})$. There is no need to redo the

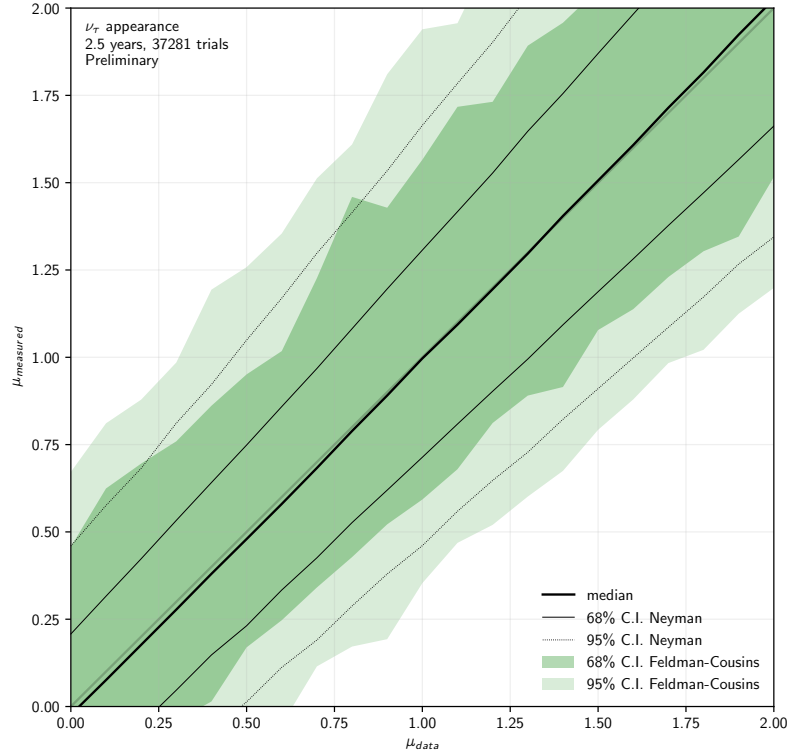


Figure 6.7: Data challenge. The y axis is the measured ν_τ (CC+NC) normalization, the x axis is the injected ν_τ (CC+NC) normalization for pseudo data.

simulation or reconstruction.

Similarly, the effect of flux-related systematics is applied by modifying the associated flux weights. For example, the flux ratio of ν_e/ν_μ is applied on the ν_e ($\bar{\nu}_e$) flux and ν_μ ($\bar{\nu}_\mu$) flux so that their ratio is changed according to the intended flux ratio value while conserving the total flux.

The normalization systematics like ν *NC normalization*, *atmospheric muon normalization*, and the *effective lifetime* (an overall scale factor on every event) are simply re-weighting factors on the specific event type of interest.

6.7.2 Discrete Systematics

Six discrete systematics are used to describe the detector response: *DOM efficiency*, *hole ice*, *hole ice forward*, *hole ice model* (also termed *spiciness*), *bulk ice scattering*, and *bulk ice absorption*. They are called discrete systematics because unlike the aforementioned smooth systematics, it's impossible to find a function that can map these detector level parameters to a high level parameter such as the event's reconstructed $(E, \cos \theta_{\text{zen}})$ on an event-by-event basis.

For example, *DOM efficiency* is a parameter to quantify the overall optical efficiency of DOMs in IceCube. An increase of *DOM efficiency* will increase the amount of light that the DOMs observe. Thus it is likely to change the reconstructed energy of an event. But there is no function that can directly connect the final reconstructed $(E, \cos \theta_{\text{zen}})$ of an event with the value of *DOM efficiency*. Also, each event is different, there is no universal function that will work for all events.

The only way to know for sure the effect on the final reconstructed $(E, \cos \theta_{\text{zen}})$ is to put this increased light sensitivity into the DOM simulation step of the simulation chain (Section 4.1) and go over all the steps in the whole chain. Then we apply the selection cuts, do the reconstructions, and produce a new data set for each new systematic value. For this analysis, there are 32 such systematics sets produced, among which one baseline set is produced at systematics set to values to the best of our knowledge.

After getting the systematics sets, we construct smooth functions to parametrize the *DOM efficiency*'s effect on the binned $(E, \cos \theta_{\text{zen}})$ histogram. The nominal value for *DOM efficiency* is 1. Six data sets are produced with *DOM efficiency* set at 0.88, 0.94, 0.97, 1.03, 1.06, and 1.12, respectively. Figure 6.8(a) shows the linear fit to the final binned event ratios inside one bin. The fit function is $y = kx + b$. Each bin has one fit. For each bin, the scale factor $k_i x + b_i$ is then multiplied by the weight of each event ending up in this bin, where k_i and b_i are the best fit coefficients from the linear fit. We can see that the larger the *DOM efficiency*, the more events we expect to see in the bin. Figure 6.8(b) shows the same procedure done for a single bin in $(E, \cos \theta_{\text{zen}})$ for the *hole ice* systematic.

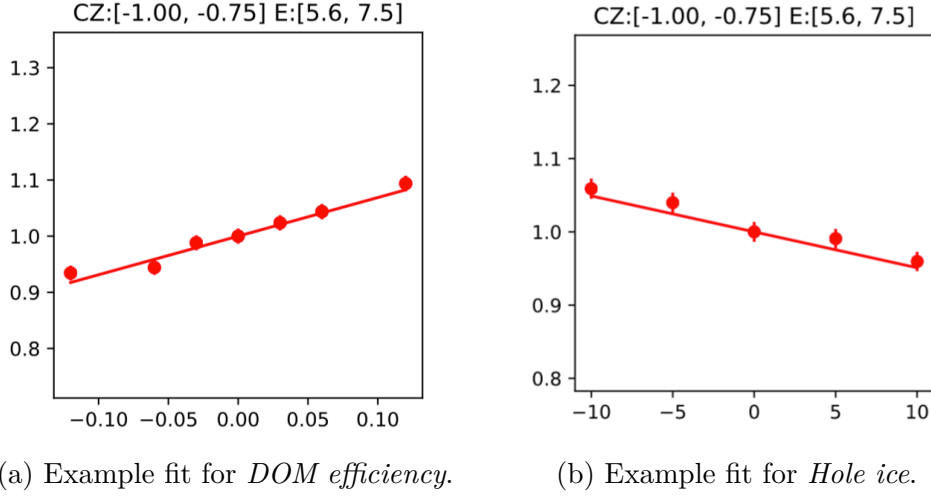


Figure 6.8: The linear fit performed inside the bin $\cos\theta_{\text{zen}} [-1, -0.75]$, energy $[5.6, 7.5 \text{ GeV}]$, ΔLLH in $[-3, 2]$. One fit is performed in each bin. (a) The y axis is the ratio of the event rates in the bin from all seven *DOM efficiency* sets to the nominal event rate from the baseline data set (*DOM efficiency* at 1). The x axis is the deviation of the *DOM efficiency* values from the nominal value 1. (b) The same fits but for *hole ice* systematics sets.

6.7.3 Hyperplane Parametrization for Discrete Systematics

Even though a linear fit is very good at describing the effect of each discrete systematic, the linear fit produces an offset value b for each fit. Thus, when putting together all six fits, the offset may get large. To solve this problem, a hyperplane fit is used instead, where the plane is in six dimensions with each dimension being each systematic. See Fig. 6.9 for the 2-d plane illustration. Just like the linear fit, the z axis is the ratio of the event rates in the bin from all the discrete systematics data sets to the nominal event rate from the baseline data set. The hyperplane fit is then a fit to the function $y = \sum_{i \in \{\text{discrete sys.}\}} k_i x_i + b$. By doing the hyperplane fit, we only have one offset value.

Figure 6.10 shows the χ^2 distribution from the hyperplane fit. The expected number of degrees of freedom (dof) is 0.78, which is calculated from $\text{dof} = (32 - 7)/32$, where 32 is the total number of data points (31 systematics sets and one baseline set) and 7 is the number of free parameters for the hyperplane function fit. The best fit χ^2 distribution's dof is 0.75, so the fits are compatible.

Figures 6.11 through Fig. 6.16 show the projected fits for each systematic.

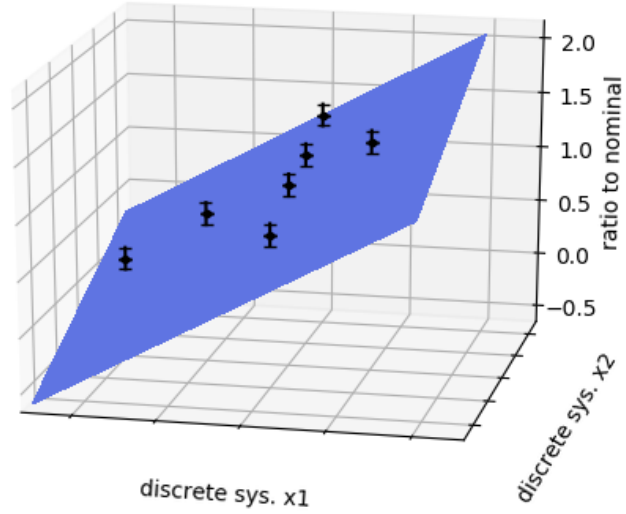


Figure 6.9: 2D plane fit to the two discrete systematics. The z axis is the ratio of the event rates from the systematics data sets with respect to the baseline set.

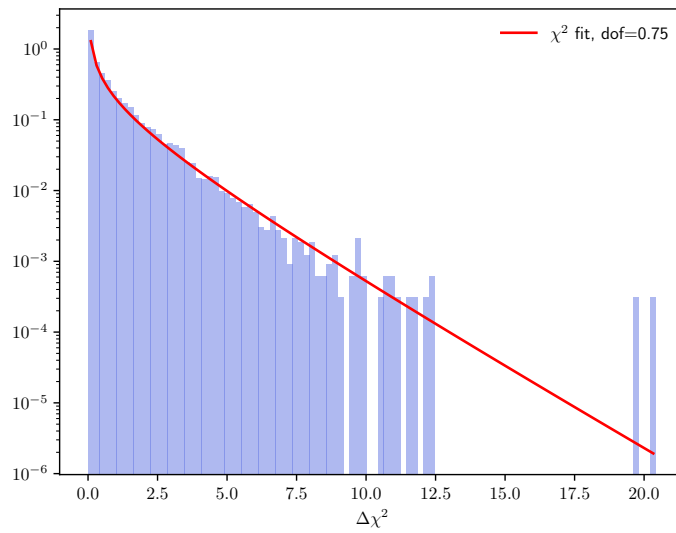


Figure 6.10: χ^2 distribution of the hyperplane fits (blue).

Each plot has 64 subplots, where each subplot corresponds to one bin in the 8 by 8 ($\cos \theta_{\text{zen}}$, energy) 2d histogram in the cascade-like channel. Since the fit results are similar for the track-like bins, only cascade-like bins are shown.

It's worth noting that in Fig. 6.14, the *spiciness* parameter does not have a physical meaning, it is merely used to represent two hole ice models. There are six sets produced with the SpiceHD model for hole ice. The other 26 sets are produced with the Dima hole ice model. A *spiciness* at one means the simulation set is produced with the SpiceHD model, and *spiciness* at zero represents the Dima model. We need this as a systematic to give a transition for the two models. See more details in Section 7.4.2.2.

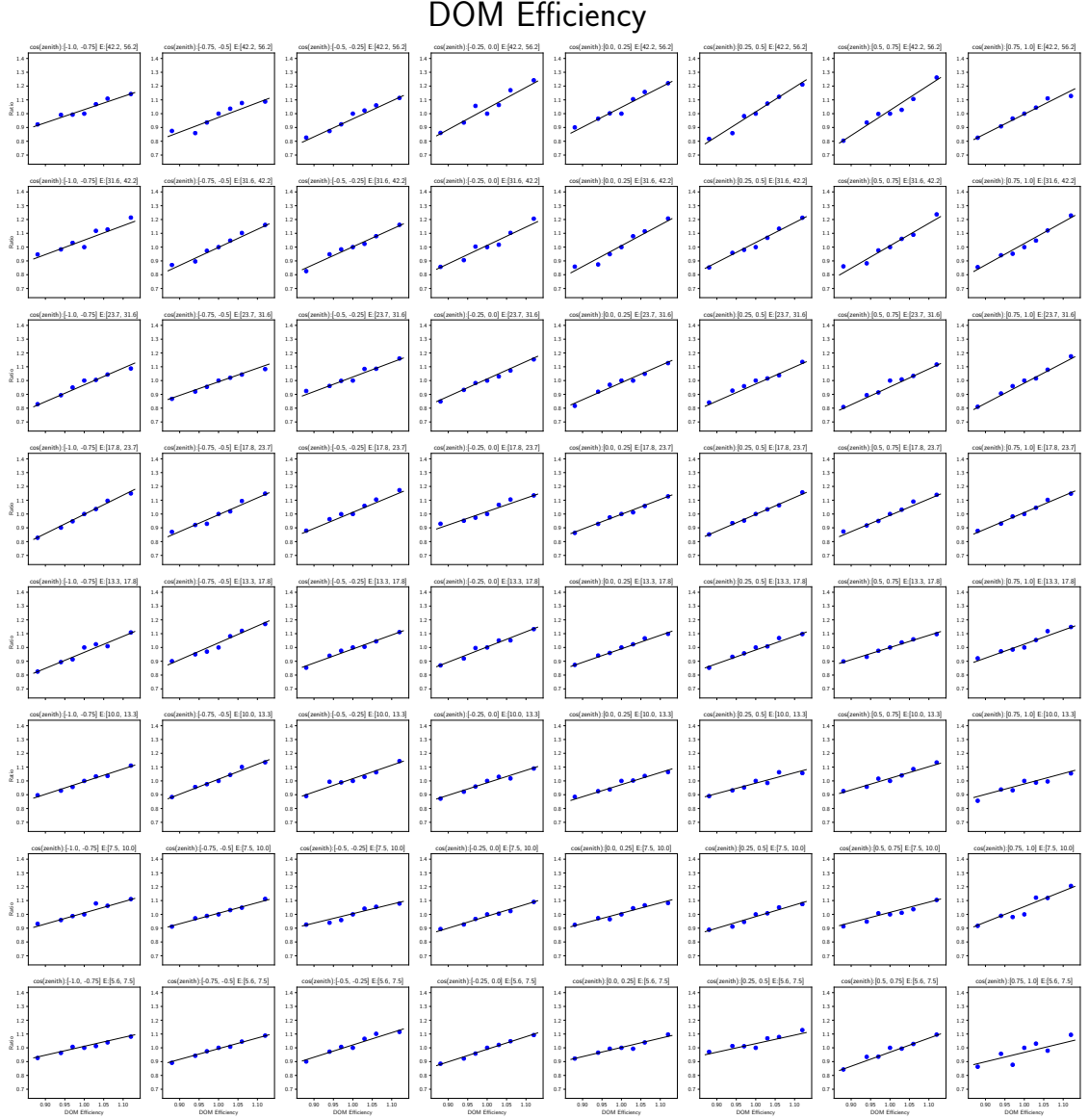


Figure 6.11: The projected hyperplane fits (for ν_μ CC events) onto the *DOM efficiency* dimension. Each subplot is for one bin in $(E, \cos\theta_{zen})$ space.

Hole Ice

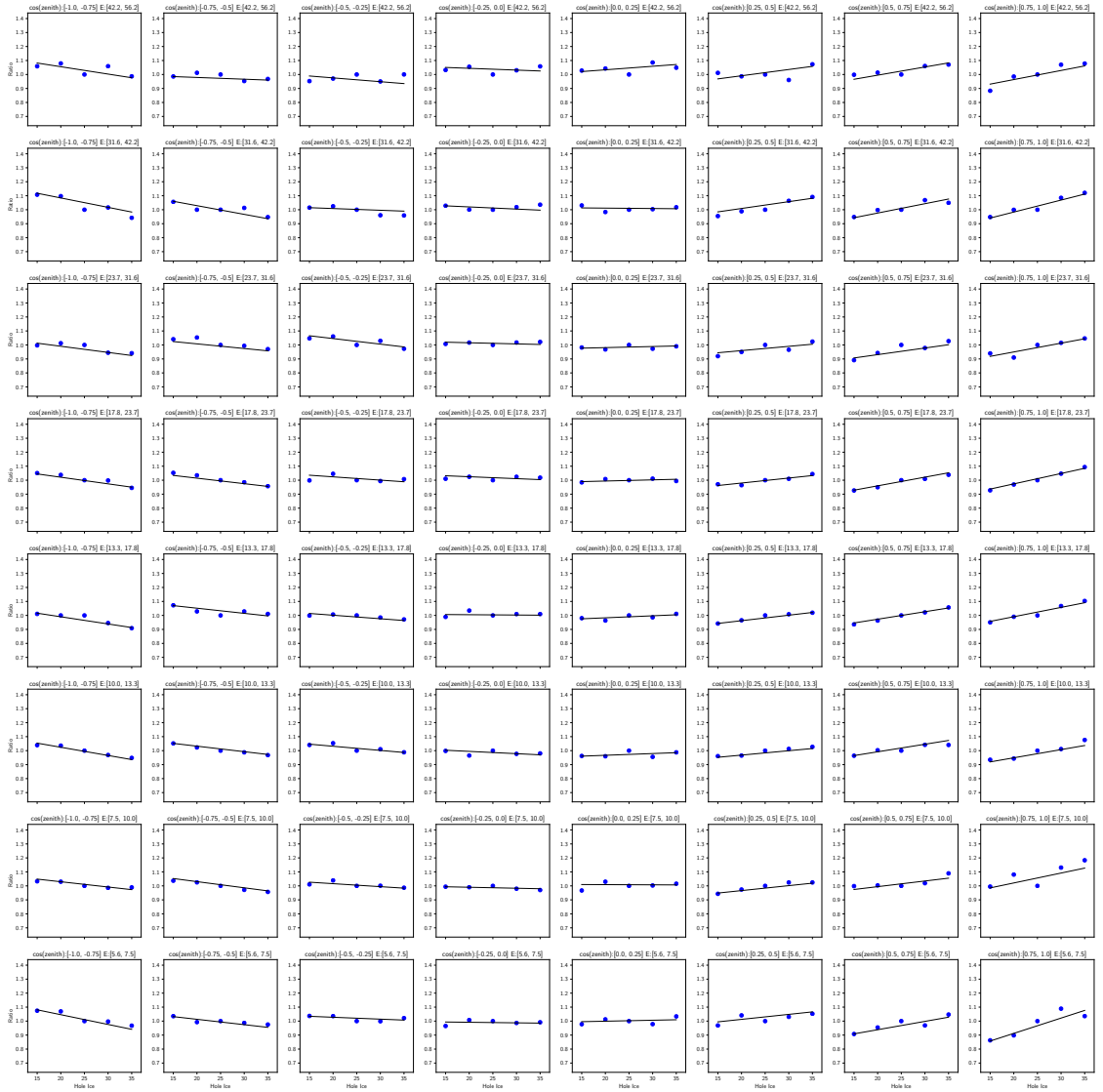


Figure 6.12: The projected hyperplane fits (for ν_μ CC flavor events) in the *hole ice* dimension. Each subplot is for one bin in $(E, \cos \theta_{\text{zen}})$ space.

Hole Ice Forward

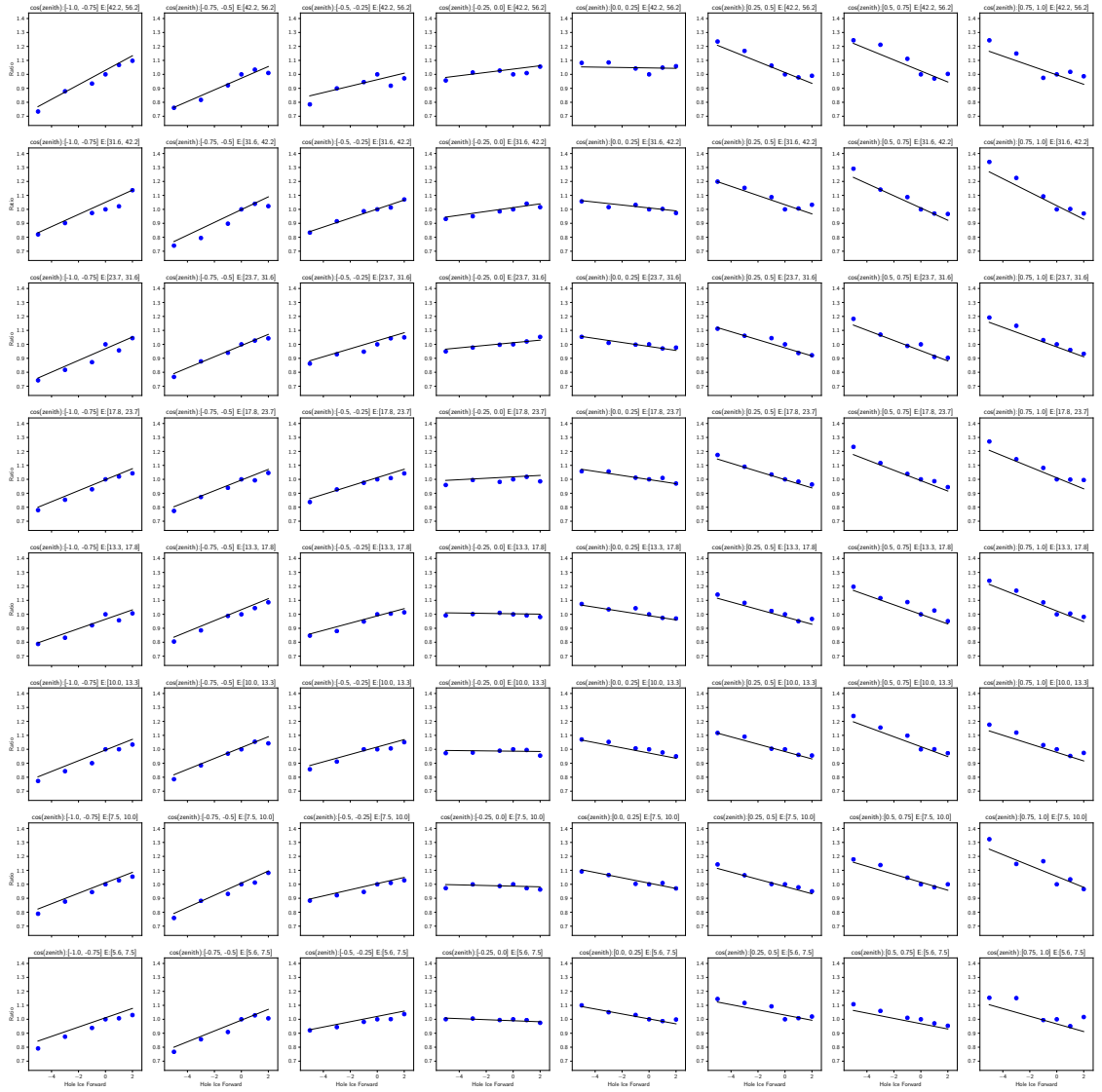


Figure 6.13: The projected hyperplane fits (for ν_μ CC flavor events) in the *hole ice forward* dimension. Each subplot is for one bin in $(E, \cos \theta_{zen})$ space.

Spiciness

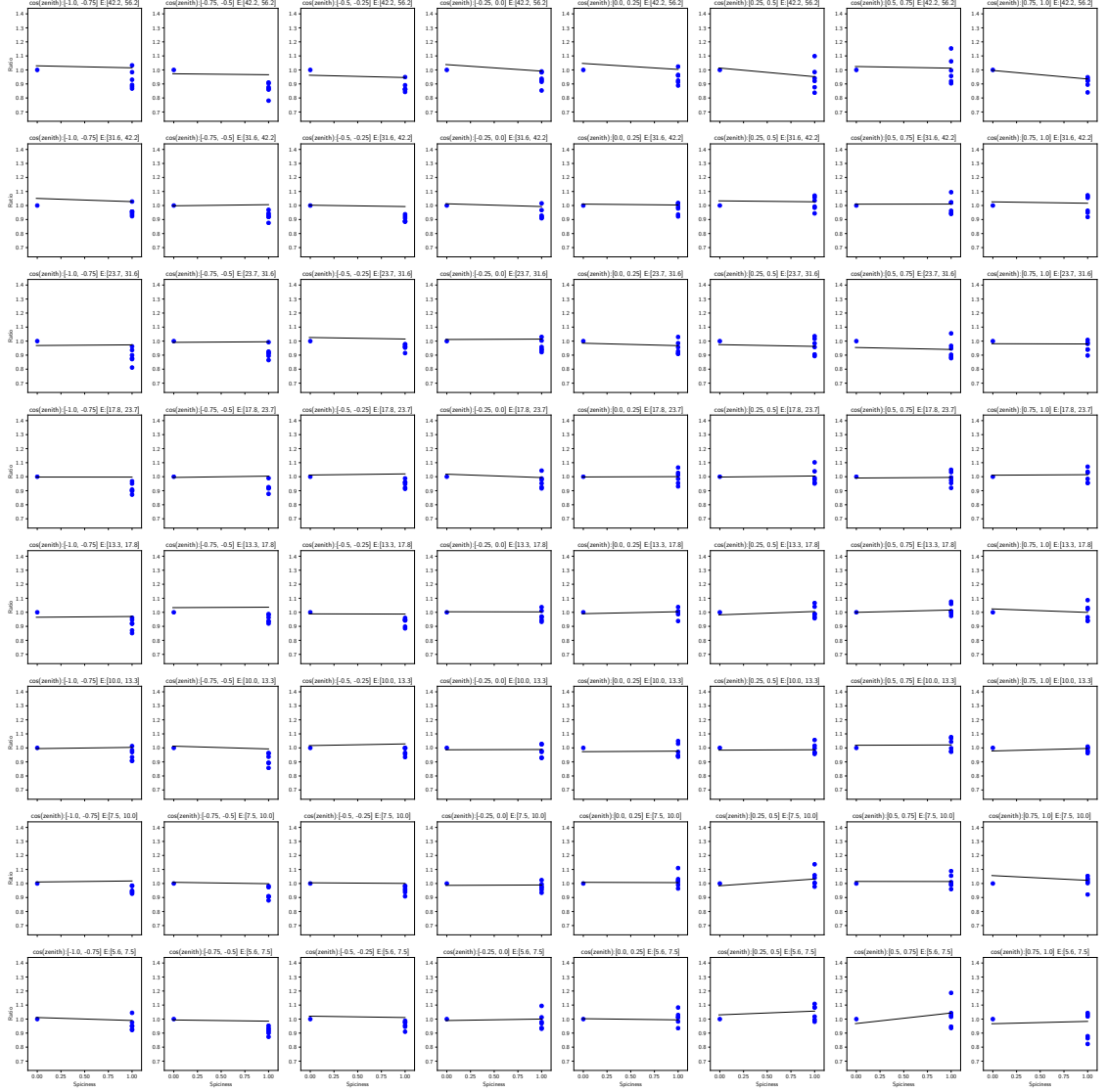


Figure 6.14: The projected hyperplane fits (for ν_μ CC flavor events) in the hole ice model (*spiciness*) dimension. Each subplot is for one bin in $(E, \cos\theta_{\text{zen}})$ space. There are six sets at one (SpiceHD model) and 28 at zero (Dima model). Each set has different model parameters, that's why we see there are multiple points at *spiciness* = 1. Each of the 28 Dima model sets also has different *DOM efficiency*, *hole ice* and *hole ice forward* values, but here only the baseline set is shown at *spiciness* = 0 because the difference between the SpiceHD model sets and the baseline Dima model set is what we care about.

Bulk Ice Scattering

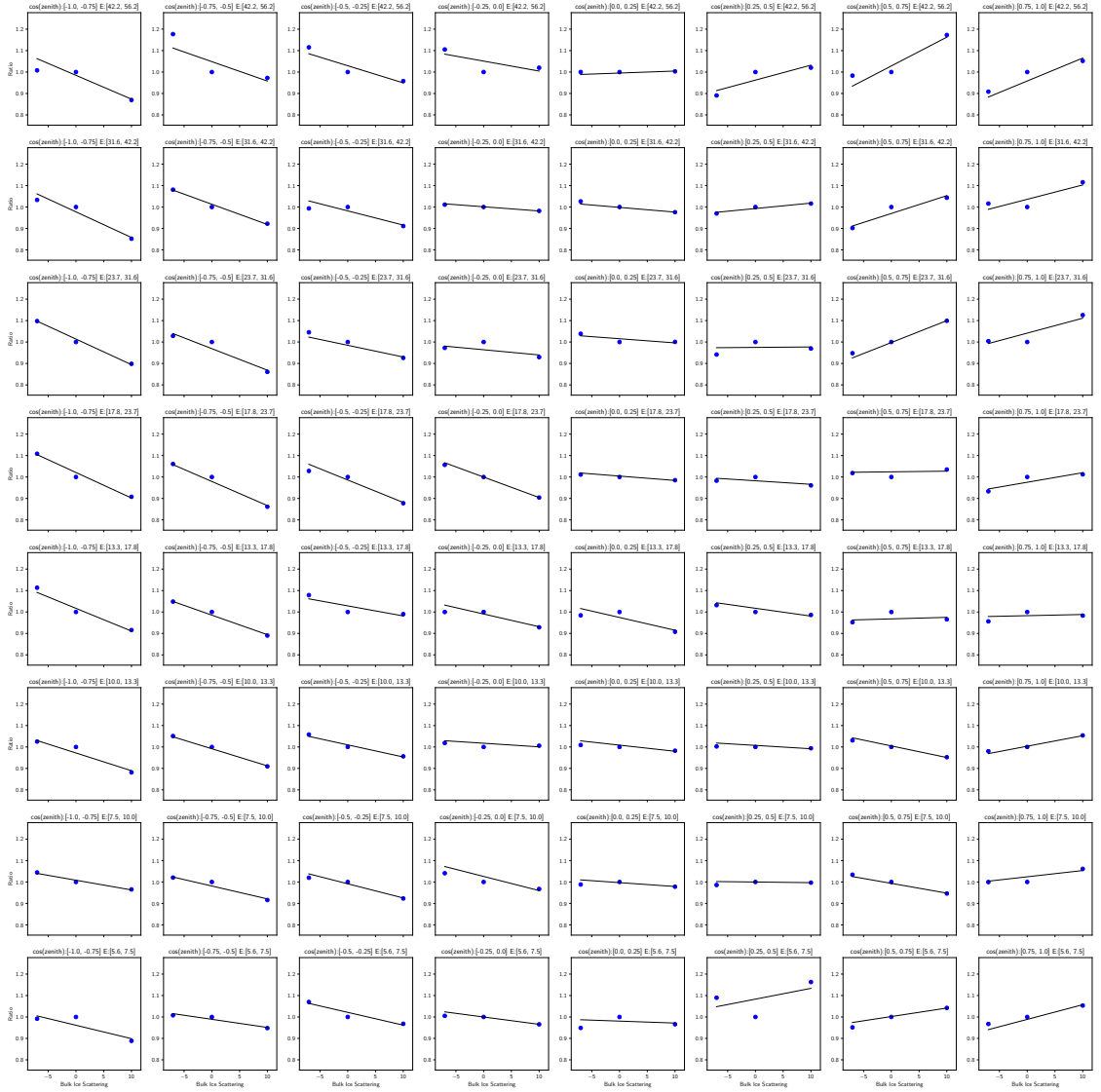


Figure 6.15: The projected hyperplane fits (for ν_μ CC flavor events) in the *bulk ice scattering* dimension. Each subplot is for one bin in $(E, \cos \theta_{\text{zen}})$ space.

Bulk Ice Absorption

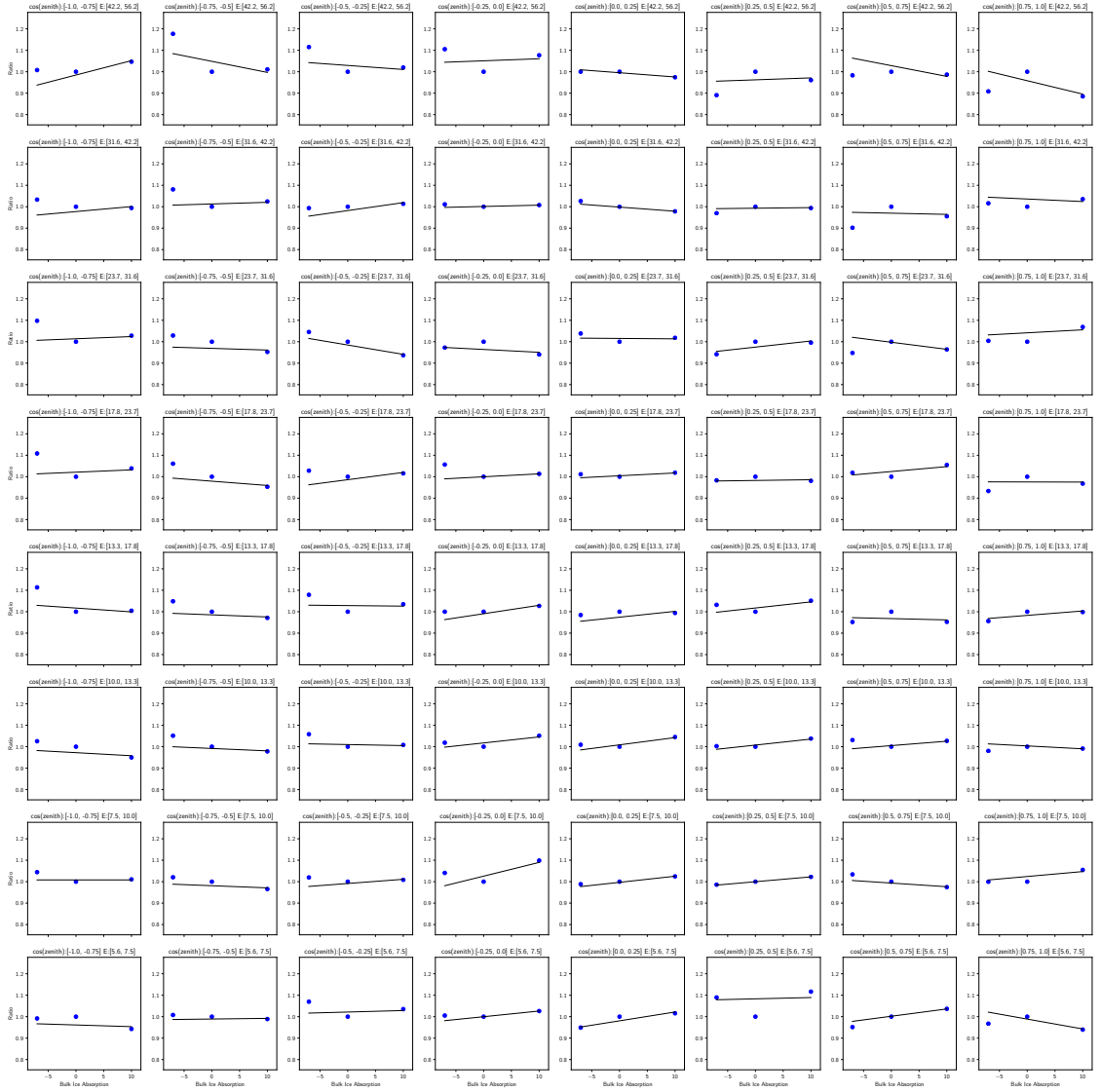


Figure 6.16: The projected hyperplane fits (for ν_μ CC flavor events) in the *bulk ice absorption* dimension. Each subplot is for one bin in $(E, \cos \theta_{\text{zen}})$ space.

Chapter 7 |

Systematic Uncertainties

This chapter discusses the uncertainties associated with the systematics, their impact on event distributions and the ν_τ (CC+NC) normalization measurement. Sections 7.1 to 7.5 cover all of them, split into five categories as shown in Table 6.2. Section 7.6 discusses the result of the N-1 test.

7.1 Flux-Related Systematics

As mentioned in Chapter 2, there are four flux-related systematics: modification of the ratio of the fluxes of the upward-going and horizontal atmospheric neutrinos up/hor ratio, modification of the ratio of the neutrino to anti-neutrino fluxes $\nu/\bar{\nu}$, deviation of spectral index ($\Delta\gamma$), ratio of the ν_e fluxes and ν_μ fluxes ν_e/ν_μ . Among them, the modifications on up/hor ratio and $\nu/\bar{\nu}$ ratio are done based on calculations done by G.D. Barr, T.K. Gaisser, S. Robbins, and T. Stanev [45], which takes into account the hadron production uncertainties (the main source of flux uncertainties) and the primary cosmic ray flux uncertainties (which have smaller contributions). The up/hor ratio compares the fluxes in two general $\cos\theta_{zen}$ regions: the upward-going region contain neutrinos with $\cos\theta_{zen} < 0.6$; the horizontal region contains neutrinos with $|\cos\theta_{zen}| < 0.3$.

Figure 7.1 shows the energy and angle dependencies of the uncertainties. The ν_e/ν_μ uses a 5% Gaussian prior, which also comes from Ref. [45].

$\Delta\gamma$ is the change in the spectral index γ for the energy dependence of neutrino flux $E^{-\gamma}$; its central value is $\Delta\gamma = 0$ with a Gaussian prior of 10%. The effects of these systematic uncertainties on the final event distribution are shown in Fig. 7.2 and Fig. 7.3.

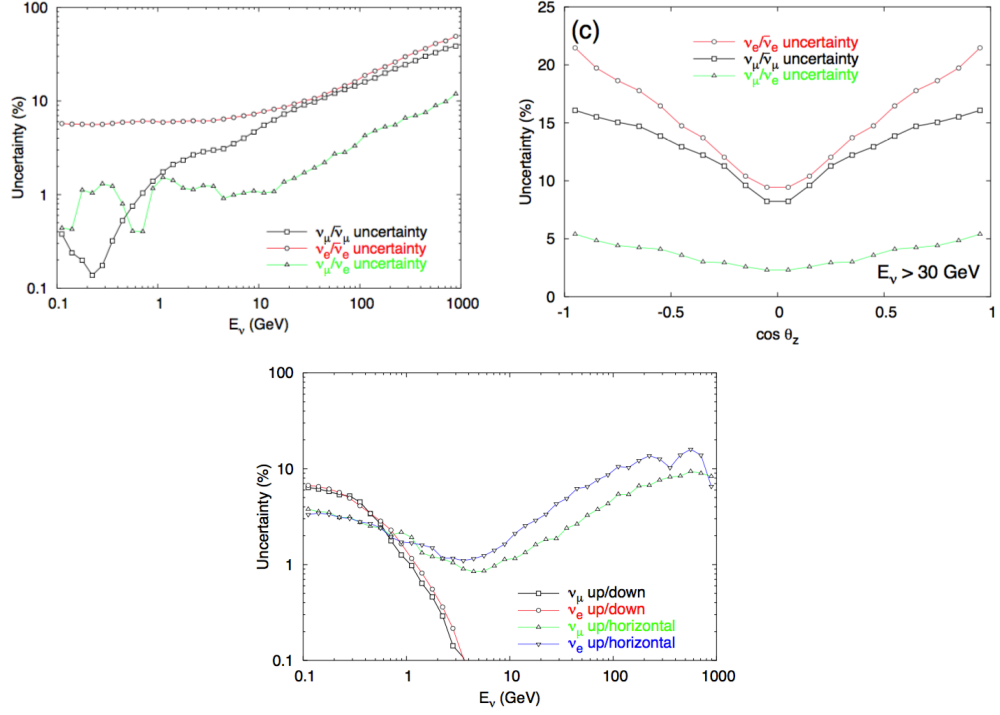


Figure 7.1: The uncertainties of $\nu/\bar{\nu}$ as a function of energy and $\cos \theta_{zen}$ and up/hor flux ratio as a function of energy [45].

7.2 Oscillation-Related Systematics

Three oscillation parameters are used: θ_{13} , $\sin^2(\theta_{23})$, Δm_{31}^2 . Figure 7.4 shows the effect of the systematics at one σ above their nominal values, where σ is the standard deviation value from the global fit [9]. The other oscillation parameters are fixed since they have minimal impact on the analysis:

$$\begin{aligned} \delta_{CP} &= 0, \\ \Delta m_{21}^2 &= 7.5 \times 10^{-5} \text{ eV}^2, \\ \theta_{12} &= 33.48^\circ. \end{aligned} \tag{7.1}$$

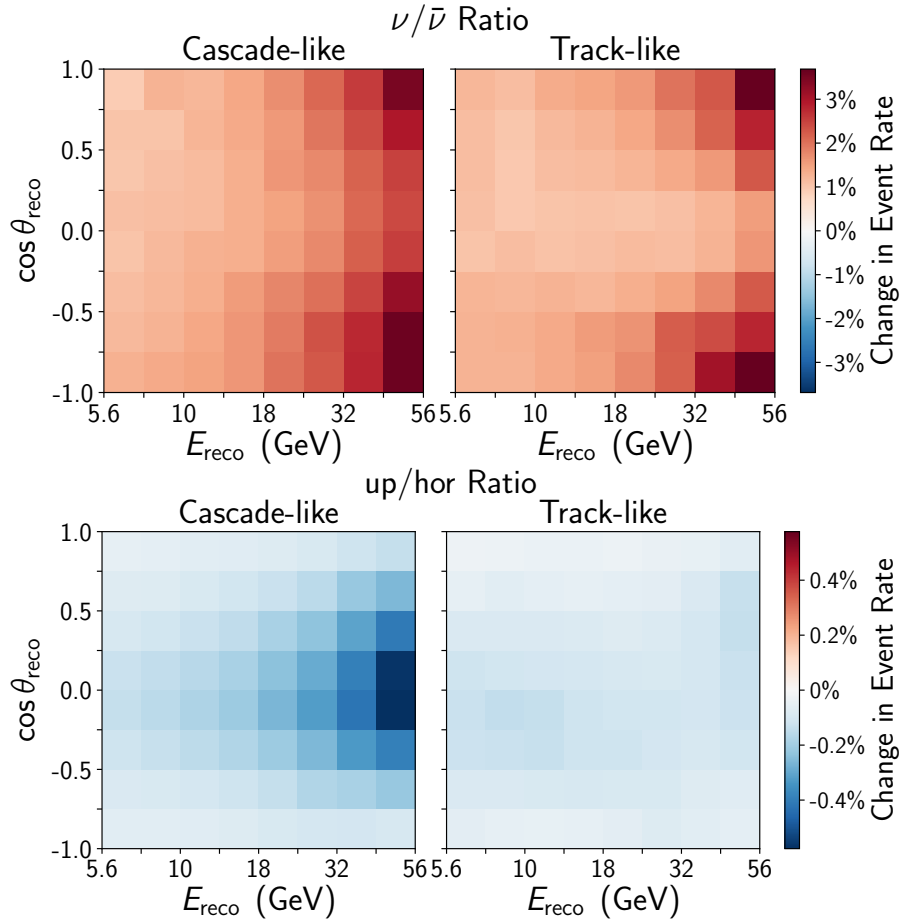


Figure 7.2: Effect of $\nu/\bar{\nu}$ ratio and up/hor ratio uncertainties on the nominal event distribution shown as a percentage change.

7.3 Neutrino Interaction Systematics

M_A^{CCQE} and M_A^{RES} are the axial mass form factors for charged-current quasi-elastic (CCQE) events and resonance (RES) events. A change in their values will change the number of CCQE and RES events, thus changing the final event histogram.

GENIE [64] is the software framework used for simulating event interactions which includes the cross section models. It provides a re-weighting package [99] that allows modifications of the event weights by changing a scale factor for the standard deviation of each parameter.

The nominal value of M_A^{CCQE} is 0.99 GeV with a standard deviation of $(-0.1485, +0.2475)$ GeV. The nominal value of M_A^{RES} is 1.12 GeV with a standard deviation

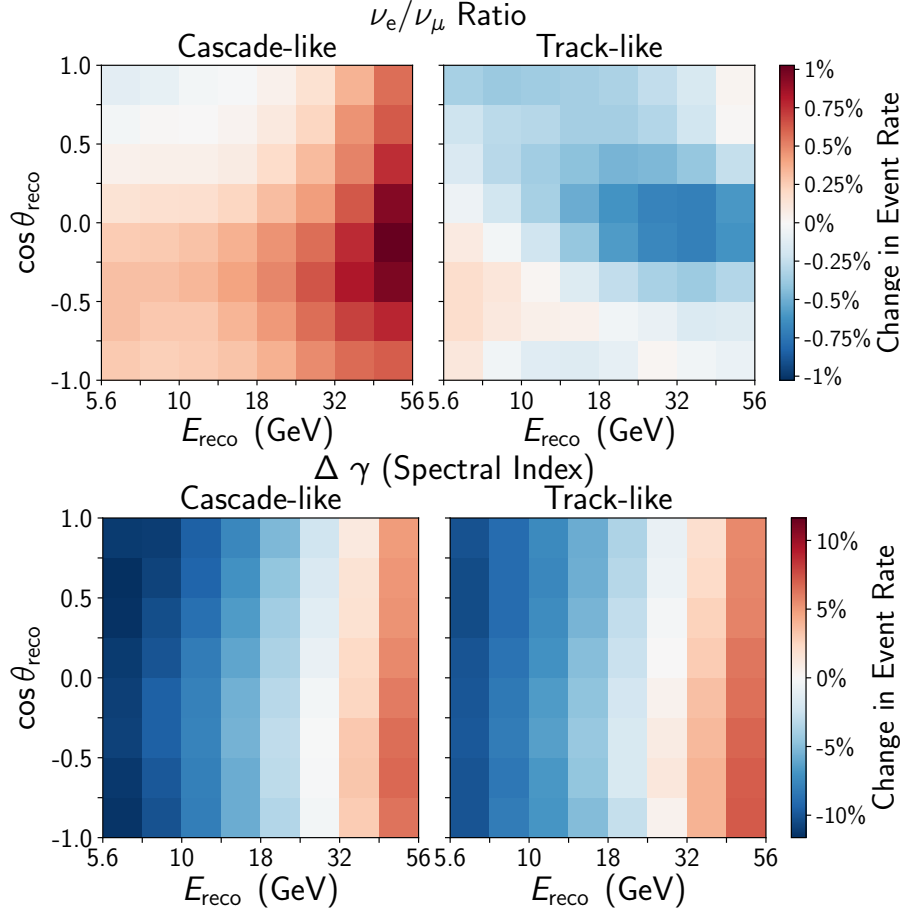


Figure 7.3: Effect of ν_e/ν_μ flux ratio and $\Delta\gamma$ uncertainties on the nominal event distribution shown as a percentage change.

of ± 0.22 GeV.

Figure 7.5 shows the effect of the two systematics at one σ above their nominal values. Their effects are small, which is expected because the lower bound of the energy range of our sample is 5.6 GeV, at higher energies, the contribution of CCQE and RES are much smaller than that from DIS, see Fig. 3.5 in Section 3.2.1. We know the contribution of CCQE and RES are small compared to deep inelastic scattering (DIS).

As for DIS related parameters, several parameters used in Bodek-Yang (BY) model are also available in GENIE. Their effects on the analysis are also evaluated, but they are so small that they are not used.

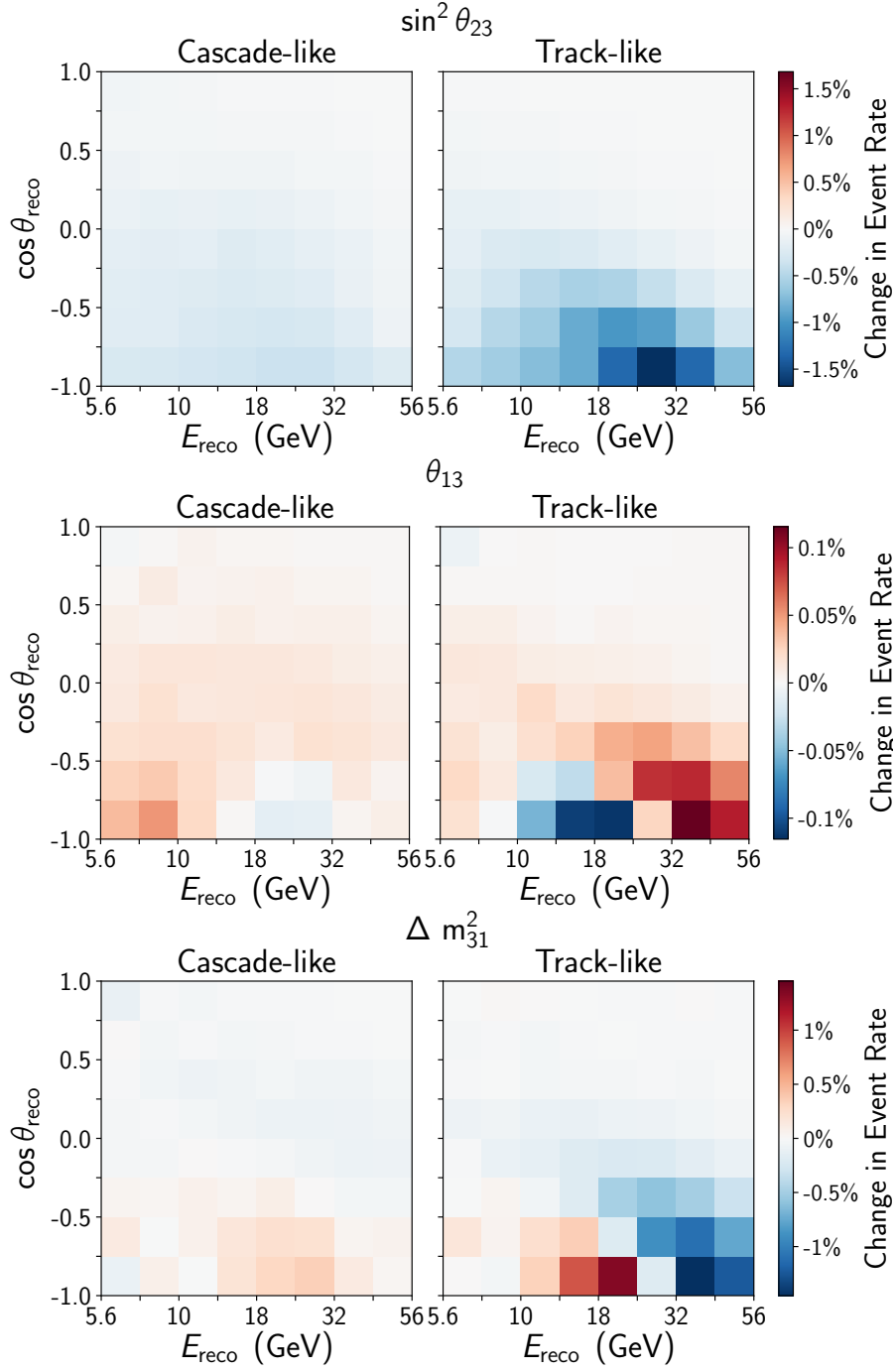


Figure 7.4: The effect on the event distribution when setting θ_{23} at 43.1° instead of 41.6° , θ_{13} at 8.705° instead of 8.5° , and Δm_{31}^2 at $2.56 \times 10^{-3} \text{ eV}^2$ instead of $2.52 \times 10^{-3} \text{ eV}^2$.

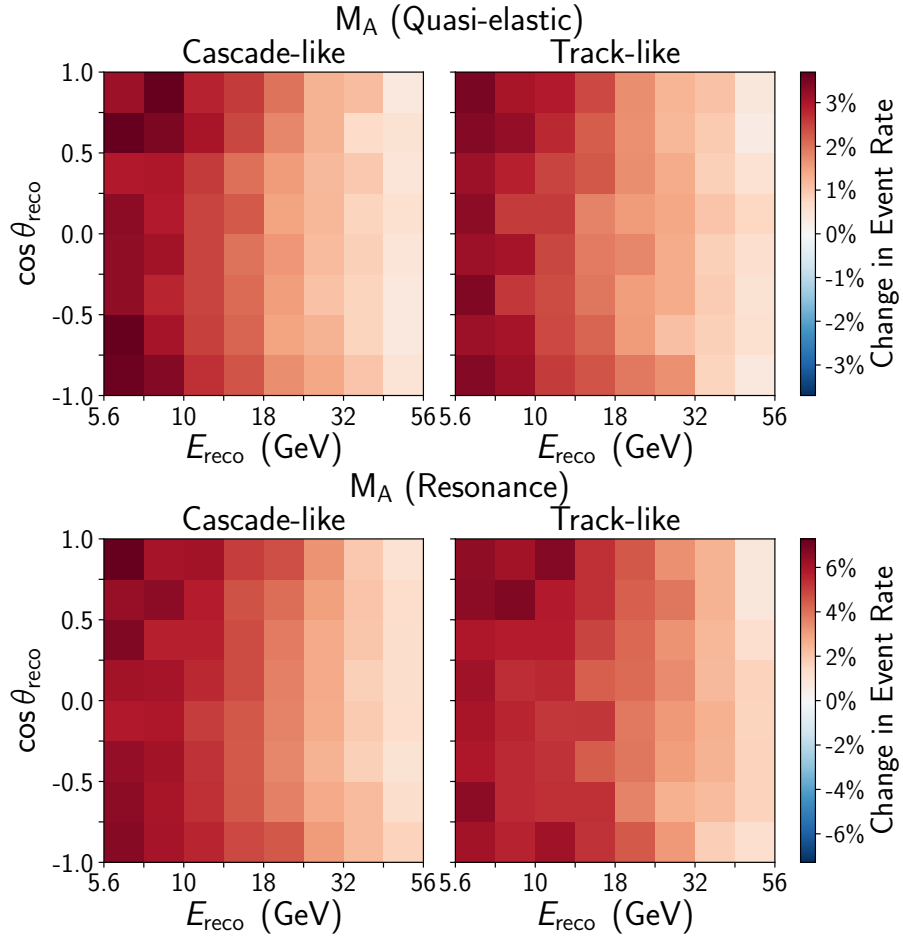


Figure 7.5: Effect of $+1\sigma M_A^{\text{RES}}$ and $+1\sigma M_A^{\text{CCQE}}$ on the nominal event distribution.

7.4 Detector-Related Systematics

7.4.1 DOM Optical Efficiency

DOM efficiency is the systematic overall optical efficiency. Its prior is a Gaussian prior of 10%, which is its uncertainty estimated from doing calibrations [46]. The impact of a +10% *DOM efficiency* on the event distribution is shown in Fig. 7.10 (bottom).

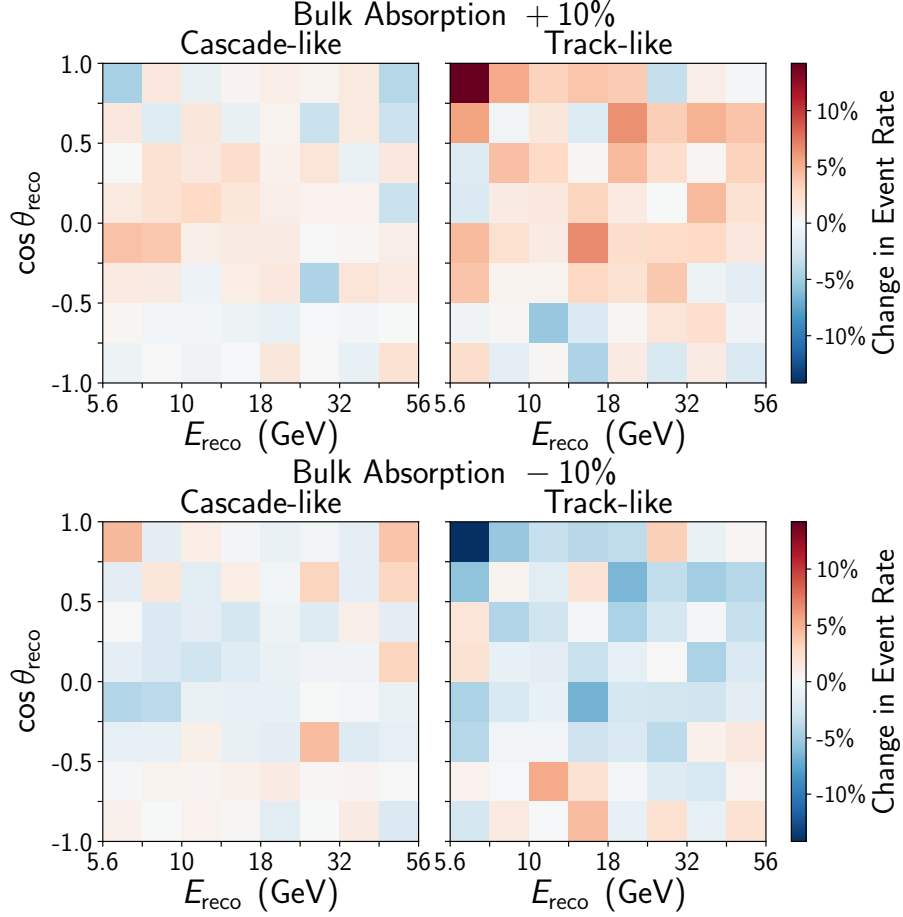


Figure 7.6: Effect of bulk ice absorption on the nominal event distribution.

7.4.2 Ice Properties

7.4.2.1 Bulk Ice

As described in Section 3.3, the bulk ice model uses two parameters: effective absorption coefficient, a_e (400 nm) and scattering coefficient, b_e (400 nm). The uncertainties on these parameters are referred to as bulk ice scattering and bulk ice absorption. Four systematics sets are available: the baseline set, a change of +10% for scattering, +10% for absorption, and a change of -7% for both scattering and absorption. The Gaussian priors used for them are 10%. The impact of a +10%(-10%) change in the two parameters on the event distributions are shown in Fig. 7.6 and Fig. 7.7.

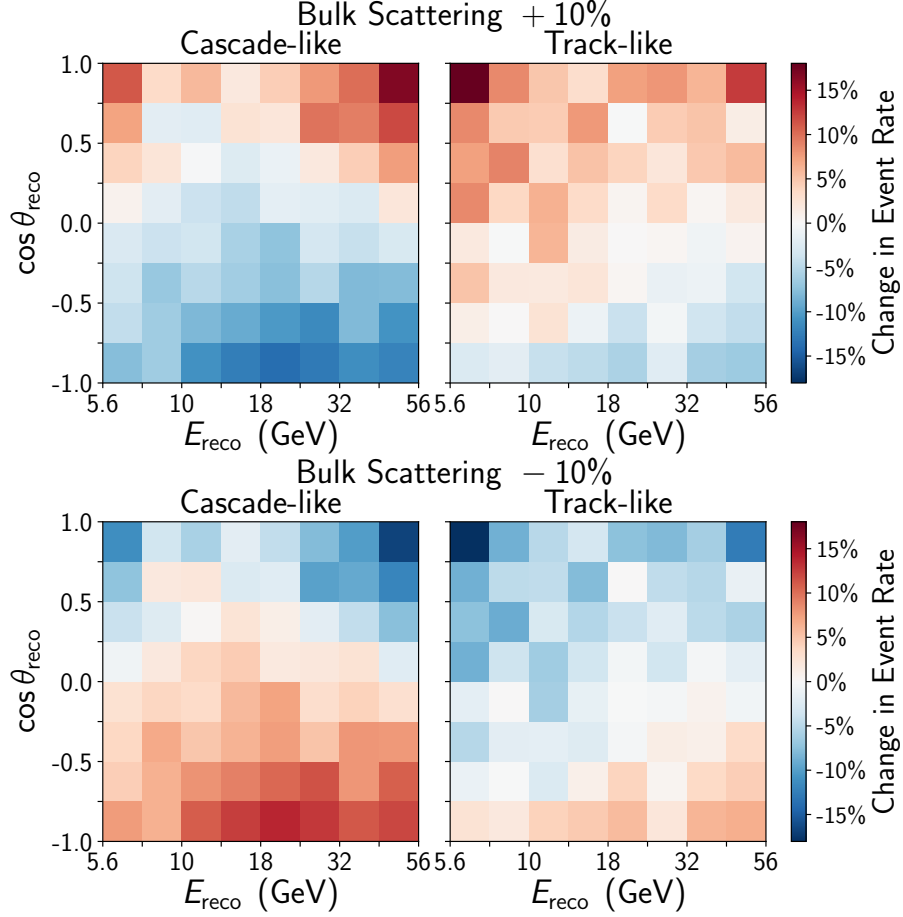


Figure 7.7: Effect of bulk ice scattering on the nominal event distribution.

7.4.2.2 Hole Ice

Hole ice is the refrozen column of ice in which the DOMs are embedded. Figure 7.8 is a simple sketch explaining hole ice and bulk ice. Hot water was used to drill the hole. The water contains air, and when the water refreezes, there are residual air bubbles left in the refrozen ice. The existence of air bubbles makes the hole ice more scattering than the bulk ice, thus affecting the amount of light the DOMs receive. Several qualitative measurements were done in AMANDA [100]. IceCube uses flasher board data and also deploys bubble cameras designed to gather information on the hole ice column. The Swedish Camera [101] is the second generation of bubble cameras. They were first deployed in 2010, but stopped working in 2018.

Generally speaking, there are three generations of hole ice models used in IceCube. The H2 model is one of the earliest models [62]. The parameter used in the

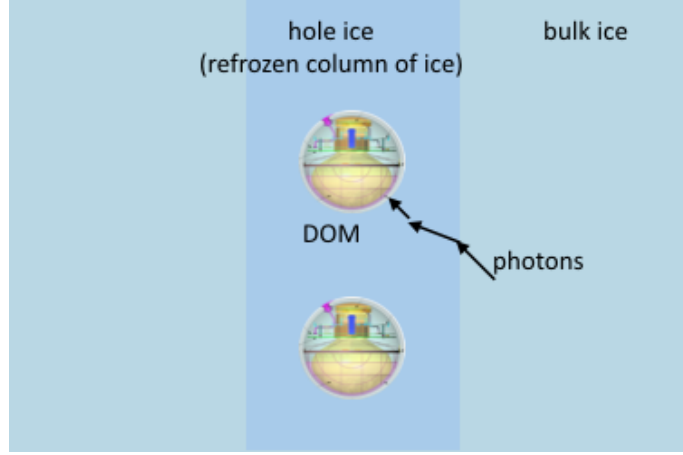


Figure 7.8: Sketch of hole ice.

H2 model is the scattering length of the bubble column. The baseline H2 model's scattering length is 50 cm. The other three values are 30 cm, 100 cm, and infinity (*i.e.*, no scattering). The parametrization of the H2 model is done through fitting to the angular acceptance curves of the DOMs. The angular acceptance is the probability for a photon to be accepted by a DOM based on its arrival direction relative to the DOM surface. In Fig. 7.9, η is the arrival direction. Photons with $\cos(\eta) = 1$ have an upward-going direction going towards the DOM.

The H2 model assumes that the entire hole ice column is full of the scattering air bubbles, which is likely wrong because according to the Swedish Camera's observations, the air bubbles accumulate around the center of the hole ice column instead of filling the whole column.

A second generation model developed by D. Chirkin (named "Dima's model") uses flasher data to apply changes in the sensitivity curves of DOMs. It uses a new parameter p instead of using the traditional scatter coefficient used in the H2 model. This parameter p does not have a physical meaning, and we refer to it as the *hole ice* parameter. The parametrization of the acceptance curves is:

$$0.34(1 + 1.5 \cos \eta - \cos^3 \eta / 2) + p \cdot \cos \eta (\cos^2 \eta - 1)^3. \quad (7.2)$$

This parameter's nominal value is 0.25. In Fig. 7.9(a), we see in the forward region of the DOM that there is a discrepancy between the Dima model sensitivity curves and the H2 curves. Each model's uncertainties are not able to cover the

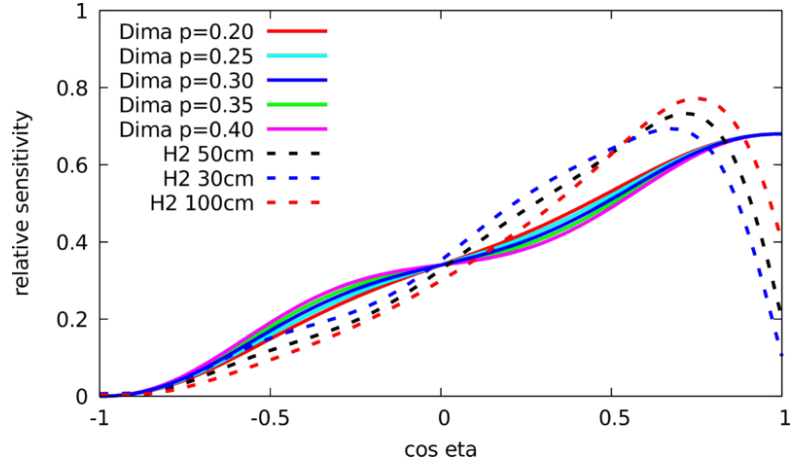
other model. To bridge the gap, a new parameter $p2$ is developed [102]. It simply adds an exponential term to the Dima model parametrization:

$$0.34(1 + 1.5 \cos \eta - \cos^3 \eta/2) + p \cdot \cos \eta (\cos^2 \eta - 1)^3 + p2 \cdot \exp(10(\cos \eta - 1.2)). \quad (7.3)$$

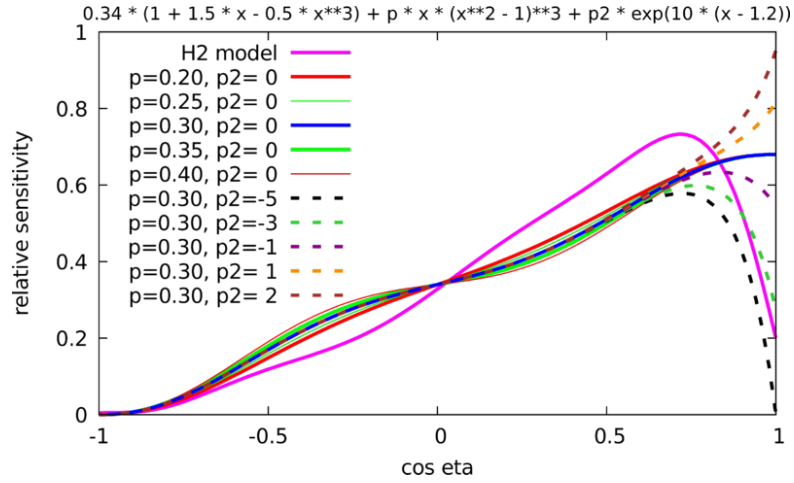
The parameter $p2$ ranges from -5 to 2 , with 0 being the nominal case. It is referred to as the *hole ice forward* parameter. We use a uniform prior for it, because we don't know what it should be, so let the actual final data fit to tell us its best fit value.

Figure 7.9 (b) shows the comparison of the two models in the acceptance curves. We see that using the Dima model combined with the forward parameter, we can cover the forward region from the H2 model up to the Dima model very well.

The SpiceHD [103] model is the newest hole ice model that uses direct propagation of photons in the bubble column, developed by M. Rongen. The fits are done with parameters such as the radius of the bubble column, scattering length, and individual DOM positions to compare the simulated flasher data to the real flasher data. It does not implement changes in the DOM angular acceptance curves like the H2 or Dima models, so it's not shown in the acceptance curve plots. The SpiceHD model is still undergoing development. At the time of the study, several SpiceHD systematics sets were available. During one statistics test where SpiceHD is used as pseudo data and fitted with the regular systematics sets (with the Dima model for hole ice), we observed a bias in the best fit ν_τ (CC + NC) normalization values. Thus, to disentangle the difference between the SpiceHD and Dima models and the ν_τ (CC+NC) signal, the systematic *spiciness* is used to give a transition between the two. It is not a physical parameter. All systematics sets created with the Dima model are assigned zero, and the six systematic sets with SpiceHD are assigned one. Similar to other discrete systematics, *spiciness* is added as an extra dimension to the hyperplane fitting method. Also, similar to *hole ice forward*, we use a uniform prior for it and let the final data fit tell us its best fit value. A *spiciness* close to zero means the data is better described by the Dima model, a *spiciness* close to one means the data is better described by the SpiceHD model.



(a) Comparison of the H2 and the Dima model



(b) Dima model with the *hole ice forward* parameter p_2 .

Figure 7.9: Relative sensitivity as a function of the arrival direction of photons $\cos(\eta)$. (a) shows the comparison between the H2 model and the Dima model. (b) shows the change made on the Dima model by adding a forward parameter p_2 in an exponential term, allowing it to transition from to H2 model (at 50 cm) in the forward region. Figure taken from Ref. [102].

7.5 Normalization Systematics

Figure 7.12 shows the percent change on the event distribution by shifting the ν NC normalization by $+1\sigma$. The effective lifetime is the overall scale factor applied to every event, so its effect is uniform. The ICC background provides the shape estimation for background, and the *atmospheric μ scale* parameter only scales it

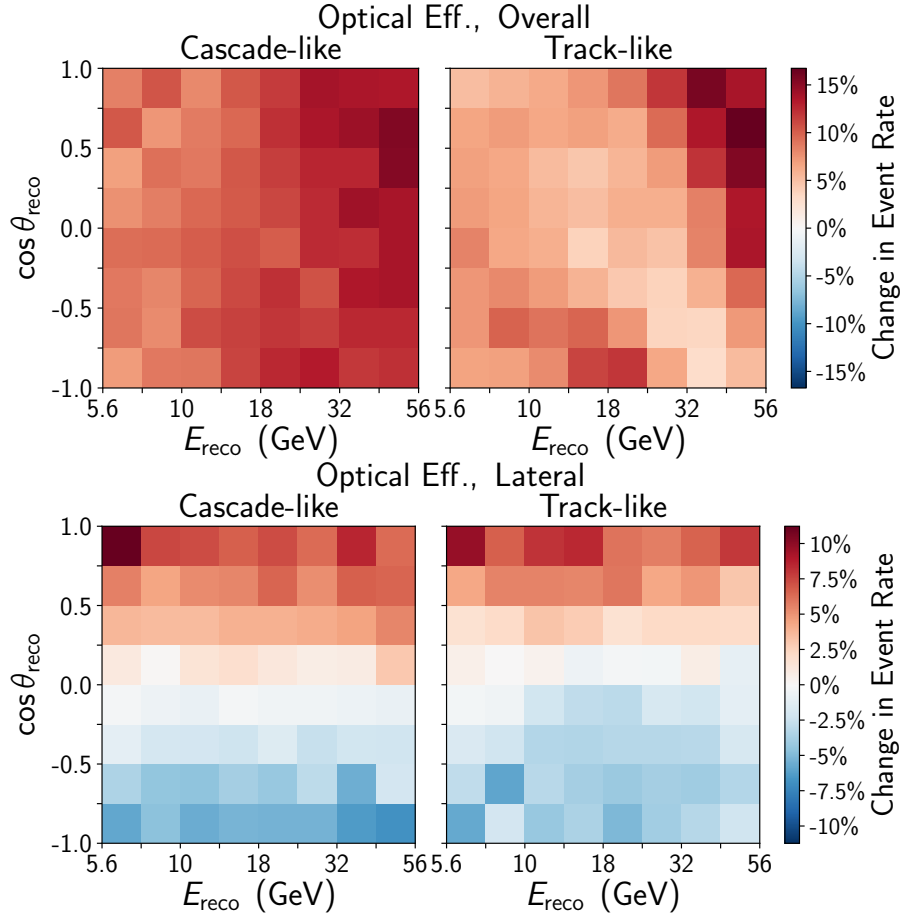


Figure 7.10: Top: Effect of DOM efficiency (overall optical efficiency) at 10% above nominal value on the nominal event distribution. Bottom: effect of *hole ice* (lateral optical efficiency).

up and down, so its effect on the event distribution is a uniform change on the μ background events.

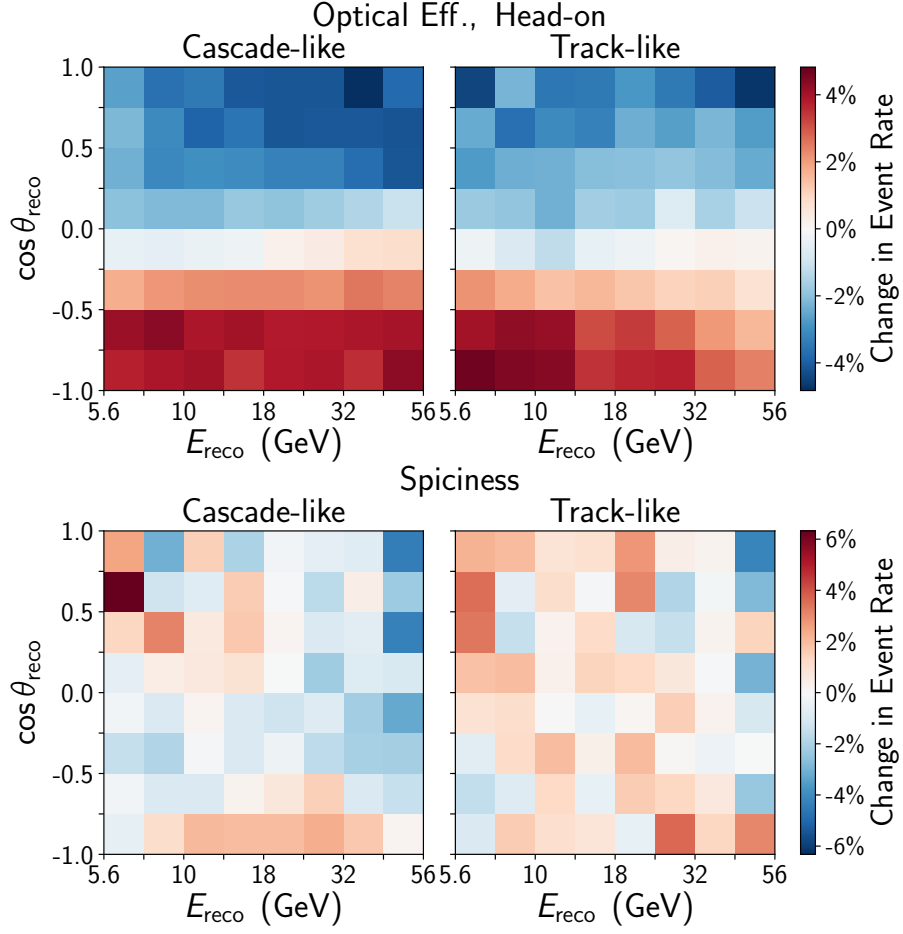


Figure 7.11: Effect of *hole ice forward* (head-on optical efficiency) and *spiciness* on the nominal event distribution.

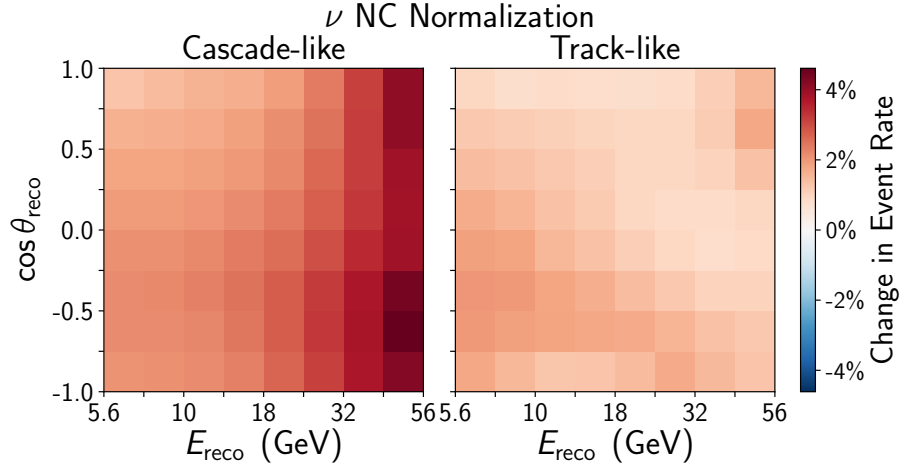


Figure 7.12: Effect of ν NC normalization at $+1\sigma$ on the nominal event distribution shown as a percentage change.

7.6 N-1 Test

The N-1 test is useful for testing the impact of the systematics on a measurement. There are different types of N-1 test. Here the hidden potential N-1 test is done, which checks how much better the result would be if we knew this parameter perfectly.

The procedure is as follows: First, generate pseudo data with the systematic fixed to the baseline value (or the value to the best of knowledge). Then, in the fitter, fix the systematic also to the baseline value. Last, perform fits and get results.

In the last step, we can either perform two fits (one at ν_τ (CC+NC) normalization at 1 and one at 0) to get the significance of the null hypothesis exclusion or do multiple ν_τ (CC + NC) normalization scans to get the sensitivity (see Section 6.5).

Table 7.1 shows the result ordered by the percentage change in the significance of the null hypothesis exclusion. The oscillation angle θ_{23} , three ice property related systematics, and ν NC normalization are the five most important ones.

Table 7.2 shows the result ordered by the percentage change in the ν_τ (CC+NC) normalization 1σ C.I.. We see the first five most important systematics are still the oscillation angle θ_{23} , ν NC normalization, and three ice property related systematics, although the order is slightly different.

	N-1 test (exclusion of null hypothesis)			
Systematics	$\Delta\chi^2$	Significance	Difference	Impact(%)
θ_{23}	16.92	4.11σ	0.37σ	9.8
<i>hole ice forward</i>	16.6	4.07σ	0.33σ	8.7
<i>bulk ice scattering</i>	15.81	3.98σ	0.23σ	6.1
<i>spiciness</i>	15.02	3.88σ	0.13σ	3.5
ν NC normalization	14.99	3.87σ	0.13σ	3.3
<i>DOM efficiency</i>	14.52	3.81σ	0.06σ	1.7
$\nu/\bar{\nu}$ ratio	14.2	3.77σ	0.02σ	0.6
atm. μ scale	14.14	3.76σ	0.01σ	0.4
nominal	14.04	3.75σ	0	0
<i>hole ice</i>	14	3.74σ	0	-0.1
$\nu/\bar{\nu}$ ratio	13.99	3.74σ	-0.01σ	-0.2
ν_e/ν_μ ratio	13.97	3.74σ	-0.01σ	-0.2
Δm_{31}^2	13.96	3.74σ	-0.01σ	-0.3
effective lifetime	13.95	3.73σ	-0.01σ	-0.3
M_A (resonance)	13.92	3.73σ	-0.01σ	-0.4
<i>up/hor</i> ratio	13.91	3.73σ	-0.02σ	-0.5
<i>bulk ice absorption</i>	13.87	3.72σ	-0.02σ	-0.6
M_A (quasi-elastic)	13.86	3.72σ	-0.02σ	-0.6
θ_{13}	13.82	3.72σ	-0.03σ	-0.8

Table 7.1: The $\Delta\chi^2$ column is the difference between the χ^2 at ν_τ (CC+NC) normalization = 0 and the best fit ν_τ (CC + NC) normalization (here =1). From Wilk's theorem, the sensitivity of excluding the null hypothesis is $\sqrt{\Delta\chi^2(\nu_\tau \text{ norm.} = 0)}$. The “nominal” row is the nominal case where none of the systematics are fixed, each the rest of the rows shows the result when fixing that systematic to its baseline value. We see that θ_{23} has the biggest impact.

	N-1 test (expected C.I.)			
Systematics	1 σ Range	Avg 1 σ Range	Difference	Impact(%)
<i>hole ice forward</i>	(0.73, 1.29)	0.28	-0.05	-14.9
<i>bulk ice scattering</i>	(0.72, 1.31)	0.3	-0.03	-9.4
<i>spiciness</i>	(0.71, 1.32)	0.3	-0.02	-7.3
ν NC normalization	(0.71, 1.33)	0.31	-0.02	-4.7
θ_{23}	(0.71, 1.34)	0.32	-0.01	-3.3
Δm_{31}^2	(0.70, 1.34)	0.32	-0.01	-2.5
$\nu/\bar{\nu}$ ratio	(0.70, 1.34)	0.32	-0.01	-1.7
<i>DOM efficiency</i>	(0.70, 1.35)	0.32	0	-1.1
$\Delta\gamma$	(0.70, 1.35)	0.33	0	-0.9
atm. μ scale	(0.70, 1.35)	0.33	0	-0.7
effective lifetime	(0.70, 1.35)	0.33	0	-0.3
<i>bulk ice absorption</i>	(0.69, 1.35)	0.33	0	-0.1
M_A^{CCQE}	(0.69, 1.35)	0.33	0	-0.1
ν_e/ν_μ ratio	(0.69, 1.35)	0.33	0	-0.1
<i>up/hor</i> ratio	(0.69, 1.35)	0.33	0	-0.1
M_A^{RES}	(0.69, 1.35)	0.33	0	0
nominal	(0.69, 1.35)	0.33	0	0
<i>hole ice</i>	(0.69, 1.35)	0.33	0	0
θ_{13}	(0.69, 1.35)	0.33	0	0.1

Table 7.2: The 1 σ Range column is the 1 σ range for ν_τ (CC + NC) normalization using Wilk’s theorem. Avg 1 σ Range is the average of the 1 σ range. The Impact column shows the percentage change in the average 1 σ C.I., the values are ordered from the biggest impact to the smallest. The “nominal” row is the nominal case where none of the systematics are fixed, each the rest of the rows shows the result when fixing that systematic to its baseline value. Fixing *hole ice forward* makes the 1 σ C.I. shrink by 14.9%.

Chapter 8 |

Analysis Results

This chapter discusses the analysis results.

8.1 ν_τ Normalization

Figure 8.1 shows the measured ν_τ (CC+NC) normalization and ν_τ CC normalization in comparison with the two previous experiments. The best fit ν_τ (CC+NC) normalization is 0.59 with the 68% C.I. being [0.34, 0.90], *i.e.*, $0.59^{+0.31}_{-0.25}$. The 90% C.I. is [0.18, 1.12]. We do not show a combined result here because it's not trivial to do so since the systematics used in each experiment are different. Super-K and IceCube/DeepCore have some common systematics, but the two experiments look for neutrinos in different energy regions.

The best fit value of ν_τ CC normalization is 0.43, with the 68% C.I. being [0.12, 0.80], *i.e.*, $0.43^{+0.36}_{-0.43}$. The 90% C.I. is [0, 1.07]. Thus, the measurement is consistent with the standard oscillation theory at 90% C.L. Super-K's 68% C.I. for ν_τ CC normalization is 1.47 ± 0.32 and OPERA's is: $1.1^{+0.5}_{-0.4}$.

The significance of excluding the no- ν_τ -appearance hypothesis is 2.5σ in the ν_τ (CC+NC) normalization fit. The significance to exclude the no- ν_τ CC-appearance is 1.4σ .

8.2 Best Fit Parameters

Table 8.1 shows the best fit parameters under both fits. Most of the nuisance parameters have an associated prior; their central value and $\pm 1\sigma$ ranges are listed

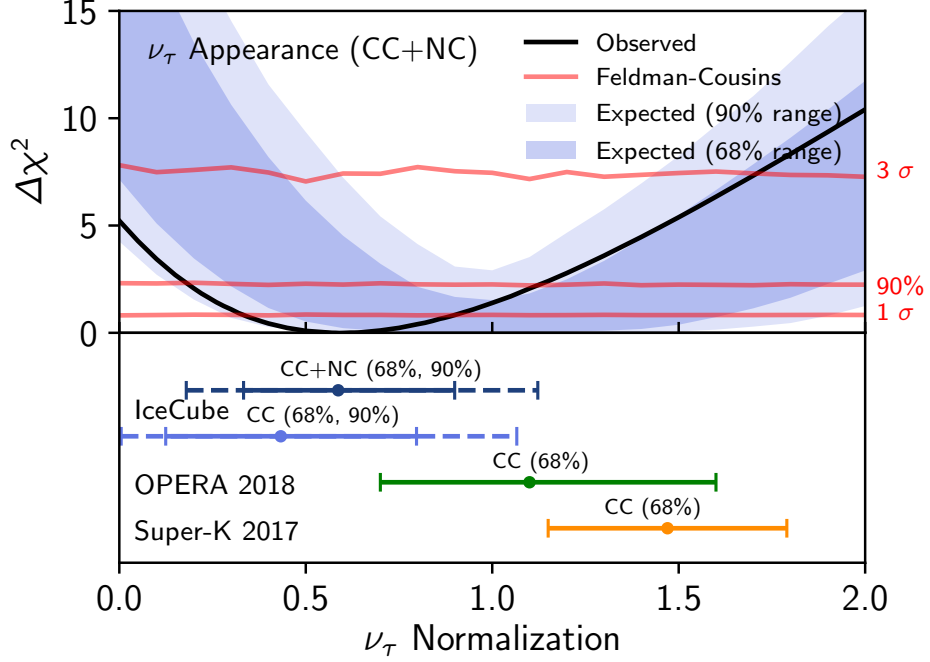


Figure 8.1: Result of the tau neutrino appearance measurement with three years of IceCube/DeepCore data. Red lines are the $\Delta\chi^2$ values obtained based on the ordering principle of Feldman-cousins construction. The x axis is the injected ν_τ (CC + NC) normalization value used in generating pseudo data. At each ν_τ (CC + NC) normalization value, roughly 30,000 fits are performed. The resulting $\Delta\chi^2$ values are ordered from smallest to largest, then we find the value below which the cumulative area of this ordered $\Delta\chi^2$ distribution is 68% (1 σ), 90% and 99.73% (3 σ). The black line is the measured $\Delta\chi^2$ at each ν_τ (CC + NC) normalization scan. The intersection of the black line and the $\Delta\chi^2 = 0$ is the best fit value. Note that the 3 σ line is not very smooth, because the number of total fits is 30,000, 3 σ corresponds to a percentage of 99.73%, so there are on average only $(0.27\% \times 30,000 =)$ 81 points beyond the 3 σ line at the tail of the ordered $\Delta\chi^2$ distribution.

in the Prior column.

As mentioned in Section 6.3, two oscillation parameters are left floating freely with a uniform prior. The best fit values for θ_{23} are 46.1° and 45.9° , respectively. Thus, the result prefers maximal mixing. Convert to $\sin^2(\theta_{23})$, the best fit values are 0.519 and 0.516.

In the fitter, Δm_{31}^2 is allowed to be either positive or negative, *i.e.*, each one

fit performs fits under both assumptions and only returns the better fit. Table 8.1 shows the best fit values for Δm_{32}^2 with $\Delta m_{21}^2 = 7.5 \times 10^{-5} \text{ eV}^2$.

The best fit values of Δm_{32}^2 are $2.38 \times 10^{-3} \text{ eV}^2$ and $2.34 \times 10^{-3} \text{ eV}^2$. Their values being positive means that normal hierarchy is preferred (though only slightly).

Table 8.1: The best fit results for all parameters.

Parameter	Prior	Best fit (CC+NC)	Best fit (CC)
Flux			
ν_e/ν_μ ratio	1.0 ± 0.05	1.03	1.03
up/hor ratio (σ)	0.0 ± 1.0	-0.25	-0.24
$\nu/\bar{\nu}$ ratio (σ)	0.0 ± 1.0	0.01	0.04
$\Delta\gamma$ (spectral index)	0.0 ± 0.1	-0.050	-0.041
Neutrino Interaction			
M_A (quasi-elastic) (GeV)	$0.99_{-0.149}^{+0.248}$	0.88	0.88
M_A (resonance) (GeV)	1.12 ± 0.22	0.85	0.85
Oscillation			
θ_{13} ($^\circ$)	8.5 ± 0.21	8.5	8.5
θ_{23} ($^\circ$)	-	46.1	45.9
Δm_{32}^2 (10^{-3} eV^2)	-	2.38	2.34
Detector			
bulk ice scattering	$0.0 \pm 10\%$	-2.6%	-2.7%
bulk ice absorption	$0.0 \pm 10\%$	2.1%	1.9%
DOM efficiency (%)	100 ± 10	105	104
hole ice (σ)	0.0 ± 1.0	-0.25	-0.27
hole ice forward (a.u.)	-	-1.15	-1.22
spiciness	-	0.02	0.07
normalization			
ν NC normalization	1.0 ± 0.2	1.25	1.26
effective lifetime (yr)	-	2.45	2.46
Atm. μ fraction	-	4.6%	4.6%
Measurement			
ν_τ normalization	-	0.59	0.43

The “Atm. μ fraction” is the ratio of the number of atmospheric μ events to the number of total events. In the fit, the parameters “Atm. μ scale” (see Section 7.5) is used as the scale factor applied on the atmospheric muon background template. Here “Atm. μ fraction” is shown as it is a more physically meaningful value to understand.

In the fit, Δm_{31}^2 is used, but here in the table, we show Δm_{32}^2 because Δm_{32}^2

is more frequently used in neutrino oscillation measurements and we can compare with their measurements. Since we fix the value of Δm_{21}^2 in the fit, it is a simply calculation: $\Delta m_{32}^2 = \Delta m_{31}^2 - \Delta m_{21}^2$, where $\Delta m_{21}^2 = 7.5 \times 10^{-5} \text{ eV}^2$.

As mentioned before, this event sample was originally developed for the ν_μ disappearance, here we want to compare the best fit values for the two oscillation parameters in the ν_μ measurement and this ν_τ measurement. The best fit value for Δm_{32}^2 in the ν_μ disappearance measurement [15] (where ν_τ (CC + NC) normalization is fixed to unity) was $2.31_{-0.13}^{+0.11} \times 10^{-3} \text{ eV}^2$ [15], with which our best fit value $2.38 \times 10^{-3} \text{ eV}^2$ is compatible. Both slightly prefer the normal hierarchy. The best fit value of $\sin^2(\theta_{23})$ in the ν_μ disappearance measurement [15] was $0.51_{-0.09}^{+0.07}$, with which our best fit value 0.519 is also compatible.

Note that, because of the apparent difference in treating ν_τ normalization and other differences like some systematics were not present in the ν_μ measurement, we don't expect to measure the same values for every parameter, but we expect them to be compatible with each other, and we have observed compatible values.

8.3 Good Runs

Three years of data are used. When selecting good data runs to use in the analysis, we use the following criteria: First, each run livetime must be ≥ 1 hour. Second, the number of active strings must be equal to 86. Third, the number of active DOMs must be larger than 5380. Table 8.2 shows the livetime of the good runs in each year using the above criteria. The total livetime is $8.83 \times 10^7 \text{ s}$, equivalent to 1022.0 days. Note, this livetime is not used in the fit, it is just the total livetime of events that pass the good run selection mentioned above. We use an overall normalization scale factor as a systematic, which scales all the events up and down, and finally convert it to an effective lifetime of 2.45 (2.46) years in our best fit.

8.4 Goodness of Fit

The minimized raw fit statistic χ^2 (defined in Section 6.3) is 113.26 for the ν_τ (CC+NC) normalization fit, and 112.79 for the ν_τ CC normalization fit. Figure. 8.2 shows the distributions from MC fits and the χ^2 values for each data fit. For the

Table 8.2: The livetime for each year.

Year	Livetime
2012	$2.80 \cdot 10^7$ s
2013	$2.96 \cdot 10^7$ s
2014	$3.07 \cdot 10^7$ s
Total	$8.83 \cdot 10^7$ s

CC+NC fit, the probability of getting a χ^2 larger than 113.26 is $P(\chi^2 \geq 113.26) = 20.3\%$, indicating that the fit is a good one. Similarly, for the CC-only fit, the probability of getting a χ^2 larger than 112.79 is $P(\chi^2 \geq 112.79) = 21.5\%$.

8.5 Number of Events Expected (After Fit)

Table 8.3 shows the number of events for each flavor and interaction type expected at final level after the fit. The number of expected ν_τ events is 1379. The total number of expected events (including both neutrinos and atmospheric muons) is 40,959, which is within statistical fluctuation with the number of events actually observed (40,902). Table 8.4 shows the number of events for the ν_τ CC normalization fit. The expected numbers of ν_τ CC (691) and ν_τ NC (764) events are different from the CC+NC fit (with ν_τ CC at 934 and ν_τ NC at 445) because the best fit normalization factor in CC fit is smaller than that in the CC+NC fit.

8.6 Event Distributions

Figure 8.3, Fig. 8.4, and Fig. 8.5 show the L/E distributions comparing best fit and data. Fig. 8.6 and Fig. 8.7 are the distributions of reconstructed energy, $\cos \theta_{\text{zen}}$ and PID after fit (for CC+NC). Figures 8.8 and 8.9 are the background-subtracted event distributions. In figures for the ν_τ (CC + NC) normalization fit, the ν_τ CC and ν_τ NC events are shown in red and orange colors, respectively. In figures for the ν_τ CC normalization fit, the ν_τ CC events are shown in red.

Figures 8.10 through 8.15 are distributions of the 11 BDT input variables (Section 5.4). Note that we do not expect very good agreement for these variables, because most of them are low level variables except the three track reconstruction best fit variables.

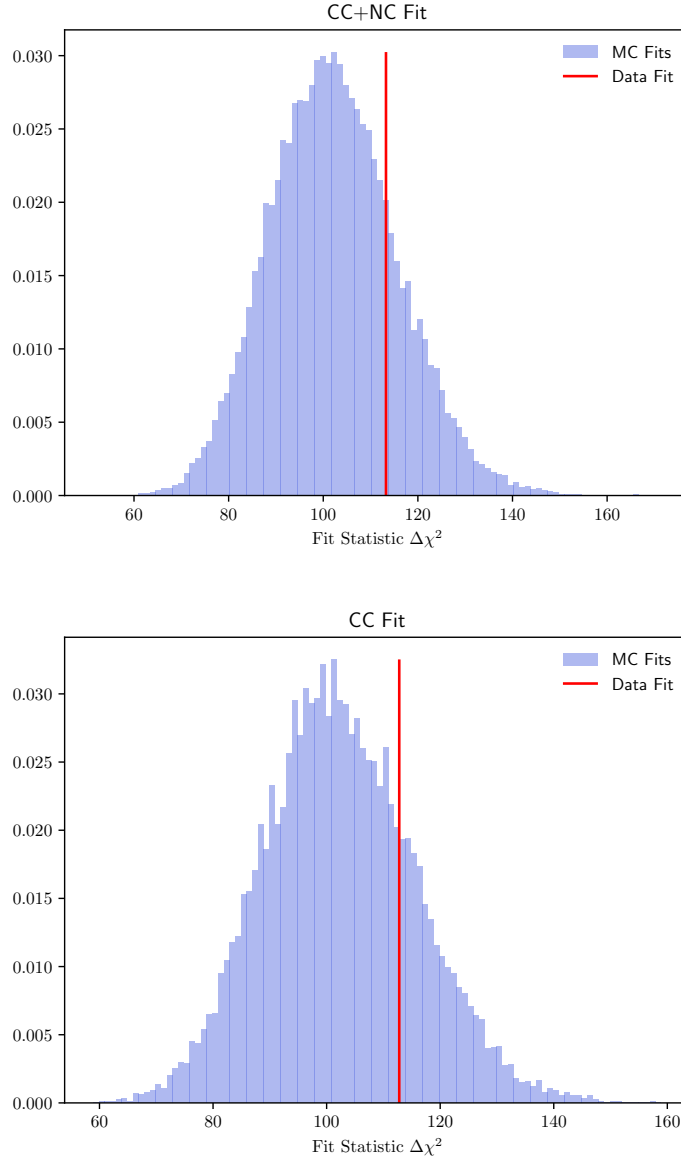


Figure 8.2: Distributions of the fit statistic χ^2 from MC fits and the χ^2 values from the data fits. Top: ν_τ (CC + NC) normalization fit. Bottom: ν_τ CC normalization fit. The blue histogram is the distribution from doing fits with Poisson-fluctuated baseline MC (with ν_τ (CC + NC) normalization or ν_τ CC normalization set to 1) as the pseudo data. The red line is the location of the minimized χ^2 value after doing the fits with data.

Table 8.3: Number of Events from ν_τ (CC + NC) normalization fit.

CC+NC best fit	Number of Events	Uncertainty
ν_e CC	9545	23
ν_e NC	923	8
ν_μ CC	23852	39
ν_μ NC	3368	17
ν_τ CC	934	5
ν_τ NC	445	4
Atm. μ	1889	45
Total Expected	40959	68
Data	40902	202

The number of events expected for each flavor and interaction type from the ν_τ (CC + NC) normalization fit. The uncertainties for muons and data are Poisson errors. The uncertainties for the six ν channels are the Monte Carlo uncertainties. The amount of ν events simulated are equivalent to 30 years of data, they are scaled to roughly three years in the fit, that's why their uncertainties are much smaller than what we expect from Poisson errors.

Table 8.4: Number of Events from ν_τ CC normalization fit.

CC-only best fit	Number of Events	Uncertainty
ν_e CC	9510	23
ν_e NC	930	9
ν_μ CC	23782	39
ν_μ NC	3398	17
ν_τ CC	691	4
ν_τ NC	764	7
Atm. μ	1882	45
Total Expected	40962	68
Data	40902	202

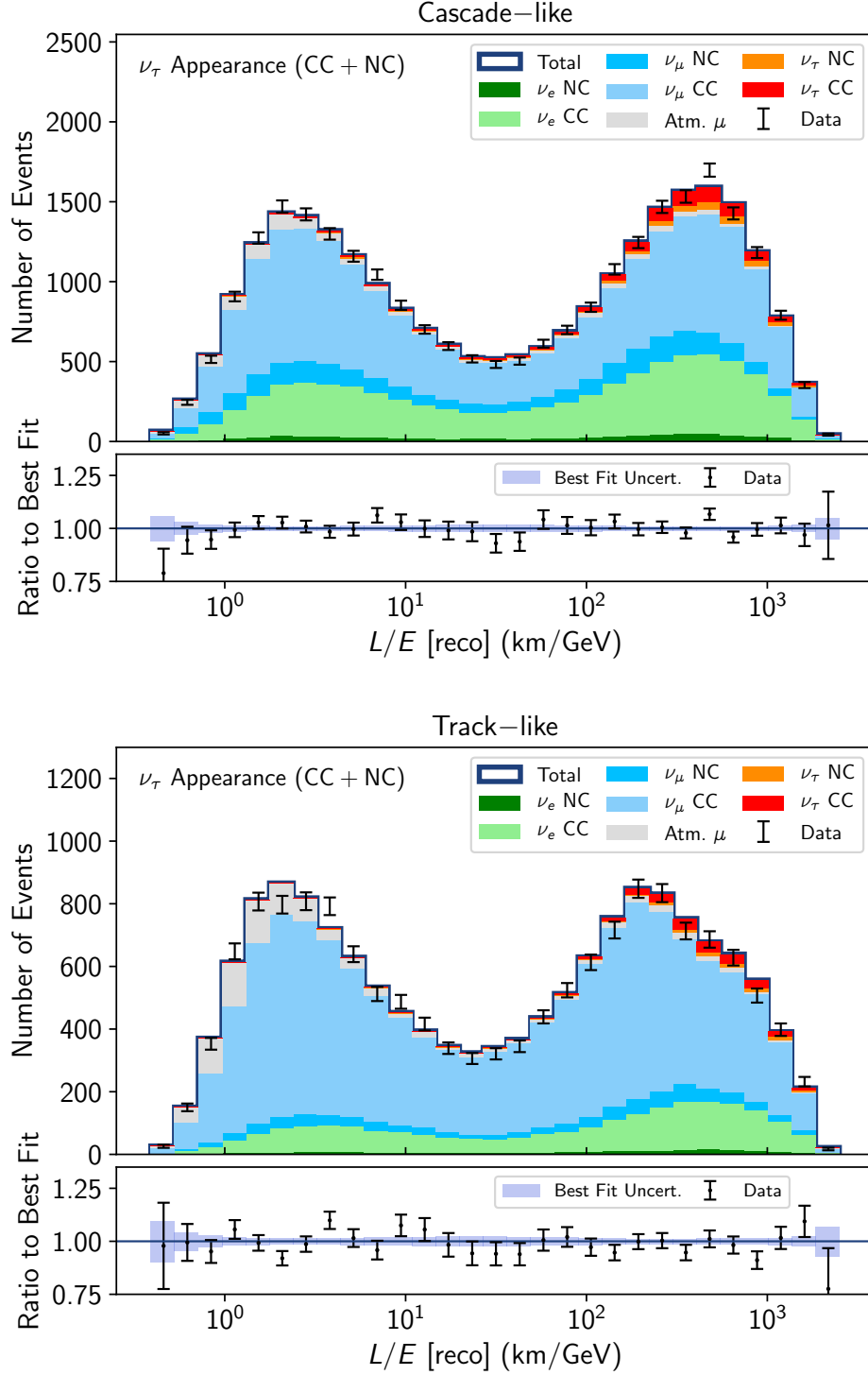


Figure 8.3: Top: L/E plot for cascade-like events. Bottom: L/E plot for track-like events. Both are after the ν_τ (CC + NC) normalization fit. Signal ν_τ CC and ν_τ NC are shown in red and orange, respectively. The ratio of data to best fit is shown in the lower part of each figure.

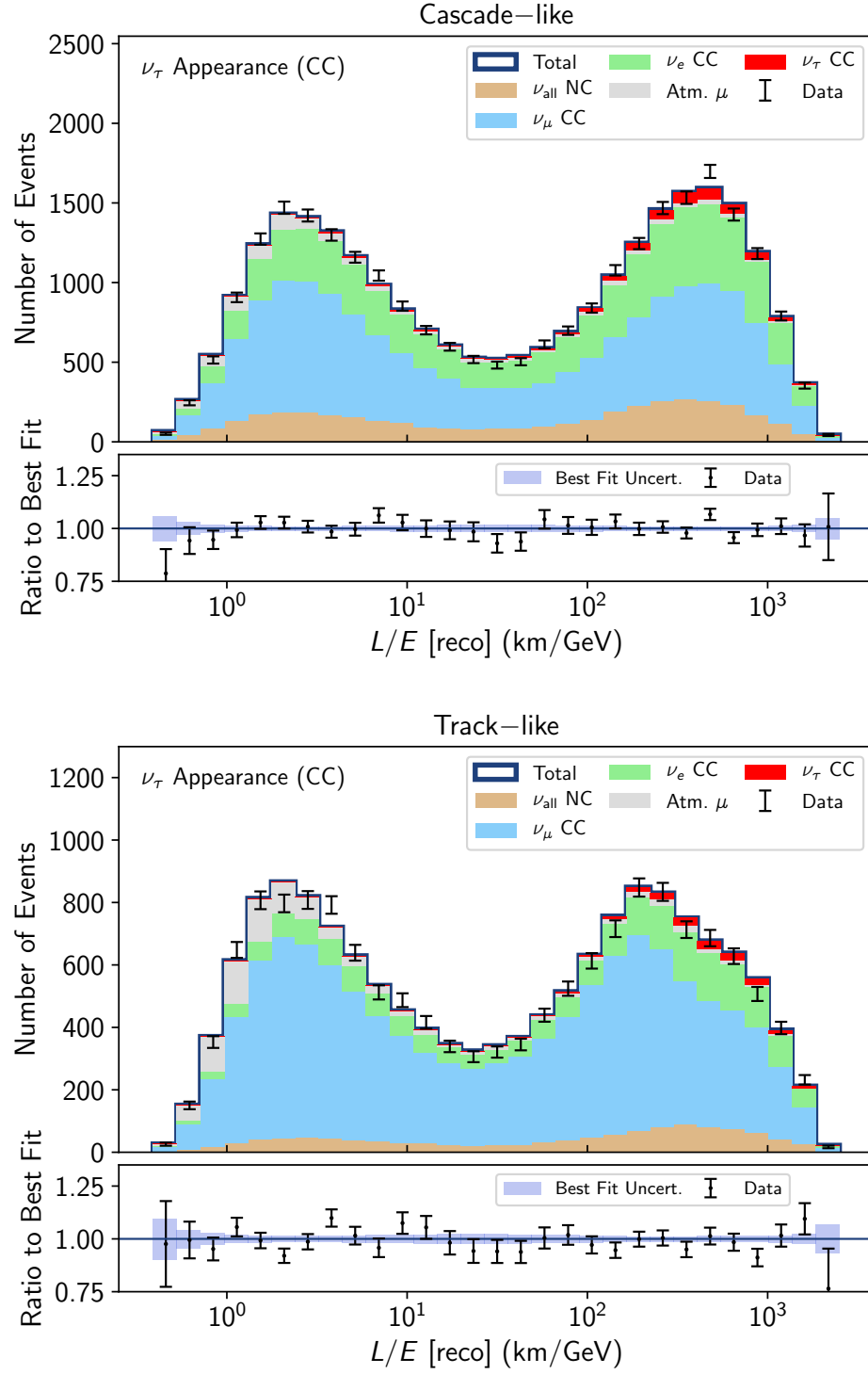


Figure 8.4: Top: L/E plot for cascade-like events. Bottom: L/E plot for track-like events. Signal ν_τ CC is shown in red. The other three colors are ν_μ CC, ν_μ NC, and ν_{all} NC.

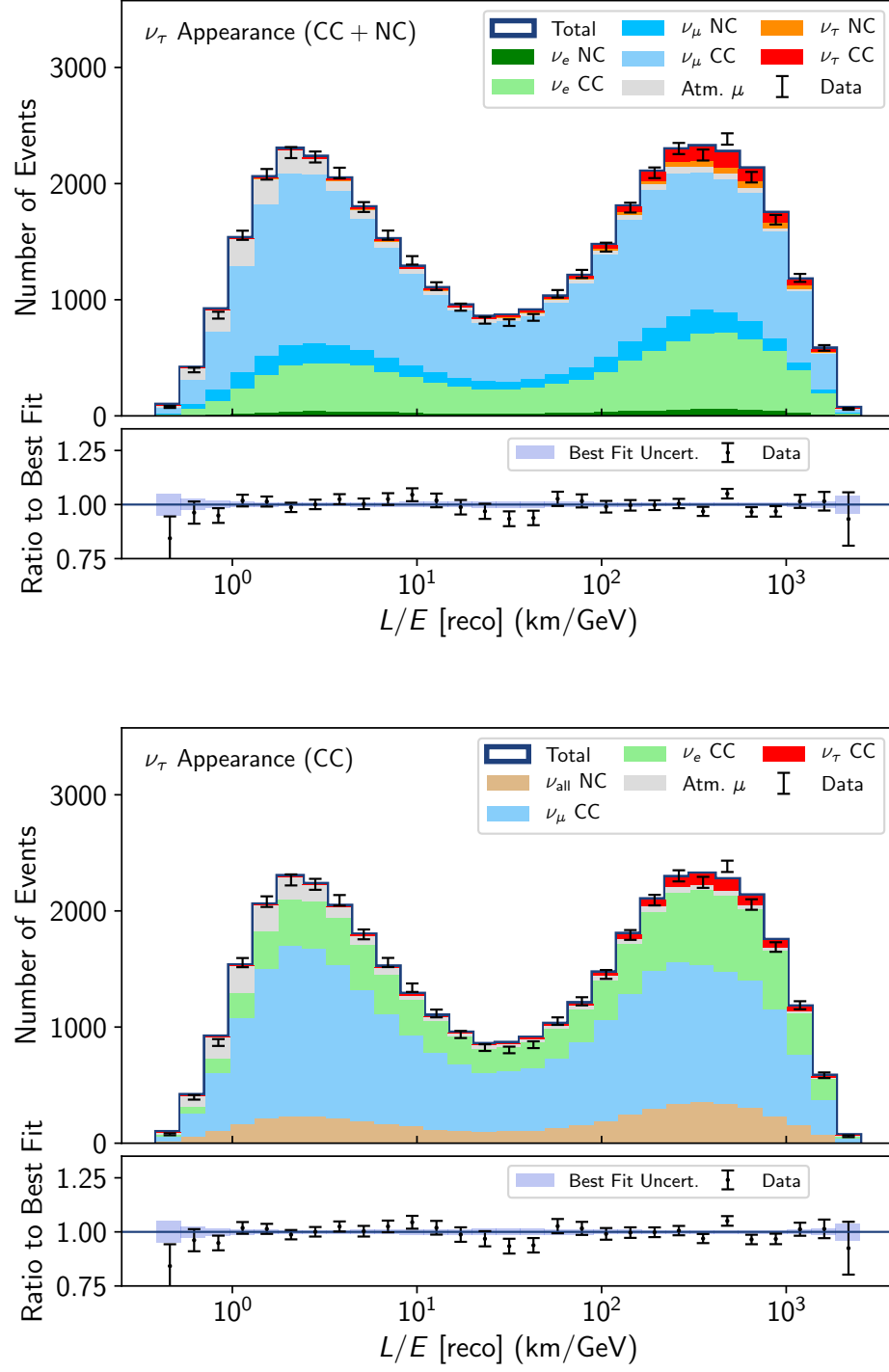


Figure 8.5: L/E plot for cascades and tracks combined. Top: L/E from the ν_τ (CC + NC) normalization fit. Bottom: L/E from the ν_τ CC normalization fit.

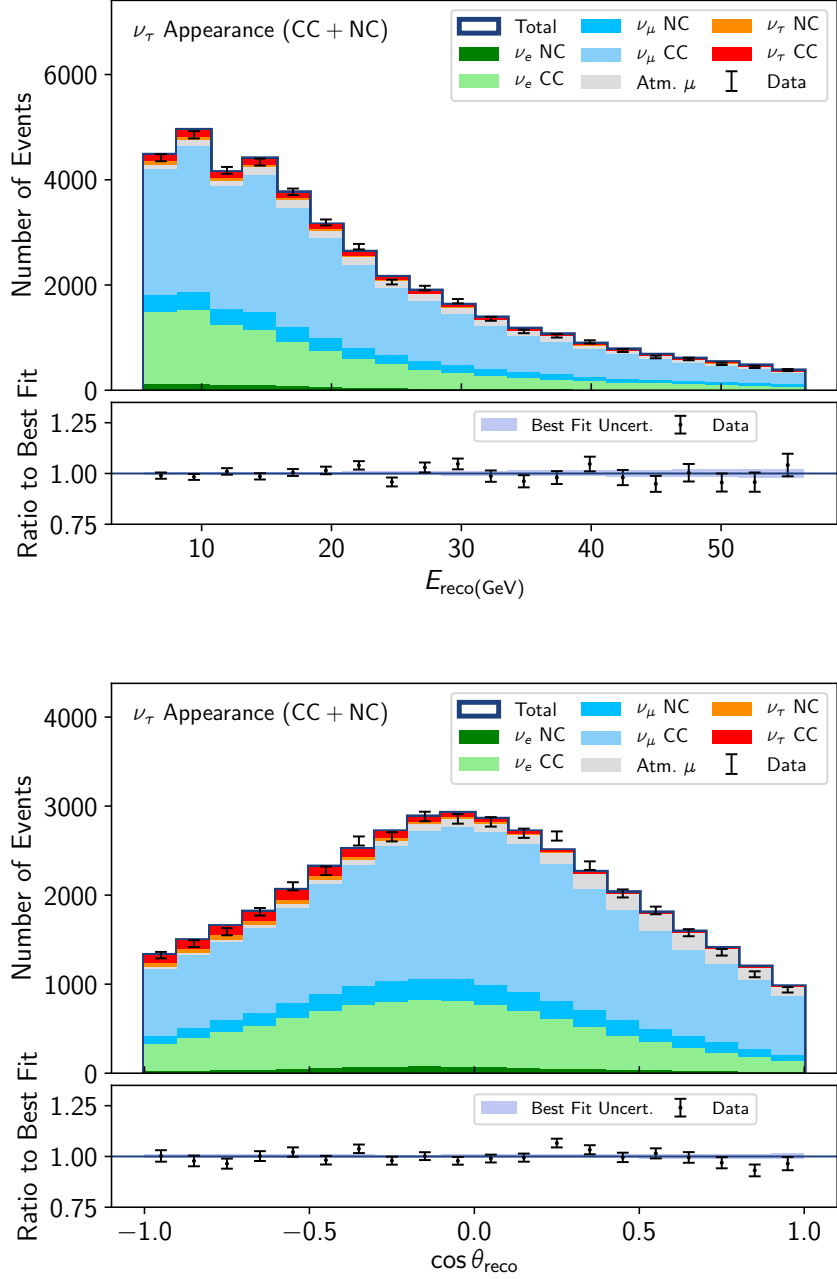


Figure 8.6: Reconstructed energy (top) and $\cos \theta_{\text{zen}}$ (bottom) distributions (cascades and tracks combined) for the ν_τ (CC + NC) normalization fit.

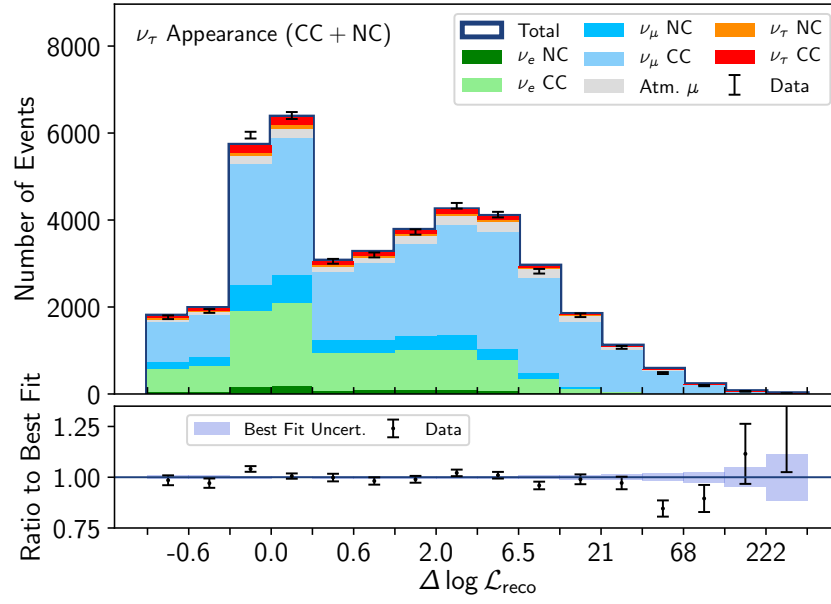


Figure 8.7: PID distributions (ΔLLH) for the ν_τ (CC + NC) normalization fit.

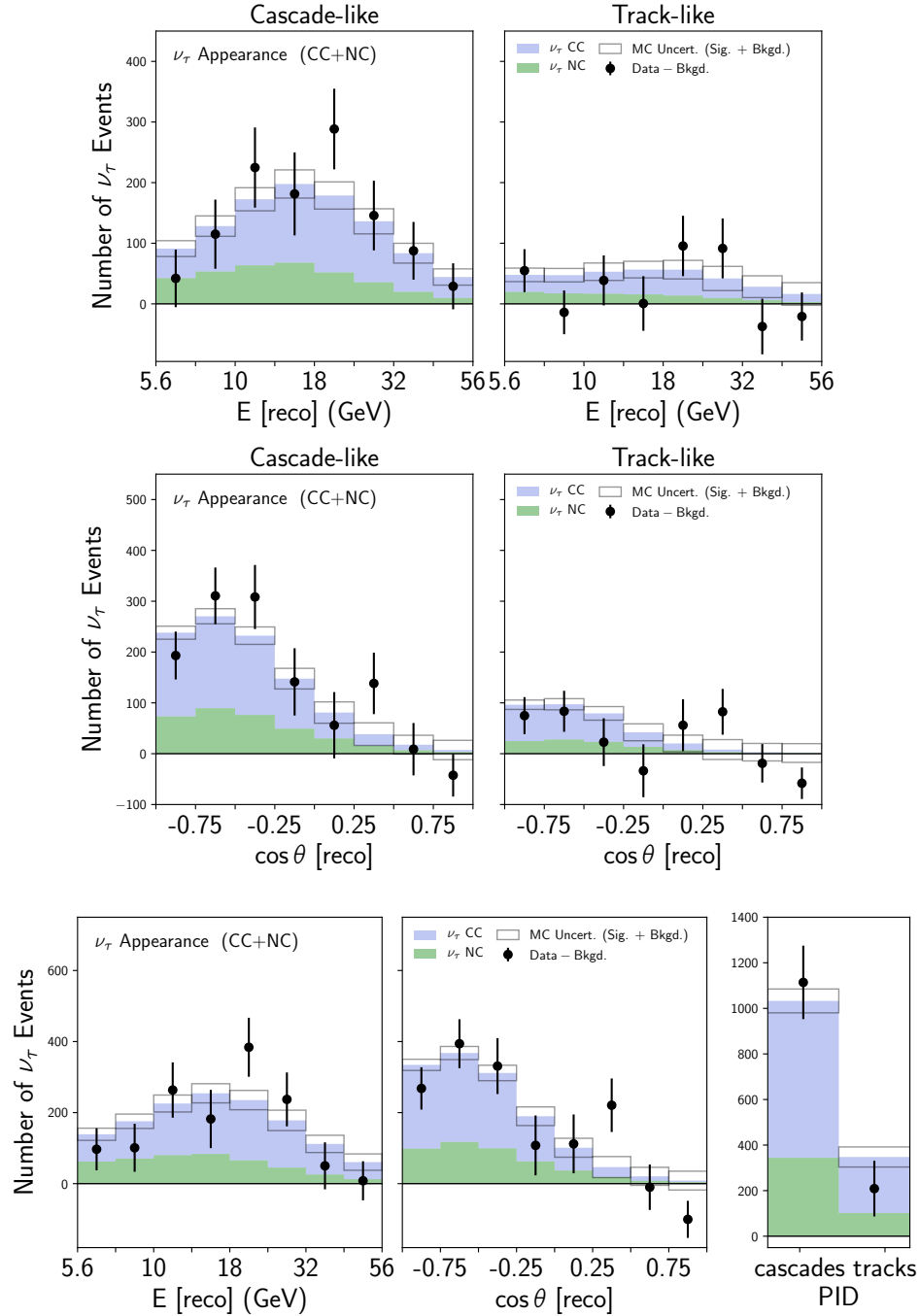


Figure 8.8: Background-subtracted event distributions for the ν_τ (CC+NC) normalization fit. Top: reconstructed energy distributions split into cascade-like and track-like channels. Middle: reconstructed $\cos \theta_{\text{zen}}$ distributions. Bottom: reconstructed energy, $\cos \theta_{\text{zen}}$, and particle identification (PID) distributions (cascades and tracks combined).

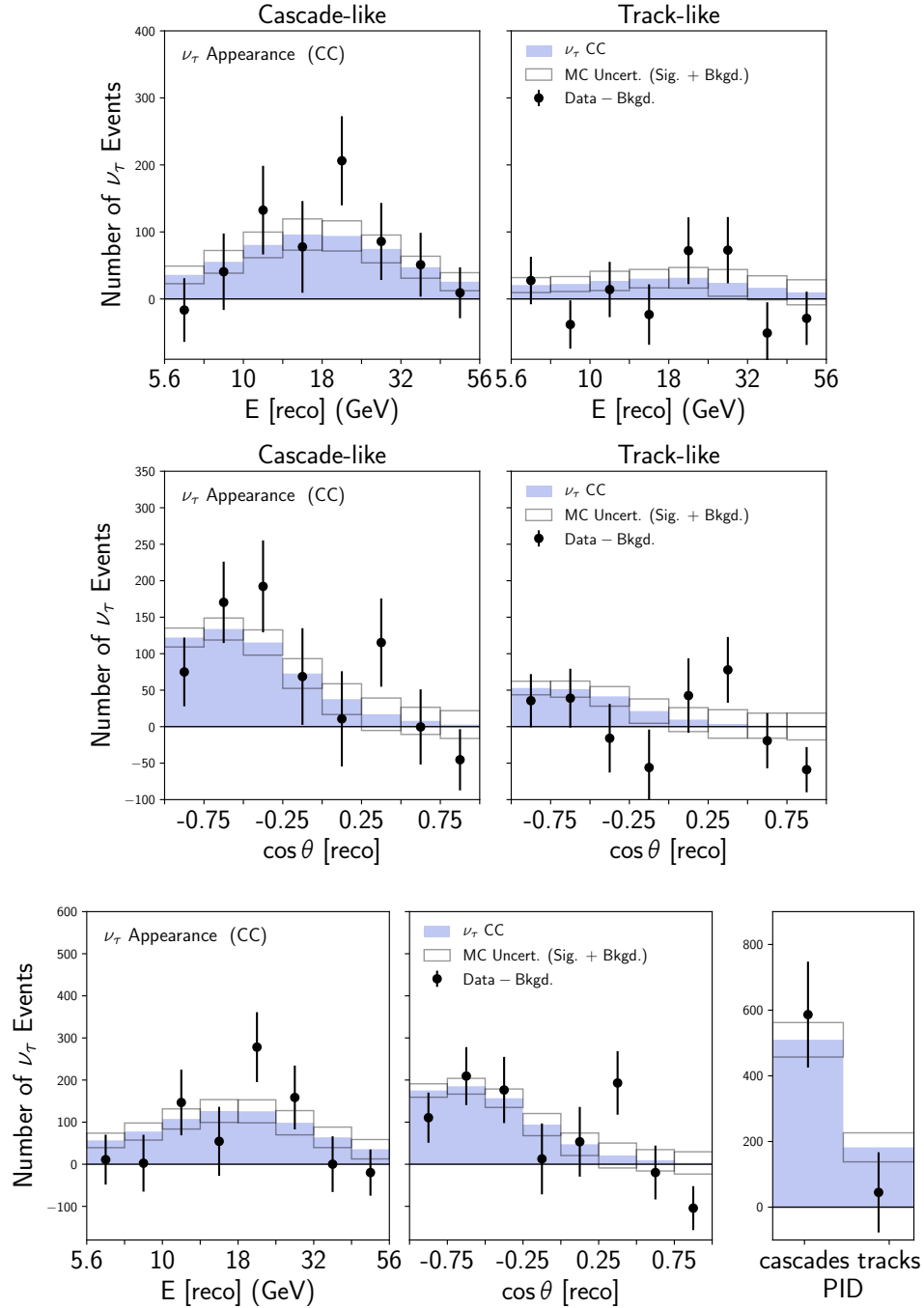


Figure 8.9: Background-subtracted event distributions for the ν_τ CC normalization fit. Top: reconstructed energy distributions split into cascade-like and track-like channels. Middle: reconstructed $\cos \theta_{\text{zen}}$ distributions. Bottom: reconstructed energy, $\cos \theta_{\text{zen}}$, and particle identification (PID) distributions (cascades and tracks combined).

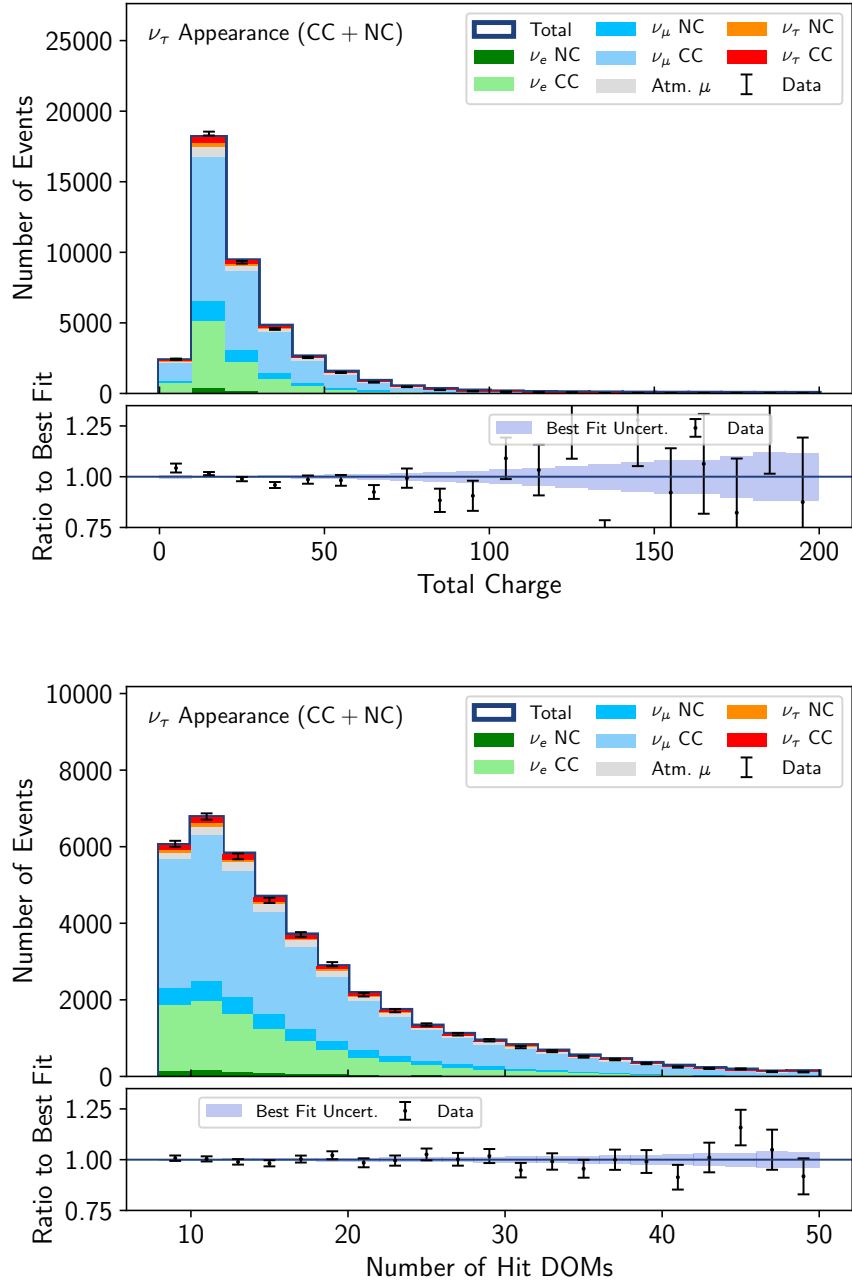


Figure 8.10: “Total charge” and “Number of hit DOMs” distributions (cascades and tracks combined) for the ν_τ (CC + NC) normalization fit. Top: “Total charge”, it is the total charge of the SRT-TW-Cleaned DCC pulses (see Section 5.3.1 for its definition). Bottom: “Number of hit DOMs”. It is the number of hit DOMs in the SRT-TW-Cleaned DCC pulses.

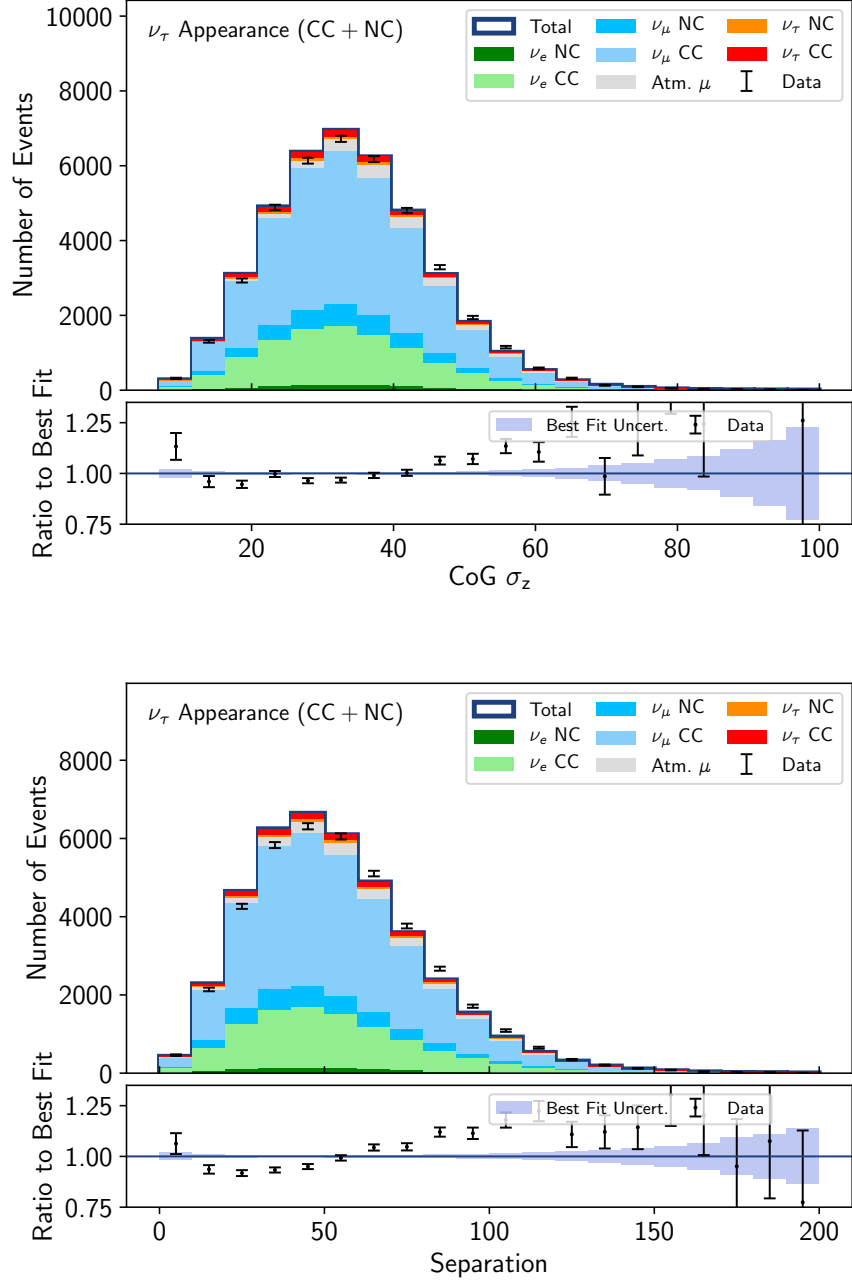


Figure 8.11: “CoG σ_z ” and “Separation” distributions (cascades and tracks combined) for the ν_τ (CC + NC) normalization fit. Top: “CoG σ_z ” is the standard deviation of the z position of the charge-weighted CoG of the SRT-TW-cleaned DCC pulses. Bottom: “Separation”. The SRT-TW-cleaned DCC pulses are sorted by time into four subsets. “Separation” (Δr) is the spatial distance between the first and the fourth subsets of the hits.

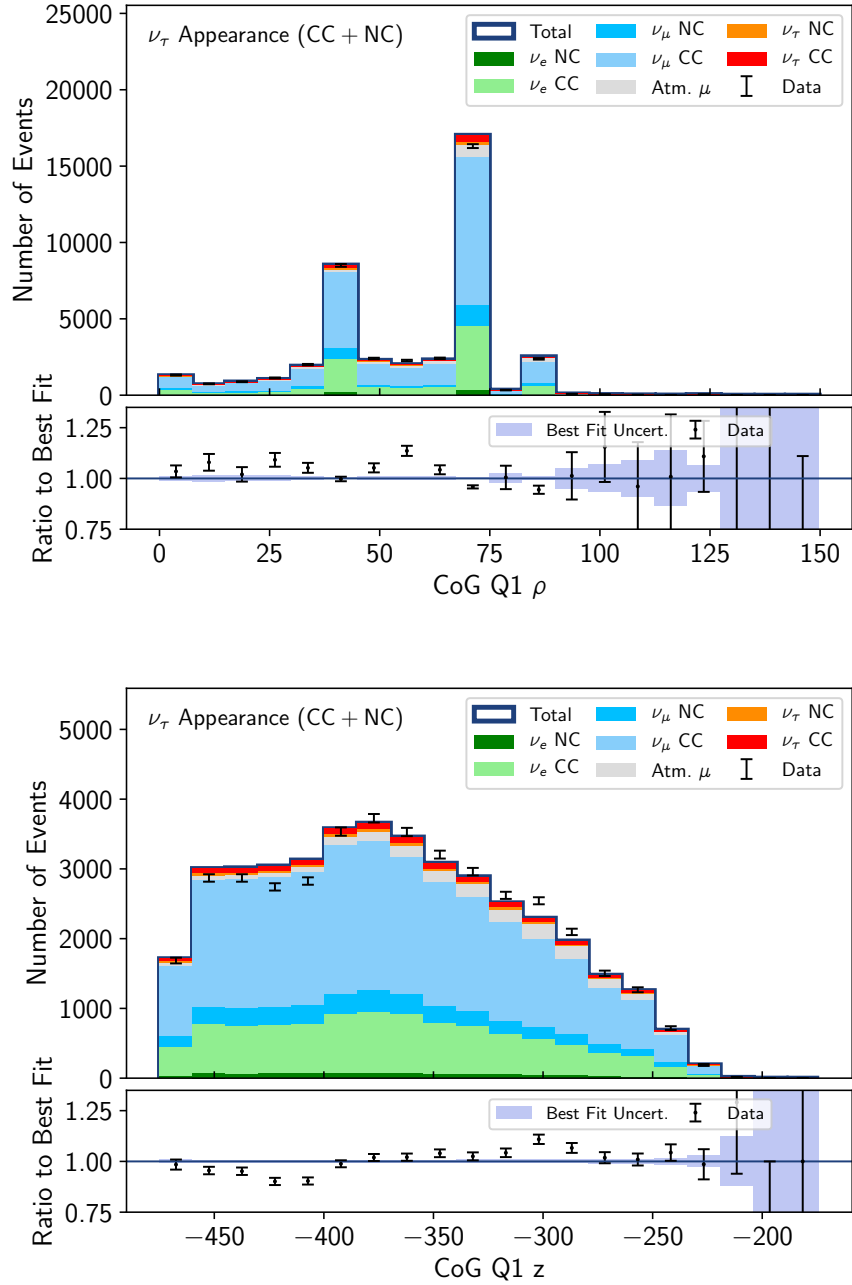


Figure 8.12: Top: “CoG Q1 ρ ” distribution (cascades and tracks combined) for the ν_τ (CC + NC) normalization fit. It is the radial distance of the CoG of the first quarter of the time-sorted SRT-TW-cleaned DCC pulses. Bottom: “CoG Q1 z ” distribution (cascades and tracks combined) for the ν_τ (CC + NC) normalization fit. It is the depth of the CoG of the first quarter of the time-sorted SRT-TW-cleaned DCC pulses.

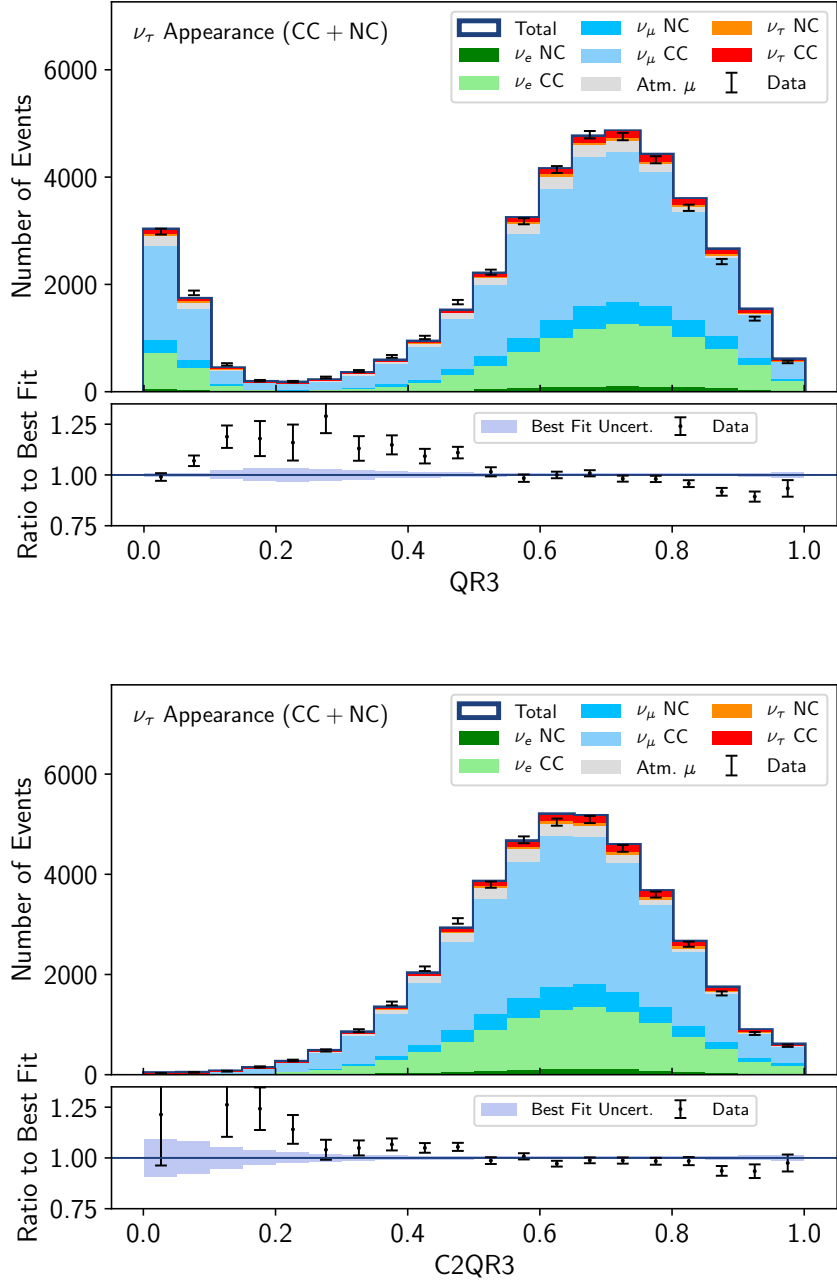


Figure 8.13: Top: “QR3” distributions (cascades and tracks combined) for the ν_τ (CC + NC) normalization fit. “QR3” is the ratio of the charge in the first 300ns after the trigger time to the total charge. Bottom: “C2QR3” distributions, C2QR3 is the same as QR3, but excluding the first two pulses to reduce the impact of noise.

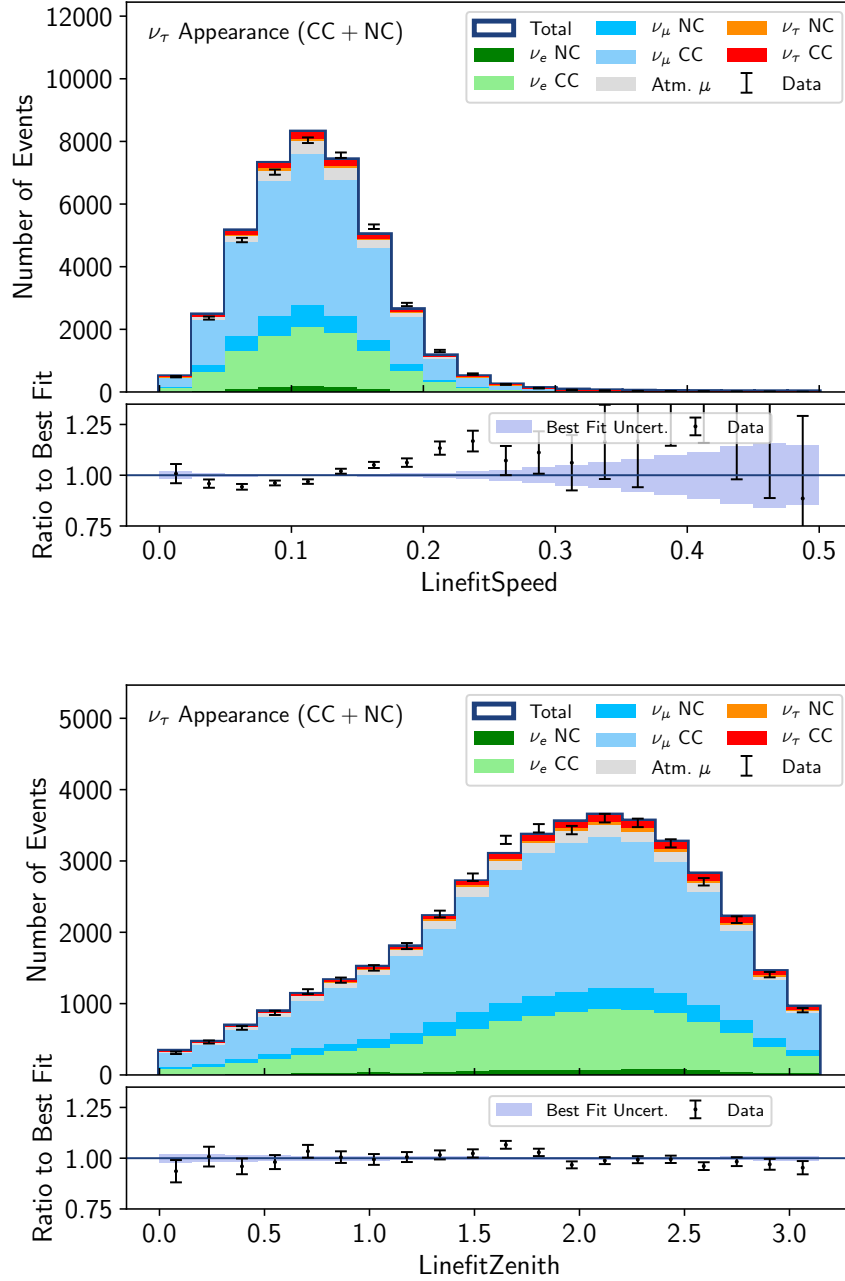


Figure 8.14: “Linefit speed” and “Linefit zenith” distributions (cascades and tracks combined) for the ν_τ (CC + NC) normalization fit. Top: “Linefit speed”. Bottom: “Linefit zenith”. They are the best fit track speed and zenith from Linefit [93].

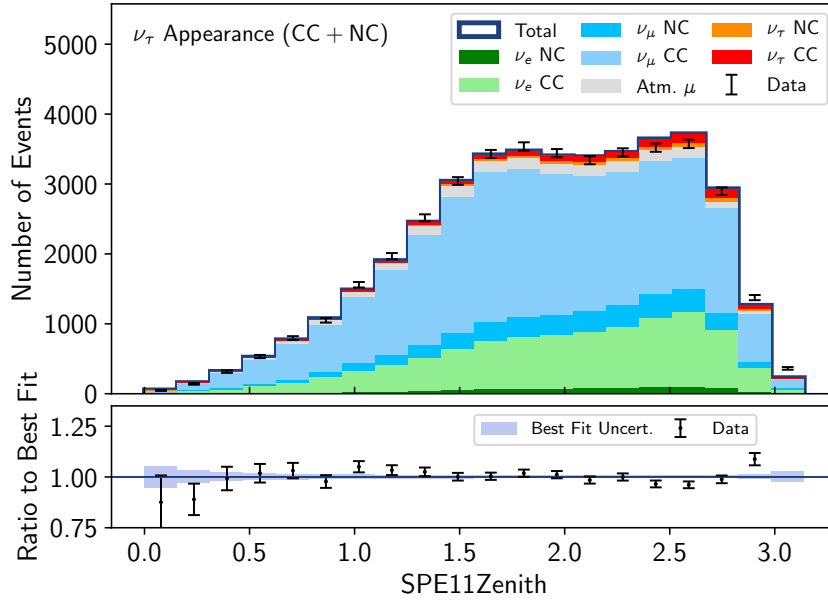


Figure 8.15: “SPE11 zenith” distributions (cascades and tracks combined) for the ν_τ (CC + NC) normalization fit. It is the best fit zenith angle from SPE11 fit [92].

Chapter 9 |

Conclusions

IceCube can measure neutrinos in a large energy range from as low as 5 GeV up to a few PeV. The low energy subarray DeepCore is designed with a geometry to be able to measure neutrinos as low as a few GeV to roughly 100 GeV.

This dissertation presented a measurement of atmospheric tau neutrino appearance with three years of IceCube/DeepCore in the 5.6 – 56 GeV neutrino energy range.

The key physics parameter is ν_τ (CC + NC) normalization, a scale factor assigned to the signal ν_τ (CC+NC) events, varying between 0 and 1, where the value of one corresponds to the expected rate under assuming the standard three-flavor neutrino oscillations.

The best fit ν_τ (CC + NC) normalization was 0.59 with the 68% C.I. in [0.34, 0.90], *i.e.*, $0.59^{+0.31}_{-0.25}$. The 90% C.I. was [0.18, 1.12]. This corresponds to 1379 ν_τ events out of a total of 40,959 events (which includes 39,070 all-neutrino-flavor events and 1,889 atmospheric muons).

To compare with the results of Super-K and OPERA, the measurement of ν_τ CC normalization was also conducted. The best fit ν_τ CC normalization was 0.43, with the 68% C.I. being [0.12, 0.80], *i.e.*, $0.43^{+0.36}_{-0.43}$, and the 90% C.I. was [0, 1.07].

Both the measured ν_τ (CC + NC) normalization and ν_τ CC normalization are consistent with existing measurements and the standard three-flavor oscillation paradigm at 90% C.L.

Appendix A |

Past Work

This appendix discusses my past work related to the software and hardware design of the Precision IceCube Next Generation Upgrade (PINGU). PINGU is the proposed low-energy extension to IceCube as shown in Fig. A.1.

Section A.1 is about the development of a faster reconstruction for low energy events in PINGU. Section A.2 contains four projects related to the physics requirements of the PINGU hardware design: dynamic range of PINGU DOMs (PDOM), DOM-to-DOM timing precision, physics requirement for the buffer length of PDOM firmware, and a sampling rate study. PDOM is one of the proposed DOM designs for PINGU. These five projects were all done with simulated PINGU data.

A.1 Development of a Faster Reconstruction with HybridReco/MultiNest

The motivation of this study is to use HybridReco (discussed in Section 4.2.2) and MultiNest [83, 84] to develop a faster reconstruction algorithm and at the same time achieve similar reconstruction resolutions. The energy range of interest is 1 – 30 GeV.

HybridReco was designed with fitting with 8 parameters for each event hypothesis ($x, y, z, t, zenith, azimuth, E_{\text{cascade}}, L_{\text{track}}$). MultiNest is used as the sampling algorithm, where the number of active points can be tuned along with other parameters. A smaller number of active points means fewer likelihood calls and less reconstruction time. But it can't be too small, because a very small number of active points means the fitter won't be able to sample enough points in the

likelihood space and thus might miss the minimum point. Generally speaking, a number of 75 is a suitable number, and was used in the standard 8D fit. Also, the boundaries for each parameter can be varied. For example, the boundary for each parameter can be set to a smaller interval to reduce reconstruction time.

The average time of doing one event reconstruction using the standard 8D fit was 15 minutes.

One way to speed up the reconstruction is to reduce the dimensions of the parameters given to the fitter. The idea is to use a combination of two lower-dimension fits, where the second fit can utilize the information from the first fit. Different combinations were tested. For example, one early design was a combination of a 5D fit and a second 4D fit.

The final resultant algorithm is a 5D+seeded-8D fit described as follows: First, fit with 5 parameters: $(x, y, z, t, E_{\text{cascade}})$. The track length L_{track} is fixed to 0, *zenith* and *azimuth* are fixed to values from a first guess fit MPEFit [92]. The SRT-TW-cleaned pulses are split into three subsets ordered by time. Only the 1st third of the SRT-TW-cleaned pulses are used in this 5-D fit, because they are the earliest pulses that are less likely from scattered light, thus are more likely to be located near the event interaction vertex. Second, fit with 8 parameters: use the (x, y, z, t) result from the 5D fit as the seed, where only a narrow dynamic boundary is allowed around the seed. Assume the best reconstructed position and time from the 5D fit are (x_0, y_0, z_0, t_0) , and we use a dynamic boundary (b_p) for the position (x_0, y_0, z_0) and a boundary (b_t) around the time t_0 , *i.e.*, the 8D fit's fitting boundaries for the position and time are $[x_0 - b_d, x_0 + b_d]$, $[y_0 - b_d, y_0 + b_d]$, $[z_0 - b_d, z_0 + b_d]$, and $[t_0 - b_t, t_0 + b_t]$. The other four parameters (*zenith*, *azimuth*, E_{cascade} , L_{track}) still have the original boundaries: $[0, \pi]$, $[0, 2\pi)$, $[0, 100 \text{ GeV}]$, $[0, 300 \text{ m}]$. Here the full SRT-TW-cleaned pulses are used, since we need the full information for reconstructing the angles and energy. The output best fit is then used as the result.

Simulated PINGU events are used to compare this 5D+seeded-8D algorithm and the original full 8D algorithm. The choice of dynamic boundaries and the number of active points were tuned. Table A.1 shows four examples of different values for the number of active points and the position boundary b_d and the corresponding average total reconstruction time.

The final settings (with one other reconstruction setting and a quality selection) used are:

Settings	(x, y, z) Boundary b_p	t Boundary b_t	Active Points for 8D fit	5D fit Time	8D fit Time	Total Time
1	5 m	25 ns	75	1.2	8.9	10.1
2	5 m	25 ns	50	1.1	6.3	7.4
3	10 m	25 ns	50	1.2	8.2	9.4
4	10 m	25 ns	35	1.1	6.4	7.5

Table A.1: Average reconstruction time per event under different settings for the 5D+seeded-8D fit.

- Dynamic boundary: $b_p = 10$ m, $b_t = 25$ ns.
- Number of active points are: 75 for the 5D fit, 50 for the 8D fit.
- Quality cut: (1) PINGU containment cut; (2) the best fit LLH - noise LLH > 10 .
- Time limits: a maximum of 75 minutes for both fits.

Under this setting, the reconstruction time of the first 5D fit is an average of 1.2 minutes; the second seeded 8D fit takes an average of 8.2 minutes (Fig. A.2 (a)), altogether the 5D+8D fit takes an average of 9.4 minutes, which is faster than the full 8D fit with an average of 15 minutes (Fig. A.2 (b)). Figure A.3 shows the resolutions, which are comparable with the original full 8D fit.

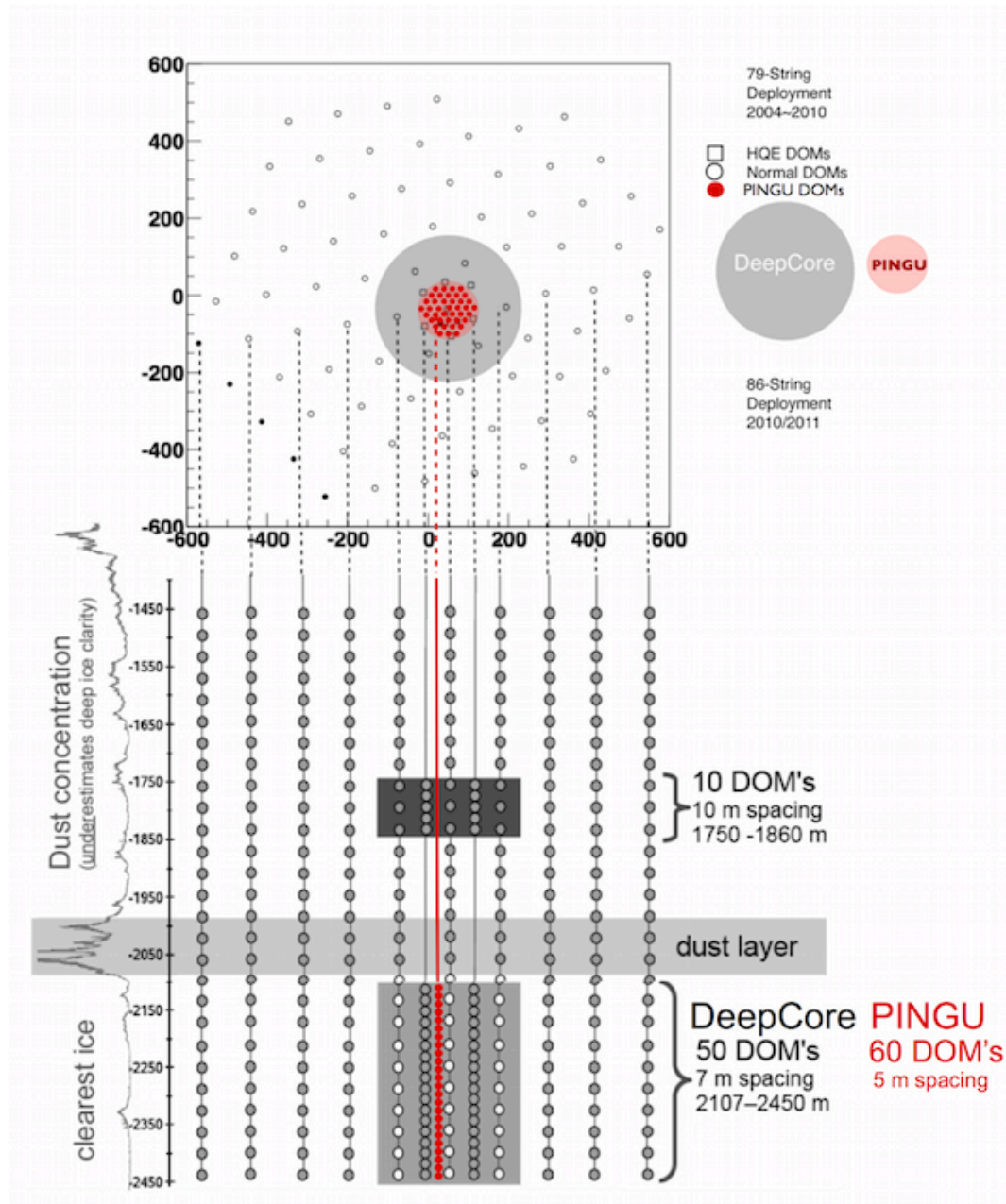
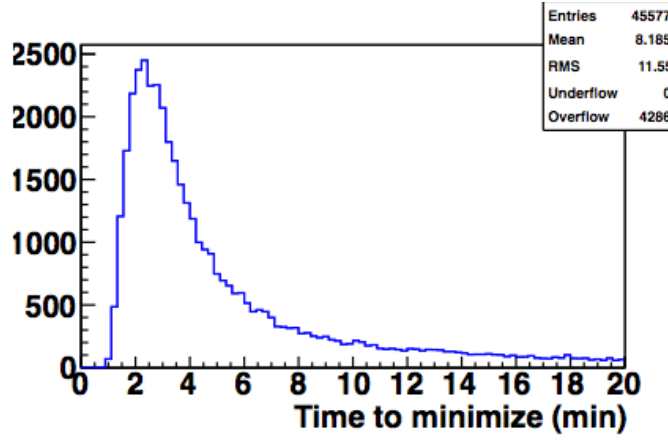
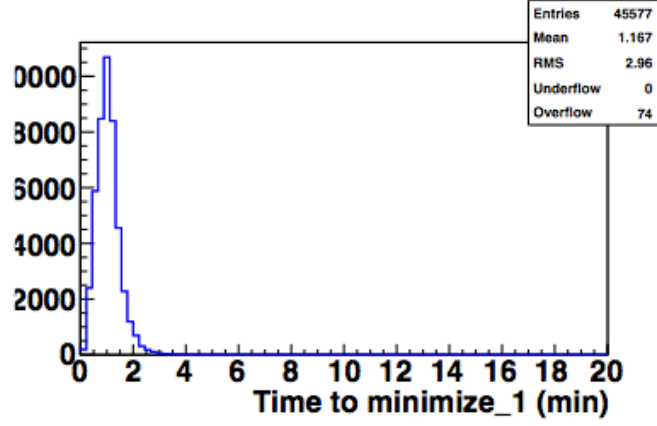
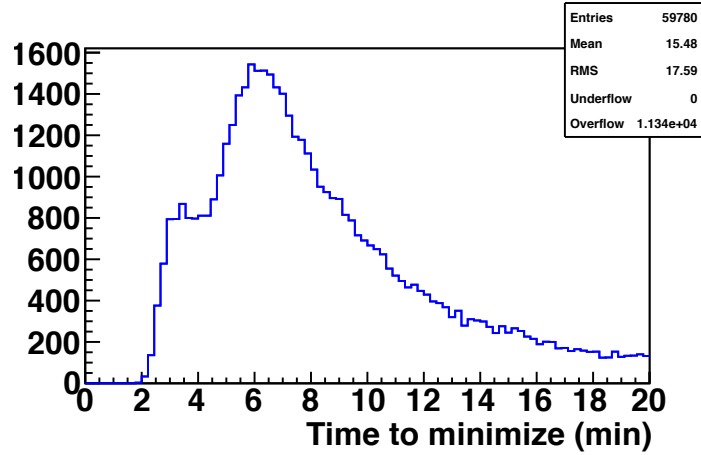


Figure A.1: The proposed PINGU detector at the time of the study. Its proposed geometry consists of 40 strings, each with 60 PDOMs on it.



(a) Time from the 5D+seeded-8D fit.



(b) Time from the full 8D fit.

Figure A.2: (a) The reconstruction time distributions for the first 5D fit (top) and the second seeded 8D fit (bottom) using a $b_d = 10$ m and 75 active points for the 5D fit and 50 active points for the 8D fit. The average times are 1.2 and 8.2 minutes, respectively. (b) The reconstruction time distributions for the full 8D fit.

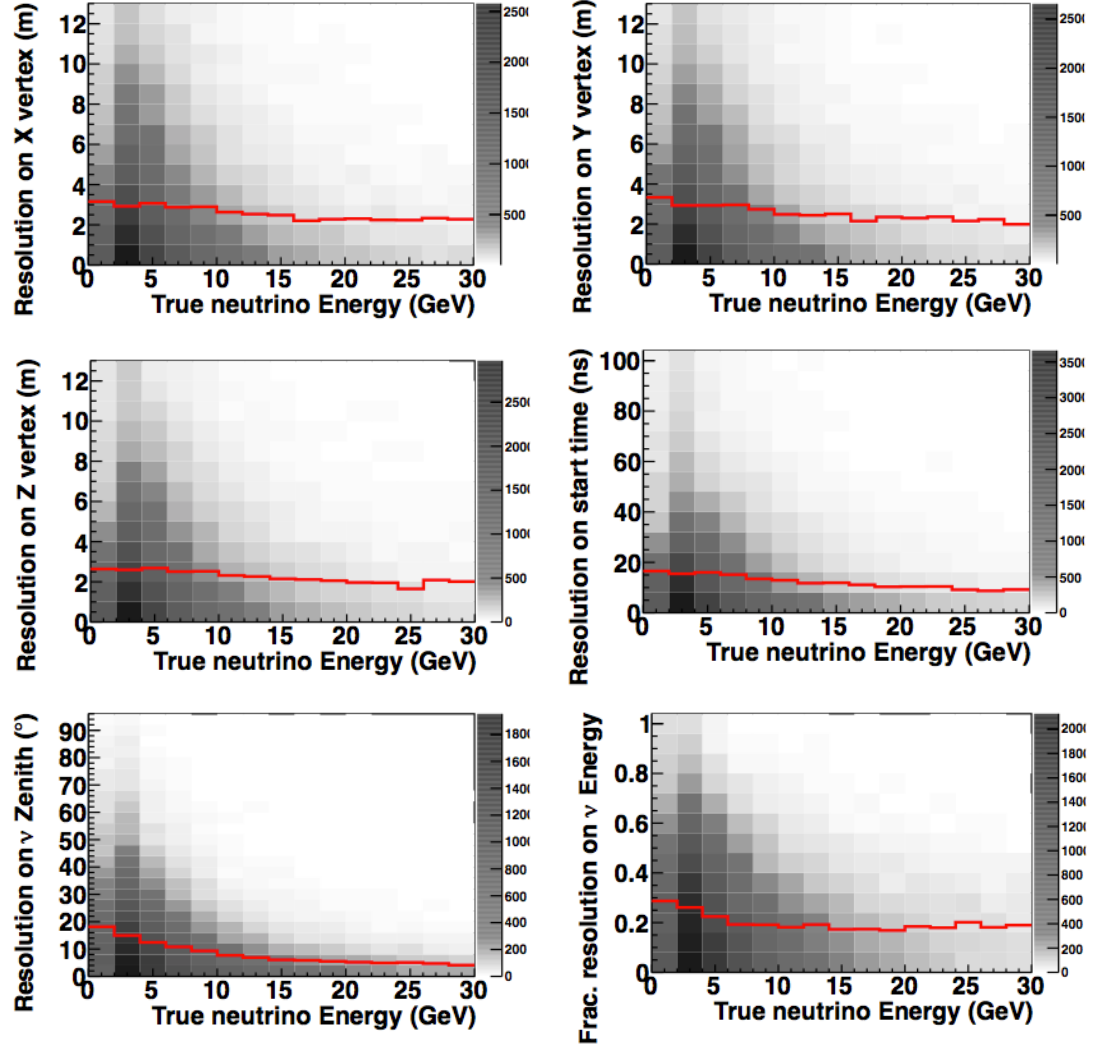


Figure A.3: The resolutions of x , y , z , t , $zenith$, and energy as a function of true neutrino energy. The red line is the median value at each energy bin. The median resolutions of the position parameters (x, y, z) are all around 3 m. The median resolution of time t is around 15 ns. For zenith angle, the median resolutions are all below 20 $^\circ$ (at energies larger than 10 GeV, less than 10 $^\circ$). The median resolution of fractional energy (fractional energy = $(E_{\text{reconstructed}} - E_{\text{true}})/E_{\text{true}}$) is about 0.2.

A.2 PINGU Hardware Studies

A.2.1 Dynamic Range of PDOM

PDOM was one of the proposed DOM designs for PINGU. The dynamic range of IceCube DOMs is 400 PE/15ns, *i.e.*, the maximum charge in a 15 ns window is 400 PE, this study examines the required dynamic range for PDOM if we aim to achieve a similar performance from PDOMs and IceCube DOMs.

The procedure to get this value is:

1. With IceCube data, get the fraction of DOMs with charge larger than 400 PE within 15 ns in respect to the total number of DOMs.
2. Estimate the charge distribution in PDOMs. The charge distribution is the maximum pulse charge inside each PDOM.
3. Use this charge distribution to find the charge value corresponding the same fraction.

In the first step, the fraction is measured to be 2×10^{-6} , this means there are two in one million DOMs that have more than a charge of 400 PE within 15 ns. The data run used was burn sample data at low energy L3 (run 118400), the data used in the second step is simulated PINGU data (PINGU geometry V15) and CORSIKA run 9775. Figure A.4 shows the results.

We draw the conclusion that the dynamic range required by PINGU DOMs is 425 ± 25 PE/15 ns, so two in one million PDOMs have more than a charge of 425 PE within 15 ns, which is not significantly different from the current performance of IceCube DOMs ($400 \pm$ PE/15 ns).

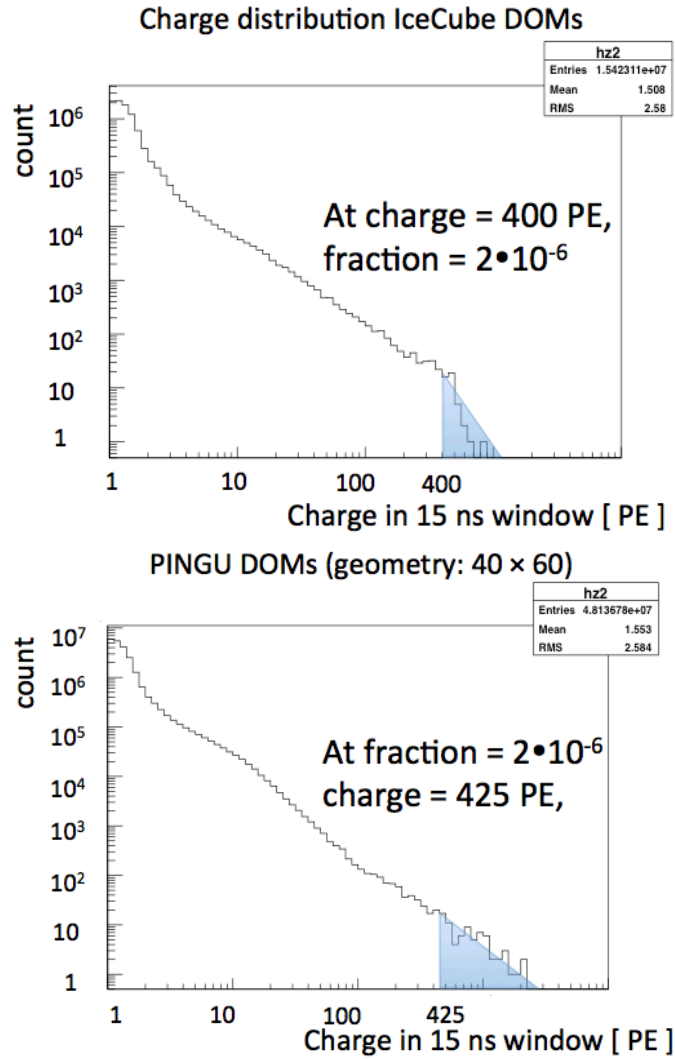


Figure A.4: Top: The distribution of maximum charge within 15 ns inside IceCube DOMs. Bottom: The distribution of maximum charge within 15 ns inside PDOMs.

A.2.2 DOM-to-DOM Timing Precision

This study evaluated the impact of the DOM timing precision on event reconstruction resolutions to characterize the requirement for DOM design in PINGU.

As mentioned in Section 4.2, the “RecoPulse” or “reco pulse” (meaning “reconstructed pulses”) are what’s used in event reconstruction. Each reco pulse contains three parameters: the pulse time, pulse charge and pulse width.

The procedure of the study is:

1. Inside each PDOM, shift the time of every reco pulse by the same amount, this time shift is sampled randomly from a Gaussian distribution. For any given DOM, the time shift of each pulse is the same, but different DOMs will in general have different time shifts drawn from the same Gaussian distribution.
2. Do a full 8D HybridReco/MultiNest reconstruction, compare the resultant resolutions with the resolutions using the original reco pulses (*i.e.*, $\sigma = 0$ ns).

Here, I used four Gaussian distributions with the $\sigma = 6, 12, 24, 48$ ns, respectively. So, there are five different reconstructions in total, including the original data that has no time shift. Figures A.5 and A.6 show the zenith and energy resolutions under these five settings.

To better quantify the effects generated by the different time shifts on the resolutions, a Gaussian fit was done on the energy (or zenith) distributions in each energy bin in Figs. A.5 and A.6. There are 15 energy bins in each subplot, so in total ($15 \times 5 =$) 75 Gaussian fits were performed for both the energy resolution and the zenith resolution. Figure A.7 shows the Gaussian fits inside each energy bin for the no-time-shift case. The plots for the other four time shifts were similar so not shown here. From the fits, we see that the standard deviation of the best fit Gaussian function is a good representation of the quality of reconstruction resolution.

So, all the Gaussian standard deviations (σ) from the Gaussian fits were gathered into Fig. A.9. As expected, zenith resolution gets worse when we increase the time shifts from a σ at 0 ns to 48 ns. The energy resolution stays about the same even when the time shift with the σ increases to 12 ns. This result agrees with our expectation, since the energy reconstruction mainly depends on the amount of

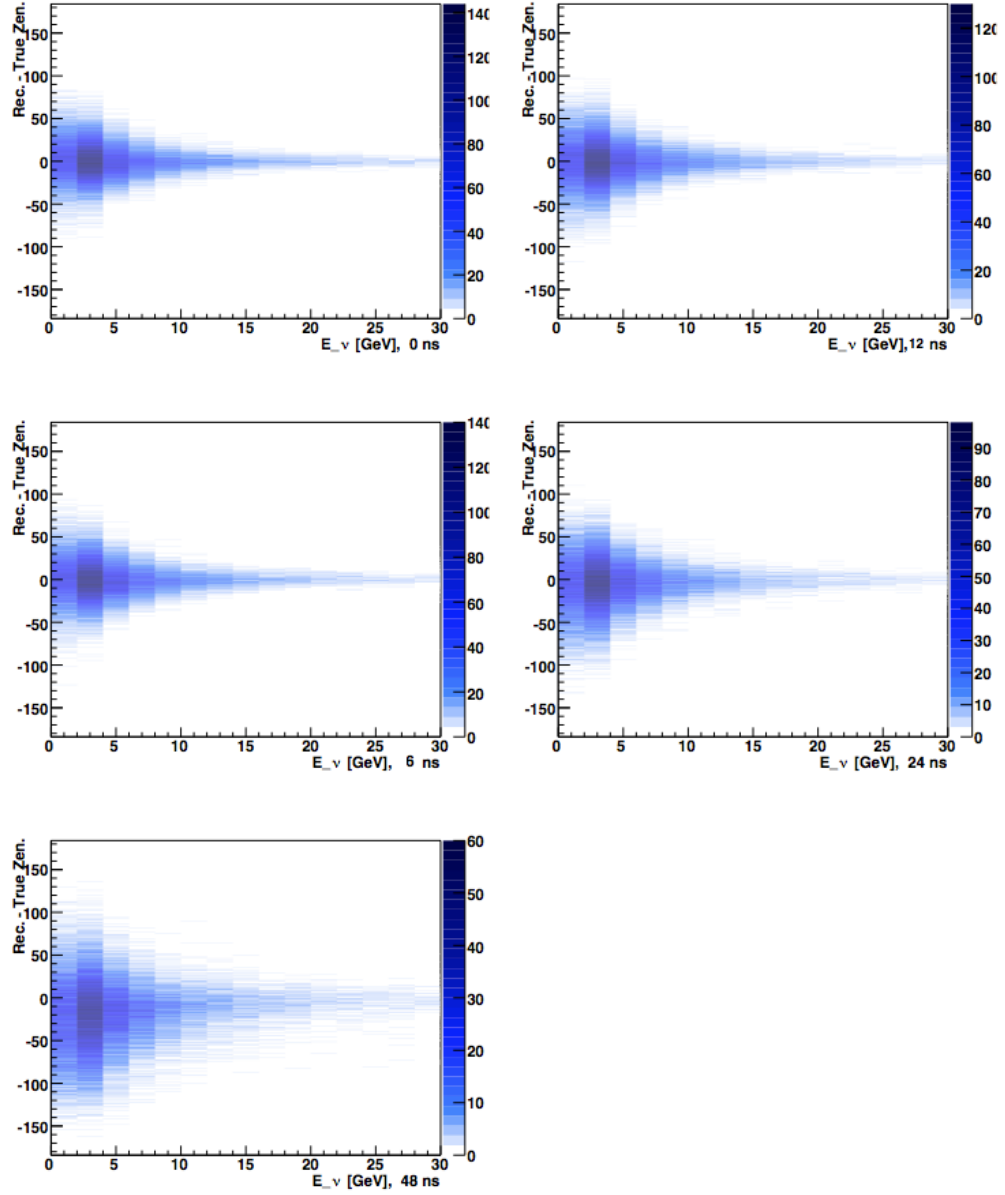


Figure A.5: The $\text{zenith}_{\text{reco}} - \text{zenith}_{\text{true}}$ as a function of true neutrino energy, from these 5 reconstructions. The plot in the top-left corner (0 ns) is no-time-shift case. We see the reconstruction gets worse when we increase the Gaussian σ value from 0 to 48 ns. See more detailed comparison in Fig. A.9

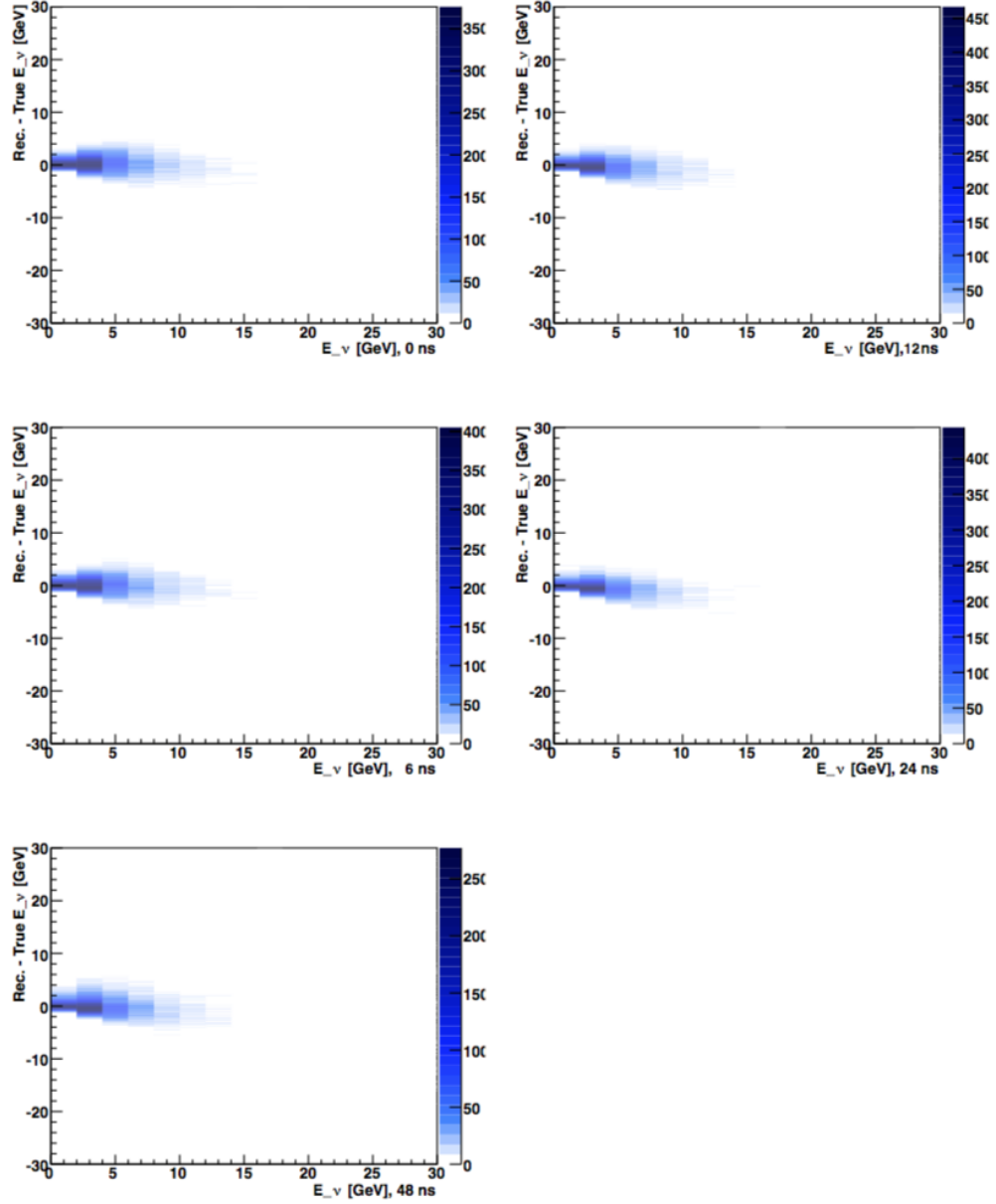


Figure A.6: The $E_{\text{reco}} - E_{\text{true}}$ as a function of the true neutrino energy from these 5 reconstructions. We see similar results for energy reconstruction, so the time shifts do not influence the energy reconstruction much. See more detailed comparison in Fig. A.9

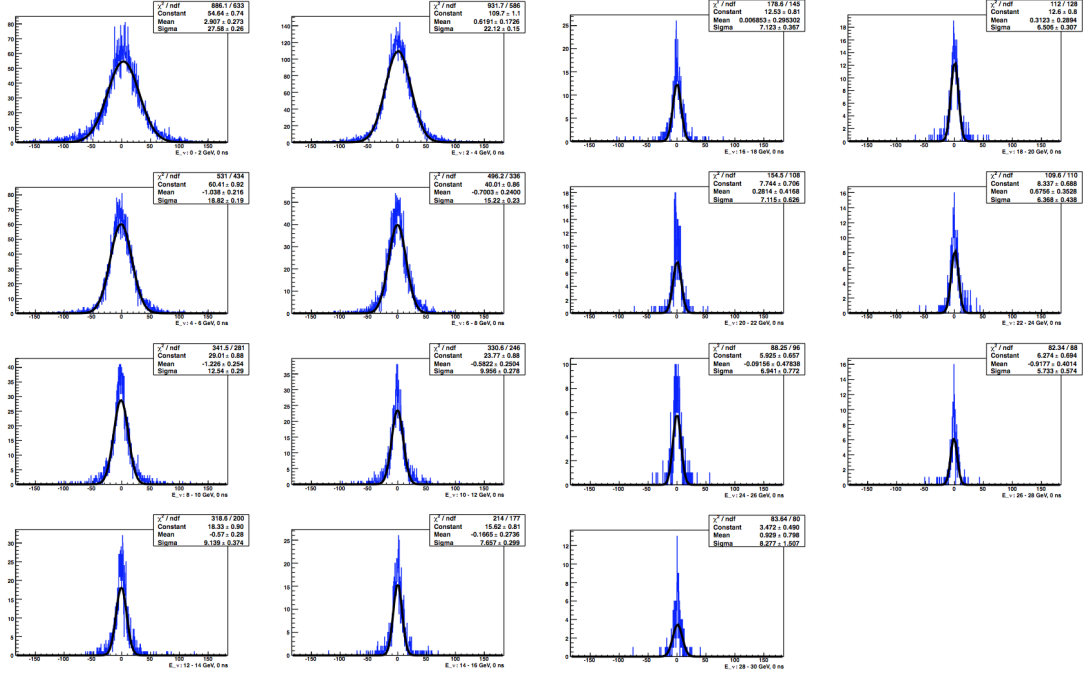


Figure A.7: Gaussian fits inside the 15 energy bins of the zenith resolution plot (Fig. A.5) with no time shift (0 ns). The x-axis name contains the energy bin range. This plot shows the distribution of $zenith_{\text{reco}} - zenith_{\text{true}}$ in each energy bin can be fitted by a Gaussian function well, so the standard deviation of the best fit Gaussian function is a good representation of the quality of reconstruction resolutions, the comparison of all the Gaussian standard deviations is shown in Fig. A.9.

charge observed by the DOMs and less influenced by the timing precision, whereas the zenith reconstruction needs good timing information.

In conclusion, from this study, we learned that a time shift sampled from the $\sigma = 6 \text{ ns}$ Gaussian distribution makes the zenith resolution worse by about 2 to 3 degrees. For the time shifts at Gaussian σ at 6 and 12 ns, the energy resolutions stay about the same. We currently can achieve less than 6 ns precision.

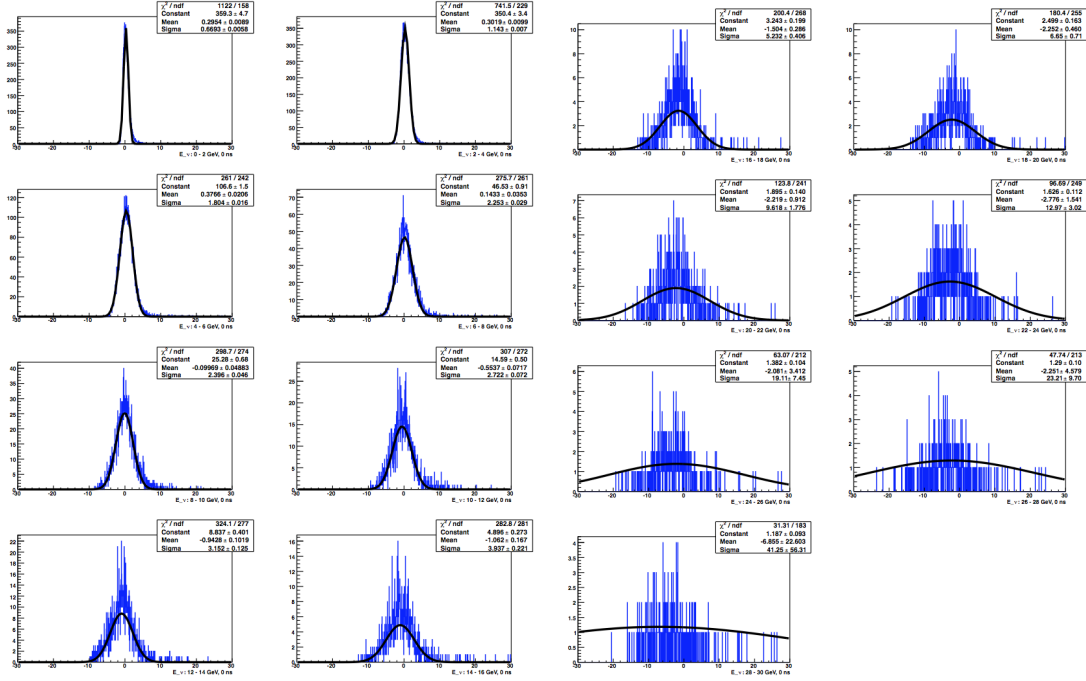


Figure A.8: Gaussian fits inside the 15 energy bins of the energy resolution plot (Fig. A.6) with no time shift (0 ns). The x-axis name contains the energy bin range. This plot shows the first 9 bins (energy range: 0 – 18 GeV) can be fitted by a Gaussian distribution well, but the rest 5 bins don't have enough statistics, so it's better to only compare standard deviations for the first 9 bins. The comparison of the Gaussian standard deviations is shown in Fig. A.9.

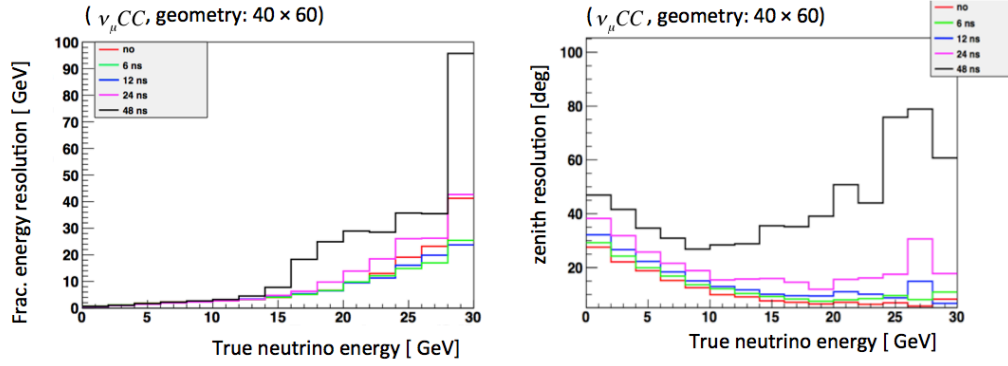


Figure A.9: The fractional energy resolution (left) and the zenith resolution as a function of true energy. The resolutions are represented by the the standard deviations of the best fit Gaussian functions in each energy bin. The red line is the no-time-shift case, the green, blue, magenta, black lines represent the $\sigma = 6, 12, 24, 48$ ns case, respectively. From 0 to 48 ns, the zenith resolution gets worse, when $\sigma = 6$ ns, the zenith resolutions decreases by about 2 to 3 degrees; energy resolution stays about the same when $\sigma = 6, 12$ ns.

A.2.3 Physics Requirement for the Buffer Length of PDOM Firmware

The PDOM firmware's proposed buffer length at the time of the study was 27 microseconds. We investigated the requirement for the PINGU DOM buffer length using the most energetic high-energy starting events (HESE) events and simulated monopole events. The procedure is to plot the FADC raw count vs time and determine the pulse length in the DOM with the longest pulse.

Results are shown in Fig. A.10 and Fig. A.11. For observed HESE events, most of the DOMs have either $6.4 \mu s$ or $12.8 \mu s$ readout. For simulated monopoles, the longest readout can be $192 \mu s$. So the conclusion of this study is: For the observed HESE events, a $27 \mu s$ long buffer length is enough. For simulated slow monopoles, full readout needs longer than $27 \mu s$. Note that zero-suppression was not included here. With zero-suppression, less buffer length will be required. This needs further investigations.

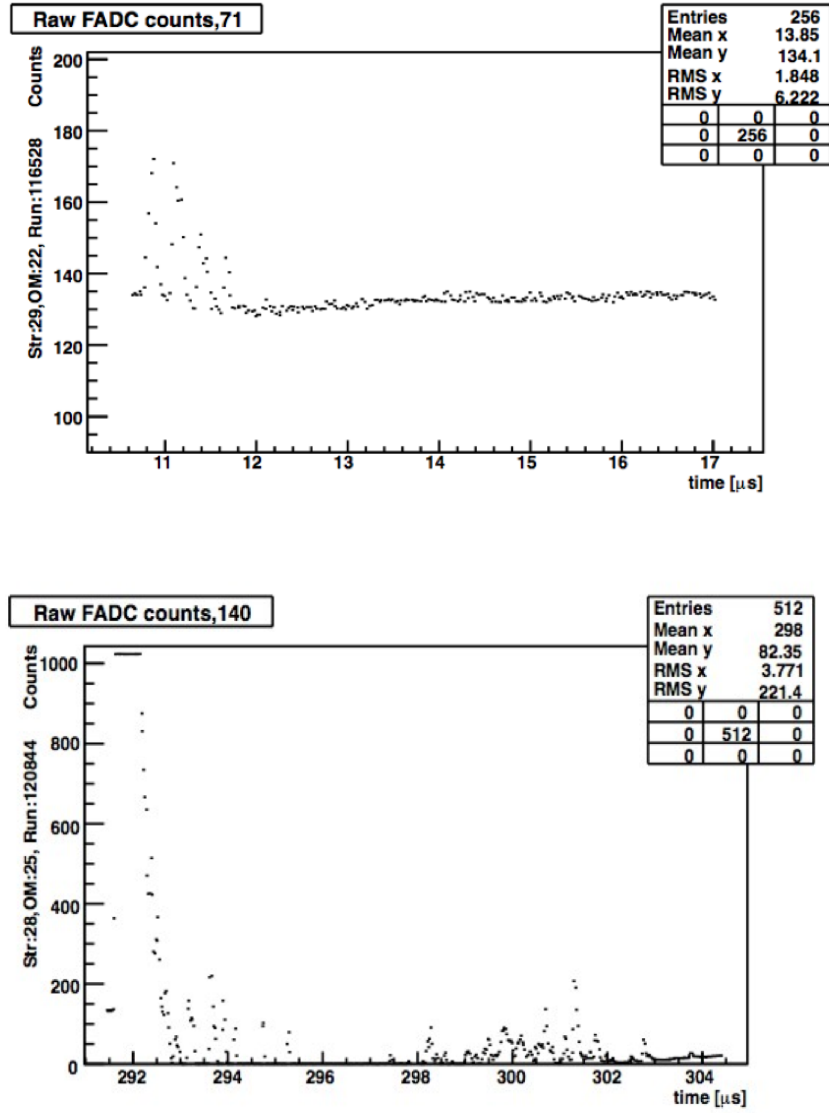


Figure A.10: FADC counts vs time for one DOM (Run 116528), each one dot is one FADC sample, there are 256 samples, the FADC bin size is 25 ns, thus the total time is $256 \times 25 \text{ ns} = 6.4 \mu\text{s}$.

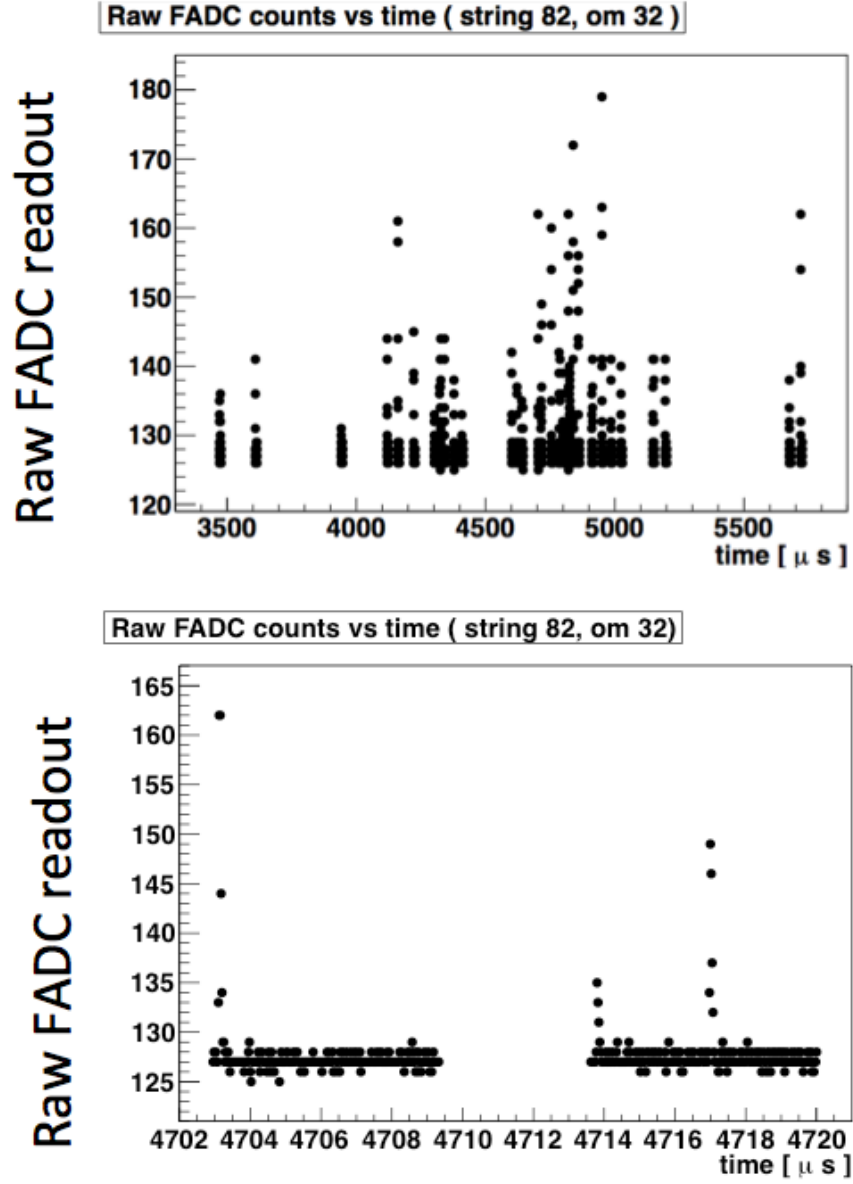


Figure A.11: The raw FADC readout for one DOM of a simulated monopole event ($\beta = 0.0001$, $\lambda = 0.1$ m). It has a $(30 \times 25 \text{ ns} =)$ $192 \mu\text{s}$ long FADC readout. The top figure shows all the readout, the bottom figure is a zoomed-in figure of the same event inside a smaller time range.

A.2.4 Sampling rate study

IceCube uses two digitizers (300 MHz ATWD and 40 MHz FADC). This study investigates the impact on data quality if simply using pulses from the slower ATWD. If we can use a slower ADC, we can reduce power consumption and simplify hardware design.

DOMLauncher [104] is the IceCube module to do the simulations of the behavior of the DOM mainboard, including launching and digitization. It takes the PMT responses as input, simulates the discriminators, local coincidence logic and digitization, and produces the digitized ATWD and FADC signals as output.

The first step of the procedure is to modify the *DOMLauncher* module so that it can produce digitized signals with different ATWD sampling rate at 250 MHz, 200 MHz, 150 MHz and 100 MHz. The second step is to send the output digitized signals into the next steps in the simulation chain, do reconstructions using the 5D+seeded-8D fit (described in Appendix A.1). Finally, we compare the resultant resolutions.

The changes made by slower ATWD sampling rates on the raw data are shown in Fig. A.12. The resolution comparisons from using the above four different sampling rates are shown in Fig. A.13.

The conclusion from Fig. A.13 is that for the simulated PINGU ν_μ CC events in the energy range (1 – 80 GeV), changing the ATWD sampling rate from 300 MHz to 100 MHz or 200 MHz doesn't change the zenith and neutrino energy resolution too much.

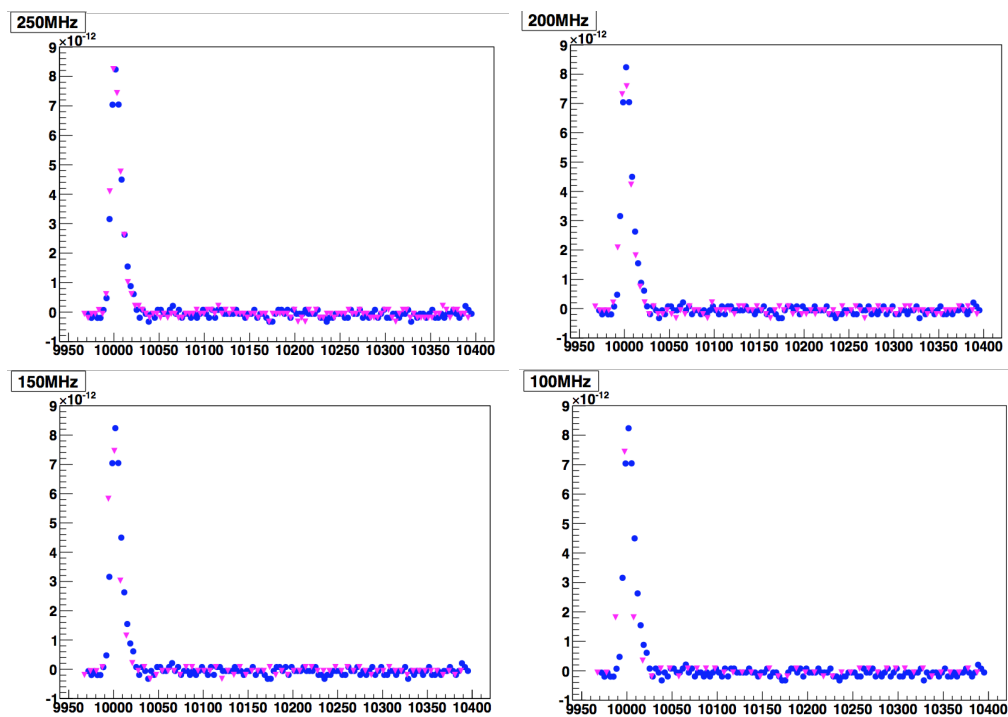


Figure A.12: The blue dots are the output DOM launches using the original 300 MHz ATWD sampling rate, the magenta triangles are the new ATWD data points.

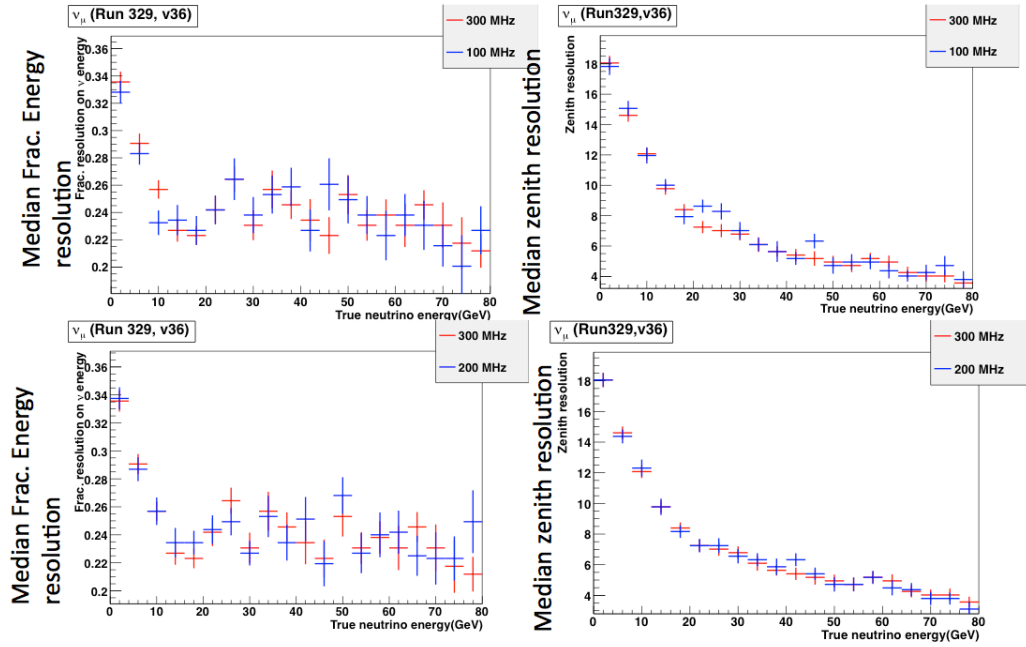


Figure A.13: The median zenith and fractional energy resolutions using different ATWD sampling rates. Data used here: PINGU simulated ν_μ CC events. The blue bins are with the original 300 MHz sampling rate. We see the resolutions between a 300 MHz rate and 200 MHz (also 100 MHz) rate are comparable.

Bibliography

- [1] COWAN, C. L., F. REINES, F. B. HARRISON, H. W. KRUSE, and A. D. MCGUIRE (1956) “Detection of the free neutrino: A Confirmation,” *Science*, **124**, pp. 103–104.
- [2] DANBY, G., J.-M. GAILLARD, K. GOULIANOS, L. M. LEDERMAN, N. MISTRY, M. SCHWARTZ, and J. STEINBERGER (1962) “Observation of High-Energy Neutrino Reactions and the Existence of Two Kinds of Neutrinos,” *Physical Review Letters*, **9**, pp. 36–44.
- [3] KODAMA, K. ET AL. (2001) “Observation of tau neutrino interactions,” *Phys. Lett.*, **B504**, pp. 218–224, [hep-ex/0012035](#).
- [4] PONTECORVO, B. (1957) “Inverse beta processes and nonconservation of lepton charge,” *Zhurnal Éksperimental’ noĩ i Teoreticheskoi Fiziķi*, **34**, p. 247.
- [5] MAKI, Z., M. NAKAGAWA, and S. SAKATA (1962) “Remarks on the Unified Model of Elementary Particles,” *Progress of Theoretical Physics*, **28**, pp. 870–880.
- [6] PARKE, S. and M. ROSS-LONERGAN (2016) “Unitarity and the three flavor neutrino mixing matrix,” *Phys. Rev.*, **D93**(11), p. 113009, [1508.05095](#).
- [7] CAHN, R. N., D. A. DWYER, S. J. FREEDMAN, W. C. HAXTON, R. W. KADEL, YU. G. KOLOMENSKY, K. B. LUK, P. McDONALD, G. D. OREBI GANN, and A. W. P. POON (2013) “White Paper: Measuring the Neutrino Mass Hierarchy,” in *Proceedings, 2013 Community Summer Study on the Future of U.S. Particle Physics: Snowmass on the Mississippi (CSS2013): Minneapolis, MN, USA, July 29-August 6, 2013*, [1307.5487](#).
URL <http://inspirehep.net/record/1243859/files/arXiv:1307.5487.pdf>
- [8] ESTEBAN, I., M. C. GONZALEZ-GARCIA, M. MALTONI, I. MARTINEZ-SOLER, and T. SCHWETZ (2017) “Updated fit to three neutrino mixing: exploring the accelerator-reactor complementarity,” *Journal of High Energy*

- Physics*, **2017**, p. 87.
 URL [https://doi.org/10.1007/JHEP01\(2017\)087](https://doi.org/10.1007/JHEP01(2017)087)
- [9] (2018), “NuFit,” .
 URL www.nu-fit.org
- [10] GIUNTI, C. and C. W. KIM (2007) *Fundamentals of Neutrino Physics and Astrophysics*.
- [11] CLEVELAND, B. T., T. DAILY, R. DAVIS, JR., J. R. DISTEL, K. LANDE, C. K. LEE, P. S. WILDENHAIN, and J. ULLMAN (1998) “Measurement of the solar electron neutrino flux with the Homestake chlorine detector,” *Astrophys. J.*, **496**, pp. 505–526.
- [12] DZIEWONSKI, A. M. and D. L. ANDERSON (1981) “Preliminary reference earth model,” *Phys. Earth Planet. Interiors*, **25**, pp. 297–356.
- [13] PERL, M. L. ET AL. (1975) “Evidence for Anomalous Lepton Production in $e^+ - e^-$ Annihilation,” *Phys. Rev. Lett.*, **35**, pp. 1489–1492, [193(1975)].
- [14] LI, Z. ET AL. (2017) “A Measurement of the Tau Neutrino Cross Section in Atmospheric Neutrino Oscillations with Super-Kamiokande,” 1711.09436.
- [15] AARTSEN, M. G. ET AL. (2018) “Measurement of Atmospheric Neutrino Oscillations at 6–56 GeV with IceCube DeepCore,” *Phys. Rev. Lett.*, **120**(7), p. 071801, 1707.07081.
- [16] MARTEAU, J. (2007) “OPERA first events from the CNGS neutrino beam,” in *Electroweak Interactions and Unifield Theories: Proceedings, 42nd Rencontres de Moriond, La Thuile, Italy, March 10-17, 2007*, pp. 377–382, 0706.1699.
 URL <https://inspirehep.net/record/752927/files/arXiv:0706.1699.pdf>
- [17] AGAFONOVA, N. ET AL. (2015) “Discovery of τ Neutrino Appearance in the CNGS Neutrino Beam with the OPERA Experiment,” *Phys. Rev. Lett.*, **115**(12), p. 121802, 1507.01417.
- [18] ——— (2018) “Final Results of the OPERA Experiment on ν_τ Appearance in the CNGS Neutrino Beam,” *Phys. Rev. Lett.*, **120**(21), p. 211801, 1804.04912.
- [19] ”ABE, K. and OTHERS” (2013) “Evidence for the Appearance of Atmospheric Tau Neutrinos in Super-Kamiokande,” *Phys. Rev. Lett.*, **110**, p. 181802, 1206.0328.

- [20] WEINBERG, S. (2008) *Cosmology*, 1 ed., Oxford University Press.
- [21] AARTSEN, M. G. ET AL. (2013) “First observation of PeV-energy neutrinos with IceCube,” *Phys. Rev. Lett.*, **111**, p. 021103, 1304.5356.
- [22] ——— (2016) “Observation and Characterization of a Cosmic Muon Neutrino Flux from the Northern Hemisphere using six years of IceCube data,” *Astrophys. J.*, **833**(1), p. 3, 1607.08006.
- [23] ——— (2016) “Constraints on Ultrahigh-Energy Cosmic-Ray Sources from a Search for Neutrinos above 10 PeV with IceCube,” *Phys. Rev. Lett.*, **117**(24), p. 241101, [Erratum: *Phys. Rev. Lett.* 119, no. 25, 259902 (2017)], 1607.05886.
- [24] ZATSEPIN, G. T. and V. A. KUZMIN (1966) “Upper limit of the spectrum of cosmic rays,” *JETP Lett.*, **4**, pp. 78–80, [Pisma Zh. Eksp. Teor. Fiz. 4, 114 (1966)].
- [25] GREISEN, K. (1966) “End to the cosmic ray spectrum?” *Phys. Rev. Lett.*, **16**, pp. 748–750.
- [26] EICHLER, D. (1979) “HIGH-ENERGY NEUTRINO ASTRONOMY: A PROBE OF GALACTIC NUCLEI?” *Astrophys. J.*, **232**, pp. 106–112.
- [27] ALBERT, A. ET AL. (2018) “All-flavor Search for a Diffuse Flux of Cosmic Neutrinos with Nine Years of ANTARES Data,” *Astrophys. J.*, **853**(1), p. L7, 1711.07212.
- [28] (2018) “Neutrino emission from the direction of the blazar TXS 0506+056 prior to the IceCube-170922A alert,” *Science*, **361**(6398), pp. 147–151.
- [29] KATZ, U. F. and C. SPIERING (2012) “High-Energy Neutrino Astrophysics: Status and Perspectives,” *Prog. Part. Nucl. Phys.*, **67**, pp. 651–704, 1111.0507.
- [30] FUKUDA, Y. ET AL. (1998) “Evidence for oscillation of atmospheric neutrinos,” *Phys. Rev. Lett.*, **81**, pp. 1562–1567, hep-ex/9807003.
- [31] ACKERMANN, M. ET AL. (2013) “Detection of the Characteristic Pion-Decay Signature in Supernova Remnants,” *Science*, **339**, p. 807, 1302.3307.
- [32] ZUBER, K. (2011) *Neutrino Physics, Second Edition*, Series in High Energy Physics, Cosmology and Gravitation, Taylor & Francis.
URL <https://books.google.com/books?id=ODRaQiIINvkC>

- [33] AVE, M., P. BOYLE, E. BRANNON, F. GAHBAUER, G. HERMANN, C. HÖPPNER, J. HÖRANDEL, M. ICHIMURA, D. MÜLLER, A. OBERMEIER, and A. ROMERO-WOLF (2011) “The TRACER instrument: A balloon-borne cosmic-ray detector,” *Nuclear Instruments and Methods in Physics Research Section A: Accelerators, Spectrometers, Detectors and Associated Equipment*, **654**(1), pp. 140 – 156.
URL <http://www.sciencedirect.com/science/article/pii/S0168900211009934>
- [34] BIETENHOLZ, W. (2013) “The most powerful particles in the Universe: a cosmic smash,” 1305.1346.
- [35] TANABASHI, M. ET AL. (2018) “Review of Particle Physics,” *Phys. Rev.*, **D98**, p. 030001.
- [36] GAISSER, T. K. and M. HONDA (2002) “Flux of atmospheric neutrinos,” *Ann. Rev. Nucl. Part. Sci.*, **52**, pp. 153–199, [hep-ph/0203272](#).
- [37] GONDOLO, P., G. INGELMAN, and M. THUNMAN (1996) “Charm production and high-energy atmospheric muon and neutrino fluxes,” *Astropart. Phys.*, **5**, pp. 309–332, [hep-ph/9505417](#).
- [38] ENBERG, R., M. H. RENO, and I. SARCEVIC (2008) “Prompt neutrino fluxes from atmospheric charm,” *Phys. Rev.*, **D78**, p. 043005, [0806.0418](#).
- [39] GAISSER, T. K. and T. STANEV (1998) “Path length distributions of atmospheric neutrinos,” *Phys. Rev.*, **D57**, pp. 1977–1982, [astro-ph/9708146](#).
- [40] BERGHAUS, P. (2009) “Direct Measurement of the Atmospheric Muon Energy Spectrum with IceCube,” [0909.0679](#).
- [41] HONDA, M. (2016) “Atmospheric Neutrino Flux Calculation with NRLMSISE-00 Atmosphere Model and New Cosmic Ray Observations,” *JPS Conf. Proc.*, **12**, p. 010008.
- [42] PICONE, J. M., A. E. HEDIN, D. P. DROB, and A. C. AIKIN (2002) “NRLMSISE-00 empirical model of the atmosphere: Statistical comparisons and scientific issues,” *Journal of Geophysical Research (Space Physics)*, **107**, 1468.
- [43] CALDWELL, D. (2013) *Current Aspects of Neutrino Physics*, Springer Berlin Heidelberg.
URL <https://books.google.com/books?id=-UTtCAAAQBAJ>
- [44] RICHARD, E. ET AL. (2016) “Measurements of the atmospheric neutrino flux by Super-Kamiokande: energy spectra, geomagnetic effects, and solar modulation,” *Phys. Rev.*, **D94**(5), p. 052001, [1510.08127](#).

- [45] BARR, G. D., S. ROBBINS, T. K. GAISSER, and T. STANEV (2006) “Uncertainties in Atmospheric Neutrino Fluxes,” *Phys. Rev.*, **D74**, p. 094009, [astro-ph/0611266](#).
- [46] AARTSEN, M. G. ET AL. (2017) “The IceCube Neutrino Observatory: Instrumentation and Online Systems,” *JINST*, **12**(03), p. P03012, [1612.05093](#).
- [47] ABBASI, R. ET AL. (2012) “The Design and Performance of IceCube Deep-Core,” *Astropart. Phys.*, **35**, pp. 615–624, [1109.6096](#).
- [48] “ATWD FADC Description,” https://docushare.icecube.wisc.edu/dsweb/Get/Document-46800/Bootcamp2008_hits.pdf, accessed: 2010-09-30.
- [49] ABBASI, R. ET AL. (2009) “The IceCube Data Acquisition System: Signal Capture, Digitization, and Timestamping,” *Nucl. Instrum. Meth.*, **A601**, pp. 294–316, [0810.4930](#).
- [50] KELLEY, J. L. (2014) “Event triggering in the IceCube data acquisition system,” *AIP Conf. Proc.*, **1630**, pp. 154–157.
- [51] FORMAGGIO, J. A. and G. P. ZELLER (2012) “From eV to EeV: Neutrino Cross Sections Across Energy Scales,” *Rev. Mod. Phys.*, **84**, pp. 1307–1341, [1305.7513](#).
- [52] PATRIGNANI, C. ET AL. (2016) “Review of Particle Physics,” *Chin. Phys.*, **C40**(10), p. 100001.
- [53] (2012) *Fundamental Physics at the Intensity Frontier*, [1205.2671](#).
URL <http://inspirehep.net/record/1114323/files/arXiv:1205.2671.pdf>
- [54] WIKIPEDIA CONTRIBUTORS (2018), “Ice core – Wikipedia, The Free Encyclopedia,” [Online; accessed 20-May-2018].
URL https://en.wikipedia.org/w/index.php?title=Ice_core&oldid=841395305
- [55] GOW, A. J., H. T. UEDA, and D. E. GARFIELD (1968) “Antarctic Ice Sheet: Preliminary Results of First Core Hole to Bedrock,” *Science*, **161**(3845), pp. 1011–1013.
URL <http://www.jstor.org/stable/1725662>
- [56] MILLER, S. L. (1969) “Clathrate Hydrates of Air in Antarctic Ice,” *Science*, **165**(3892), pp. 489–490, <http://science.sciencemag.org/content/165/3892/489.full.pdf>.
URL <http://science.sciencemag.org/content/165/3892/489>

- [57] HONDOH, A. H. G. A. E. A., T. (1990) “The crystallographic structure of the natural air-hydrate in Greenland dye-3 deep ice core,” *Incl Phenom Macrocycl Chem.*
- [58] PRICE, P. B. (1995) “Kinetics of conversion of air bubbles to air hydrate crystals in Antarctic ice,” *Science*, **267**, p. 1802, [astro-ph/9501073](#).
- [59] ACKERMANN, M. ET AL. (2006) “Optical properties of deep glacial ice at the South Pole,” *J. Geophys. Res. Atmos.*, **111**(D13), p. D13203.
- [60] UCHIDA, T., W. SHIMADA, T. HONDOH, S. MAE, and N. I. BARKOV” *Appl. Opt.*,.
- [61] MIE, GUSTAV “Beiträge zur Optik trüber Medien, speziell kolloidaler Metallösungen,” *Annalen der Physik*, **330**(3), pp. 377–445, <https://onlinelibrary.wiley.com/doi/pdf/10.1002/andp.19083300302>.
URL <https://onlinelibrary.wiley.com/doi/abs/10.1002/andp.19083300302>
- [62] AARTSEN, M. G. ET AL. (2013) “Measurement of South Pole ice transparency with the IceCube LED calibration system,” *Nucl. Instrum. Meth.*, **A711**, pp. 73–89, [1301.5361](#).
- [63] CHIRKIN, D. “Evidence of optical anisotropy of the South Pole ice,” in *Proceedings, 33rd International Cosmic Ray Conference (ICRC2013): Rio de Janeiro, Brazil, July 2-9, 2013*, p. 0580.
URL <http://www.cbpf.br/%7Eicrc2013/papers/icrc2013-0580.pdf>
- [64] ANDREOPOULOS, C. ET AL. (2010) “The GENIE Neutrino Monte Carlo Generator,” *Nucl. Instrum. Meth.*, **A614**, pp. 87–104, [0905.2517](#).
- [65] HOSHINA, K., “GENIE high energy patch,” http://icecube.wisc.edu/~hoshina/blog/Special_Blog?cmd=post&id=7, 2014.
- [66] BODEK, A. and J. L. RITCHIE (1981) “Further Studies of Fermi Motion Effects in Lepton Scattering from Nuclear Targets,” *Phys. Rev.*, **D24**, p. 1400.
- [67] YANG, T., C. ANDREOPOULOS, H. GALLAGHER, and P. KEHAYIAS (2007) “A hadronization model for the MINOS experiment,” *AIP Conf. Proc.*, **967**, pp. 269–275.
- [68] KOBAYASHI, Z., H. B. NIELSEN, and P. OLESEN (1972) “Scaling of multiplicity distributions in high-energy hadron collisions,” *Nucl. Phys.*, **B40**, pp. 317–334.

- [69] SJOSTRAND, T., S. MRENNNA, and P. Z. SKANDS (2006) “PYTHIA 6.4 Physics and Manual,” *JHEP*, **05**, p. 026, [hep-ph/0603175](#).
- [70] GAZIZOV, A. and M. P. KOWALSKI (2005) “ANIS: High energy neutrino generator for neutrino telescopes,” *Comput. Phys. Commun.*, **172**, pp. 203–213, [astro-ph/0406439](#).
- [71] HECK, D., G. SCHATZ, T. THOUW, J. KNAPP, and J. N. CAPDEVIELLE (1998) “CORSIKA: A Monte Carlo code to simulate extensive air showers,” .
- [72] BECHERINI, Y., A. MARGIOTTA, M. SIOLI, and M. SPURIO (2006) “A parameterisation of single and multiple muons in the deep water or ice,” *Astroparticle Physics*, **25**(1), pp. 1 – 13.
URL <http://www.sciencedirect.com/science/article/pii/S092765050500157X>
- [73] KOEHNE, J. H., K. FRANTZEN, M. SCHMITZ, T. FUCHS, W. RHODE, D. CHIRKIN, and J. BECKER TJUS (2013) “PROPOSAL: A tool for propagation of charged leptons,” *Comput. Phys. Commun.*, **184**, pp. 2070–2090.
- [74] AGOSTINELLI, S. ET AL. (2003) “GEANT4: A Simulation toolkit,” *Nucl. Instrum. Meth.*, **A506**, pp. 250–303.
- [75] RADEL, L. and C. WIEBUSCH (2012) “Calculation of the Cherenkov light yield from low energetic secondary particles accompanying high-energy muons in ice and water with Geant 4 simulations,” *Astropart. Phys.*, **38**, pp. 53–67, 1206.5530.
- [76] KOPPER, C. ET AL., <https://github.com/claudiok/clsim>.
- [77] CHIRKIN, D. and W. RHODE (2004) “Muon Monte Carlo: A High-precision tool for muon propagation through matter,” [hep-ph/0407075](#).
- [78] LARSON, M. J. (2013), “SIMULATION AND IDENTIFICATION OF NON-POISSONIAN NOISE TRIGGERS IN THE ICECUBE NEUTRINO DETECTOR,” .
URL https://docushare.icecube.wisc.edu/dsweb/Get/Document-68303/LarsonThesis_final.pdf
- [79] “WaveDeform,” <http://software.icecube.wisc.edu/documentation/projects/wavedeform/index.html>, accessed: 2018-07-07.
- [80] AARTSEN, M. G. ET AL. (2014) “Energy Reconstruction Methods in the IceCube Neutrino Telescope,” *JINST*, **9**, p. P03009, 1311.4767.

- [81] WIEBUSCH, C. H. (2003) “Muon track reconstruction and data selection techniques in AMANDA,” in *Technical aspects of a Very Large Volume Neutrino Telescope in the Mediterranean Sea. Proceedings, Workshop, VLVnuT Workshop, Amsterdam, Netherlands, October 5-8, 2003*, pp. 129–133.
URL <http://www.vlvnt.nl/proceedings/>
- [82] AARTSEN, M. G. ET AL. (2015) “Determining neutrino oscillation parameters from atmospheric muon neutrino disappearance with three years of IceCube DeepCore data,” *Phys. Rev.*, **D91**(7), p. 072004, 1410.7227.
- [83] FERROZ, F., M. P. HOBSON, and M. BRIDGES (2009) “MultiNest: an efficient and robust Bayesian inference tool for cosmology and particle physics,” *Mon. Not. Roy. Astron. Soc.*, **398**, pp. 1601–1614, 0809.3437.
- [84] FERROZ, F., M. P. HOBSON, E. CAMERON, and A. N. PETTITT (2013) “Importance Nested Sampling and the MultiNest Algorithm,” 1306.2144.
- [85] LUNDBERG, J., P. MIOCINOVIC, T. BURGESS, J. ADAMS, S. HUNDERTMARK, P. DESIATI, K. WOSCHNAGG, and P. NIESSEN (2007) “Light tracking for glaciers and oceans: Scattering and absorption in heterogeneous media with Photonics,” *Nucl. Instrum. Meth.*, **A581**, pp. 619–631, astro-ph/0702108.
- [86] WHITEHORN, N., J. VAN SANTEN, and S. LAFEBRE (2013) “Penalized Splines for Smooth Representation of High-dimensional Monte Carlo Datasets,” *Comput. Phys. Commun.*, **184**, pp. 2214–2220, 1301.2184.
- [87] CONTRIBUTORS, W. (2018), “Bayes’ theorem — Wikipedia, The Free Encyclopedia,” [Online; accessed 25-February-2018].
URL https://en.wikipedia.org/w/index.php?title=Bayes%27_theorem&oldid=827199439
- [88] SKILLING, J. (2004) “Nested Sampling,” in *American Institute of Physics Conference Series* (R. Fischer, R. Preuss, and U. V. Toussaint, eds.), vol. 735 of *American Institute of Physics Conference Series*, pp. 395–405.
- [89] DUNKMAN, M. G. (2015) *Measurement of Atmospheric Muon Neutrino Disappearance with IceCube-DeepCore*, Ph.D. thesis, The Pennsylvania State University.
- [90] AGUILAR, J. A. ET AL. (2011) “A fast algorithm for muon track reconstruction and its application to the ANTARES neutrino telescope,” *Astropart. Phys.*, **34**, pp. 652–662, 1105.4116.
- [91] HOCKER, A. ET AL. (2007) “TMVA - Toolkit for Multivariate Data Analysis,” *PoS*, **ACAT**, p. 040, physics/0703039.

- [92] AHRENS, J. ET AL. (2004) “Muon track reconstruction and data selection techniques in AMANDA,” *Nucl. Instrum. Meth.*, **A524**, pp. 169–194, [astro-ph/0407044](#).
- [93] AARTSEN, M. G. ET AL. (2014) “Improvement in Fast Particle Track Reconstruction with Robust Statistics,” *Nucl. Instrum. Meth.*, **A736**, pp. 143–149, [1308.5501](#).
- [94] YANEZ, J. P., “Corridor Cut,” .
URL https://wiki.icecube.wisc.edu/index.php/DeepCore_CorridorCut
- [95] DUNKMAN, M., “IC86 Muon Disappearance Analysis,” .
URL https://wiki.icecube.wisc.edu/index.php/IC86_Muon_Disappearance_Analysis
- [96] NEYMAN, J. (1937) “Outline of a Theory of Statistical Estimation Based on the Classical Theory of Probability,” *Phil. Trans. Roy. Soc. Lond.*, **A236**(767), pp. 333–380.
- [97] FELDMAN, G. J. and R. D. COUSINS (1998) “A Unified approach to the classical statistical analysis of small signals,” *Phys. Rev.*, **D57**, pp. 3873–3889, [physics/9711021](#).
- [98] WILKS, S. S. (1938) “The Large-Sample Distribution of the Likelihood Ratio for Testing Composite Hypotheses,” *Annals Math. Statist.*, **9**(1), pp. 60–62.
- [99] ANDREOPOULOS, C., C. BARRY, S. DYTMAN, H. GALLAGHER, T. GOLAN, R. HATCHER, G. PERDUE, and J. YARBA (2015) “The GENIE Neutrino Monte Carlo Generator: Physics and User Manual,” [1510.05494](#).
- [100] ANDRES, E. ET AL. (2000) “The AMANDA neutrino telescope: Principle of operation and first results,” *Astropart. Phys.*, **13**, pp. 1–20, [astro-ph/9906203](#).
- [101] RONGEN, M. (2016) “Measuring the optical properties of IceCube drill holes,” *EPJ Web Conf.*, **116**, p. 06011.
- [102] DE ANDRÉ, J. P., https://wiki.icecube.wisc.edu/index.php/MSU_Forward_Hole_Ice.
- [103] RONGEN, M., <https://wiki.icecube.wisc.edu/index.php/SpiceHD>.
- [104] “DOMLauncher,” <http://software.icecube.wisc.edu/documentation/projects/DOMLauncher/DOML.html>, accessed: 2018-07-07.

Vita

Feifei Huang

Education **2012 - 2018: Ph.D., Physics, The Pennsylvania State University**
2008 - 2012: B.A., Physics, Wuhan University, China

Research **2013 - 2018: The Pennsylvania State University**
Graduate Research Assistant
Main project: Atmospheric tau neutrino appearance with IceCube/DeepCore.
Past Projects: The speed-up and optimization of the implementation of an event reconstruction algorithm, the dynamic range required for the proposed optical module called “pDOM” for the next generation of IceCube, buffer length, the effect of the timing variations, and the possible lowering of the ATWD sampling rate for the pDOM.

2011.08: IHEP (Institute of High Energy Physics), China
Undergraduate summer research, the WCDA (Water Cherenkov Detector Array) group of LHAASO (Large High Altitude Air Shower Observatory)

Teaching **Department of Physics, The Pennsylvania State University**
2012 - 2014: Teaching Assistant, Undergraduate physics courses

Talks **2018.06: CIPANP (Conference on the Intersections of Particle and Nuclear Physics), CA, USA**
IceCube Results on Neutrino Properties with Atmospheric Neutrinos

Acronyms

ATWD Analog Transient Waveform Digitizer. 32–34

BDT Boosted Decision Tree. 36, 57

CORSIKA COsmic Ray SIMulations for KAScade. 48, 140

DAQ Data Acquisition System. 34, 35

DIS deep inelastic scattering. 37, 38

DOM Digital Optical Modules. 29, 30, 32–34, 36, 39, 41

EM electromagnetic. 48

FADC Fast Analog to Digital Converter. 32

FPGA Field-Programmable Gate Array. 32

HLC Hard Local Coincidence. 34

HQE High Quantum Efficiency. 30

LC Local Coincidence. 33, 34

MMC Muon Monte Carlo program. 48, 49

MSW Mikheyev–Smirnov–Wolfenstein effect. 10

PE photoelectron. 33, 67, 71

PMT photomultiplier tube. 29

PnF Processing and Filtering. 35

PREM Preliminary Reference Earth Model. 10

QE quasi-elastic. 37

RES resonance production. 37

RFG Relativistic Fermi Gas. 47

RTV Room-Temperature-Vulcanizing. 33

SANTA The Single string ANTares-inspired Analysis. 50, 63

SLC Soft Local Coincidence. 34

SLOP Slow Particle (SLOP) trigger. 34

SMT Simple Multiplicity Trigger. 34

SPICE South Pole Ice. 43, 49